



**TECHNISCHE
UNIVERSITÄT
WIEN**

DISSERTATION

**Optimization of biotransformations in *Escherichia coli*:
from biocatalyst to the process level**

ausgeführt zum Zwecke der Erlangung des akademischen Grades eines
Doktors der technischen Wissenschaften unter der Leitung von

**Univ. Ass. Dipl.-Ing. Dr. techn. Florian Rudroff und
Univ.-Prof. Dipl.-Ing. Dr. techn. Marko D. Mihovilovic**

Institut für Angewandte Synthesechemie

eingereicht an der Technischen Universität Wien
Fakultät für Technische Chemie

von

Sofia Milker, M.Sc.

Matrikelnummer: 1229600

Singrienergasse 5/7

1120 Wien

Wien, 14.08.2017

The two most powerful warriors are patience and time.
- Leo Tolstoy

Acknowledgements

After the long and hard journey to finally finish this scientific novel, I have to thank a few people, without whom this adventure would not have been possible.

First, I want to thank Prof. Marko D. Mihovilovic for the possibility to prepare this thesis in his research group. The interdisciplinary research group taught me a lot and I definitely have a better understanding for chemists and their way of thinking.

Second, I want to thank Dr. Florian Rudroff that I could work with him on his FWF project (P-24483-B20) and in the COST action Systems Biocatalysis, visit exciting summer schools and conferences, learn a lot and of course publish several papers.

My thanks also go to the external correctors of this thesis, Dr. Roland Ludwig and Dr. Oliver Spadiut.

Speaking of: Oliver and his students Britta Eggenreich, Vignesh Rajamanickam, Thomas Gundinger and Alexandra Hofer I also want to thank for the help with preparation of internal standards for metabolomics, fun with successful and unsuccessful fermentations, protein purification and overall a very friendly and welcoming atmosphere. Thank you guys!

Petra Volejnik and Benedikt Putz I want to thank for their help with the HPLC-MS/MS system.

I want to thank Michael Fink for the very fruitful work and extremely fast paper corrections. It has been a scientific pleasure and I've learned a lot!

A big shout-out goes to Florian Untersteiner, the man who is responsible for almost everything, you can imagine. A big thanks for all your help, funny discussions and Mr. Robot references!

I want to thank my dear colleagues on bio projects, who made everything better.

Thomas Wiesinger, Thomas Bayer and Patricia Schaaf: we started together and you have been there all the way. Wiesi, thank you for your wise words on life! The concept of babysteps will be remembered. Thomas, I want to thank you for everything you've done for me, all the work-related and non-work related support! Even working late is fun when you're around! Trisch, thank you for your very pragmatic and straight-forward advice. It helped a lot!

Leticia Goncalves I want to thank for so many things: the help and advice in research, her advice on life, her friendship and support, and her soup when I got sick. You are one of

the most caring and wonderful people I know!

Nikolin Oberleitner and Anna Ressmann I want to thank for the fun in the biolab and their advice how to survive a PhD. Without Marcello Entner, Jakob Reiterlehner and Hamid Mansouri the work would have been less fun. In general, I want to thank all the people that have inhabited the biolab in the last years.

Of course I want to thank all present and past members of the FGMDM group. I want to thank Christian Stanetty for interesting discussions. You get an award for being a great office neighbour! Michael Schnürch I want to thank for always having an open door. Many thanks to Dominik Dreier and Markus Draskovits for the fun in the breaks between all the work. Laszlo Czollner and Irena Jelenkovic-Didic I want to thank for all their assistance with the HPLC. I want to thank the (now) all-girls lab - Rafaela, Blanca, Daniela, Leila and Maria-Theresa - for your uplifting positivity, especially in the last months of my practical work.

Last but not least, my biggest thank you goes to my friends and family. You always kept me grounded, showed me that working towards a PhD is just a tiny bubble in this big world and reminded me of the things that matter. Your unshakable believe in me kept me going. Thank you.

Abstract

This thesis deals with tools for optimization of biocatalytical transformations. The optimization of biocatalysis should be performed on different levels: on the catalyst level, on the fermentation/cultivation level, and on the process level as well as the downstream processing (DSP) level. All levels contribute to the enhancement of productivity and examples for their optimization are given in the following theses.

In the first chapter, the optimization was performed on all the levels mentioned above. The development of a biocatalytic process on the multi-dozen gram scale for the synthesis of a precursor to Nylon-9, a specialty polyamide, was established. Such materials are growing in demand, but their corresponding monomers are often difficult to synthesize, giving rise to biocatalytic approaches. Here, the cyclopentadecanone monooxygenase as an *Escherichia coli* (*E. coli*) whole-cell biocatalyst was chosen as a catalytic entity and produced in a stable expressing system (biocatalyst level) in a defined medium, which was optimized prior to up-scaling (cultivation level). Together with the implementation of a substrate feeding-product removal concept, an DSP was established (process/DSP level). A previously described hazardous peracid-mediated oxidation was thus replaced with a safe and scalable protocol, using aerial oxygen as oxidant and water as reaction solvent. The engineered process converted 42 g (0.28 mol) starting material ketone to the corresponding lactone with an isolated yield of 70 % (33 g), after highly efficient DSP with 95 % recovery of the converted material, translating to a volumetric yield of 8 g pure product per liter.

Subsequently, the possibility of optimization on whole-cell biocatalyst level was investigated. A kinetic model for the simulation and optimization of an *in vivo* redox cascade in *E. coli*, using a combination of an alcohol dehydrogenase, an enoate reductase, and a Baeyer-Villiger monooxygenase (CHMO) for the synthesis of lactones was developed. The model was used to estimate the concentrations of active enzyme in the sequential biotransformations to identify bottlenecks together with their reasons and how to overcome them. The adapted Michaelis-Menten parameters from *in vitro* experiments with isolated enzymes were estimated, and these values were used to simulate the change in concentrations of intermediates and products during the *in vivo* cascade reactions. The model indicated the CHMO, the fastest enzyme, to be rate-determining due to the low concentration of the active form, opening up reversible reaction channels towards side products. Substantial experimental evidence was provided, that a low intracellular concentration of flavin and nicotinamide cofactors drastically throttled the performance of the *in vivo* cascade.

As a next step, the performance of the CHMO in a whole-cell catalyst was investigated to obtain knowledge about its poor performance *in vivo* and to propose optimization strategies (catalyst level). The measurement of *in vivo* activity and stability of the CHMO in the recombinant host *E. coli* was performed. This enzyme was often described as poorly stable *in vitro*, and has recently been found to deactivate rapidly in the absence of its essential cofactors and of anti-oxidants. Additionally, it was identified as the rate limiting step of an

enzymatic cascade in the previous chapter. Its stability *in vivo* was scarcely studied, so far. The activity and stability of CHMO in *E. coli* during common conditions for over-expression was measured, and the ability of the host to support these properties by metabolomics analyses was investigated. The results showed that *E. coli* failed to provide the intracellular levels of cofactors required to functionally stabilize CHMO, although the biocatalyst was produced in high concentration, and was invariably detectable after protein synthesis had stopped. Biotechnological applications in this host possibly relied on a residual activity of approx. 5 %. Other microorganisms might thus offer a more efficient solution for recombinant production of CHMO, and related enzymes.

As the last optimization step on the catalyst and cultivation level, an *in vivo* characterization of dihydroxyacetone kinase (DhaK) expressed in *E. coli* was presented with regard to physiological and metabolic changes compared to *E. coli* wt strain. This enzyme can facilitate aldol reactions *in vivo* by increasing intracellular dihydroxyacetone phosphate (DHAP, aldol donor molecule) concentrations. The DhaK phosphorylates dihydroxyacetone (DHA) to DHAP by consuming ATP. Overall, despite the metabolic burden of plasmid maintenance and protein expression, the DhaK strain showed similar physiological behavior compared to the wt strain. In contrast to *E. coli* wt, the DhaK strain took up DHA during the exponential growth phase and showed higher intracellular concentrations of DHAP. Metabolomics analysis also indicated that the pool of ATP, which is needed for the enzymatic phosphorylation of DHA, was too low under non-growing conditions, so that the reaction could only proceed during exponential growth. Modeling both strains revealed the possibility of bypassing the upper glycolysis by expressing DhaK and feeding DHA, which needs to be investigated further with carbon source ¹³C labeling by dynamic metabolomics approaches. In summary, the presented system was modeled together with an aldol producing enzymatic cascade in *E. coli* and was found to be of benefit for DHAP-dependent aldol reactions *in silico*.

The combination of the different levels of optimization applied in this theses - accompanied by the methods modeling, metabolomics and optimizational tools for reaction design - were successfully applied to facilitate biotransformations in living systems.

Kurzfassung

Diese Dissertation behandelt Methoden, die für eine Optimierung biokatalytischer Transformationen nützlich sind. Optimierungen von biokatalytischen Prozessen sollten in verschiedenen Projektphasen durchgeführt werden: in der Phase der Katalysatorentwicklung, der Fermentations-/Kultivierungsentwicklung und der Bioprozess- sowie der Produktaufarbeitungsentwicklung. Verbesserungen in allen genannten Phasen tragen zur Produktivitätssteigerung bei. Beispiele für solche Optimierungen sind in dieser Dissertation aufgeführt.

Im ersten Kapitel wurde die Biotransformation in allen vier im letzten Abschnitt genannten Phasen optimiert. Ein biokatalytischer Prozess zur Synthese von Nylon-9, einem Spezialpolymer, wurde in der Grössenordnung von mehreren Dutzend Gramm etabliert. Die Nachfrage nach Spezialpolymeren wie Nylon-9 wächst; jedoch ist die chemische Synthese der entsprechenden Monomere oft kompliziert. Diese Tatsache erleichtert die Etablierung biokatalytischer Syntheseverfahren. In dieser Arbeit wurde Cyclopendadecanone Monooxygenase (CPDMO) in *Escherichia coli* als Ganzzellkatalysator verwendet. Das Expressionssystem wurde angepasst, um stabile Expression des Enzyms zu garantieren (Phase der Katalysatorentwicklung). Die Expression wurde in einem definierten und optimierten Medium etabliert (Phase der Kultivierungsentwicklung). Die Implementierung des "Substrat-Feed-Product-Removal" (SFPR) Konzepts mit der entsprechenden Produktaufarbeitung rundete die Optimierung des Prozesses ab (Phase der Bioprozess-/Produktaufarbeitungsentwicklung). In dem Prozess wurde eine vorher beschriebene, gefährliche Persäure-katalysierte Oxidation durch einen sicheren und skalierbaren biokatalytischen Prozess mit Sauerstoff als Oxidant und Wasser als Lösungsmittel ersetzt. Der verbesserte Prozess setzte 42 g (0.28 mol) Keton zum entsprechenden Lakton um. Die isolierte Ausbeute nach einer sehr effizienten Produktaufarbeitung mit 95 % Wiederfindung der umgesetzten Stoffmenge betrug dabei 70 % (33 g), was einer volumetrischen Ausbeute von 8 g pures Lakton pro Liter Kulturvolumen entsprach.

Im Folgenden wurde die Möglichkeit der Optimierung eines Ganzzellkatalysators untersucht (Phase der Katalysatorentwicklung). Ein kinetisches Modell für die Simulation und Optimierung einer enzymatischen *in vivo* Redox-Kaskade in *Escherichia coli* (*E. coli*) wurde erstellt, bestehend aus der Kombination einer Alkoholdehydrogenase (ADH), einer Enoatreduktase (ERED) und einer Baeyer-Villiger Monooxygenase (BVMO, speziell Cyclohexanone Monooxygenase (CHMO)). Die Kaskade diente zur Synthese von Laktonen. Das Modell wurde verwendet, um die aktiven intrazellulären Enzymkonzentrationen in den sequenziellen Biotransformationen zu bestimmen und um daraufhin den Engpass in der Laktonproduktion zu identifizieren sowie Optimierungsstrategien zu erstellen. Die in *in vitro* Experimenten mit isolierten Enzymen ermittelten Michaelis-Menten Parameter wurden verwendet, um die Verläufe der Intermediat- und Produktkonzentrationen in den *in vivo* Kaskadenreaktionen zu simulieren. Das Modell zeigte, dass das schnellste Enzym, die CHMO, der geschwindigkeitsbestimmende Schritt der Kaskade war. Der Grund dafür war die geringe Konzentration der aktiven Form des Enzyms, die die Bildung von reversiblen Nebenreaktionen ermöglichte. Es

wurde ein wesentlicher experimenteller Beweis erbracht, dass die geringe Konzentration an Flavin- und Nicotinamidkofaktoren der Grund für die drastisch verminderte Leistung der *in vivo* Kaskade verantwortlich waren.

Als Nächstes wurde das Verhalten von CHMO im Ganzzellsystem untersucht, um Gründe für die geringe Leistung *in vivo* zu finden sowie um Optimierungsstrategien zu erarbeiten (Phase der Katalysatorentwicklung). Die Messungen der *in vivo* Aktivität und Stabilität der CHMO erfolgten im *E. coli* Ganzzellsystem. Die CHMO wurde oft als *in vitro* instabil beschrieben. Vor Kurzem wurde postuliert, dass sich das Enzym in Abwesenheit von notwendigen Kofaktoren und Antioxidantien sehr schnell deaktiviert. Zudem wurde das Enzym im letzten Kapitel als der geschwindigkeitsbestimmende Schritt einer im Ganzzellsystem exprimierten enzymatischen Kaskade identifiziert. Jedoch wurde die *in vivo* Stabilität dieses Enzyms soweit kaum erforscht. Die Aktivität und Stabilität der CHMO wurde unter gängigen *E. coli* Expressionsbedingungen gemessen sowie die Fähigkeit des Wirtsorganismus diese Eigenschaften der CHMO aufrechtzuerhalten mittels Metabolomics analysiert. Es zeigte sich, dass *E. coli* nicht in der Lage war, die notwendigen Kofaktorkonzentrationen bereitzustellen, die notwendig sind, um CHMO zu stabilisieren. Dennoch wurde die CHMO in ausreichenden Konzentrationen im *E. coli* produziert und die Konzentrationen waren nach der Produktion für den Zeitraum der Messungen bis zum Experimentende unverändert. Biotechnologische Anwendungen in diesem Wirtsorganismus mussten somit bisher mit der Restaktivität der CHMO von 5 % auskommen. Deswegen könnten andere Mikroorganismen effizientere Produktionsplattformen für die Produktion der CHMO und verwandter Enzyme bieten.

Als letzter Optimierungsschritt in der Phasen der Katalysator- und Kultivierungsentwicklung wurde die *in vivo* Charakterisierung der Dihydroxyacetonkinase (DhaK), produziert in *E. coli*, präsentiert. Der Schwerpunkt lag dabei auf den physiologischen und metabolischen Veränderungen im Expressionssystem im Vergleich mit dem *E. coli* Wildstamm. Die DhaK kann zur Synthese von Dihydroxyacetonphosphat (DHAP) aus Dihydroxyaceton (DHA) unter ATP Verbrauch eingesetzt werden und könnte somit zur Erleichterung von Aldolreaktionen *in vivo* dienen, da DHAP für viele Aldolasen ein Donormolekül darstellt. Trotz der metabolischen Last der Enzymsynthese und Plasmiderhaltung, zeigte der DhaK Stamm ähnliche physiologische Charakteristika wie der Wildtyp. Im Gegensatz zum Wildtyp, zeigte die DhaK Mutante Aufnahme von DHA sowie erhöhte intrazelluläre DHAP Konzentrationen während des exponentiellen Wachstums. Die Metabolomanalyse zeigte, dass der ATP Pool, der für die enzymatische Phosphorylierung von DHA benötigt wird, während der nicht-wachsenden Bedingungen zu gering war und diese somit nur unter wachsenden Bedingungen stattfinden konnte. Die Modellierung beider Stämme zeigte die Möglichkeit eines Bypasses der oberen Glykolyse durch die Expression der DhaK und die Zugabe von DHA. Diese Ansätze bedürfen weiterer Untersuchungen, vor Allem mit ¹³C-Metabolischer Flussanalyse. Abschliessend wurde das vorgestellte System mit einer Aldolproduzierenden enzymatischen Kaskade in *E. coli* modelliert und *in silico* als förderlich für DHAP-abhängige Aldolreaktionen befunden.

Die Optimierungen der verschiedenen Phasen einer biokatalytischen Transformation wurden in dieser Arbeit kombiniert angewendet und verschiedene Methoden wurden unterstützend herangezogen - Modellierung, Metabolomanalyse und Optimierungen im Reaktionsdesign. Diese wurden erfolgreich angewendet, um Biotransformationen in lebenden Ganzzellsystemen zu ermöglichen.

Contents

Acknowledgements	i
Abstract	iii
Kurzfassung	v
1 General introduction	1
1.1 Biocatalysis - chemistry with enzymes as catalysts	1
1.2 Single redox biotransformations and redox cascades	2
1.3 Methods to overcome challenges in biocatalysis	6
1.3.1 Biocatalyst development	7
1.3.2 Fermentation/cultivation development	8
1.3.3 Process and DSP development	8
1.4 Productivity enhancement by <i>in vivo</i> and <i>in silico</i> strategies	11
1.4.1 Metabolomics: quantification of intracellular metabolites	27
1.5 Scope of this thesis	29
2 Results and discussion	31
2.1 Upscaling of a cyclopentadecanone monooxygenase (CPDMO) whole-cell biotransformation towards polyamide-9 precursors	31
2.1.1 General aspects	31
2.1.2 Baeyer-Villiger monooxygenases (BVMOs)	33
2.1.3 Selection of a suitable biocatalyst	35
2.1.4 Comparison of different expression systems for CPDMO performance	37
2.1.5 Transfer to a controlled bioreactor and optimization of the cultivation	40
2.1.6 Substrate-feed-product-removal (SFPR) concept facilitates up-scaling to a higher ketone titer	44
2.1.7 Downstream processing	52
2.1.8 Conclusion and outlook	54
2.2 Kinetic modeling of an enzymatic redox cascade <i>in vivo</i>	55
2.2.1 General aspects	55
2.2.2 Development of the kinetic model	59
2.2.3 Tagging, expression and purification of the cascade enzymes	61
2.2.4 Determination of inhibition parameters of ethanol on LK-ADH	77
2.2.5 Determination of Michaelis-Menten parameters	81
2.2.6 Modeling of the cascade reactions	87
2.2.7 Conclusion and outlook	101
2.3 Stability and activity of the prominent BVMO cyclohexanone monooxygenase CHMO _{Acineto} <i>in vivo</i>	102
2.3.1 General aspects	102
2.3.2 Development of hypothesis and their experimental validation	104

2.3.3	Establishment of conditions for CHMO expression	107
2.3.4	Preparation of ¹³ C internal standard for metabolomics	108
2.3.5	CHMO bioprocess in whole cells - elucidating stability, activity and metabolomics	111
2.3.6	Conclusion and outlook	126
2.4	Characterization and stoichiometric modeling of a system connected to the central carbon metabolism of <i>E. coli</i> for boosting DHAP - dependent aldolase activity <i>in vivo</i>	127
2.4.1	General aspects	127
2.4.2	Model development	131
2.4.3	Pareto-analysis for cascade optimization	132
2.4.4	Dihydroxyacetone kinase as a tool for increasing intracellular DHAP concentrations	139
2.4.5	Stoichiometric modeling of the influence of a DHAP - producing reaction <i>in vivo</i> on intracellular fluxes of <i>E. coli</i>	147
2.4.6	Development of a HPLC-MS/MS method for measurement of isotopomers to perform ¹³ C-metabolic flux analysis (¹³ C-MFA)	152
2.4.7	Conclusion and outlook	157
2.5	Conclusion and outlook of the thesis	158
3	Experimental Part	161
3.1	Chemicals and materials	161
3.2	Bacterial strains, culture conditions and plasmids	161
3.2.1	Lysogeny Broth (LB) medium	161
3.2.2	Teriffic Broth (TB) medium	161
3.2.3	LB-0.8G medium	162
3.2.4	Autoinduction medium (AIM)	162
3.2.5	M9 medium	162
3.2.6	Verduyn medium	163
3.2.7	Antibiotics and inducers	165
3.2.8	Permanent cultures and working cryo stocks	165
3.3	General methods	166
3.3.1	Agarose gel electrophoresis	166
3.3.2	Chemical transformation of plasmids into <i>E. coli</i> cells	166
3.3.3	SDS-PAGE	167
3.3.4	OD measurements	170
3.3.5	OTR/CTR calculations <i>via</i> the gas-balancing method	170
3.4	Preparation of labeled ¹³ C-internal standard for metabolomics	171
3.4.1	Yeast fermentation with labeled ¹³ C - glucose	171
3.4.2	Quenching procedure of the fermentation broth	172
3.4.3	Extraction of labeled biomass	172
3.5	Preparation of the metabolomics MonsterMix for calibration of the LC-MS/MS	173
3.6	Biocatalytic oxidation of nylon-9 monomer by CPDMO	178
3.6.1	Cultivation media	178
3.6.2	Preculture cultivation	178
3.6.3	Cloning of the CPDMO into the pET26b(+) vector	178
3.6.4	Cultivation experiments for the characterization of CPDMO constructs on the shake flask scale	179

3.6.5	Conditions for scale-up reactor experiments	179
3.6.6	CPDMO activity measurement after the SFPR biotransformation . . .	180
3.6.7	Downstream processing	180
3.6.8	Analytical techniques	181
3.6.9	Fitting of the biomass concentration curve	182
3.6.10	Carbon balancing	183
3.7	Cloning, expression and purification of the stand-alone cascade (SAC) enzymes	183
3.7.1	Tagging of the alcohol dehydrogenase from <i>Lactobacillus kefir</i> (LK-ADH) with a His-Tag	183
3.7.2	Tagging of the alcohol dehydrogenase from <i>Lactobacillus kefir</i> (LK-ADH) with an intein-CBD-Tag	184
3.7.3	Control digest with <i>PvuII</i> restriction enzyme	186
3.7.4	Expression of the different cascade enzymes	187
3.7.5	Enzyme purification <i>via</i> affinity chromatography	188
3.7.6	Partial enzyme purification <i>via</i> centrifugal devices with a 50 kDa cut-off	189
3.7.7	Thrombin restriction of the LK-ADH-His ₆ construct	189
3.8	Activity assays of the stand-alone cascade (SAC)	190
3.8.1	Activity assay for LK-ADH	190
3.8.2	Activity assay for XenB	191
3.8.3	Activity assay for CHMO _{acineto}	191
3.9	Kinetic parameter estimation for the stand-alone cascade (SAC)	192
3.10	Synthesis of non-commercial substrates for kinetic measurement	193
3.10.1	Synthesis of (2 <i>R</i> ,5 <i>S</i>)-dihydrocarvone 7c	193
3.10.2	Synthesis of 2-methylcyclohex-2en-1-ol 8a	194
3.11	Biocatalytic screenings of the stand-alone cascade (SAC)	195
3.12	Stability and activity of CHMO <i>in vivo</i>	196
3.12.1	Bacterial strain and culture conditions in the fermentation	196
3.12.2	Physiology	196
3.12.3	Quantification of soluble CHMO	196
3.12.4	<i>E. coli</i> Metabolomics	197
3.12.5	LC-MS/MS measurements	197
3.12.6	CHMO activity measurements <i>in vivo</i>	198
3.12.7	Propagation of uncertainty	198
3.13	Characterization of dihydroxyacetone kinase (DhaK) in <i>E. coli</i>	199
3.13.1	Physiology	199
3.13.2	Metabolomics measurements	199
3.14	Stoichiometric modeling of the different <i>E. coli</i> constructs	200
3.14.1	Model construction	200
3.14.2	Pareto analysis	208
3.14.3	Method development for ¹³ C metabolic flux analysis	209

Curriculum Vitae and List of Publications	212
4 Bibliography	215
List of Figures	231
List of Tables	235

1 General introduction

1.1 Biocatalysis - chemistry with enzymes as catalysts

The use of microorganisms for production of various products e.g. beer, wine and bread has been established for several thousand years. The use for production of chemical compounds from other chemical building blocks, however, began approximately a century ago^[1], starting with basic industrially relevant applications^[2] and developing into more complex biocatalytic processes e.g. the production of acrylamide from acrylonitrile^[3] (Fig. 1.1 A) or synthesis of semi-synthetic antibiotics by acylases (Fig. 1.1 B).^[4]

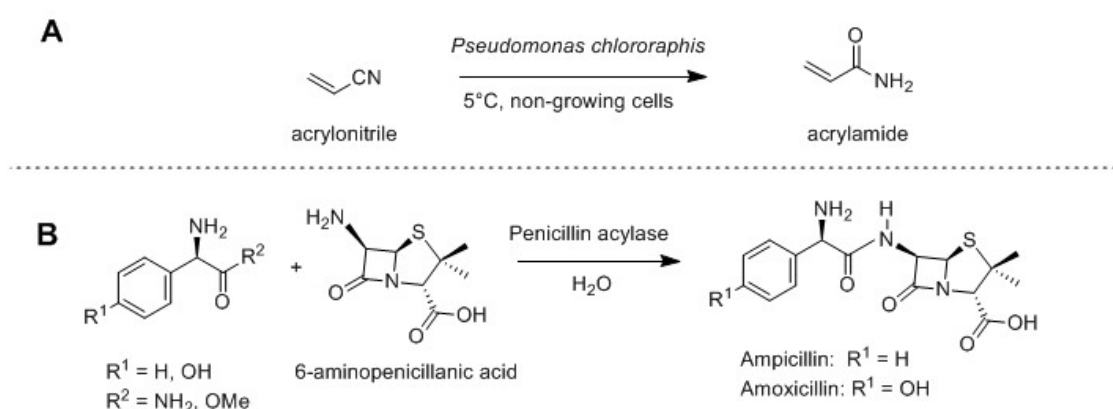


Figure 1.1: Biocatalytic examples: A: production of acrylamide from acrylonitrile by *Pseudomonas chlororaphis*^[3] and B: production of antibiotics by penicillin acylase.^[4]

The biocatalytic synthesis is coupled with challenges that need to be overcome to obtain a high performance. In the following chapters, the different types of biotransformations are explained. After introduction of typical biotransformation processes, the different possible levels for development of a biocatalytic transformation are discussed along with possible methods to overcome arising limitations.

1.2 Single redox biotransformations and redox cascades

There are many ways to establish a biotransformation process. The biotransformation can be performed either *in vitro* or *in vivo*. In the *in vitro* case, redox enzymes have to be supplemented with cofactors and a cofactor recycling system for a redox reaction.^{[5][6]} To avoid the addition of a cofactor recycling system, many redox biotransformations are performed in whole-cells (*in vivo*). In a whole-cell system, the host cell is recycling the required cofactors e.g NADPH/NADPH/ATP for the redox enzyme, which is catalyzing the desired reaction. However, sometimes the *in vitro* use of isolated enzymes for biocatalysis is required, e.g. when a competing enzymatic reaction is taking place in the host cell, either consuming the substrate or the product of the biotransformation reaction (Figure 1.2). However, for the use of cell-free extracts or isolated enzymes, it is important that the enzymes are stable in a cell-free environment.^[7] A possible circumvention of that problem would be a modification of the host cell, by removing the competing enzymatic activity (Knock-out; KO).

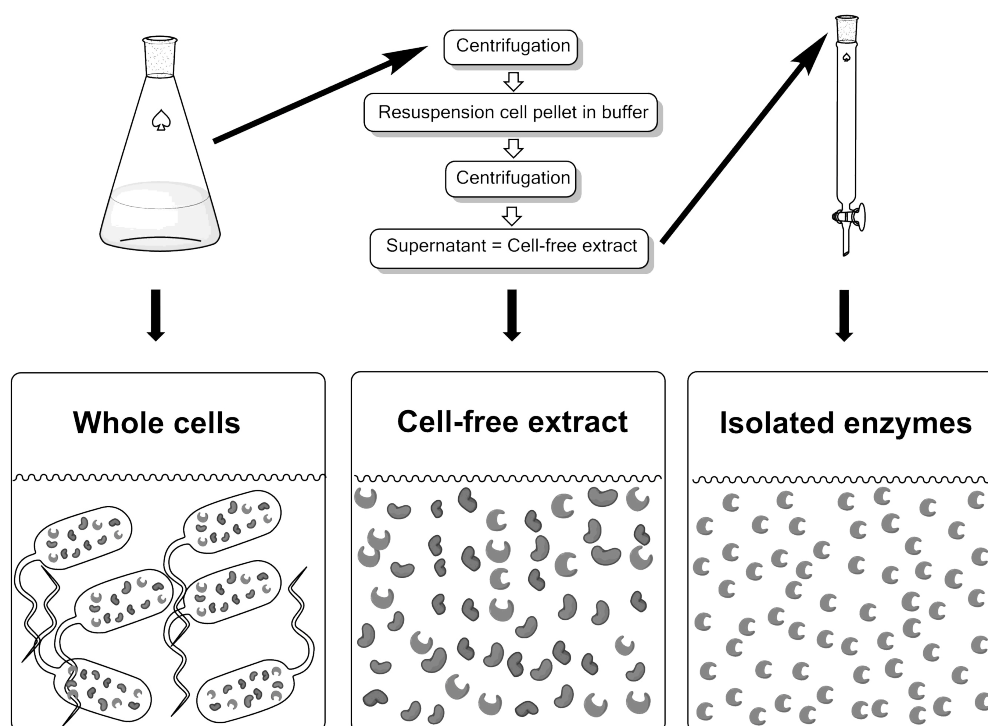


Figure 1.2: From whole cells, to cell-free extracts and isolated enzymes as biocatalysts.

A single biotransformation step can be useful. However, if a multi-step synthesis of a com-

pound is required, the execution of each step separately can be tedious and time-consuming. Therefore, multistep biotransformations were developed, also known as biocatalytic cascades. In this case, non-related enzymes are combined in one vessel (*in vitro*) or one host (*in vivo*). The reaction sequence is then performed without purification of the intermediates, yielding the desired product.

The *in vivo* cascades can be constructed in two different ways. Linear enzymatic cascades do not share common intermediates with the host metabolism except for a possible consumption of redox equivalents, which are recycled by the host. The second type of cascades is connected to the carbon metabolism of the host and uses next to the recycling system of the host also cell intermediates for cascade reactions. This is especially beneficial, if the used cell intermediates are complicated to synthesize or are instable under *in vitro* conditions.

In the last years there has been a lot of progress concerning the construction of enzymatic cascades *in vivo*.^{[8][9]} Turner and coworkers have reported the generation of a successful whole-cell *de novo* enzyme cascade for the diastereoselective and/or enantioselective conversion of linear keto acids into valuable cyclic amine products (Figure 1.3).^[10]

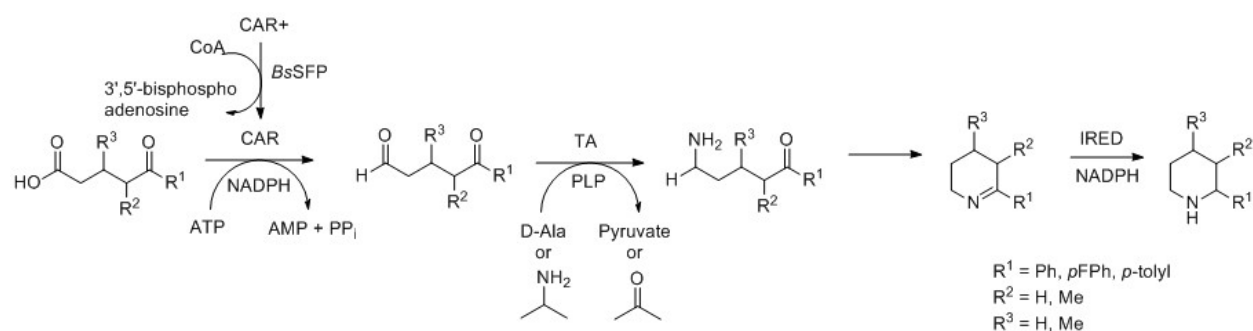


Figure 1.3: Whole-cell synthesis of chiral cyclic amines

BsSFP: 4'-phosphopantetheinyl transferase; *CAR*: carboxylic acid reductase; *TA*: transaminase; *IRE*D: imine reductase

Two different carboxylic acid reductases, transaminases and imine reductases were used for construction of several cascades to be able to convert keto acids diastereo- and /or enantioselectively. The whole process was carried out in *E. coli* with conversions of up to 93% and high enantiomeric excess (93%).

In another example for whole-cell biocatalysis with *de novo* cascades, Foo *et al.* established a two step *de novo* cascade in *Saccharomyces cerevisiae* (*S. cerevisiae*) for production of alkenes from fatty acids (Figure 1.4).^[11]

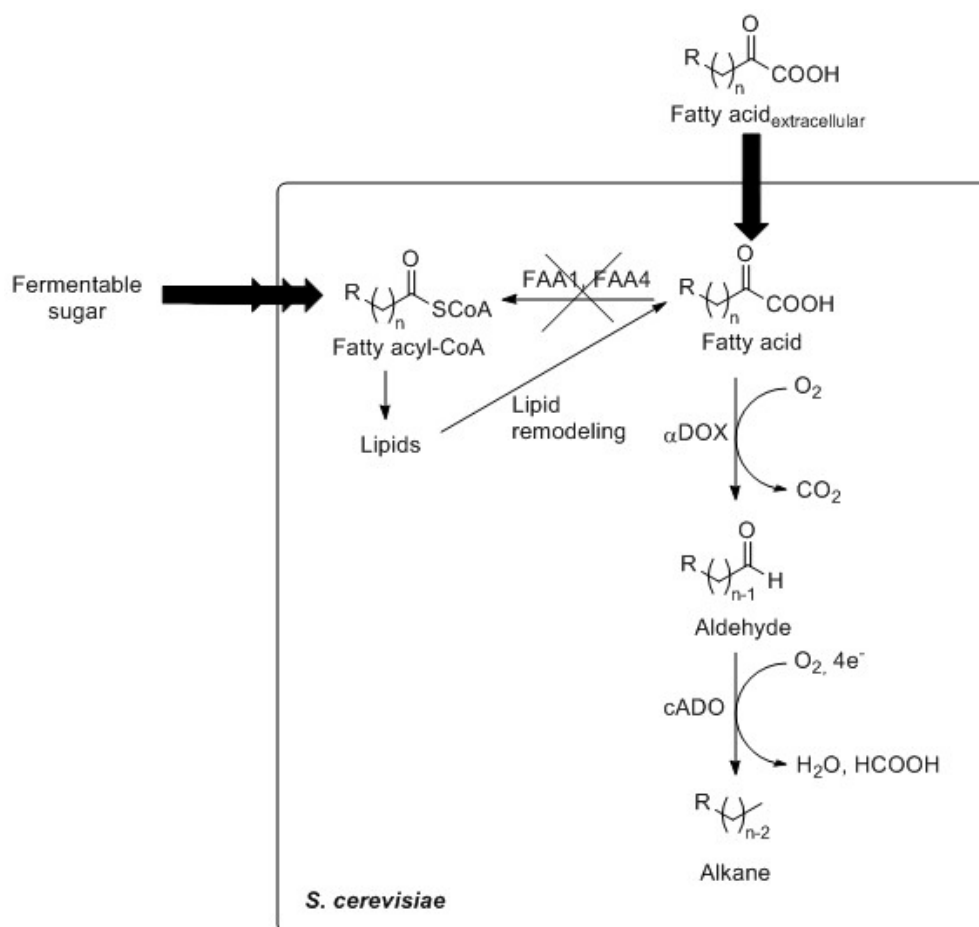


Figure 1.4: Whole-cell synthesis of alkanes from free fatty acids

α DOX: α -dioxygenase; cADO: cyanobacterial aldehyde deformulating oxygenase. FAA1 and FAA4 deletion enabled accumulation of free fatty acid precursors from intracellular pathways.

The final titers were up to 4 mg L^{-1} culture depending on the specific fatty acid and bio-transformation condition. The authors noted that this was only a proof of principle and that this system can be improved further, e.g. by exchanging the enzymes by more productive variants.

Even though the construction of enzymatic cascades *in vivo* has made a lot of progress, such cascades in whole-cell biocatalysts have to overcome several obstacles on different levels. In general, the tight interaction between the newly introduced pathway and the metabolism of

the host on the genetic as well as on the metabolic level may result in increased probability of side reactions, competition for metabolites (e.g. redox cofactors), toxicity of pathway intermediates and, therefore, decreased overall productivity^[12] (Figure 1.5). Other factors may include the burden of plasmid maintenance and protein expression, which increases with increased *de novo* pathway complexity. The host organism is usually able to cope with the burden of overexpressing one enzyme, but can be already struggling with plasmid maintenance and overexpression of two enzymes on two plasmids. As another objective insufficient uptake of substrate and product release from the cell becomes an issue which can be addressed by reaction engineering. In the following chapter, such challenges will be discussed and methodological background as well as optimization strategies to overcome these obstacles will be outlined. The following introduction is partially published^[13] and deals with the aspects in the focus of this work in greater detail.

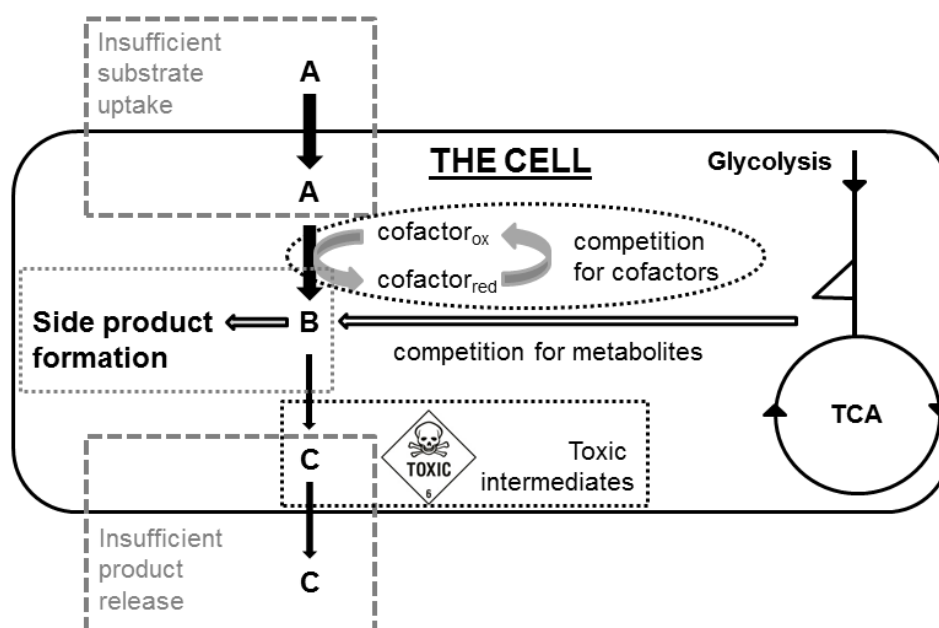


Figure 1.5: Obstacles in whole-cell biocatalysis: decrease in overall productivity.

1.3 Methods to overcome challenges in biocatalysis

For new biocatalytic synthesis routes to reach industrialization it is necessary to adopt a deep knowledge of the system. The system consists out of three different levels, which all three need to be separately developed and optimized. The first level is the biocatalyst development, which includes the choice and improvement of the enzymatic system. The correct enzymes to perform the biotransformation need to be identified or enzymes with similar substrates like the substrate of interest need to be engineered to alter the substrate acceptance. Additional factors that have to be taken into account are enzymatic activity and stability, since they can affect the yields of biotransformations to a high extend. In case of whole-cell biocatalysts, unwanted host enzyme activities on substrate, intermediates or products should be removed. The second level is the fermentation development/cultivation development, in which the biocatalyst is placed in an environment, where the biotransformation can be performed, while maintaining suitable conditions for the biocatalyst itself. In a whole-cell biocatalyst, optimized expression conditions for the enzymes are important. The third level is the process and DSP development and deals with the establishment of an industrially relevant instrumentation to perform the biotransformation, usually with an up-scaling step, and a subsequent DSP protocol, to enable a high isolated yield of the synthesized product.

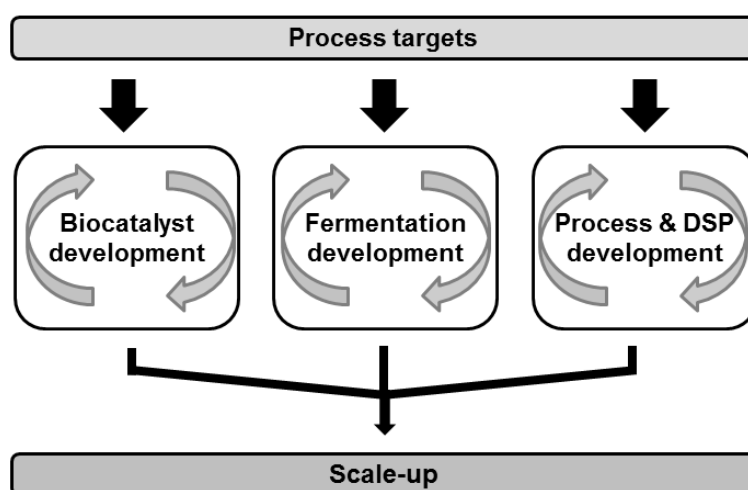


Figure 1.6: Schematic representation for development of biocatalytic processes.

Each of the three process targets is an iterative process.

DSP: downstream processing. Adapted from^[14].

1.3.1 Biocatalyst development

Since most enzymes are very chemo-, stereo- and regioselective and efficient catalysts, they often do not accept the desired enantiomers or substrate derivatives that are required to obtain the correct product. Therefore, methods were developed to furthermore improve enzymatic processes either by careful selection of the enzymatic variants for the correct biotransformation^[15] or by protein engineering e.g. directed evolution^[16] to broaden the substrate scope. Examples for such engineering achievements are control over the regioselectivity^[17] and enantioselectivity^[18] of enzymes or the substrate size^[19]. Other engineering efforts were performed to obtain higher activities^[20] and/or stabilities^[21]. Several examples for successes of protein engineering in biocatalysis were summarized by M. T. Reetz.^[22]

With the rise in the method portfolio and the overall knowledge about protein modifications, protein engineering explored the possibilities to catalyse non-natural reactions. A prominent example is the modification of cytochrome *c* from *Rhodothermus marinus* to perform a carbon-silicon bond formation with more than 15-fold higher turnover than state-of-the-art synthetic catalysts 1.7.^[23] The broadening of the substrate scope of cytochrome *c* to perform a non-natural reaction in a very efficient way is a very powerful example for biocatalyst development.

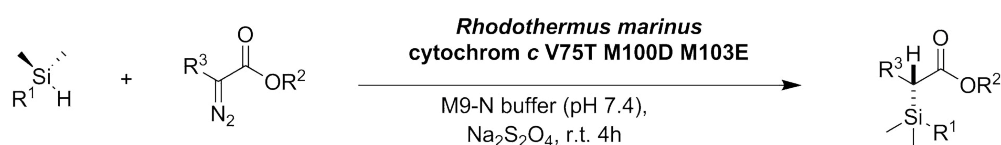


Figure 1.7: Optimization of a biocatalyst: non-natural carbon-silicon bond formation by an engineered cytochrome *c* variant from *Rhodothermus marinus*.^[23]

The catalysis of non-natural transformations is not the only strategy, in which biocatalysis uses classical chemical methods for molecule synthesis. Another concept, that found its way into biocatalysis, is the concept of retrosynthesis.^[24] The trend in biocatalysis is to apply biological catalysts for conversion of chemical functional groups to obtain the required target molecule. Therefore, the target molecule is analyzed in a retrosynthetic fashion and disassembled into a set of substrates, which can be converted by a set of suitable enzymatic reactions into the target molecule.^[25] This development was facilitated by an increased knowledge of enzymatic mechanisms and substrates, and readily available gene sequences

for the enzymes of interest, which can nowadays be ordered at a low price and used in a recombinant fashion. Two very comprehensive reviews on the topic of biocatalysis in organic synthesis were published very recently, extensively covering the different reaction types, required in synthesis (C-C/C-N bond formation and cleavage, hydrolysis and condensation reactions, redox reactions etc.) with enzymatic examples, which facilitate the construction of *de novo* biocatalytic pathways with non-related enzymes.^{[26][27]}

1.3.2 Fermentation/cultivation development

After successfully constructing the biocatalyst, in the step of fermentation development, the cultivation conditions are developed and optimized with regard to the cultivation medium^{[28][29]}, the pH, the temperature and other cultivation factors to either sustain growth, the metabolism or the stability.^[30] An important decision on cultivation is whether the recombinant microorganism should be grown in rich or minimal medium.^[31] For recombinant expression of enzymes, the expression conditions need to be established first, since the biotransformation cannot take place without a active catalyst. If for example, the temperature for expression and the optimal temperature for the biocatalysis itself differ, the enzyme production phase can be uncoupled from the biotransformation by introducing a secondary limitation in the medium (e.g. nitrogen, phosphate etc.) and perform a temperature shift in between. The cultivation development and expression studies usually take place on a small scale in the first step. Subsequently, the cultivation can also be analyzed on a larger scale, which facilitates the application of controlled conditions and online analytics. Additionally, the biocatalyst needs to meet several requirements. The catalyst has to perform under operational conditions required in the industrial process, which very often deviate from the natural conditions e.g. by addition of organic solvent for better substrate solubility.^[32] The catalyst should be characterized comprehensively, especially with regard to kinetics of the biotransformation.^[33]

1.3.3 Process and DSP development

After establishing the cultivation conditions, the up-scaling is performed and a cultivation mode beneficial for the process (e.g. batch, fed-batch, continuous) has to be set^[34]. Critical process engineering parameters such as aeration, stirring and if necessary feed/dilution rates need to be set and further optimized to obtain the high yields in the desired biotransformation. Especially, for oxygen-consuming reactions, like Baeyer-Villiger oxidations, a

satisfactory saturation of the bioreactor with oxygen is important.^[35]

If a model is used to simulate the biocatalyst performance in a bioprocess, it has to be fitted to describe the rate of the reaction in the full conversion range^[36]. Additionally, a process concept has to be made to define targets for the performance of the biocatalyst. The requirements are often improved in an iterative procedure, which is not very efficient. To avoid that, catalyst kinetics have to be determined and put in the center of the development. Biocatalytic processes feature rate laws, the conditions for the biotransformation e.g. temperature, pH, solvent and the thermodynamics of the process. The thermodynamics can be important, if the biotransformation is performed in the thermodynamically unfavorable direction for synthetic purposes. In these cases, different methods for equilibrium shifting are required as use an excess of an reactant or redirecting the undesired reaction^[37], remove the product *in-situ*^{[38][39]}, or couple the unfavored reaction with favored and/or irreversible ones^[40].

When the process met the set requirements, the formed product needs to be isolated in the previously defined quality by means of DSP. The strategy for DSP is based on the chemical properties of the product and the impurities in the reaction media. In general, downstream processing follows the guidelines of the RIPP Scheme (Figure 1.8).^[41]

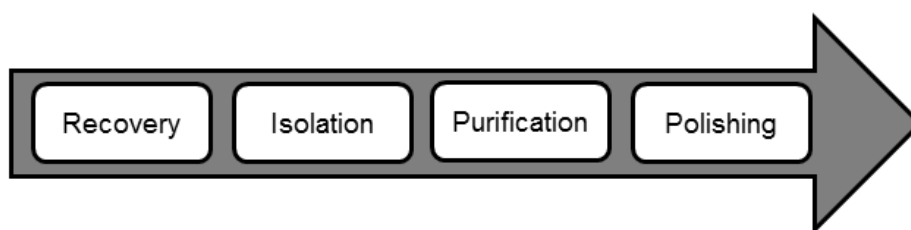


Figure 1.8: The RIPP Scheme of downstream processing.

The Recovery step usually represents the separation of solids and liquids and a possible cell rupture, if the product is produced within the cell and is not secreted. In the isolation step, extraction or precipitation are the usual methods for product isolation. The purification step often uses membrane technology to purify the product. In the polishing step, chromatographic methods are typically applied to obtain a high purity for the desired product, but usually not on industrial scale. The RIPP procedure is rounded up by a formulation

step, which consists of evaporation of solvent and drying of the product. To optimize the downstream processing, many different strategies can be pursued, depending on the target molecule. DSP for biomolecules like DNA, RNA or proteins can be simplified by using a tag for efficient purification^[42]^[43]. The purification of extracellular compounds can be accomplished by *in-situ* extraction^[44], *in-situ* filtration^[45] or substrate-feed-product-removal (SFPR) techniques.^[46]^[47]^[38]

1.4 Productivity enhancement by *in vivo* and *in silico* strategies

Several proof-of-concept studies including novel biosynthetic routes have been established in the last decades. As *in vivo* cascade reactions were used in biocatalysis, many challenges that were discussed in the last chapter, needed to be addressed. A major challenge is the progress beyond lab scales in order to demonstrate the potential for industrial processes. In addition to establishment of a general workflow with studies that report not only the overall success but also the reaction parameters in great detail, a low overall productivity represents a significant obstacle at present which needs to be overcome to enable an industrially relevant and profitable exploitation.

In general, there are two different strategies which can be applied for a whole-cell catalyst improvement, especially expressing several unrelated enzymes; a knowledge based classical *in vivo* and a more holistic *in silico* approach. *In vivo* methods usually improve a system one step at a time: one parameter is changed to optimize a certain condition, the output of the experiment is observed and a hypothesis is derived from the observation. In the next step, the next parameter is changed. This procedure requires a lot of time and experimental effort and is a recursive method. Additionally, improvements can only be performed, if the hypothesis was chosen correctly. One example is the targeting of specific side reactions by obvious gene knock-outs based on known metabolic network structures in order to rewire the flux through the synthetic pathway with the aim to improve overall productivity. The computational approach as second strategy requires a holistic view of the whole-cell biocatalyst as a system. If a model of the system exists, several factors can be changed at the same time in different combinations to obtain the best optimization result. For the above mentioned example with unwanted side reactions, the microorganism can be modeled as a set of reactions, which correspond to the metabolic pathways within the cell or as a kinetic model of either a single enzyme or an enzymatic cascade. The model can then propose possible KOs which would enhance the product yield of the system. This would directly lead to the experiments with the best chances to succeed. Both, the *in vivo* and the *in silico* approaches are frequently used tools in the field of metabolic engineering and can be also related to the field of systems biocatalysis. The differences between *in vivo* and *in silico*

methods are summarized in Figure 1.9.

<i>in vivo</i> methods	<i>in silico</i> methods
- limited view of the system	- holistic view of the system
- only obvious improvement strategies can be tested	- improvements are predicted by the model, unexpected modifications possible
- high experimental effort	- low experimental effort
- cost-intensive	- no additional costs
- work-intensive	- only computational work

Figure 1.9: Comparison of *in vivo* and *in silico* methods for biocatalysis optimization.

The classical optimization approach was established due to historical developments as the first microorganisms were used as wild-type strains and their natural ability for production of certain chemicals was exploited. Fermentative production of ethanol by the yeast *S. cerevisiae* represents the most prominent example.^[48] Organic acids of the tricarboxylic acid (TCA) cycle like citrate or succinate are mostly produced on industrial scale by different microorganisms. For example, *Aspergillus niger* is used for citric acid, *Lactobacillus rhamnosus* for lactic acid, and *E. coli* for succinic acid production, respectively.^[49] With increasing knowledge about the biochemistry and the network structures of different organisms, productivity improvements were mainly based on both rational knock-out/knock-in strategies to remove unwanted side reactions in combination with adjustment of target protein expression. Other modifications included balancing enzyme overexpression to increase product fluxes, consolidation of the pathway from two plasmids into one, codon optimization, and knock-outs for flux rerouting.^[50] Of course these classical methods cannot be classified as biocatalysis, which is performed nowadays, since the starting point for all production methods was the sugar utilized by the producing strain, so only natural products could be accessed. However, the developed methods were transferred to optimize the whole-cell applications in biocatalysis.

In biocatalysis, especially in redox processes, whole-cell transformations were extensively

used in the past^[51]. The living organism provides a convenient and cheap cofactor recycling system which facilitates the whole process and reduces costs significantly. In general, both *in vitro* and *in vivo* classical applied recycling systems for NAD(P)H are formate dehydrogenase, glucose dehydrogenase, or glucose-6-phosphate dehydrogenase with their respective substrates formate, glucose or glucose-6-phosphate. These methods, among many other strategies for cofactor recycling have been summarized elsewhere.^[52]

Overall, whole-cell redox biocatalysis is applied in many different research areas, for example, for the synthesis of various pharmaceutical compounds with different reductases or oxidases.^[53]^[54] With the extension from single enzyme reactions to the construction of multi-enzyme mini-pathways, attention focused on the host itself, potential interfering side reactions, and metabolic bottlenecks. Due to the increasing complexity of the system, other methods e.g. from the field of metabolic engineering, were applied. In contrast to many fermentative processes in the metabolic engineering area, the complexity of multi-enzyme biocatalysis is significantly lower because of the combination of metabolically unrelated enzymes which are used for conversion of functional groups. Nevertheless, very recently, Oberleitner *et al.* combined *in vitro* and *in vivo* experiments of an artificial mini-cascade consisting of three redox enzymes to improve the productivity by identifying a competing side reaction and deleting the responsible gene in *E. coli*.^[55] The native enoate reductase *NemA* was removed from the host and different heterologously expressed EREDs were introduced with a distinct substrate profile and stereo-preference. Additionally, the group of Reetz targeted the same background reaction (*NemA*) to establish another evolutionary non-related mini-pathway in *E. coli*^[56] (Figure 1.10).

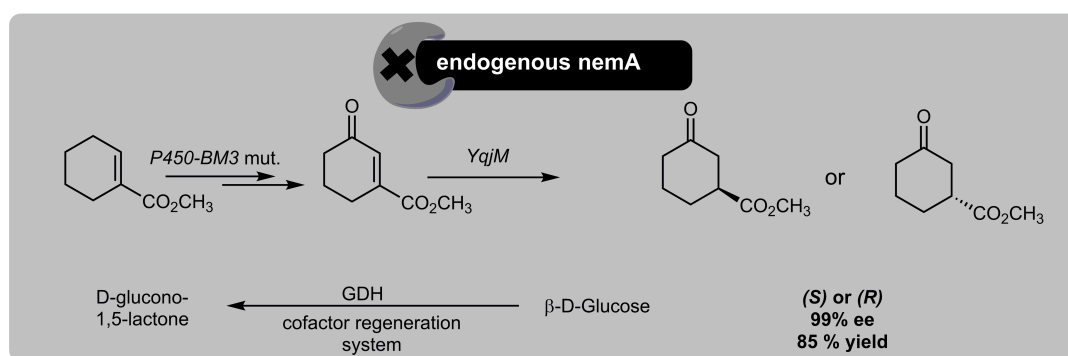


Figure 1.10: Knock-out of *NemA* enables stereoselective biocatalysis.^[55]^[56]

Prather and coworkers also enhanced the performance of a whole-cell biocatalyst by knocking-out different enzymes (specifically aldehyde reductases) in their CAR expressing strain in order to produce and accumulate aldehydes in a whole-cell environment. Due to the KOs, the aldehyde reducing activity of the host was minimized. The group successfully produced vanillin from vanillate or L-phenylacetylcarbinol from benzoate and pyruvate^[57] (Figure 1.11).

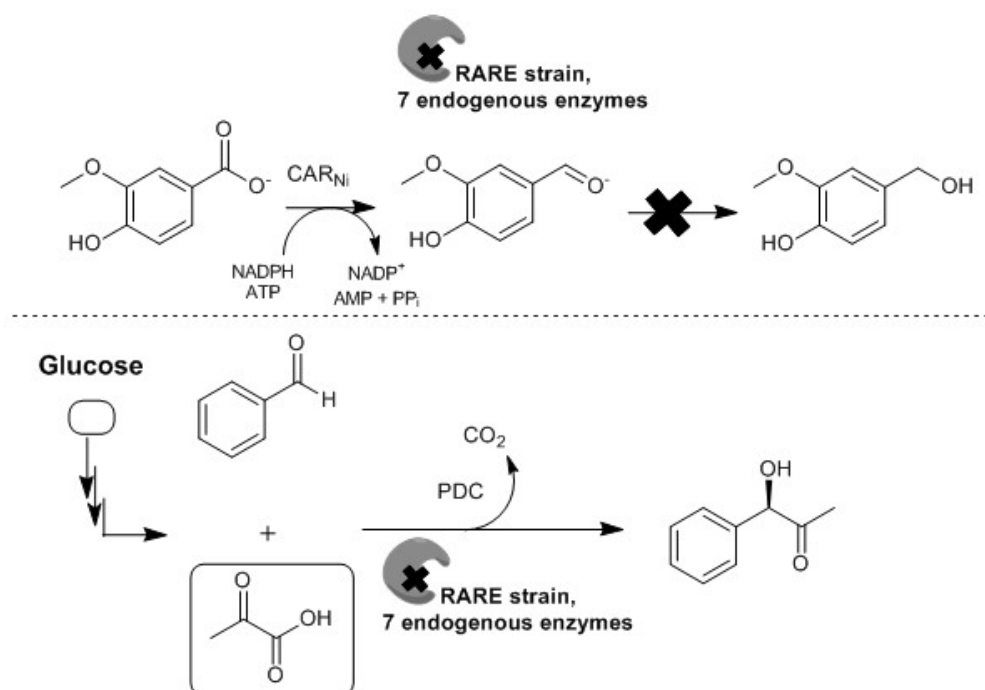


Figure 1.11: Knock-out of 7 endogeneous genes improves aldehyde stability *in vivo* for biocatalysis.^[57]

In a recent example, Li and his coworkers constructed four different enzyme modules, which they subsequently mixed and matched to create three different whole-cell biocatalysts (Figure 1.12).^[58]

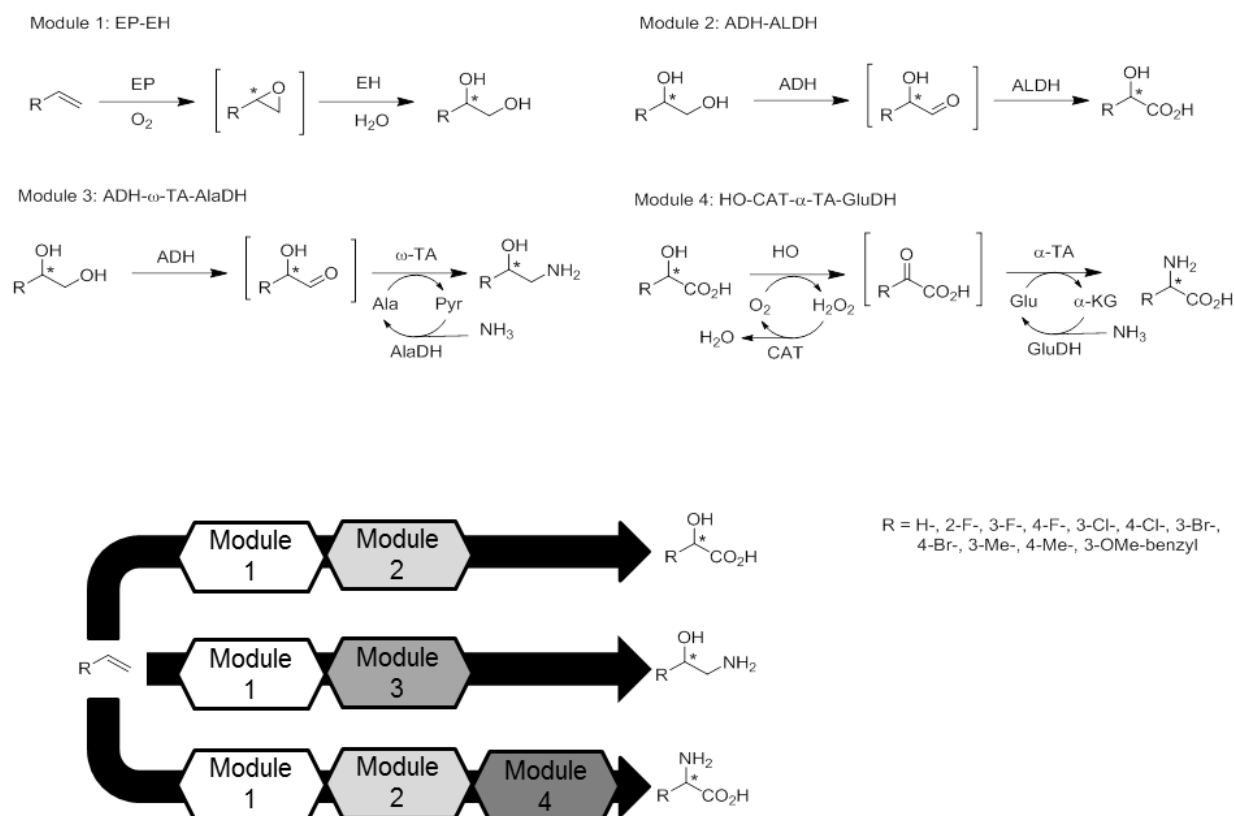


Figure 1.12: Modular *in vivo* biocatalysis.^[58]

EP: epoxidase; EH: hydrolase; ADH: alcohol dehydrogenase; ALDH: aldehyde dehydrogenase; ω -TA: ω -transaminase; AlaDH: alanine dehydrogenase; HO: hydroxyacid oxidase; α -TA: α -transaminase; CAT: catalase; GluDH: glutamate dehydrogenase

The plasmid construction and medium formulation was optimized to achieve balanced enzyme expression. Additionally, the enzymes were chosen due to their high activities to avoid accumulation of intermediates, which usually result from bottlenecks in the cascade. With these optimizations, the Li group was able to produce chiral α -hydroxy acids, 1,2-amino alcohols and α -amino acids from terminal alkene substrates.

As mentioned before, the increased complexity of biocatalysts led to the investigation of systems *in silico* before conduction of selected experiments based on computational simula-

tions. This is a holistic while complex method which is only possible, since computer-aided applications have drastically facilitated the design of experiments in many different research areas. From predictions of artificial biochemical production pathways with enzymes from databases^[59] to kinetic enzymatic models^[60], computational approaches have been broadly applied in order to gain further knowledge and deeper understanding of biological systems. These methods enable researchers to perform optimizations of the whole system and to identify crosslinks and relationships, which are not obvious on first sight due to the complexity of the applied cellular system. Additionally, it is a resource and time saving strategy, which leads to a better experimental design.

In the following, the methods of kinetic modeling, flux balance analysis (FBA), metabolic flux analysis (MFA) will be addressed to demonstrate their possibilities with regard to optimization of biocatalytic transformations. Kinetic modeling is usually applied for smaller systems, with many defined kinetic parameters. In contrast to kinetic modeling, FBA is applied for large systems with little kinetic information. The model is based on the reaction network of the microorganism. MFA is mostly used for validation of FBA results or for identification of constraints, which are necessary for FBA.

Kinetic modeling of biocatalytical processes

Many biological processes which are used in industrial biotechnology are non-stationary systems; their dependence on time and the inputs to the system are high e.g. addition of substrate to a biotransformation. Usually, these systems are modeled dynamically: biochemical reactions are represented as mathematical expressions for the reaction rates of these reactions. These types of mathematical models are called kinetic models. Kinetic models are important for gaining insights into factors limiting biotransformation performance by simultaneously saving experimental effort, since previously established hypotheses can be tested *in silico* prior to developing or performing the required experiments. The modeled system can consist out of one enzyme or a cascade, and both *in vivo* or *in vitro* systems can be modeled. For optimization of biotransformations, kinetic models can theoretically be applied at all three stages of optimization (catalyst, cultivation and process development), if the system can be characterized in great detail. The average work-flow for setting up such a kinetic model is visualized in Figure 1.13.

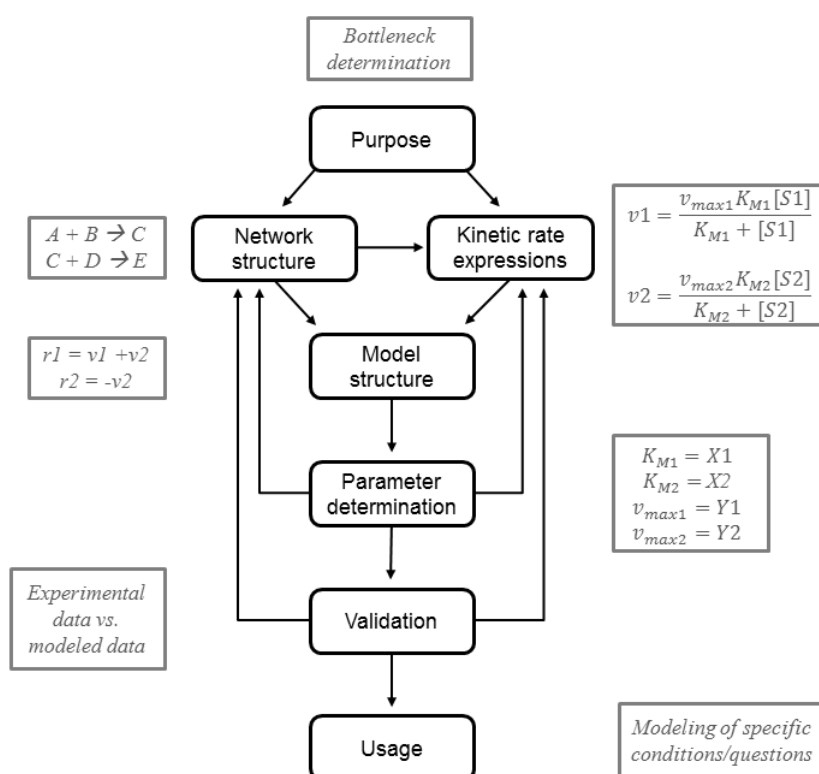


Figure 1.13: Main steps of kinetic model development; adapted from^[61].

average workflow of the model in black; specific examples for an enzymatic multi-enzyme reaction cascade in grey.

The building of a model can be an iterative process, depending on the data input in the beginning and improvement with new accessible data and addition of new elements to the model e.g. deactivation of catalysts, evaporation of solvent etc. Figure 1.13 depicts examples for an enzymatic model, based on the Michaelis-Menten kinetics and determination of bottlenecks as the main purpose of the model. In general, the usage of kinetic models is wide-ranging. One example is the local parameter sensitivity analysis, e.g. metabolic control analysis (MCA) for linking response to perturbations to the individual components of the system. It is used for investigating and understanding control and regulation of metabolism by relating the properties of metabolic systems to the kinetic characteristics of the component enzymes.^[62]^[63] It was successfully used to identify the key parts for the optimization of glucose uptake by the phosphotransferase transport system (PTS) and for serine biosynthesis.^[64] Another example for usage of kinetic modeling is improvement of process design. In that case, kinetic models are used to predict the behaviour of cell factories in response to different external conditions. These models take usually the mass balance of substrates, products and biomass formation into account. For example such models can be used for media feed optimization in order to maximize the volumetric productivity of heterologous protein production.^[65]

For modeling of enzymatic cascades, kinetic modeling of *in vitro* or *in vivo* enzymes or whole pathways only have been explored in few publications. Cofactor recycling of a Baeyer-Villiger monooxygenase (BVMO) reaction of a cyclohexanone monooxygenase (CHMO) by an alcohol dehydrogenase was modeled *in vitro* to increase the information for biocatalytic process optimization^[66]. Simulation and prediction of a three-enzyme cascade system was performed *in vitro* to compare the batch mode with a fed-batch approach.^[67]

Modeling of reaction cascades and fitting experimental data can be troublesome, due to a high correlation of the parameters within such models.^[68] This is problematic for determination of a global minimum (unique solution) for the objective function. Model-based design of experiments (MBDoE) is often required to obtain information for reduction of correlation.^[68]^[69] So far, it is necessary to have a good initial guess of the individual model parameters and therefore use a stepwise approach to fit the data, to obtain the best initial guess.

Since kinetic modeling requires a lot of computational effort and many input parameters, it

is so far limited to smaller systems. When modeling larger networks, usually stoichiometric modeling is applied. One method for stoichiometric modeling is flux balance analysis (FBA).

Flux balance analysis (FBA)

In the last two decades researchers in the field of systems biology put tremendous efforts into understanding and describing (quantitatively) various microorganisms by computational models. Knowledge about a distinct metabolic flux distribution in production hosts with respect to productivity becomes more and more important especially in the area of biotechnology. Computational models were used for predictions and simulations to reduce unnecessary experimental work. The method of flux balance analysis (FBA) is based on genome-scale metabolic models and is a tool for simulations of flux distribution in a cell (Figure 1.14).^[70] Similar to kinetic modeling, the method can be applied at the stages of catalyst, cultivation development, and process development. A simplified workflow is described in the following paragraph.

Different software tools create a stoichiometric matrix from all known reaction equations, including artificial reactions for formation of biomass or transport reactions for substrates like glucose or oxygen. The matrix is then multiplied with a flux vector that represents the fluxes through all the reactions in the metabolism. These fluxes are unknown variables which have to be identified during an FBA. For every flux analysis, constraints like substrate availability or oxygen uptake are set to minimize the possible solution space. These are fluxes which are already known, e.g. acquired by measuring the uptake rates experimentally. Other fluxes can be restricted to certain values (e.g. to only positive or negative values) if a reaction is unidirectional. Since FBA is mostly performed at steady-state conditions, the change over time equals zero. A certain objective function is chosen which has to be optimized during the analysis.^[71] Different objective functions are responsible for different results in predicting flux distributions in the cell.^[72] Simulating growing cells, the most frequently used objective function is the maximum formation of biomass. For simulation of non-growing conditions it is more difficult to choose an appropriate objective function. In case of redox catalysis, one possibility can be the maximization of cofactor recycling.

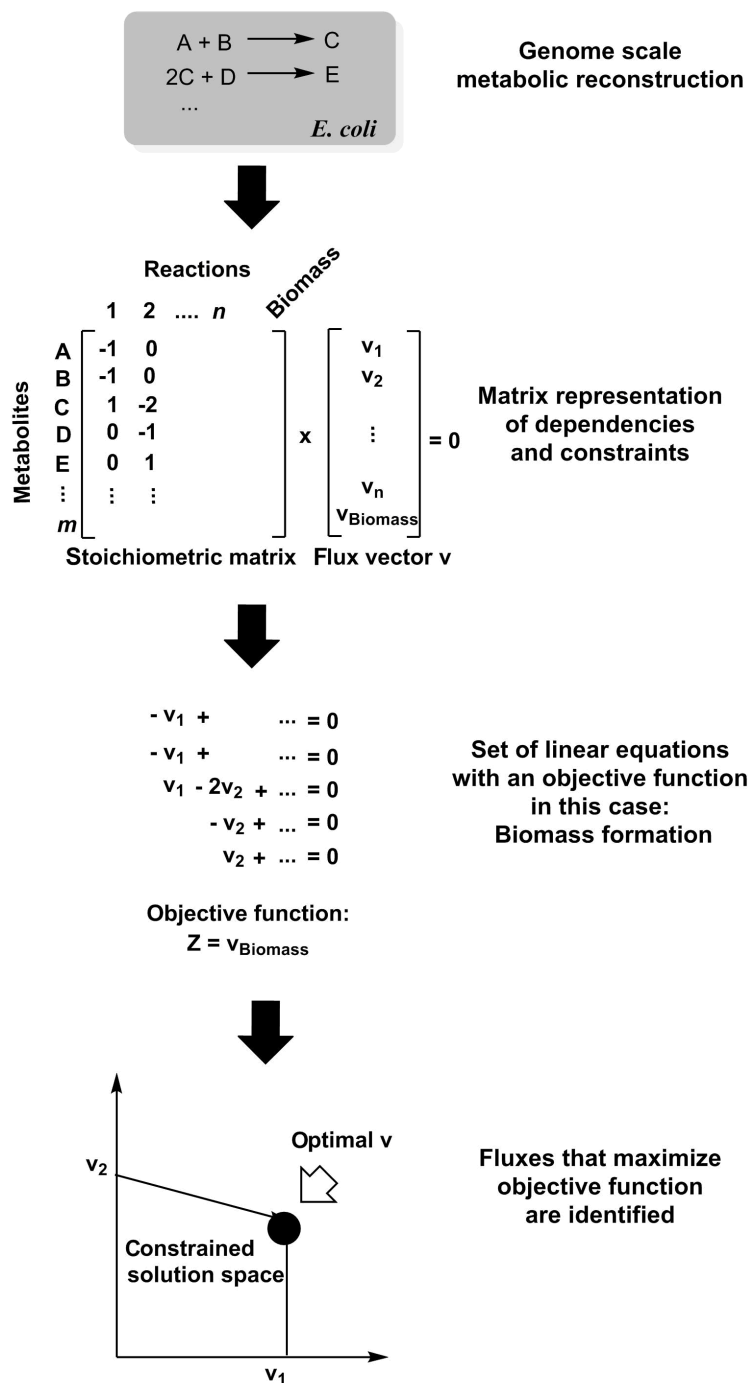


Figure 1.14: FBA analysis.

The reactions within the metabolic pathways from a genome scale metabolic reconstruction are transformed into a matrix form and multiplied with a flux vector. The steady-state conditions set the change over time to zero. This set of linear equations determines the constraints and dependencies in the cell. If the objective function is maximized, defined solutions within the solution space can be identified.

A genome-scale metabolic network reconstruction, either from online platforms like the

Model SEED^[73] or BIGG^[74] or other metabolic model databases represents the initial requirements for this kind of analysis. These models represent stoichiometric reaction equations of the reactions in the metabolism of the specific microorganism and can be either analyzed with online tools (www.theseed.org) or with the free available MATLAB COBRA toolbox^[75] for MATLAB or Python. A variety of online tools and toolboxes for FBA were compared and evaluated by Lakshmanan et al.^[76] Although these tools are improving in terms of user convenience, the application of such tools by scientists in biocatalysis or biology is still not widely established.

FBA has been shown to be an effective tool for predictions of phenotypes of different knock-out mutants. Within an elaborate study for *S. cerevisiae* with a library of 4658 mutants under five different environmental conditions the high predictive accuracy of the applied model was successfully demonstrated, which ranged between 96-98% for viable phenotypes and 73-80% for lethal phenotypes.^[77] The accuracy of predictions enables such simulations of different growth conditions and constraints to perform knock-out studies for product maximization *in silico*. Therefore, this approach saves time or provides new ideas for knock-out strategies, which were not obvious in the first place. Special focus is put on prevention of lethal knock-outs for the whole-cell biocatalyst, which can be identified with FBA. It is a general advantage of FBA that the concept is independent from kinetic data, although hybrid models are also investigated and applied by the biosystems community which partly consider dynamic attributes in FBA^[78]. In the last years, efforts were made to equip the classical stoichiometric models with kinetic properties to be able to model systems, which are not in a steady-state. The dynamic FBA models were used to represent dynamic environments e.g. fermentation, but used size-limited networks consisting only of the key reactions in central carbon metabolism.^{[79][80]} This issue was circumvented by building the first dynamic genome-scale model, which consisted out of four building blocks. The model was based on an iterative optimization of an stoichiometric matrix. As a first step fixed constraints to be used throughout fermentation were defined (genetic background/nutritional requirements). Subsequently, dynamic constraints were defined as boundary fluxes, which were set by intracellular/extracellular conditions. At intervals of 30 mins, the linear programming solved the metabolic flux distribution, the consumption and production rates. The resulting rates from the previous step are used as inputs for the differential equations solved using a variable step

integration routine. As a result, product profiles and concentrations of metabolites were calculated.^[81] The models for dynamic FBA had in common that they started from stationary fluxes and introduced pseudo-kinetic behaviour. For conversion of metabolic reconstructions into large-scale kinetic models of metabolism, a workflow was constructed.^[82] Several examples for use of dynamic FBA exist.^{[83][84]} Still so far, the complicated construction of these models restricted the broad use of dynamic FBA for users with limited background in bioinformatics.

The production of fumaric acid in *E. coli* represent a prominent example for the combination of classical metabolic engineering with FBA (Figure 1.15). Initially, the *iclR* gene for the isocitrate lyase repressor was knocked-out and TCA flux was redirected to the glyoxylate shunt. The most obvious genes, namely the three fumaric acid hydratases *fumA*, *fumB* and *fumC* were deleted in order to enhance fumaric acid production. Additionally, several other genes such as *aspA* were deleted after performing in silico flux responses. The resulting strain displayed a threefold increased fumaric acid production compared to the classically modified strain.^[85]

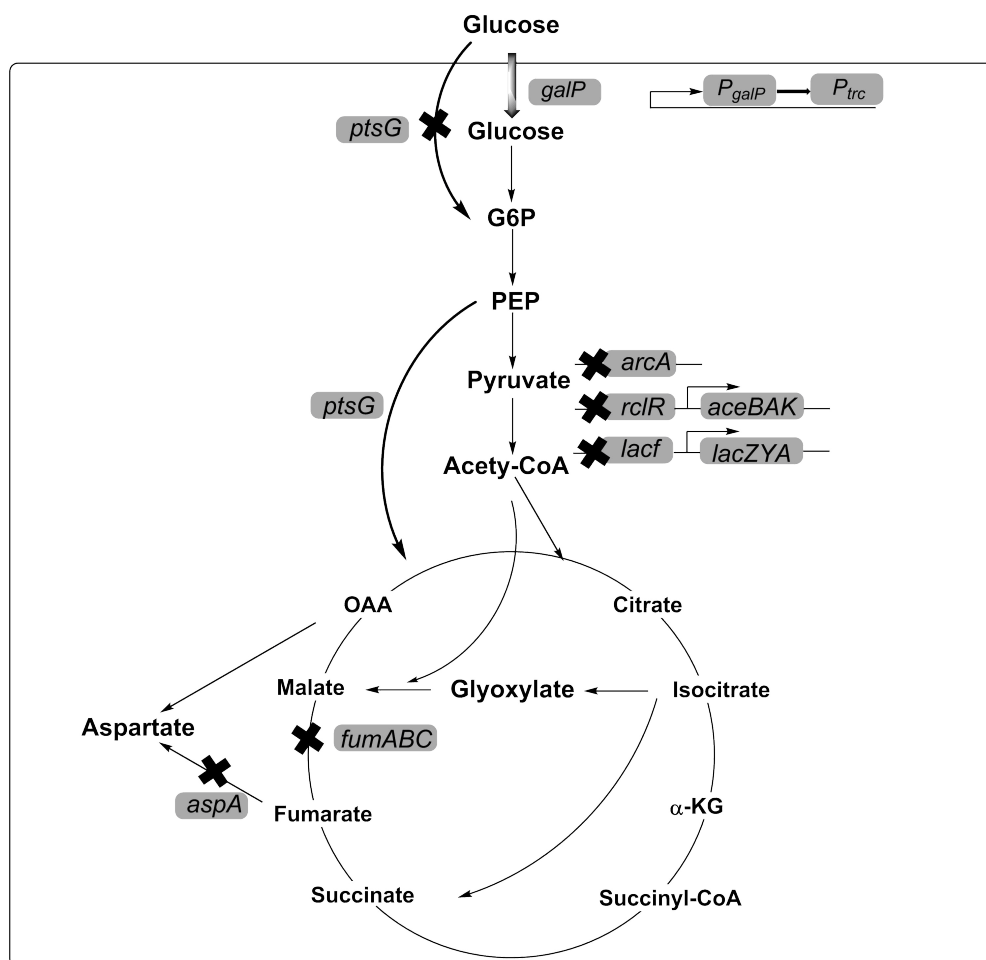


Figure 1.15: Knock-out (KO) strategies for fumaric acid production.

KO of the *iclR* gene for the isocitrate lyase repressor and KO of three fumaric acid hydratases *fumA*, *fumB* and *fumC* enhanced the fumaric acid production. *In silico* predicted KO of *aspA* resulted in an additional increase of the fumaric acid yield.

In another case study, two different *E. coli* knock-out mutants were predicted computationally for the improvement of L-phenylalanine production, constructed *in vivo* and showed high redundancies in the central carbon metabolism of *E. coli*.^[86] This study enables a more precise FBA development and an easier improvement of the L-phenylalanine production in the future, since the L-phenylalanine yield remained the same compared to the reference strain without the Knock-outs. The reduced solution space makes future FBAs more precise to predict improvement strategies.

A triple knock-out in *E. coli* central carbon metabolism lead to a 7.4-fold increase (3.9 ± 1.2 C-mol%) in the production of 3-hydroxypropionic acid (3HP) from glycerol. This was achieved with a gene knock-out simulation prior to constructing the strain *in vivo*.^[87]

In this dissertation, the FBA methodology will be applied to simulate fluxes within a biocatalyst with a *de novo* enzymatic cascade which is coupled to the central metabolism of *E. coli*.

¹³C-metabolic flux analysis

Apart from FBA, the impact of cascades which are coupled to the carbon metabolism of a microorganism can be evaluated *via* ¹³C metabolic flux analysis. This method is used to analyze the actual flux distributions of the central metabolism and to validate simulated FBA results, once the biocatalyst is actually constructed. It can support all development levels as shown for kinetic modeling and FBA, but as a regulatory instrument. For this method, experiments with [1-¹³C]-labeled glucose (heavy carbon on the C1 position) and uniformly [U-¹³C]-labeled glucose (heavy carbon on all positions (C1-C6)) as only carbon source are performed. Cultures are grown on labelled substrates and harvested during steady-state. Proteins are hydrolyzed and amino acids are derivatized for GC-MS measurements. Since every pathway of the central carbon metabolism shows a characteristic fragmentation pattern of the applied carbon source, it can be identified *via* differences in the ¹³C-labeling patterns of amino acids. The analysis is usually performed *via* GC-MS and computational analysis has to be performed with a suitable software like FiatFlux^[88], ¹³CFLUX^[89] or OpenFLUX^[90]. The software applications for quantitative metabolic flux analysis^[91] and general methods^[92] were recently reviewed elsewhere. The resulting flux ratios between the different metabolic pathways can be used for calculation of absolute fluxes if uptake and secretion rates of substrate(s) and product(s) are provided (Figure 1.16).^{[93][94][95]}

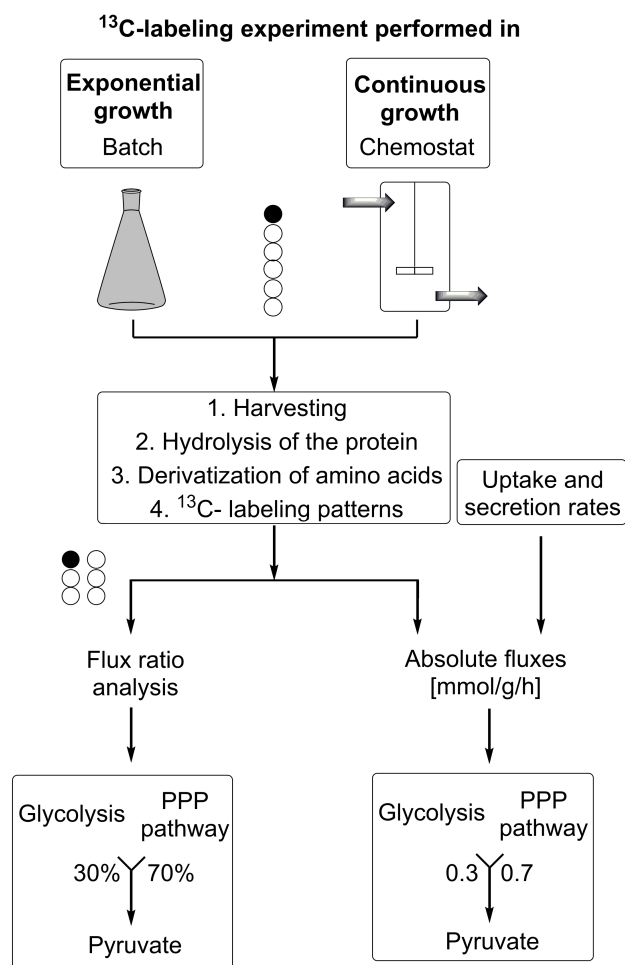


Figure 1.16: ^{13}C -metabolic flux analysis workflow.

The cultures are grown on labelled substrates and harvested during steady-state. The proteins are hydrolysed and the amino acids derivatized for GC-MS measurements. The labelling patterns are recognized by specific software and result either in flux ratios or, with additional information about uptake and secretion rates, in absolute fluxes.

Within a recent study ^{13}C -MFA was used very efficiently to show that fluxes towards the pentose phosphate pathway (PPP) of *Corynebacterium glutamicum* were not altered after enhancement of cofactor ability by altering the coenzyme specificity of the native NAD^+ -dependent glyceraldehyde 3-phosphate dehydrogenase to NADP^+ . The desired lysine production could be improved by approximately 60%.^[96] In another study recently published by the Antoniewicz group, a complementary parallel labeling experiments technique for metabolic flux analysis (COMPLETE-MFA) was established. In this study, 14 parallel labeling experiments with 8 differently ^{13}C -labeled glucose tracers were performed in *E. coli*.

The best tracers for resolving the fluxes in the upper (glycolysis and PPP) and lower (TCA cycle and anaplerotic reactions) metabolism were identified. By doing so, it was shown that the best tracers for upper metabolism displayed a poor performance for lower metabolism and vice versa. This result should clearly be considered for future design of experiments.^[97] Overall, *in silico* methods can facilitate the planning of *in vivo* experiments for product enhancement in whole-cells and reduce the experimental workload, therefore, saving time, money and also offering new insights into all possible solutions.

This method should be applied for cross-validation of FBA results in order to improve the constructed model and set new constraints. Another non-computational powerful validation method for all the *in silico* computations, is the quantification of metabolites within the cell (metabolomics), which is illustrated in the next chapter.

1.4.1 Metabolomics: quantification of intracellular metabolites

Metabolomics measurement is an important tool frequently applied in metabolomic engineering and systems biology. With the increase of complexity of the biocatalytic systems due to construction of artificial *de novo* pathways *in vivo*, metabolomics became relevant for the field of biocatalysis. Absolute quantification of metabolites in the host cell is an important method as it provides the information on a possible maximal yield of the product. It also exposes possible bottlenecks within the metabolism especially when it comes to cofactor recycling and cofactor availability.^[98] Additionally, it is useful to correct FBA results since they mostly do not contain kinetic data which could be a (major) limitation in depicting real flux distributions in the cell. The quantification of intracellular metabolites, referred to as metabolomics, is a powerful tool to both refine and control the simulated results and improve computational models. Metabolomics is a very powerful method, which can be applied at all levels of development for optimizing conditions or production. However, if it is already used at the catalyst and cultivation development, it may save experimental effort at later development stages.

Several analytical techniques (GC-MS or LC-MS/MS) are known and depend on the properties and the origin of the metabolic compounds. Since the physical and chemical properties of metabolites vary from very polar (glycolytic intermediates) to strongly lipophilic (lipids, fatty acids) it has not been possible so far to cover the whole metabolome with only one analytical method. In the case of metabolic engineering and redox multi-step catalysis, investigations of the central carbon metabolism are most prominent. Methods tend to cover glycolysis, TCA cycle metabolites, amino acids, PPP intermediates and cofactors (e.g. NAD(P)⁺/H, FAD). The accuracy of these methods relies on the use of proper internal standards and is usually performed with ¹³C-labeled cell extracts to obtain reproducible results and reduce matrix effects.^[99] This is necessary because the intracellular compounds can be quite unstable and tend to decompose rapidly. In order to have a reference with comparable individual decomposition rates, the same compounds are applied as fully ¹³C-labeled analogs. Hence, a fast sampling with rapid quenching or rapid extraction of metabolites is mandatory. Otherwise, the metabolic reactions will progress under non-experimental conditions, experimental error will increase and results might not be representative anymore. This is especially the case if dynamic behavior of the metabolome is investigated.^[100] The difference between bacteria

and yeast or fungi should be taken into account since the cell membranes of these species have different stability and the treatment method has to be adjusted in order to prevent metabolic leakage.^[101] As bacterial outer membranes are less stable, filtration techniques are favored with a subsequent quenching/extraction step. In case of more stable cell walls (e.g. yeast), samples are quenched with cold methanol, for example, and extracted afterwards. The quantification is usually performed *via* LC-MS/MS.^[102] Metabolomics were recently used to identify the successful metabolic engineering of *E. coli* for triglyceride accumulation; within this study a high conservation of triglyceride composition was confirmed.^[103] Another recent example for the success of metabolomics as a control strategy was disclosed by metabolic flux redirection towards a synthetic pathway with a metabolic toggle switch for changing the *E. coli* metabolism to isopropanol production. Metabolomics were used to follow the changes in the intracellular fluxes.^[104]

In the following, the different levels of optimization described above (biocatalyst level, fermentation/cultivation level, process and DSP level) are applied in various combinations to biocatalytic systems and biocatalytic transformations. The resulting successes and drawbacks of the optimization methods are described, to obtain knowledge of the limitations of the biocatalytical transformations and to develop better performing biocatalytical processes.

1.5 Scope of this thesis

For a successful biotechnological transformation, the optimization of the process should be performed on different levels. The performance of the catalyst on the catalyst level, on the fermentation/cultivation level, and on the process and DSP level, all contribute to the enhancement of productivity. This thesis deals with optimization of biocatalytic processes. Even though biocatalysis has been established in the Mihovilovic group, the main part of the thesis focused mainly on establishment of new methods, such as modeling and metabolomics, in biocatalysis. Therefore, several strategies were pursued:

- development and up-scaling of a biocatalytic process with stable conditions
- kinetic modeling of an artificial metabolic pathway in *E. coli* to determine bottlenecks and propose strategies to resolve them
- determination of BVMO stability and activity *in vivo* for biocatalytic purposes
- stoichiometric modeling and metabolomics to develop a tool for boosting DHAP-dependent aldolase biotransformations *in vivo* to predict bottlenecks and optimized biotransformation conditions *in vivo*

For the development of the biocatalytic process, a suitable Baeyer-Villiger monooxygenase (BVMO) was chosen, which converted the chosen racemic substrate without distinguished preference for either enantiomer, since our desired lactone product, a polymer precursor, would undergo a ring opening and therefore would lose chirality. A stable expression of the BVMO in *E. coli* BL21 (DE3) was established, which equals a optimization on the biocatalyst level. The cultivation in a bioreactor including stable biotransformation conditions and medium formulation was achieved, with optimization on a fermentation level. With an application of a substrate-feed-product-release concept (SFPR) the process level was optimized, including an optimization of the DSP. As a result, the biotransformation yielded the desired product on multigram scale.

In the second chapter, the focus was put on biocatalyst optimization. A previously published enzymatic redox cascade consisting out of three enzymes (alcohol dehydrogenase (ADH), enoate reductase (ERED), BVMO) was used to study the performance of this *de novo* metabolic mini-pathway with regard to the performance of the single enzymes *in vivo*. Since

the cascade was only connected *via* redox cofactors to its host *E. coli*, a kinetic model was built to identify bottlenecks in the cascade and derive optimization strategies from the *in silico* experiments. The bottleneck of the cascade was identified and optimization strategies were proposed. The proposed optimization dealt with the system on an enzymatic level in a whole-cell environment (biocatalyst optimization).

In the third chapter, the last step of the enzymatic cascade from the second chapter, the BVMO, was investigated in terms of bioprocess stability *in vivo*. The biocatalyst itself was investigated for possible limitations of its catalytic performance. The main focus was to identify key factors for the repeatedly low stability of BVMOs, which are mostly used in whole-cell processes to increase activity and stability of these enzymes. With application of several methods, among those were metabolomics and enzyme quantification *in vivo*, a bottleneck for high BVMO activity *in vivo* was identified and strategies to circumvent the low biocatalyst performance were proposed, to be able to optimize the biocatalyst in the future.

In the fourth and last chapter, the biocatalyst as well as the cultivation level were assessed with means of stoichiometric modeling and metabolomics. The stoichiometric modeling was used to model *E. coli* with an introduced dihydroxyacetone kinase (DhaK), to elucidate the advantages of such a catalyst for generation of dihydroxyacetone phosphate (DHAP) from dihydroxyacetone (DHA). The elevated levels of this glycolytic compound could be used for aldol reactions *in vivo* with DHAP-dependent aldolases. The model as well as metabolomic measurements showed DhaK to be a potent tool for facilitating aldol reactions *in vivo*. Furthermore, a stoichiometric model for a enzymatic cascade reaction in *E. coli* was built, consisting of an ADH, an aldolase and a phosphatase and optionally, the DhaK investigated earlier. The two potential biocatalysts were compared in terms of their productivity and their optimized conditions *in silico*. The optimization was investigated on two different levels: the biocatalyst level (a whole-cell system with or without DhaK) and on the cultivation level (growing vs non-growing conditions). Additionally, a HPLC method for ^{13}C metabolic flux analysis was developed for being able to investigate the stoichiometric modeling results with the catalysts in experiments and possibly adjust the chosen constraints for this kind of modeling.

2 Results and discussion

2.1 Upscaling of a cyclopentadecanone monooxygenase (CPDMO) whole-cell biotransformation towards polyamide-9 precursors

2.1.1 General aspects

In the following chapter, all development/optimization levels for a biocatalytical process, discussed in the introduction, were applied to develop and improve a biocatalytic transformation for polyamide-9 precursor synthesis.

Aliphatic polyamide materials constitute a multi-billion euro market with applications in the automotive, film and coating, and electronic devices industries.^[105] With rising demand of artificial polymer materials in general, and polyamides (PAs) in particular, the industry explores bio-based production solutions to reduce dependence on fossil resources and to increase sustainability.^[106] The PA types PA 6 and PA 6.6 form the largest market share. Several biocatalytic processes have been established for the production of muconic acid^[107], which can be converted *via* hydrogenation to adipic acid, the monomer for PA 6.6.^[108] Odd carbon-numbered PAs often yield materials with superior properties^[109], but successful commercialization of those heavily depends on the availability of cheap precursors with an odd carbon count, e.g. from ricinolic acid after oxidative cleavage.^[110] Naturally, fatty acid-derived molecules with odd carbon number are scarce, although engineered microbes that overproduce them have been described.^{[111][112]} Monomers coming from cost-intensive multistep syntheses, or with high bulk material costs, limit the use of these polymers on broad scale.^[113] Biocatalytic processes towards polymer precursors can improve the economics of monomer synthesis^[114], as has been demonstrated for the Nylon 12 monomer ω -

aminododecanoic acid methyl ester^[115]. Compared to PA 6 and PA 6.6, PA 9 has enhanced polyethylene-like properties (e.g. low water absorption, dimensional stability under different conditions of humidity, impact strengths, good behavior at low temperatures, low density, etc.), while maintaining some properties of polyamides (e.g. high melting points, good aesthetic properties, good processability, and resistance to hydrocarbon solvents). These physical properties make PA 9 very useful in the manufacture of precision components.^[116] In 1981, Minisci et al. developed a convergent pathway for the synthesis of monomers for PA 9, commercialized as Perlagon^[117], starting from the readily available bulk chemicals cyclohexanone and acrylonitrile, leading to ketone **1**^[118] (Figure 2.1). Their process was later optimized by Cotarca et al. by improving the synthesis of lactone **2**. Still, both routes used stoichiometric amounts of an alkylcarboxylic peracid - explicitly described as explosive - while heating above room temperature to perform the key Baeyer-Villiger oxidation step. The hazard of explosion is a clear disadvantage, and requires specific safety measures.

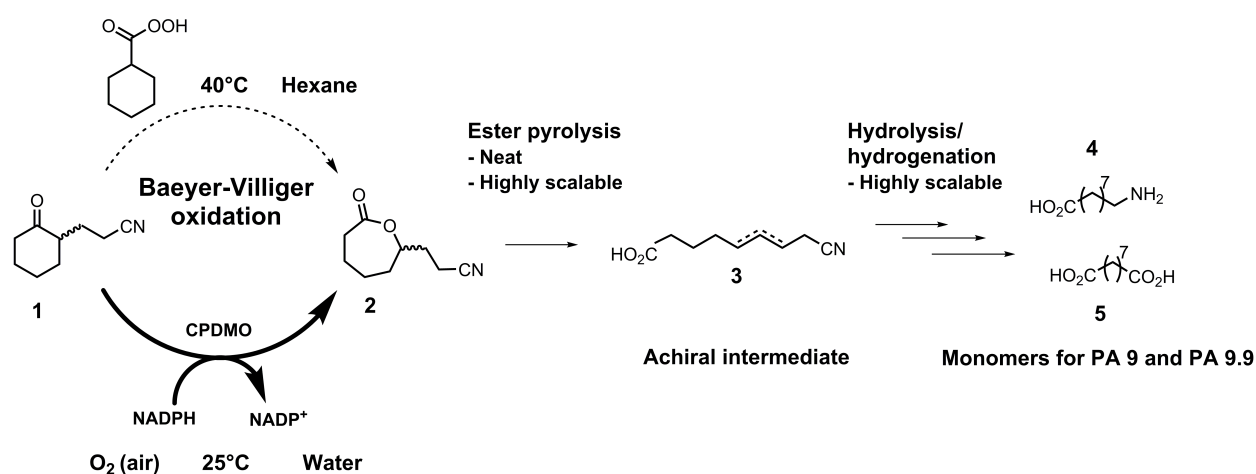


Figure 2.1: Schematic comparison of the chemical Baeyer-Villiger process by Cortaca *et al.* (dashed arrow) vs the enzymatic BVMO transformation described in this chapter (solid arrow).

The process by Cotarca et al. contained a problematic H_2O_2 - mediated ring cleavage of ketone **1** *via* Baeyer-Villiger oxidation with alkylcarboxylic peracid to lactone **2** and subsequent ester pyrolysis to the unsaturated achiral 9-aminoperlagonic acid **3** and further modification *via* hydrolysis and hydrogenation to 9-aminoperlagonic acid **4** and azelaic acid **5**, which are the monomers for PA 9 and PA 9.9.

The strategy for lowering the hazard was to use aerial oxygen as terminal oxidant, operating at room temperature and in water. The idea was to substitute the chemical Baeyer-Villiger

oxidation of the process from ketone **1** to lactone **2** by a whole-cell biotransformation on a multi-dozen gram scale. The up-scaling was accompanied by optimization of the catalyst, the cultivation conditions, the process, and the downstream processing.

2.1.2 Baeyer-Villiger monooxygenases (BVMOs)

Baeyer-Villiger monooxygenases are enzymes, which catalyze the conversion of linear ketones into esters or cycling ketones into lactones. So far, all discovered BVMOs are NAD(P)H dependent flavoproteins. They use aerial oxygen and insert one oxygen atom into the the substrate, while the other oxygen atom is reduced to water.^[119] The reaction mechanism of BVMOs is shown in Figure 2.2.

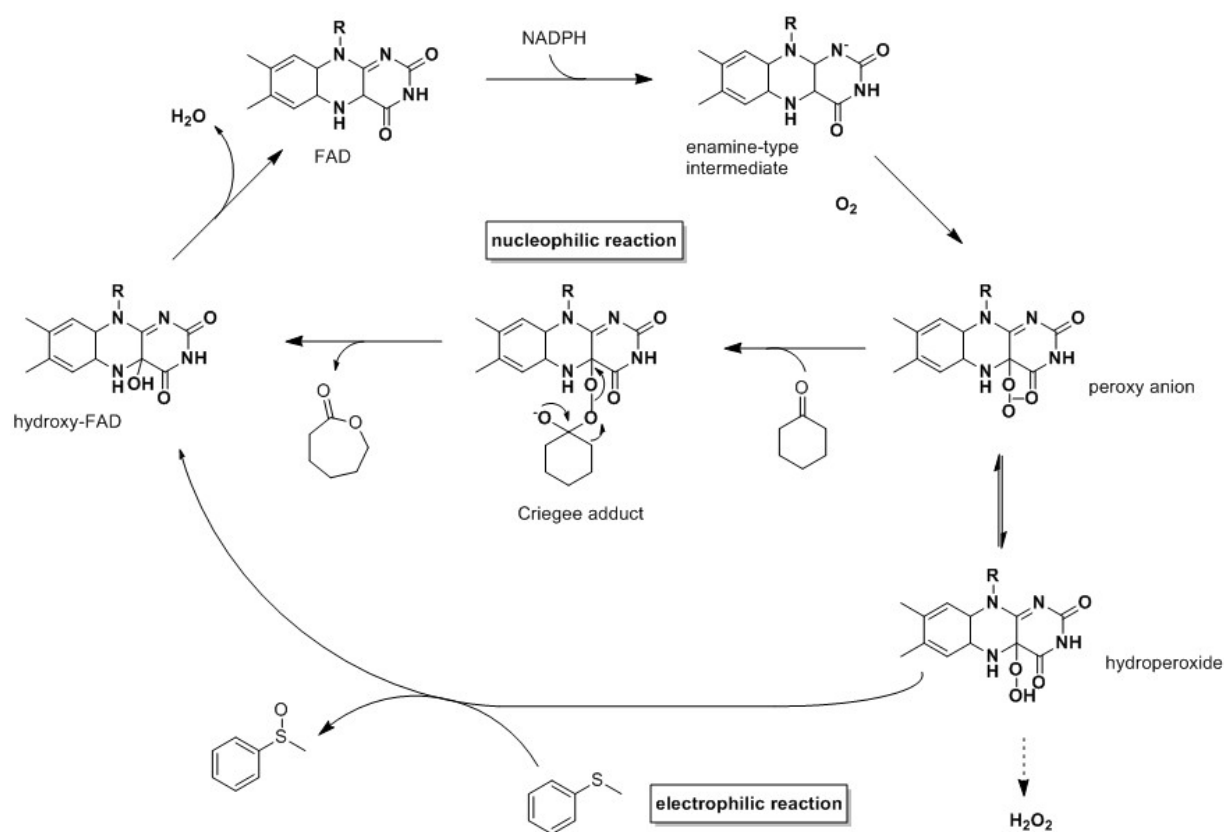


Figure 2.2: Mechanism and catalytic cycle of flavin-containing BVMOs.

Example for cyclohexanone monooxygenase from *Acinetobacter* adapted from^{[120] [121] [122]}

In this mechanism, the FAD is reduced by NADPH, forming an enamine-type intermediate. This species reacts with molecular oxygen and forms a peroxy anion. If the substrate

(in this case cyclohexanone) is present, the peroxy anion performs a nucleophilic attack at the carbonyl group of the substrate, leading to the formation of the Criegee adduct. Due to stereoelectronic and conformational effects, a rearrangement takes place, releasing the formed lactone product. The resulting hydroxy-FAD is regenerated to FAD by elimination of water, which closes the catalytic cycle.

The peroxy anion is in an equilibrium with corresponding hydroperoxide. In the absence of the substrate, the hydroperoxide form becomes prominent. This intermediate is responsible for oxygenation processes of heteroatoms in an electrophilic reaction. However, if no substrate is present, the unstable hydroperoxide decays into superoxide, which in water rapidly reacts to hydrogen peroxide.

Further information on BVMOs such as substrate acceptance and regio- and stereoselectivity can be found in in several recently published papers and reviews.^{[123] [17] [121] [122]}

2.1.3 Selection of a suitable biocatalyst

Two BVMOs were already known to accept ketone **1**, but the described catalysts preferentially converted the (R)-enantiomer, leaving the (S)-ketone untouched, or oxidizing it at a very low rate.^[124] The trend for pronounced kinetic resolutions was found to hold true for many other BVMOs.^[123] Since any chiral information is lost in the pyrolytic ring-opening elimination of lactone **2** to the unsaturated acid **3**, the Baeyer-Villiger oxidation (BVOx) should proceed non-selectively to increase both reaction rate and yield. Therefore, it was important to find a non-selective enzyme. Initially, a previously designed library of variants of cyclohexanone monooxygenase from *Acinetobacter calcoaceticus* NCIMB 9871 and cyclopentanone monooxygenase from *Comamonas* sp. NCIMB 9872 (Clouthier et al. 2006; Reetz et al. 2004) were screened. Unfortunately, both enzymes were selective for one stereoisomer, or the conversion was not complete after 24 h, even at the low substrate loading used in these screening reactions (4 mM) (Figure 2.3).

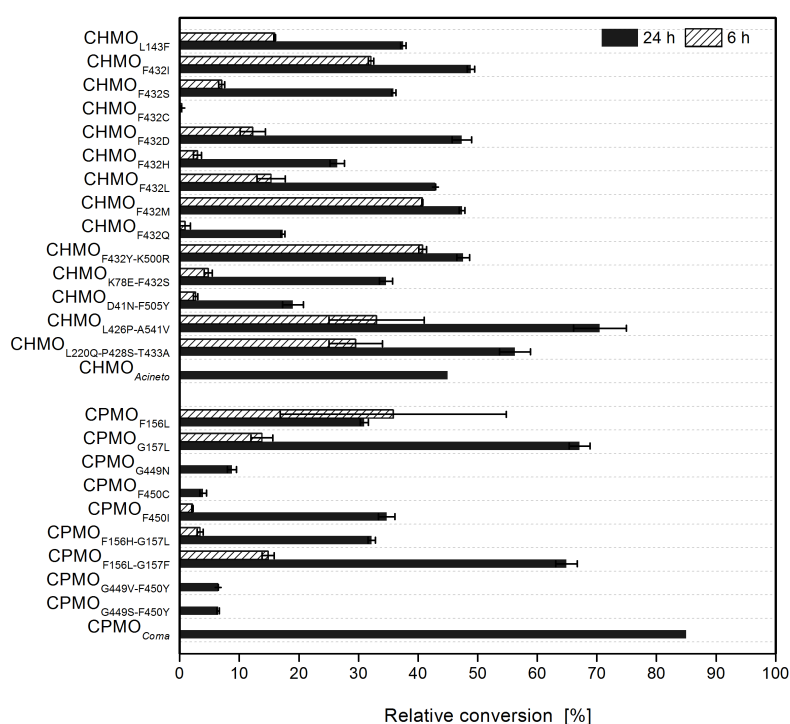


Figure 2.3: Screening of CHMO_{Acineto}, CPMO_{Coma} and their mutants

Conversion of racemic ketone **1** (4 mM) in LB medium. GC results from achiral GC measurements. Adapted from^[125].

In the course of a systematic study on BVMO-catalyzed oxidations of nitriloketones^[123], ex-

periments on an analytical scale showed that a cyclopentadecanone monooxygenase (CPDMO) from *Pseudomonas* sp. HI-70^[126] catalyzed the transformation of both starting material enantiomers with low selectivity ($E = 5-16$) and at a high rate. Another BVMO, 2-oxo- Δ^3 -4,5,5-trimethylcyclopentenylacetyl-CoA monooxygenase (OTEMO) from *Pseudomonas putida*^[127] was even less selective ($E = 2$) in the experiments (Figure 2.4), but due to its reportedly poor stability^[128] CPDMO was chosen as a candidate for further optimization.

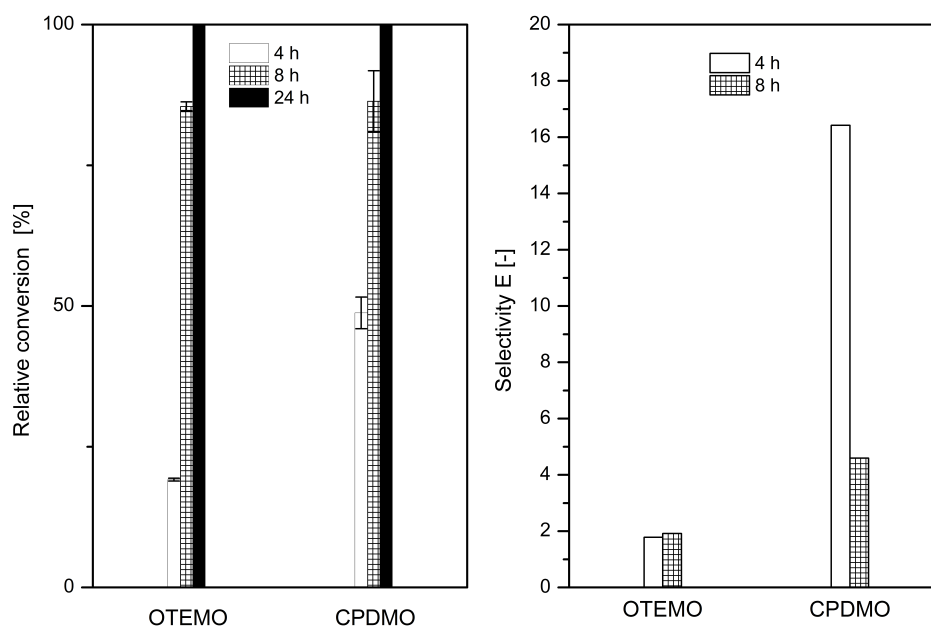


Figure 2.4: Screening of OTEMO and CPDMO towards conversion of racemic ketone

1.

Conversion of racemic ketone **1** (4 mM) to the lactone **2** in LB medium. Conversion and selectivity determined by chiral GC-FID.

2.1.4 Comparison of different expression systems for CPDMO performance

The overall aim was to establish the biotransformation process in a minimal medium to enable better scalability and control. Additionally, glucose should be used as a defined carbon source. The implementation of a secondary substrate limitation after biomass generation and protein production should be introduced to avoid oxygen limitation in standard bioreactors, as this would be unfavorable for an oxygen-consuming reaction. NADPH-dependent BVMO reactions benefit from high intracellular NADPH concentration^[129], supported by the proper carbon source. Since the metabolization rate of glycerol is lower than that of glucose, a cultivation of *E. coli* exclusively on glycerol as carbon source may be insufficient for cofactor recycling when high substrate amounts are applied.

To this end, the CPDMO gene was recloned from a TOP10 pBAD system into an IPTG-inducible expression vector, the pET26b(+). Glucose could not be used for the rhamnose-induced pBAD expression system due to inhibited uptake of other sugars by catabolite repression from glucose^[130].

As a first step, the pBAD_cpdm0 construct as well as the empty pET26b(+) were digested with *SalI* and *NdeI* and the constructs were separated on agarose gel. The CPDMO insert as well as the pET26b(+) backbone (Figure 2.5) were cut out of the gel and purified with the Promega kit.

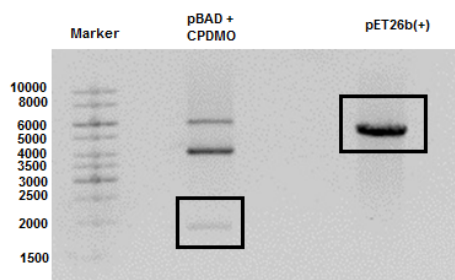


Figure 2.5: Restriction of pBAD_cpdm0 and pET26b(+) and purification of CPDMO insert and pET26b(+) backbone

Restriction with *SalI* and *NdeI*. Cutting of highlighted CPDMO insert (approx. 1600 bp) and linearized pET26b(+) (approx. 5300 bp) out of agarose gel and purification.

The insert and backbone were ligated according to the fast ligation protocol from Promega and transformed with chemical transformation into *E. coli* BL21 (DE3). The *E. coli* BL21

(DE3) pET26b(+)_cpdmo expression was tested in M9 medium with glucose (Figure 2.6) as well as the biotransformation activity which showed full conversion of 5 mM after 24h.

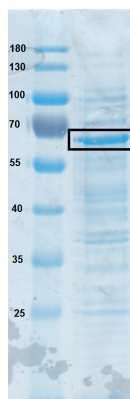


Figure 2.6: Expression of pET26b(+)_cpdmo in M9 minimal medium.

Cell-free extracts of CPDMO expression (64 kDa).

The newly established expression system pET26b_cpdm in *E. coli* BL21(DE3) was compared in terms of biotransformation velocity to a rhamnose-induced pBAD_cpdm expression system in the L-leucine-auxotrophic *E. coli* TOP10 strain. Both strains were grown in shake-flask experiments in 10 mL M9 minimal medium, and then tested with 5 mM ketone. Experiments with the TOP10 strain were supplemented with L-leucine. Here, glycerol was used as carbon source for both strains to ensure comparability in metabolic rates.

The pET vector system showed slower biotransformation performance in comparison to the pBAD system (18 h vs 13 h to full conversion), since exogenous supply of L-leucine to the auxotrophic TOP10 strain likely reduces the ribosomal burden and thus leads to a faster protein production. It was observed, that addition of L-leucine to the culture was problematic, since even trace impurities in several batches of high purity grade leucine inhibited growth of the organism significantly (Figure 2.7).

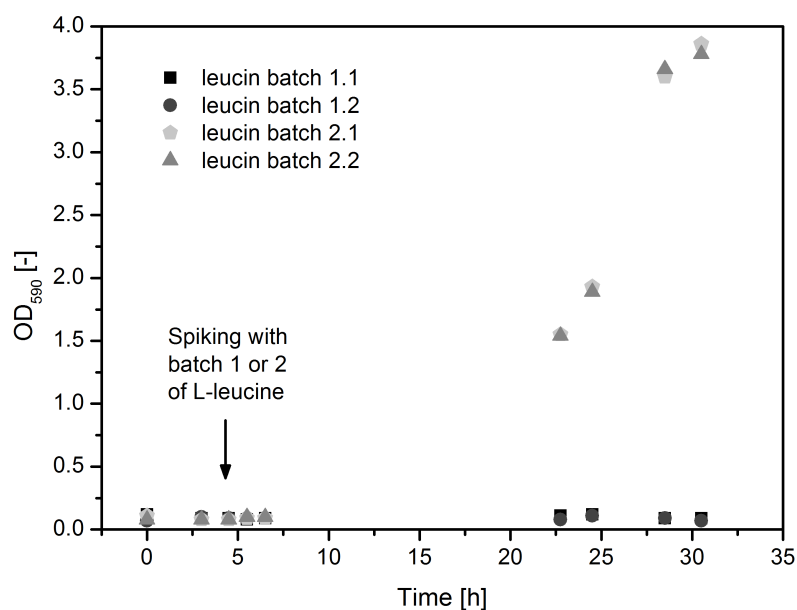


Figure 2.7: Comparison of two different L-leucine batches with purity ≥ 99 %.

Comparison of *E. coli* TOP10 pBAD_cpdmo in M9 medium with glycerol as carbon source (20 g L^{-1}). Spiking of L-leucine to a final concentration of 2 g L^{-1} after 3.5 h of cultivation.

Since only one out of four L-Leucine batches showed growth, application of this supplement was rather problematic. Hence, the new pET expression system was chosen for further development; it did not limit the operational space for a potential process in terms of carbon source and the purity requirements for the additive. The optimization on the biocatalyst level was successfully completed.

2.1.5 Transfer to a controlled bioreactor and optimization of the cultivation

As a first upscaling experiment, a cultivation in a bioreactor on a 4 L scale was set up, monitoring physiological parameters, respiratory activity and the biotransformation efficiency to establish stable conditions.

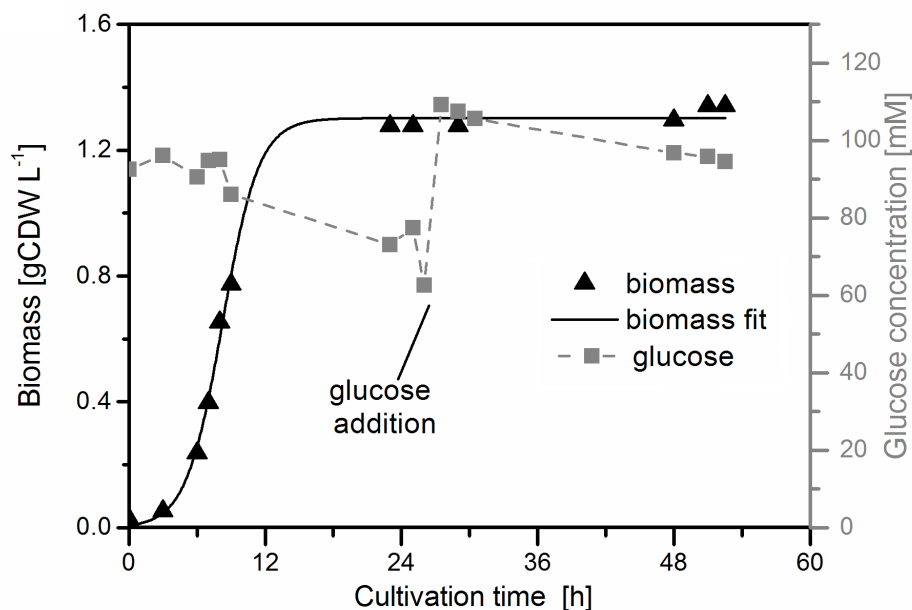


Figure 2.8: Biotransformation on 4 L scale with simultaneous *E. coli* BL21(DE3) CPDMO expression during the growth phase: biomass formation, glucose consumption.

M9 medium with 20 g L⁻¹ glucose, 1000 rpm agitation speed, 1 vvm specific aeration, $T_{initial} = 37$ °C, $T_{expression} = 24$ °C, induction with 0.2 mM IPTG at OD = 1.0.

The growing phase of the culture ended after approximately after 17 h, followed a by nitrogen-limited stationary phase. The biomass concentration then remained stable until the end of the experiment after 52 h (1.34 gCDW L⁻¹; Figure 2.8). The expected biomass concentration with the applied ammonium concentration of 0.22 g L⁻¹ was 1.07 gCDW L⁻¹.^[131] According to the fit of the biomass concentration, the maximum growth rate μ_{max} was 0.63 h⁻¹.

Overflow metabolites (e.g. acetate, pyruvate and ethanol) were not detected in the HPLC

analysis, although acetate is known to be formed under nitrogen limitation, even with low glucose consumption.^[132] That was beneficial, since acetate accumulation inhibits the growth of recombinant *E. coli* cells stronger than of wild-type cells in minimal media.^[133] Carbon balancing calculations revealed that approx. 70 mM carbon was not accounted for (total carbon: 264 mM), leading to the conclusion that overflow metabolites must have been formed, that were possibly not detectable with the applied HPLC protocol. Another possible uncertainty could derive from a different carbon content compared to the value in the literature.^[134] The glucose concentration was intermittently monitored, and glucose was added to the medium shortly before the second substrate load to have comparable conditions for the two rounds of biotransformation.

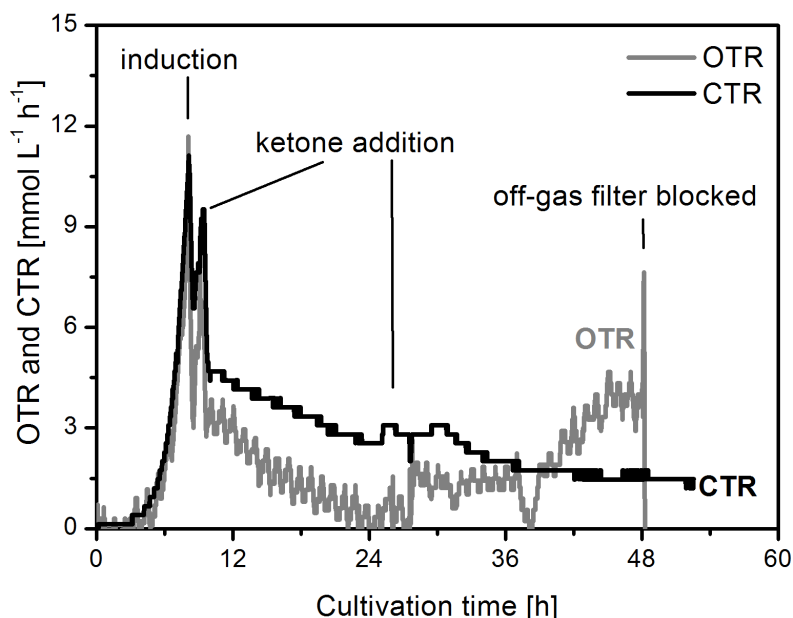


Figure 2.9: Biotransformation on 4 L scale with simultaneous *E. coli* BL21(DE3) CPDMO expression during the growth phase: Off-gas analysis of the process (OTR and CTR).

M9 medium with 20 g L⁻¹ glucose, 1000 rpm agitation speed, 1 vvm specific aeration, $T_{initial} = 37$ °C, $T_{expression} = 24$ °C, induction with 0.2 mM IPTG at OD = 1.0.

The oxygen transfer rate (OTR) and carbon dioxide transfer rate (CTR) plots clearly indicated a decline in respiratory activity as a response to induction with IPTG, and to the addition of the ketone (Figure 2.9). The maximum transfer rates were found around the time

of induction (approx. $11 \text{ mmol L}^{-1} \text{ h}^{-1}$ OTR, approx. $12 \text{ mmol L}^{-1} \text{ h}^{-1}$ CTR). The absence of a permanent maximum in the OTR plot indicated that the culture was not oxygen-limited, which would be disadvantageous for our oxygenating synthetic reaction. In the stationary phase OTR values were below $5 \text{ mmol L}^{-1} \text{ h}^{-1}$, with average CTR values of $6.5 \text{ mmol L}^{-1} \text{ h}^{-1}$.

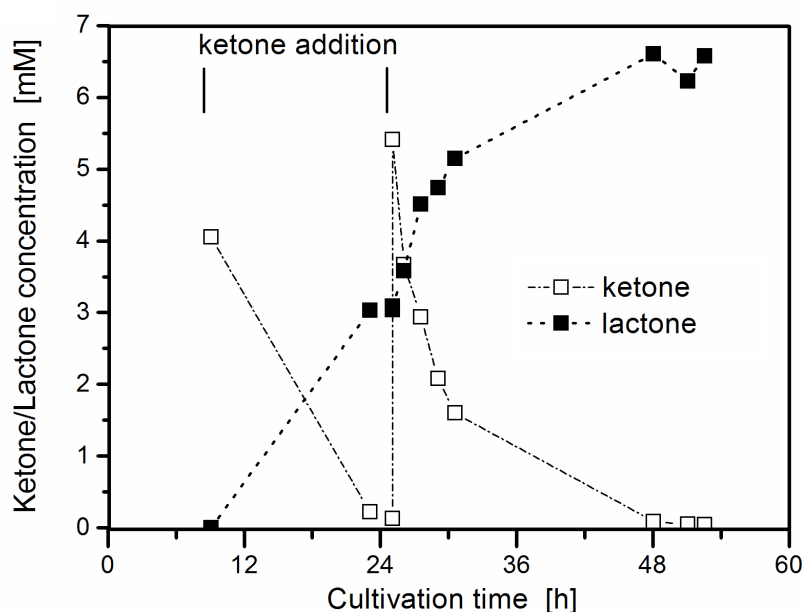


Figure 2.10: Biotransformation on 4 L scale with simultaneous *E. coli* BL21(DE3) CPDMO expression during the growth phase: ketone and lactone concentrations.

M9 medium with 20 g L^{-1} glucose, 1000 rpm agitation speed, 1 vvm specific aeration, $T_{\text{initial}} = 37 \text{ }^\circ\text{C}$, $T_{\text{expression}} = 24 \text{ }^\circ\text{C}$, induction with 0.2 mM IPTG at OD = 1.0.

The ketone was added 9 h after inoculation as a 2.5 M solution in dioxane to a final concentration of approx. 4 mM. The concentration of the co-solvent dioxane was negligible (Figure 2.11). The substrate was completely consumed after 16 h, yielding exclusively the desired lactone according to GC analysis (Figure 2.10). The culture was then charged with a second load of starting material to a final concentration of approx. 5 mM to evaluate its residual activity. Full conversion to the corresponding lactone was reached again after 23 h (from the point of addition).

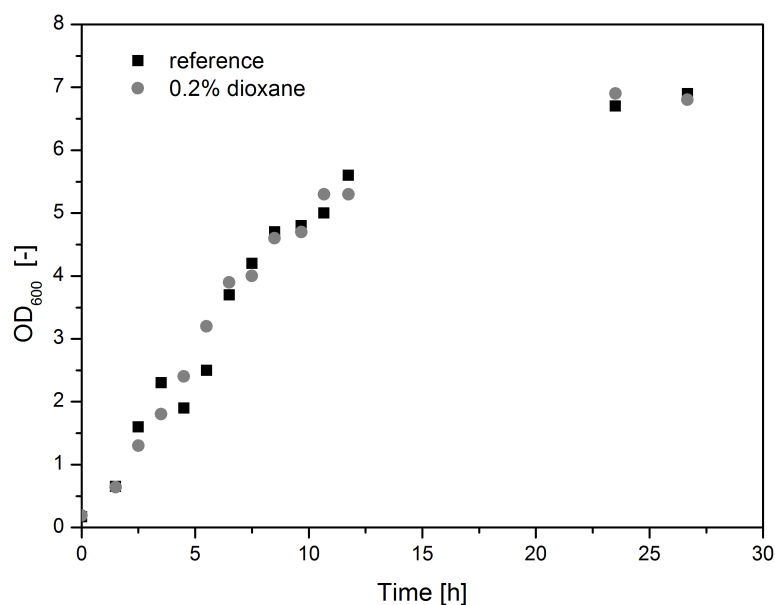


Figure 2.11: Influence of dioxane on *E. coli* growth.

10 mL LB medium in 250 mL non-baffled Erlenmeyer shake-flask, 350 rpm, $T_{initial} = 37\text{ }^{\circ}\text{C}$, $T_{expression} = 24\text{ }^{\circ}\text{C}$, induction with 0.2 mM IPTG at OD = 1.0.

The reaction mass for ketone and lactone could not be fully balanced. That was attributed to evaporation of the ketone due to the aeration of the culture, a known issue for volatile ketones in aerated biotransformations.^[46] The reaction time for achieving full conversion was only slightly shorter in the late-exponential phase than in stationary phase.

In summary, the cultivation in the bioreactor on a 4 L scale was successful by operating (i) without any oxygen limitation, which would reduce biotransformation velocity, (ii) without acetate formation, which would inhibit the recombinant system in minimal medium, and (iii) with similar biotransformation velocity under growing and non-growing conditions. Since most catalytic turnovers would take place in the stationary phase, after a short growth period, the development for higher productivity by increasing the final concentration of biomass under controlled conditions was continued.

2.1.6 Substrate-feed-product-removal (SFPR) concept facilitates up-scaling to a higher ketone titer

The next step was to increase the reaction rate by applying a higher concentration of biomass *via* engineering of the cultivation medium, while mitigating negative effects of higher ketone and lactone concentrations in the medium. To tackle the first challenge, we tripled the concentrations of ammonium sulfate (sole nitrogen source) and magnesium sulfate. This way, the culture reached a threefold higher final value (4.42 gCDW L⁻¹ vs. 1.43 gCDW L⁻¹ in regular M9). Triplication of magnesium only gave a final titer of 1.70 gCDW L⁻¹, indicating that the limiting secondary nutrient was nitrogen. The optimization of cultivation conditions was successfully completed.

Subsequently, the toxicity and growth inhibition of the ketone **1** on the *E. coli* cells was investigated. The experiment was performed with and without CPDMO expression to determine the optimum concentration judged by overall biotransformation performance. In both cultures, with and without inducer, a concentration of 10 mM ketone already decreased the final biomass concentration by 30% in comparison with the reference cultivation without ketone addition. Conversely, the data did not show any acute toxicity effects, even at 20 mM ketone titer (Figure 2.12).

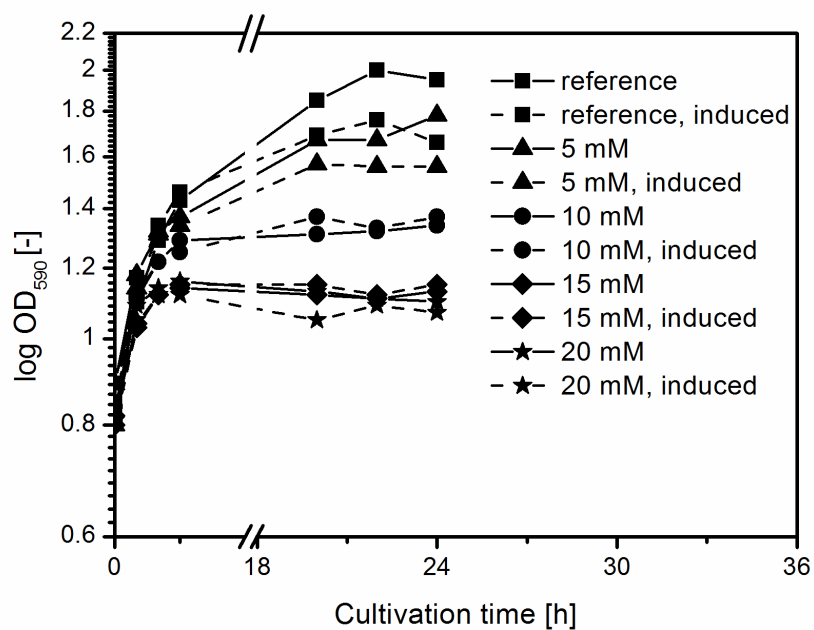


Figure 2.12: Growth curves of *E. coli* TOP10 harbouring pBAD_CPDMO plasmid with different concentrations of ketone 1.

Logarithmic growth curves of *E. coli* TOP10 harbouring pBAD_CPDMO plasmid, induced (solid) and uninduced (dashed), with different concentrations of ketone 1; reference: no addition of ketone.

However, a decrease in growth rate with rising ketone concentrations was observed (Figure 2.13).

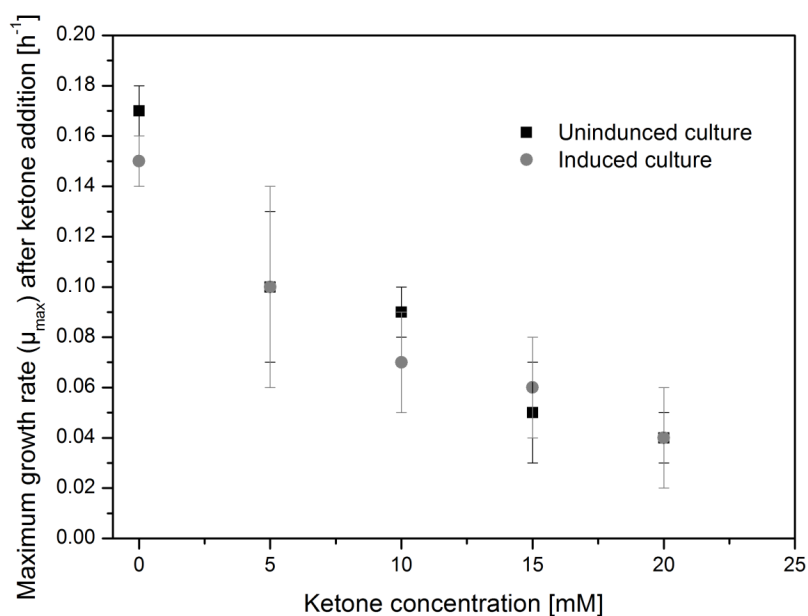


Figure 2.13: Influence of ketone 1 addition on the growth of *E. coli*, with and without CPDMO expression at 24 °C. Calculated from Figure 2.12.

Two strategies to overcome the problematic growth inhibition were contemplated: i) addition of the substrate only when the culture had grown to its final density, or ii) implementation of a concept of feeding the substrate into the biotransformation while simultaneously removing the product. The possibility of a product inhibition, a known obstacle for BVMO-mediated reactions^[135], should be circumvented and the increased evaporation of the starting material due to the gassing of the liquid phase should be reduced. Additionally, one goal was to enable efficient downstream processing. The substrate-feed-product-removal (SFPR) concept was used^{[136][46][47]}, which is based on the equilibrium of adsorption of substrate and product to an apolar cross-linked polystyrene resin with high specific surface area (Lewatit VP OC 1163). A constant concentration of the organic reactants in the liquid phase would avoid growth-inhibiting concentrations and simplify the downstream processing, since the product would absorb on the resin material. It was reported earlier that fed-batch operations with continuous removal of the product by heterogeneous adsorption were not as successful as the SFPR concept^[136] due to product inhibition. Even though a bioprocess without SFPR would be simpler in terms of implementation, it would complicate the downstream processing. The equilibrium load constants X_{eq} for ketone **1** were determined by incubating the resin and various amounts of ketone in medium and analyzing supernatant concentration *via*

calibrated GC. The optimized M9 medium in combination with the SFPR concept was applied to convert 42.5 g substrate (281 mmol), adsorbed on the polymer resin (177.1 g, $X_{eq} = 0.40$). A constant substrate concentration of approx. 5 mM (Figure 2.14) in the liquid phase was maintained, minimizing negative effects of substrate or product on the culture.

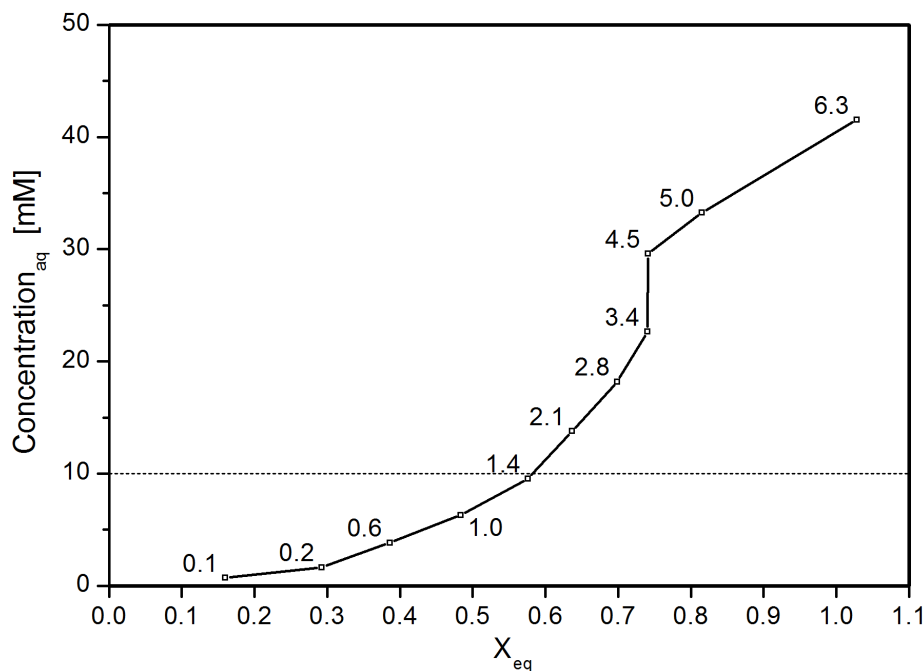


Figure 2.14: Resin loading study, ketone 1 on Lewatit VP OC 1163 resin.

C_{aq} : concentration of ketone 1 in aqueous phase, X_{eq} : equilibrium load ratio ($X_{eq} = m_i/m_{dryads}$, with m_i = weight of the compound i and m_{dryads} = weight of the dry adsorbent^[136]) Dashed line: arbitrary toxicity threshold of 10 mM. Data labels: concentration of ketone 1 in $g L^{-1}$. Adapted from^[125].

Biomass formed with a slightly higher rate as in the previous experiment on a 4 L scale ($\mu_{max} = 0.82 h^{-1}$), and reached a higher final value due to the modification of the medium composition ($3.49 gCDW L^{-1}$). The slightly higher maximum growth rate was due to onset of the nitrogen limitation occurring at a later time point. We added a higher amount of glucose ($\approx 110 mM$) at the beginning, sufficient to maintain the cofactor recycling for the first 46 h, plus two more additions in the stationary phase (Figure 2.15).

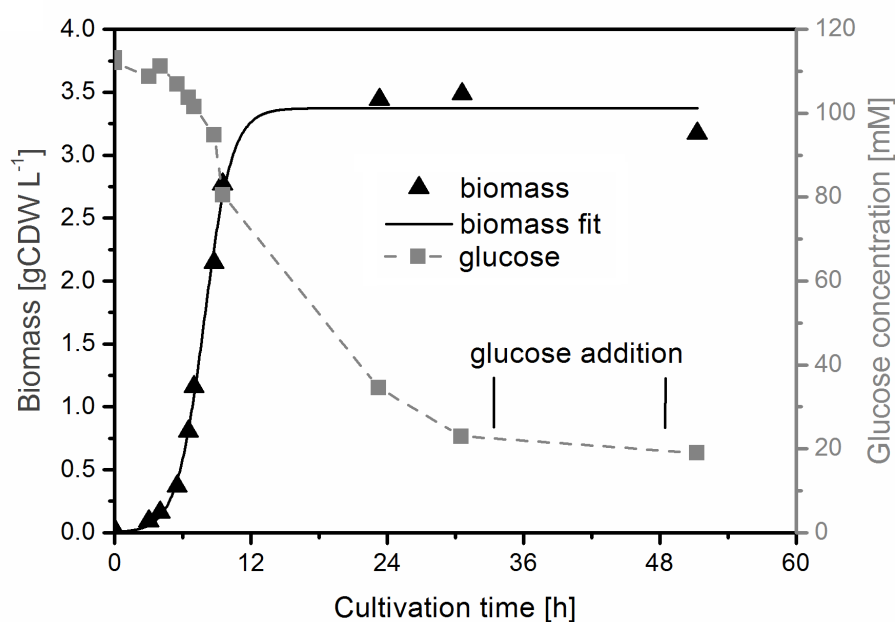


Figure 2.15: Biotransformation on a 4 L scale with ketone bound to Levatit VP OC 1163 resin material: biomass formation and glucose concentration.

Modified M9 medium ($3 \times \text{MgSO}_4$ and $3 \times (\text{NH}_4)_2\text{SO}_4$) with 20 g L^{-1} glucose, 1000 rpm agitation speed, 1 vvm specific aeration, $T_{\text{initial}} = 37^\circ\text{C}$, $T_{\text{expression}} = 24^\circ\text{C}$, induction with 0.2 mM IPTG at OD = 2.6, immediate effect of glucose pulses on glucose concentration was not observed due to the sampling interval/constant consumption by *E. coli* cells.

During the stationary phase, the glucose concentration was intermittently monitored with glucose test stripes (Accu-Chek, Roche, Basel), and glucose was added to the medium to keep the glucose concentration above approx. 18 mM to maintain the cells' cofactor recycling system. Again, although no overflow metabolites could be detected using HPLC, carbon balancing revealed a gap of 197 mM carbon missing from the balance (total carbon 732 mM). The unaccounted amount was directly proportional to the triplication in biomass (70 mM carbon were missing with 1.34 gCDW L^{-1} in the previous cultivation). This inaccuracy was attributed to a problem in resolution of the peak for ethanol in the HPLC chromatograms.

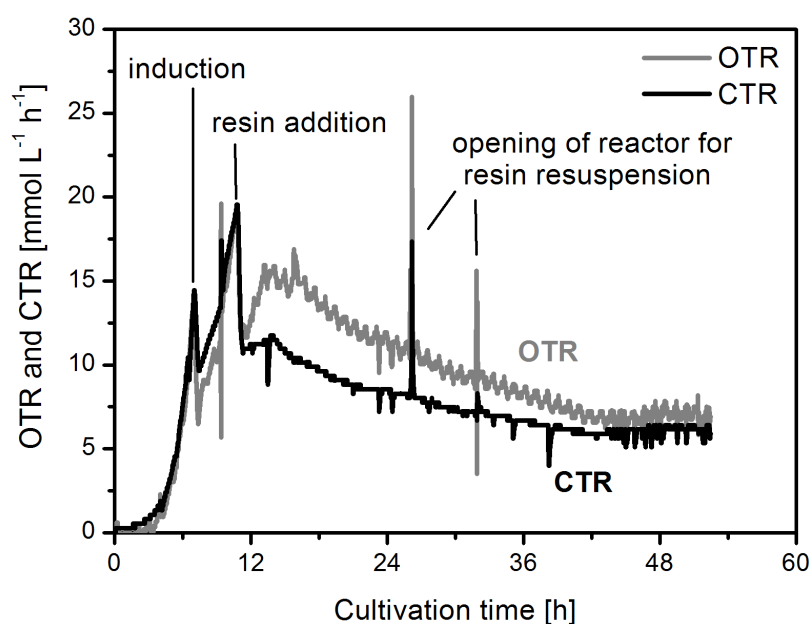


Figure 2.16: Biotransformation on a 4 L scale with ketone bound to Levatit VP OC 1163 resin material: off-gas analysis (OTR and CTR).

Modified M9 medium ($3 \times \text{MgSO}_4$ and $3 \times (\text{NH}_4)_2\text{SO}_4$) with 20 g L^{-1} glucose, 1000 rpm agitation speed, 1 vvm specific aeration, $T_{\text{initial}} = 37^\circ\text{C}$, $T_{\text{expression}} = 24^\circ\text{C}$, induction with 0.2 mM IPTG at $\text{OD} = 2.6$.

OTR and CTR values were highest in the exponential phase ($20 \text{ mmol L}^{-1} \text{ h}^{-1}$). In the stationary phase rates of $10\text{-}15 \text{ mmol L}^{-1} \text{ h}^{-1}$ were reached, which directly correlated to the triplication of biomass concentration compared to the previous upscaling experiment (Figure 2.16). Still, no oxygen limitation or overflow metabolites were observed during the entire cultivation. Especially oxygen limitation can be a problem in SFPR BVMO processes, when higher cell densities are reached.^[137] Directly after substrate addition, higher OTR values were observed: we could monitor the consumption of molecular oxygen by the enzymatic Baeyer - Villiger oxidation, and thus the reaction progress, *via* the OTR signal at this higher substrate load. As substrate conversion proceeded, less molecular oxygen was consumed by the CPDMO-catalyzed reaction, and the OTR values gradually converged with the CTR values. After 42h identical values of OTR and CTR were reached. Measurement of the conversion progress in the culture broth medium and on the resin material also showed stagnation of the reaction rate (Figure 2.17).

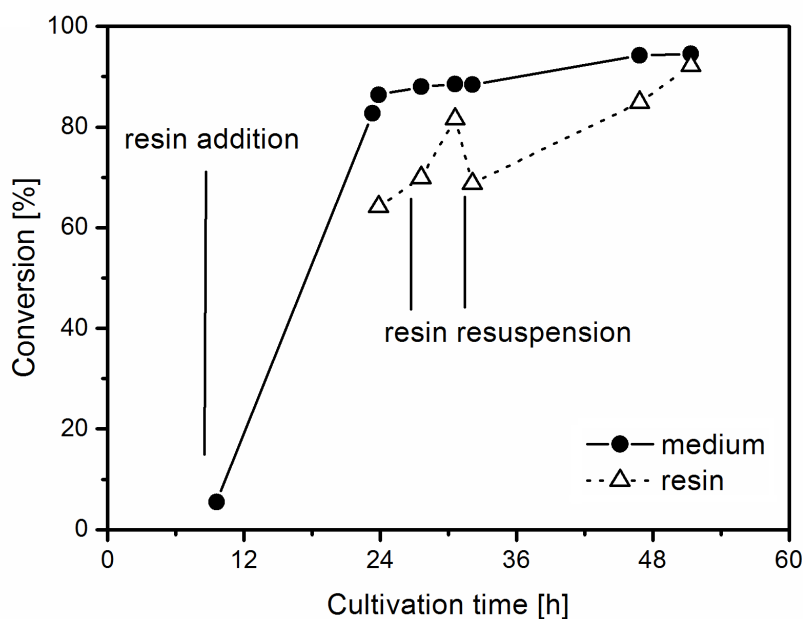


Figure 2.17: Biotransformation on a 4 L scale with ketone 1 bound to Levatit VP OC 1163 resin material: conversion of ketone 1 to lactone 2.

Modified M9 medium ($3 \times \text{MgSO}_4$ and $3 \times (\text{NH}_4)_2\text{SO}_4$) with 20 g L^{-1} glucose, 1000 rpm agitation speed, 1 vvm specific aeration, $T_{\text{initial}} = 37^\circ\text{C}$, $T_{\text{expression}} = 24^\circ\text{C}$, induction with 0.2 mM IPTG at OD = 2.6, relative conversion of ketone to lactone in the liquid phase and on the resin material during the cultivation, GC analysis.

The conversion in the medium was very fast with more than 90% conversion after 24 h. The ratio of product to substrate on the resin increased with a slower rate, which suggested that the reaction was limited by the exchange of ketone and lactone on the adsorbed material, and not by the enzymatic reaction itself.

Throughout the reaction a considerable amount of the resin was unintentionally deposited on the upper walls and the lid of the bioreactor as a result of agitation and aeration. It could therefore not directly interact with the biotransformation mixture anymore. Hence, after 24.5 and 26 h we briefly opened the reactor and manually washed down the deposited material, showing as spikes in the OTR and CTR signals. After the first resin resuspension, the conversion of the starting material on the resin increased, but did not change in the liquid phase (Figure 2.17). After the second resuspension, the conversion in the resin dropped from 80% to 70%, showing that the resin deposited on the walls and lid had indeed not taken part in the reaction. The experiment was stopped after both liquid and resin analyses showed a

conversion of >90% after 52 h.

We tested the residual biotransformation activity by adding 5 mM ketone **1** to a 10 mL sample of the culture broth. The biotransformation velocity was $0.29 \text{ mmol gCDW}^{-1} \text{ L}^{-1}$, corresponding to 64% of the velocity measured for the pET system and glucose. The duration of the biotransformation could therefore have been prolonged, eventually even with a higher resin concentration. A total of 70 mM substrate in the biotransformation mixture (approx. 5 mM in the liquid phase) was approx. three times higher than previously published value of SFPR-based scale-up with BVMOs.^[138] In general, the efforts in up-scaling of the biotransformation successfully led to stable process parameters and a stable enzymatic activity over 52 h, and even beyond, which led to the conclusion that the process optimization was successful. We next focused on the development of an efficient product isolation and purification protocol.

2.1.7 Downstream processing

Methyl t-butyl ether (MTBE) was chosen as the solvent for all extraction steps: it was suitable for the extraction of lactone **2** and it was highly scored by the ACS GCI Pharmaceutical Roundtable Solvent Selection Guide. Ethyl acetate - another suitable solvent with good extractive properties for lactone **2** - was ranked lower with respect to waste production.^[139] The aim was to compare possible ways of product recovery for their efficiency: step-wise vs. continuous extraction while separating the liquid and the solid phase. Therefore, the culture was divided into equal fractions. The cultivation broth and the resin were treated separately. The resin was collected by coarse filtration and then continuously extracted in a cellulose thimble using a Soxhlet apparatus. The first 20 extraction cycles yielded 39.0 g of crude product, another 40 cycles with fresh MTBE gave an additional 3.0 g. Pooled together, the two fractions had a lactone content of 75% w/w in the crude product (31.5 g, calculated value).

The supernatant of the centrifuged culture broth was divided into two equal fractions. One was manually extracted three times, yielding 0.9 g crude product (84% w/w lactone). The other was continuously extracted in a perforator, yielding 2.2 g with 93% w/w lactone content. These values clearly showed that a continuous extraction is mandatory, if the lactone should be efficiently recovered from the medium, since it gave fourfold higher extraction efficiency for the lactone with equal solvent consumption. Overall, 93% of the total recovered material were collected from the resin (86% from the first 20 cycles of extraction, another 7% from additional 40 cycles). The medium only held 7% of the crude product mass (8% of final product mass by calculation).

All crude fractions were pooled, and a total lactone content of 74% was determined. The lactone was separated from remaining starting material ketone by short-path distillation under vacuum, and subsequently purified to >99% (GC) by recrystallization. Overall, a high efficiency of 95% was reached in the DSP: 70% isolated yield from 74% content in the crude reaction product. The development and optimization of the DSP was successful.

The incomplete conversion of ketone during the reaction could not be avoided, even though the walls and the lid were rinsed twice to wash the resin back into the culture. Not all of the material was re-submerged again during these washing steps. This problem could be tackled

by specific reactor design: implementation of an appropriate macroporous containment for the resin beads would prevent their permanent separation from the aqueous phase, while still allowing equilibration of the adsorbed molecules with the solution. Overall, a volumetric yield of 8.2 g L^{-1} , based on isolated pure product from the 42 g ketone batch, was calculated. Additionally, the extraction solvent MTBE was recycled to 84% with a purity indistinguishable by NMR from the purchased material.

2.1.8 Conclusion and outlook

A non-hazardous process for the synthesis of a Nylon-9 precursor using BVMO catalysis was developed. The reaction was translated from the initial catalyst discovery and optimization stage to a multi-dozen gram scale process under controlled conditions. The non-stereoselective enzyme CPDMO was successfully implemented as whole-cell biocatalyst in a minimal medium. Cultivation and bioprocess development enabled a biotransformation on the 42.5 g (281 mmol) scale in a 4 L bioreactor, converting the substrate in the SFPR-batch culture to 74% in 52 h. It was shown, that longer reaction times were possible, and that reactor design issues were the main obstacle for a complete conversion of the starting material. Continuous extraction of the polymer resin quickly recovered 85% of the total product. The organic solvent used for the downstream processing could also be recycled to a high extent. The product was isolated from the crude mixture in $\geq 99\%$ purity using short path distillation and recrystallization in 70% isolated yield. The efficient downstream processing had a 95% mass efficiency from crude to pure product. Overall, the optimized biotransformation conditions, resulted in a volumetric yield of 8 g pure lactone per liter culture, without chromatographic separation.

Future BVMO-upscaling studies can benefit from the possibility to monitor the reaction *via* off-gas analysis and the stable biotransformation conditions presented. However, several improvements in regard to the containment of the resin in the liquid phase have to be made. Nevertheless, the application of all development/optimization levels was very successful and led to a high productivity of the biocatalytical process. In the next chapter, the identification of the limits of the biocatalyst itself and proposition of possible optimization strategies was targeted.

2.2 Kinetic modeling of an enzymatic redox cascade *in vivo*

2.2.1 General aspects

As the last chapter dealt with optimization on various levels of the biocatalytic process, in this chapter, the focus was shifted towards the biocatalyst level of optimization. The investigated system was a whole-cell catalyst expressing an enzymatic cascade.

In recent years, enzymatic cascades have gained popularity due to the high compatibility of biocatalysts in a one-pot or whole-cell environment, thereby circumventing the need to purify intermediates, or to install protective groups.^[140] Following the guidelines of retrosynthesis in designing artificial pathways, the key transformations can easily be identified, and the connectivity of reactions can be established.^{[141][25]} This approach, however, does not consider the performance of the pathway quantitatively. So far, optimization required considerable experimental effort to identify problematic steps. Similar to the first part of the study in the previous chapter, the following study dealt with the optimization on a biocatalyst level. However, the biocatalyst had a higher complexity to the previous study, since it expressed an enzymatic cascade. Many methods for optimization towards maximum yield and productivity have been successfully applied on enzyme cascades.^{[56][57]} Their success, however, depended on the straightforward identification of the limiting factor; failing that, the process involved tremendous experimental work. Computational approaches, such as kinetic modeling of *in vitro* or *in vivo* enzymatic reactions, have only been explored in few studies, e.g. cofactor recycling *in vitro*^[66], modeling of aldolase stability^[142], simulation of a three-enzyme cascade system for synthesis of 6 hydroxyhexanoic acid^[67], or a three-enzyme cascade for the biotransformation of sucrose to cellobiose^[143]. These studies were important to gain insights into the limiting factors for biotransformation performance, and largely replaced experimental effort, since hypotheses could reliably be tested *in silico*. So far, most enzymatic kinetic models were based either on known concentrations of enzymes with an *in vitro* system^{[142][143]}, or the enzymes were assumed to be in excess compared to the substrates in the cell^[144]. Only few models have taken into account the intracellular concentration of enzymes, mostly simulating natural metabolic pathways.^{[145][146]} Here, the aim was to develop such a kinetic model based on a well-characterized, but artificial pathway. This reaction cascade was previously used to study the sequential operation of three unrelated redox enzymes

with shared cofactors, both *in vitro*^[147], and in a whole-cell system^[55] (Scheme 2.18).

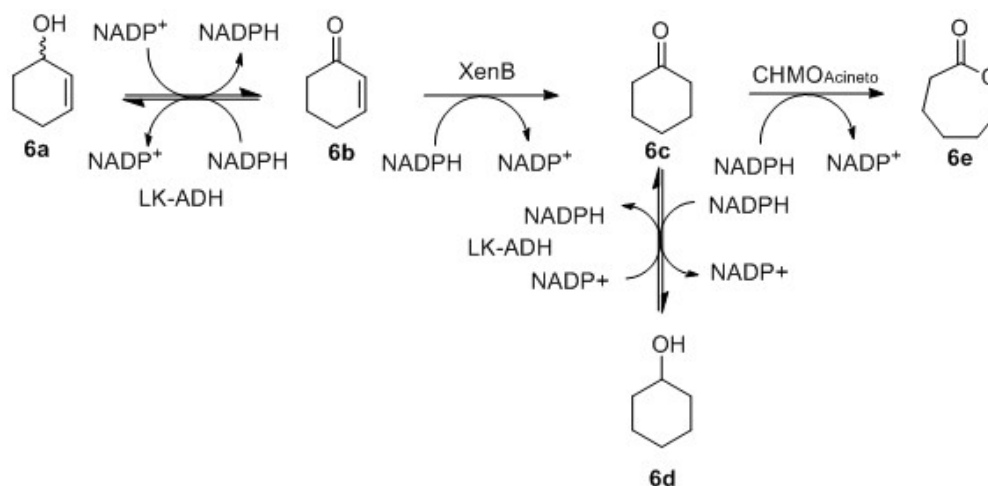


Figure 2.18: Cascade reaction from cyclohexenol **6a** to ϵ -caprolactone **6e**.

The cascade connected the oxidation of a secondary alcohol, a Michael-type reduction, and a Baeyer-Villiger oxidation, catalyzed by an alcohol dehydrogenase (ADH), an enoate reductase (ERED) and a Baeyer-Villiger monooxygenase (BVMO), respectively. The ADH (from *Lactobacillus kefir*)^[30] depended on magnesium, and the other two enzymes required non-covalently attached flavins as redox-active components (flavin mononucleotide, FMN, for the ERED from *Pseudomonas putida*^{[55][148]}, and flavin adenine dinucleotide, FAD, for the BVMO from *Acinetobacter calcoaceticus*)^[149]. The starting material cyclohexenol **6a** was converted to ϵ caprolactone **6e** via intermediates **6b** (cyclohexanone) and **6c** (cyclohexanone) in the particular cascade; the transformation was shown to proceed comparably well on several other examples, including the conversion of (1*S*,5*S*)-carveol **7a** to the corresponding lactone **7e** (Scheme 2.19) and 2-methyl-cyclohexenol **8a** to the corresponding lactone **8e** (Scheme 2.20).

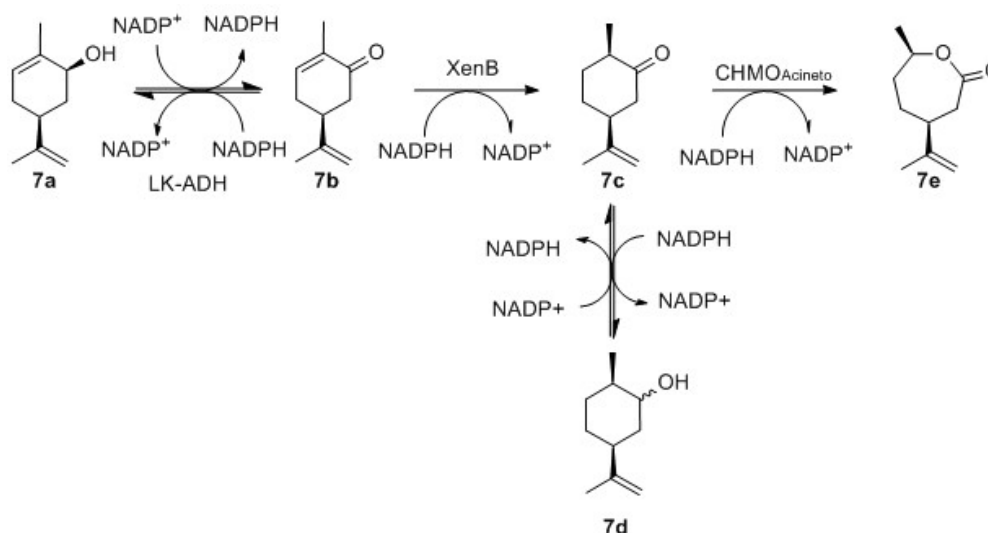


Figure 2.19: The cascade example from starting from (1S,5S)-carveol 7a.

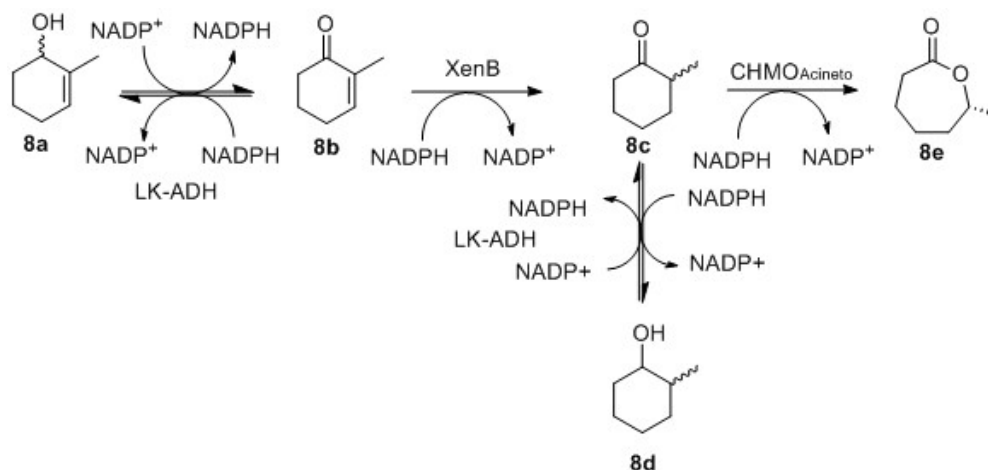


Figure 2.20: The cascade example from starting from 2-methyl-cyclohex-2-en-1-ol 8a.

The ADH also catalyzed the redox equilibration between cyclohexanone **6c** and the side product cyclohexanol **6d** and 2-methylcyclohexanone **8c** to 2-methylcyclohexanol **8d**^[55]. Since all reactions catalyzed by the ADH were reversible at room temperature (25 °C), the formation of intermediates **6d** and **8d** merely extended the reaction time towards the desired product. Within the present study, we aimed at identifying the origin for the reduced productivity, and propose optimization strategies *via* simulations with minimum experimental effort. The specific objectives of the model were:

- to estimate the enzyme concentrations in the reaction to locate the rate-determining step

- to identify possible extrinsic reasons for its reduced velocity within the cascade
- to propose an optimization strategy to overcome this limitation and increase the overall performance of the cascade

As a first step, the model had to be established, to know which parameters are required to be determined experimentally. The rate laws for all cascade reactions were derived based on the Michaelis-Menten (MM) theory. The idea was to determine the kinetic parameters *via* initial rate measurements, and to use them as constant parameters in non-linear fitting of experimental data from *in vivo* cascades. This way, the concentrations of active enzymes can be estimated. The resulting model should serve to simulate three cascade examples, and to formulate hypotheses pertaining the limiting factors to the performance of the cascade. These hypotheses are then tested both *in silico*, and by experiments *in vitro*.

2.2.2 Development of the kinetic model

First, we postulated the generic rate laws for all reactions, beginning with the starting material a (eq. 2.1), then the intermediates b (eq. 2.2) and c (eq. 2.3), the side product d (eq. 2.4), and the final product e (eq. 2.5).

$$\frac{d[a]}{dt} = -v_{a \rightarrow b} + v_{b \rightarrow a} \quad (2.1)$$

$$\frac{d[b]}{dt} = v_{a \rightarrow b} - v_{b \rightarrow a} - v_{b \rightarrow c} \quad (2.2)$$

$$\frac{d[c]}{dt} = -v_{c \rightarrow d} + v_{d \rightarrow c} + v_{b \rightarrow c} - v_{c \rightarrow e} \quad (2.3)$$

$$\frac{d[d]}{dt} = v_{c \rightarrow d} - v_{d \rightarrow c} \quad (2.4)$$

$$\frac{d[e]}{dt} = v_{c \rightarrow e} \quad (2.5)$$

The assumption was that the concentration of the essential cofactors NADP⁺ and NADPH would remain approximately constant over the course of the reaction *in vivo*, since viable *E. coli* cells would actively regulate the redox balance for homeostasis^[150]. Furthermore, it was assumed that all enzymes would suffice the conditions for Michaelis-Menten kinetics, possibly with inhibition, and the individual rates of the reactions based on eq. 2.6 were calculated (for explanation of all parameters see Table 2.1)

Table 2.1: List of symbols and abbreviations for MM kinetics.

Symbol	Name	Unit
$k_{cat,S}$	turnover number for substrate S	s ⁻¹
[S]	substrate concentration	μM
K_M, S	Michaelis-Menten constant for substrate S	μM
[I]	inhibitor concentration	μM
K_I	inhibition constant towards the enzyme	μM
K_{II}	inhibition constant towards the enzyme substrate complex	μM
[ENZ]	apparent initial enzyme concentration	μM

$$v = \frac{v_{max}[S][ENZ]}{K_M + [S]} = \frac{k_{cat}[S]}{K_M + [S]} \quad (2.6)$$

For all ADH-catalyzed reactions, we added terms for mixed inhibition (eq. 2.7), since we later observed that the enzyme was inhibited by the initially used co-solvent ethanol.

$$v = \frac{v_{max}[S]}{K_M(1 + \frac{[I]}{K_i}) + [S](1 + \frac{[I]}{K_{ii}})} \quad (2.7)$$

Substitution with the enzyme- and substrate-specific parameters lead to the Michaelis-Menten rate laws, described by eq. 2.8-2.10, for the productive reactions of the cascade

$$v(a \rightarrow b) = \frac{k_{cat,a}[a][ADH]}{K_{M,a}(1 + \frac{[I]}{K_i}) + [a](1 + \frac{[I]}{K_{ii}})} \quad (2.8)$$

$$v(b \rightarrow c) = \frac{k_{cat,b}[b][ERED]}{K_{M,b} + [b]} \quad (2.9)$$

$$v(c \rightarrow e) = \frac{k_{cat,c}[c][ERED]}{K_{M,c} + [c]} \quad (2.10)$$

and the rate laws for the ADH-catalyzed back and side reactions, described by eq. 2.11-2.13:

$$v(b \rightarrow a) = \frac{k_{cat,b}[b][ADH]}{K_{M,b}(1 + \frac{[I]}{K_i}) + [b](1 + \frac{[I]}{K_{ii}})} \quad (2.11)$$

$$v(c \rightarrow d) = \frac{k_{cat,c}[c][ADH]}{K_{M,c}(1 + \frac{[I]}{K_i}) + [c](1 + \frac{[I]}{K_{ii}})} \quad (2.12)$$

$$v(d \rightarrow c) = \frac{k_{cat,d}[d][ADH]}{K_{M,d}(1 + \frac{[I]}{K_i}) + [d](1 + \frac{[I]}{K_{ii}})} \quad (2.13)$$

These equations were later used for non-linear fitting to the experimental data from *in vivo* cascades, after substitution with the parameters from *in vitro* experiments.

2.2.3 Tagging, expression and purification of the cascade enzymes

For performing *in vitro* initial rate measurements to determine MM-parameters, the strategy was to use purified enzymes. The use of purified enzymes is beneficial, since no background reactions catalyzed by other enzymes from the *E. coli* metabolome can occur. The easiest way to purify enzymes is by introducing a polyhistidine-tag into the enzyme sequence and and purify it *via* affinity chromatography with bivalent ions, e.g. nickel.

Unsuccessful purification of alcohol dehydrogenase from *Lactobacillus kefir* with a polyhistidine tag (his-tag)

As a first step for the his-tag purification, the LK-ADH gene was isolated by restriction digestion the original pET21b(+)_LK-ADH construct with restriction enzymes *NdeI* and *XhoI*. The pET28a(+) was treated equally and both, the backbone and the LK-ADH gene were isolated from an agarose gel and ligated. After transformation into *E. coli* BL21 (DE3), several clones were picked and checked if the correct construct was present. All picked clones showed the expected band pattern after *PvuII* digestion (Figure 2.21).

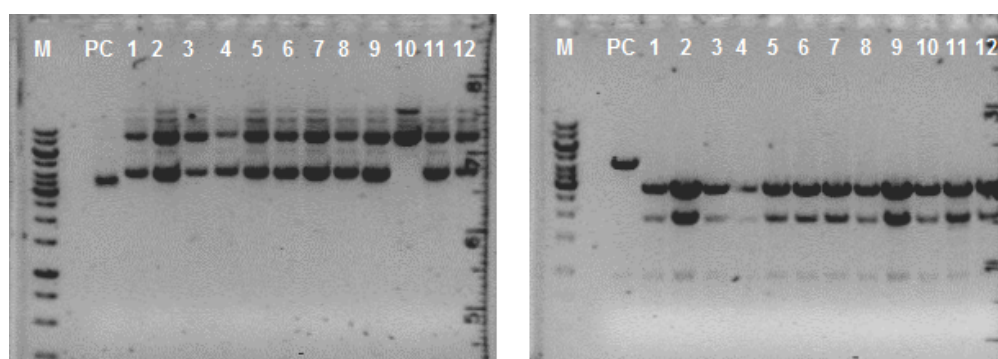


Figure 2.21: Plasmid isolation and control digest of the pET28a_LK-ADH construct.

A Plasmid isolation M: marker, PC: positive control (pET28a), 1-12: isolated plasmids of 12 colonies

B Control digest with *PvuII*. M: marker, PC: digested positive control (pET28a), 1-12: digested plasmids of **A**.

Four of the positive clones were sequenced and the resulting clone with the correct sequence with an N-terminal polyhistidine tag without any mutations in the genetic sequence of the LK-ADH was chosen for expression studies (Figure 2.22).

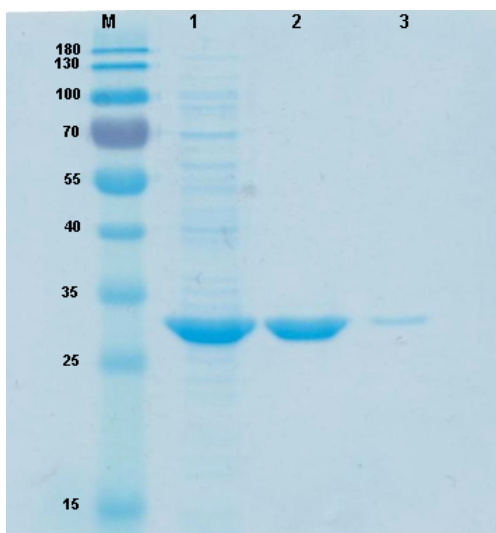


Figure 2.22: Expression and purification of Poly-His-tagged LK-ADH.

M: Marker, 1: Cell-free extract and the 2: first and 3: last fraction of the purification.

The LK-ADH was expressed in the soluble fraction and had the corresponding size of around 26.8 kDa, which represents the size of one subunit of this homotetrameric protein. The purification was achieved as well (Figure 2.22 Line 2 and 3). The cell - free extracts were tested regarding the reduction of cyclohexanone to cyclohexanol *in vitro* with a recycling system. After one hour, 5 mM cyclohexanone were completely converted to cyclohexanol, which was the final proof for the establishment of a succesful construct.

The active cell-free extracts containing extracts of LK-ADH were purified according to the His-tag protocol. After purification, the enzyme was neither active according to GC nor according to measurements of activity in the photometer by observing NADPH consumption at 340 nm. A stabilization approach with addition of 1 mM CaCl₂ to all of the purification buffers resulted in active LK-ADH, which had a specific activity in the activity assay with 10 mM acetophenone of 9.9 U/ μ mol LK-ADH. In this case, the measurement of activity was performed not on the same day as the purification and concentration of the enzyme.

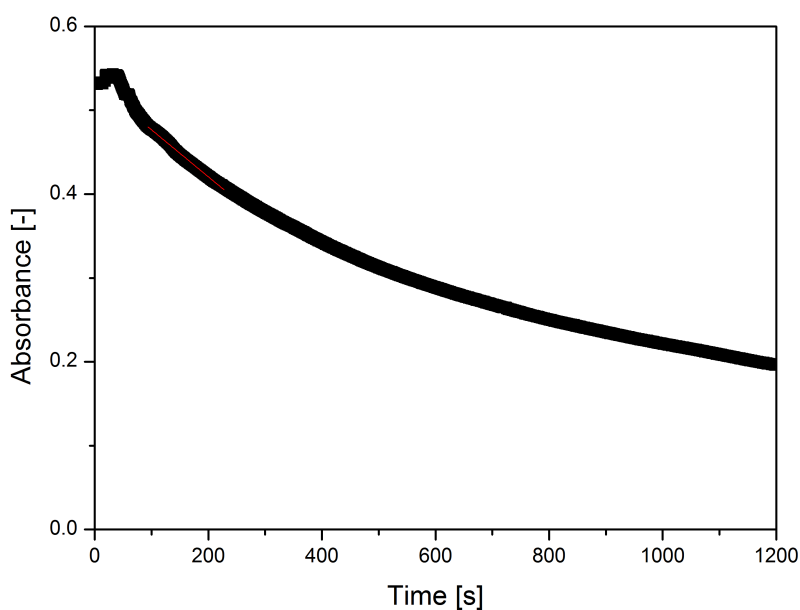


Figure 2.23: Activity assay of His-tagged LK-ADH after purification with CaCl_2 addition.

Conditions: $1.64 \mu\text{M}$ His-Tagged LK-ADH monomer, standard photometric activity assay with acetophenone without MgCl_2 .

Unfortunately, the purified and His-tagged LK-ADH showed a decline in activity over time, despite being stored at 4°C . Since the catalytic function of this enzyme is dependent on the incorporated Mg^{2+} -ions it was investigated, if the addition of MgCl_2 leads to an increased catalytic activity (Figure 2.24).

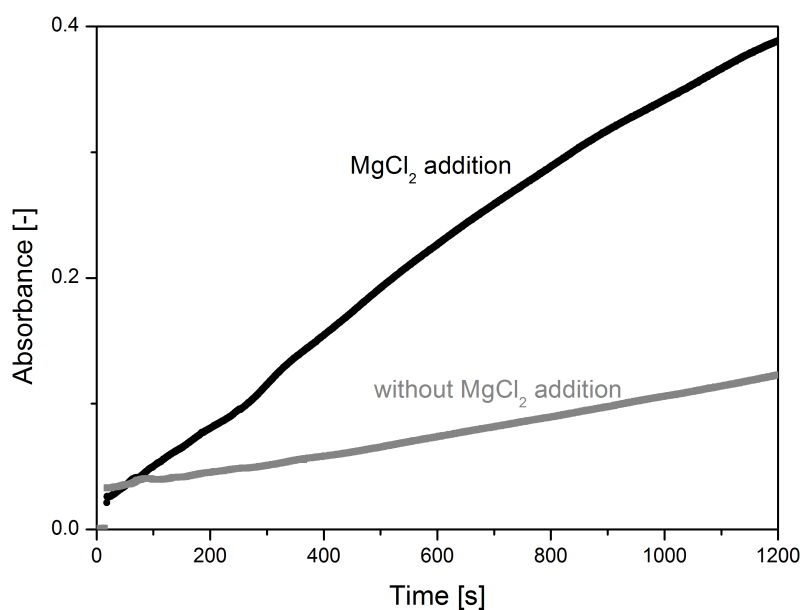


Figure 2.24: Activity measurement with purified His-tagged LK-ADH with MgCl₂ addition.

Conditions: 1 μ M His-tagged LK-ADH, 20 mM cyclohexanol in 50 mM Tris-HCl pH 7.5, 0.1 mM NADP⁺, optionally 1.6 mM MgCl₂ addition to the photometric measurement.

With increasing amounts of MgCl₂, the enzyme activity could be partially restored. However, the long term stability and activity of the His-tagged enzyme was compromised by the introduction of the tag. In contrast to the published non-affected stability over several months at 4 °C^[30], the activity of the His-tagged construct declined in one week at 4 °C from 220 U μ mol (cell-free extract preparation, purification and activity measurement on the same day) to 36 U μ mol (79 % activity loss). This deactivation was attributed to binding of the His-tagged N-terminus to the activity domain with the Mg-ion, located at the C-terminus. The enzyme was therefore inactivated and precipitated after approx. 2 weeks at 4 °C. The higher MgCl₂ concentration was likely beneficial by not only stabilizing the active site of the enzyme but also by binding to the N-terminal His-tag and preventing the enzyme from deactivating itself completely. Since the sequence of the LK-ADH contained a thrombin restriction site, the next step was cleave the N-terminal His-tag to avoid deactivation.

The purified enzyme was treated according to the protocol described in the experimental

section and according to the workflow in Figure 2.25. The LK-ADH was restricted with a negative control (LK-ADH in restriction buffer only) at 20 °C for 14 h and the restriction was purified *via* a second round of purification with affinity chromatography.

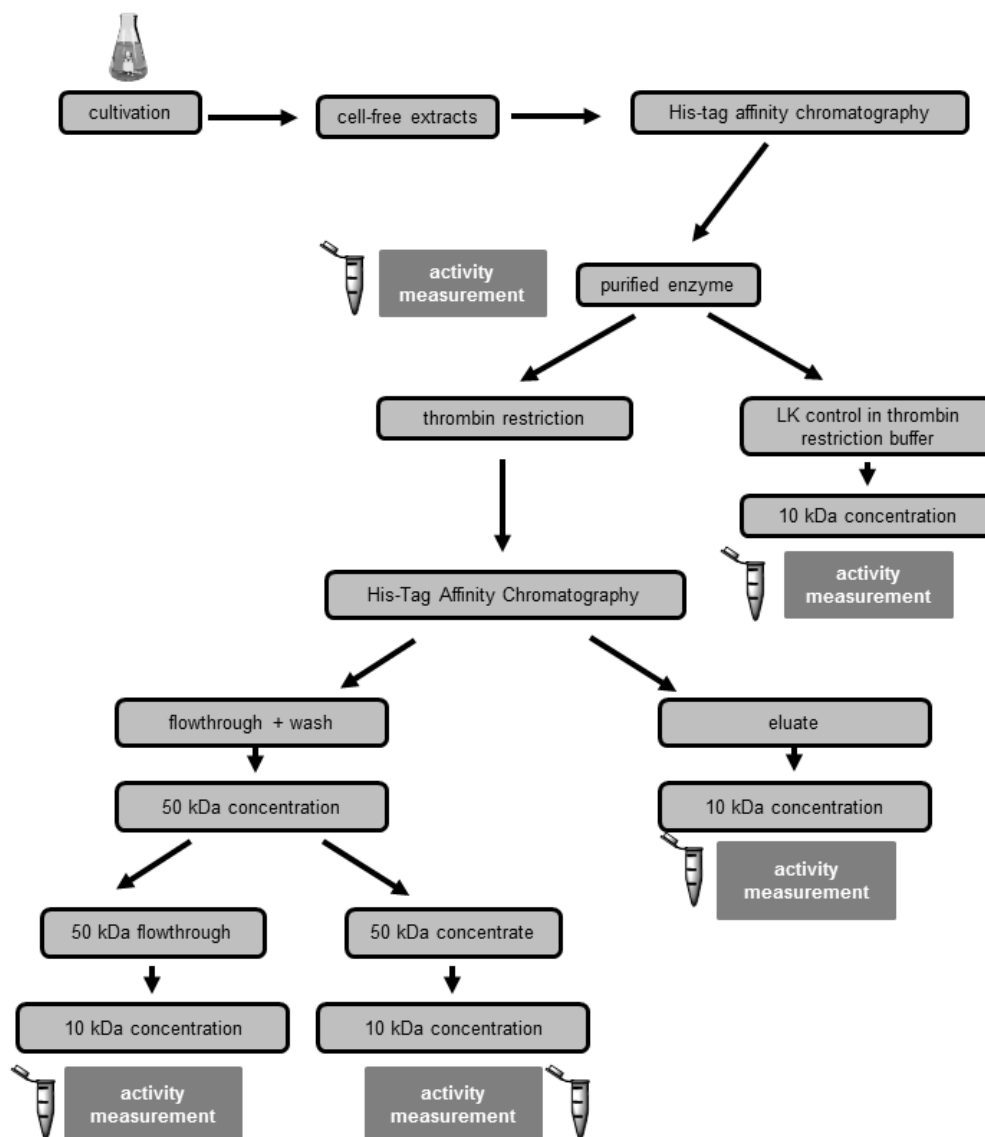


Figure 2.25: Workflow of the thrombin restriction experiment.

Activity measurements are indicated in the workflow and are accompanied by samples for SDS-PAGE represented by eppendorf reaction tubes.

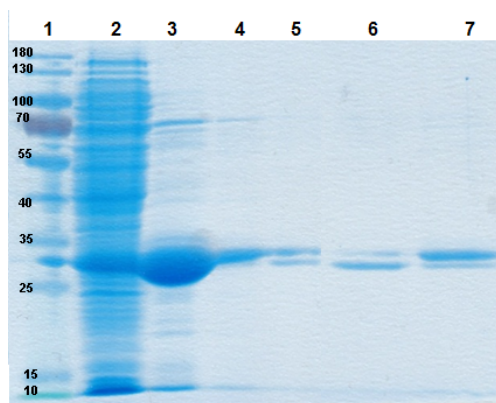


Figure 2.26: Gel of the thrombin restriction experiment.

1: marker, 2: cell-free extracts, 3: purified LK-ADH, 4: LK-restriction control 5: flowthrough and wash of His-trap column, 50 kDa concentrate 6: flowthrough and wash of His-trap column, 50 kDa flowthrough 7: His-trap column eluate.

The SDS-PAGE (Figure 2.26) indicated that the purified LK-ADH as well as the negative restriction control had the full length of approx. 27 kDa (lane 3 and 4) while the fractions from the restriction by thrombin showed a pattern of two bands (lane 5-8); one was the full LK-ADH monomer and the other band was slightly smaller. While the flowthrough and wash of His-trap column, 50 kDa flowthrough (lane 5) showed a distribution between the restricted and non-restricted form accompanied by low LK-ADH concentrations as expected, the 50 kDa concentrate (lane 6) of the same fractions, showed mostly restricted LK-ADH. That means, that restricted LK-ADH mostly did not bind to the column anymore and was forming the homotetramer structure directly after purification. The eluate of the column of the restriction (lane 7) contained mostly unrestricted protein as expected. These fractions were also subjected to an activity assay (substrate: acetophenone, co-solvent ethanol; table 2.2).

Table 2.2: Activity of fractions in the thrombin restriction experiment of His-LK-ADH.

Fraction	Activity [U μmol^{-1}]
purified LK-ADH	218
LK-ADH restriction control	56
His-Trap flowthrough and wash, 50 kDa flowthrough	72
His-trap flowthrough and wash, 50 kDa concentrate	356
His-trap eluate	356

During the course of the incubation, the restriction control showed deactivation by 74 % compared to the purified enzyme stored at 4 °C as well as the enzyme contained in the 50 kDa flowthrough by 67 %. Since the enzyme cannot pass in high amounts through the 50 kDa cut-off in its tetrameric form (approx. 108 kDa), only the monomers (approx. 27 kDa) were able to pass through. The enzyme is inactive in its monomeric form and therefore showed lower activity, since it was only partially able to restore its tetrameric form. However, the restricted enzyme in the 50 kDa concentrate, which was in its tetrameric form, showed an increase in activity compared to the purified enzyme stored at 4 °C by 63 %. The same was true for the His-trap eluate, though in this case, the solution contained mostly the not restricted enzyme. The increase in the activity can be explained by the fact, that only non complexated His-tags of the proteins are bound to the column. Since the enzyme was deactivating itself, it meant that only non-deactivated enzyme was in the eluate fraction and therefore exhibited the maximal activity as the restricted tetrameric fraction. These results were promising, but it was tough to reproduce these results since the conditions for thrombin restriction showed to be harsh for the enzyme, leading to enzyme precipitation in the control as well as in the actual restriction. Therefore, we pursued another tagging strategy, which should avoid any interference with the active site of the LK-ADH.

Unsuccessful purification of alcohol dehydrogenase from *Lactobacillus kefir* with a CBD-intein-tag

The chosen tagging strategy for LK-ADH was to insert the gene into a pTYB21 vector from the IMPACT kit (NEB). The LK-ADH gene (target gene) is expressed with a chitin-binding domain (CBD), which has a high affinity to chitin. Between the CBD and the target protein, an intein tag is incorporated, which is a domain, that is cleaved upon addition of reducing agents, e.g. dithiothreitol (DTT). Upon addition of DTT, the target protein is released without a tag (Figure 2.27). The chitin resin can be regenerated by NaOH.

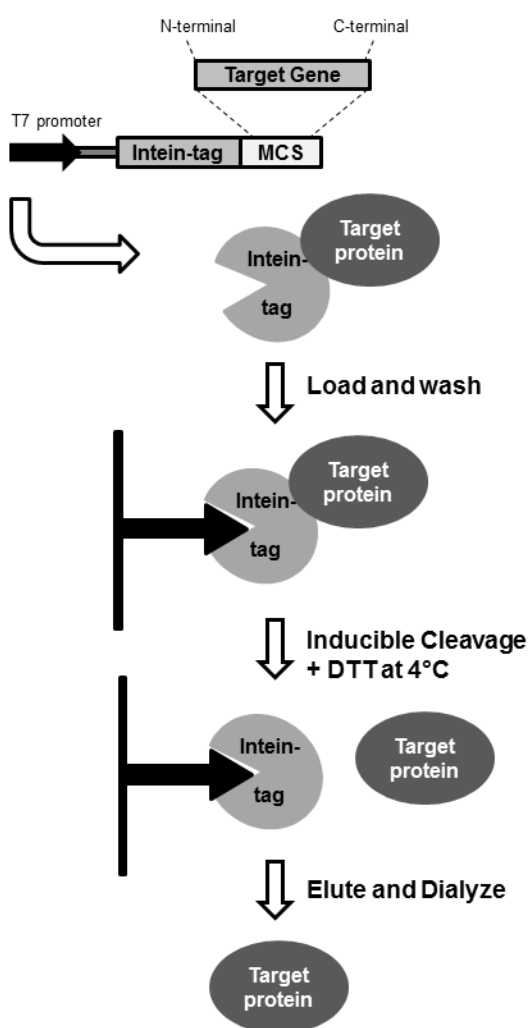


Figure 2.27: IMPACT KIT purification strategy.

Adapted from the^[42] kit manual.

The target *lk-adh* gene was amplified *via* PCR from the pET21b(+)_{lk-adh} template. Both, the target vector pTYB21 and the insert were restricted with *SapI* and *NcoI* and then ligated.

After chemical transformation into *E. coli* cells and reisolation, the *Pvu*II control digest was performed. *Pvu*II digestion produced the expected DNA fragments from the putative pTYB21_intein-CBD:lk-adh construct (4.05 kb, 3.37 kb, 0.75 kb, and 0.09 kb; Figure 2.28).

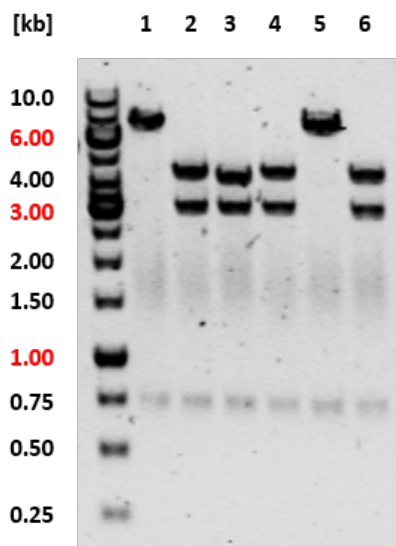


Figure 2.28: *Pvu*II control digestion of pTYB21_intein-CBD:lk-adh plasmids.

Digestion of the empty pTYB21 vector (lane 1) and putative positive clones 1-5 (lanes 2-5). The empty vector produced the expected DNA fragments of 6.67 kb and 0.75 kb; the 0.09 kb fragment could not be detected due to the small size (lane 1). Clones 1-3 (lanes 2-4) and 5 (lane 6) produced the desired DNA fragment pattern of 4.05, 3.37, and 0.75 kb. Again, the 0.09 kb fragment was not detected as expected.

The sanger sequencing revealed the correct sequence for the LK-ADH, with methionine as first amino acid after the intein cleavage side.

The expression conditions at 25°C in LB medium for proof of expression of CBD-intein-LK-ADH yielded in exclusively insoluble protein (Figure 2.29). The CBD-intein-tag alone expressed only in the soluble fraction.

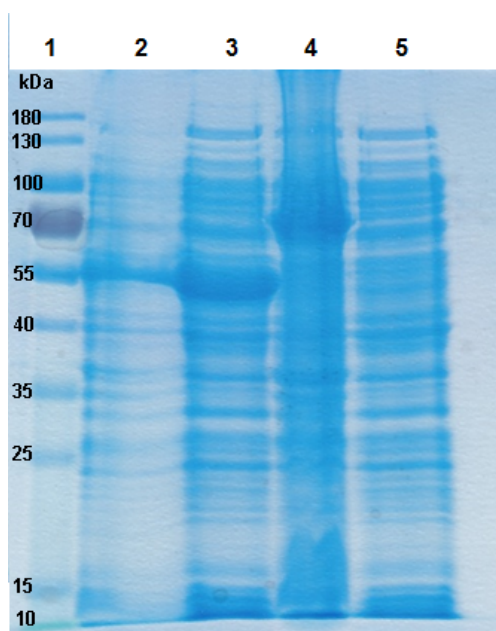


Figure 2.29: Expression of the CBD-intein-LK-ADH constructs at 25 °C.

Expression was performed in LB medium, 1 mM IPTG, 20 h. 1: marker; 2: CBD-intein, insoluble; 3: CBD-intein, soluble; 4: CBD-intein-LK-ADH, insoluble; 5: CBD-intein-LK-ADH, soluble. Size of CBD-intein: 56 kDa; size of CBD-intein-LK-ADH: 85 kDa.

The expression was optimized in a temperature and medium screening Table 2.3.

Table 2.3: Expression screening for CBP-intein-LK-ADH.

Medium	Expression temperature [°C]	Expression level
LB	20	traces of soluble LK-ADH
	25	traces of soluble LK-ADH
	30	traces of soluble LK-ADH
modified M9 (M9-N*)	15	~ 50 % soluble LK-ADH
	20	traces of soluble LK-ADH
	25	traces of soluble LK-ADH
	30	traces of soluble LK-ADH

The only option for expression discovered in the screening for expression conditions was an expression at 15 °C yielding approximately the same amount in soluble and insoluble frac-

tion. Since the growth of the *E. coli* was slow due to the low temperature, the expression had to be performed for 40 h.

After the establishment of expression conditions, the protocol for on column DTT cleavage of the target protein was adapted. As a first step, the CBD-intein-LK-ADH construct was loaded onto the resin and purified (Figure 2.30). The wash with DTT was performed and the resin was incubated at 4 °C for 3 days.

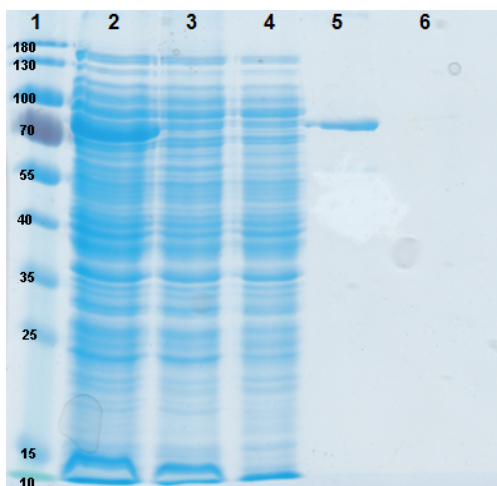


Figure 2.30: Purification and start of on-column cleavage of CBD-intein-LK-ADH construct.

1: marker, 2: cell-free extract, 3: flowthrough of chitin resin, 4: wash of chitin resin, 5: sample of resin with target enzyme, 6: DTT wash.

The loading onto the resin worked well (Figure 2.30). However, the cleavage after 3 days was poor (Figure 2.31 lane 8.) The cleavage efficiency is dependent from the first amino acid of the sequence. Therefore, the gene sequence of the construct was analyzed. The first amino acid was methionine, which, according to the IMPACT manual, shows the highest cleavage efficiency. The cleavage was not only incomplete, but below 50 %.

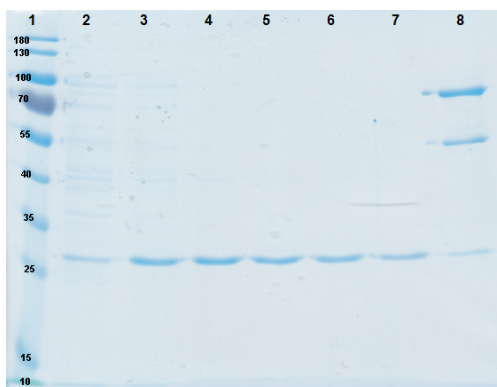


Figure 2.31: Elution fractions of LK-ADH and cleavage progress on column at 4 °C.

1: marker, 2-7: elution fractions 1-6, 8: resin sample.

To improve cleavage, the same column was further incubated at 15 °C for 48h (Figure 2.32 lane 9). The cleavage was still incomplete, so the cleavage was performed once again at 20 °C.

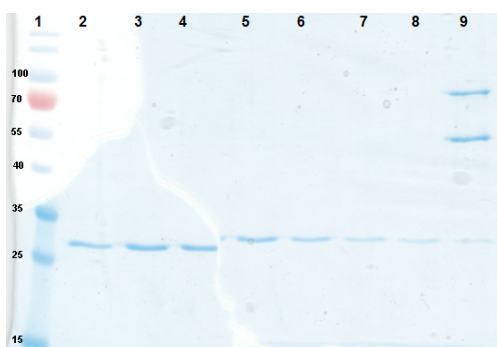


Figure 2.32: On-column cleavage of CBD-intein-LK-ADH construct at 15 °C.

1: marker, 2-8: elution fractions 1-6, 9: resin sample.

The cleavage of the CBP-intein-LK-ADH constructs at 20 °C for 48 h was more efficient as at lower temperatures 2.33. Therefore, these settings for cleavage were chosen as final conditions.

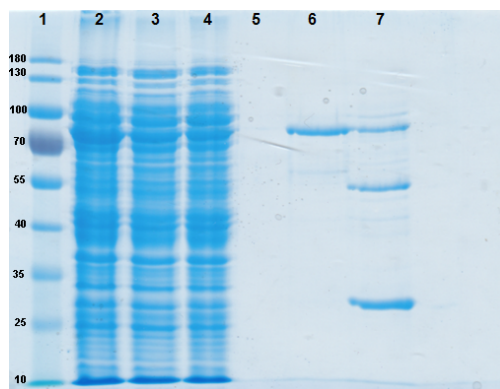


Figure 2.33: Purification and on-column cleavage of CBD-intein-LK-ADH at 20 °C.

1: marker, 2: cell-free extract, 3: flow-through of chitin resin,
4: wash of chitin resin, 5: wash with DTT, 6: resin sample before cleavage, 7: resin sample after cleavage.

The initial activity of the enzyme was $48 \pm 1 \text{ U } \mu\text{mol}^{-1}$ (substrate: acetophenone, co-solvent ethanol). After one month of storage at 4 °C the enzyme still showed 55 % of initial activity. Unfortunately, the purified and cleaved amount obtained with this expression and purification system was too low to be able to perform kinetic measurements, even on a 0.8 L scale. Therefore, the next purification approach was chosen to be a partial purification *via* filtration/concentration with a centrifugal device.

Partial purification of alcohol dehydrogenase from *Lactobacillus kefir* with a centrifugal device

After all previously executed purification strategies did not result in either active or satisfactory amounts of protein, the LK-ADH was simply expressed in autoinduction medium (*E. coli* BL21 (DE3) pET21_LK-ADH without tag) and concentrated with a centrifugal concentrator with a cut-off of 50 kDa. Due to high expression levels of LK-ADH, the host background expression was negligible (Figure 2.34).

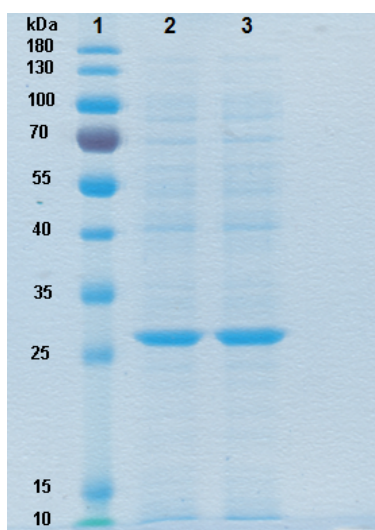


Figure 2.34: LK-ADH expression and concentration with a 50 kDa centrifugal device.

1: marker, 2: cell-free extract, 3: 50 kDa concentrate.

Since there was no column chromatography, the homotetrameric structure of Lk-ADH was not disrupted, which resulted in a size of approximately 107 kDa. The activity of the LK-ADH with this method was $328 \pm 16 \text{ U } \mu\text{mol}^{-1}$ (substrate: 50 mM TRIS-HCL, pH 7.5, acetophenone as substrate, 100 μM NADPH, co-solvent ethanol, 25 °C). Compared to that, the purified LK-ADH from literature^[30] showed higher activity of $994 \mu\text{mol}^{-1}$, but with different conditions (substrate: acetophenone, 250 μM NADPH, unknown or no co-solvent, TEA-buffer, pH 7.0, 30 °C). However, since the activity of LK-ADH is doubled from pH 7.5 to pH 7.0, the values are in the same range.

Purification of enoate reductase XenB from *Pseudomonas putida* with a polyhistidine tag

The enoate reductase XenB from *Pseudomonas putida*^[148] was expressed in the pGaston vector with a C-terminal polyhistidine tag. The expression was induced with 0.02 % L-rhamnose and expressed and purified according to the expression and purification conditions in the experimental section of this thesis (Figure 2.35).

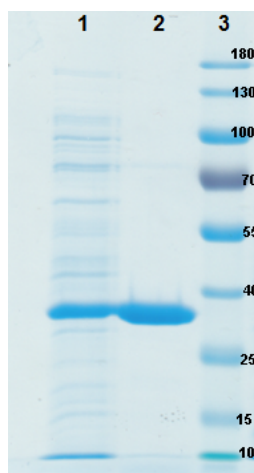


Figure 2.35: XenB expression and purification.

1: cell-free extract, 2: purified enzyme , 3: marker.

The activity assay was performed with the standard substrate cyclohexenone (in acetonitrile), which revealed a specific activity of $90 \pm 3 \text{ U } \mu\text{mol}^{-1}$. The enzyme did not lose activity for at least two weeks at 4 °C.

Purification of the BVMO cyclohexanone monooxygenase (CHMO) with a polyhistidine tag

The BVMO, CHMO from *Acinetobacter* NCIB 9871 was expressed in a pET22b(+) vector with a C-terminal polyhistidine tag. The expression was induced with 0.1 mM IPTG and expressed and purified according to the expression and purification conditions in the experimental section of this thesis (Figure 2.36).

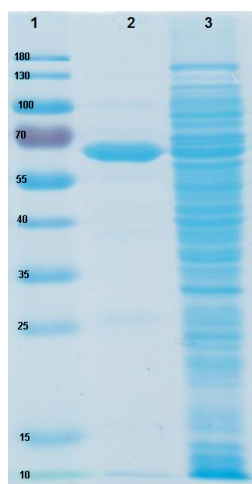


Figure 2.36: Expression and purification of XenB.

1: marker, 2: purified enzyme , 3: cell-free extract.

The activity assay was performed with the standard substrate cyclohexanone (in acetonitrile), which revealed a specific activity of $5730 \pm 56 \text{ U } \mu\text{mol}^{-1}$. The enzyme did not lose activity for at least two weeks at 4 °C.

2.2.4 Determination of inhibition parameters of ethanol on LK-ADH

The influence of ethanol on the performance of the cascade was investigated, as it had previously been used to add the substrates to the reaction (0.4 %, approx. 69 mM).^[55] Its technical properties as a solvent (stable, benign, water-miscible, bio-compatible, volatile)^[151] advocated its use in enzymatic cascades^[152], but as a primary alcohol, it might interfere with the function of ADHs. As a first step, the activity assay, which was performed with acetophenone and ethanol as co-solvent was performed with acetonitrile as co-solvent. As a result, the enzyme was 2.5 times more active in presence of acetonitrile as in presence of ethanol. Therefore, the type of inhibition and the inhibition parameters were determined in additional experiments.

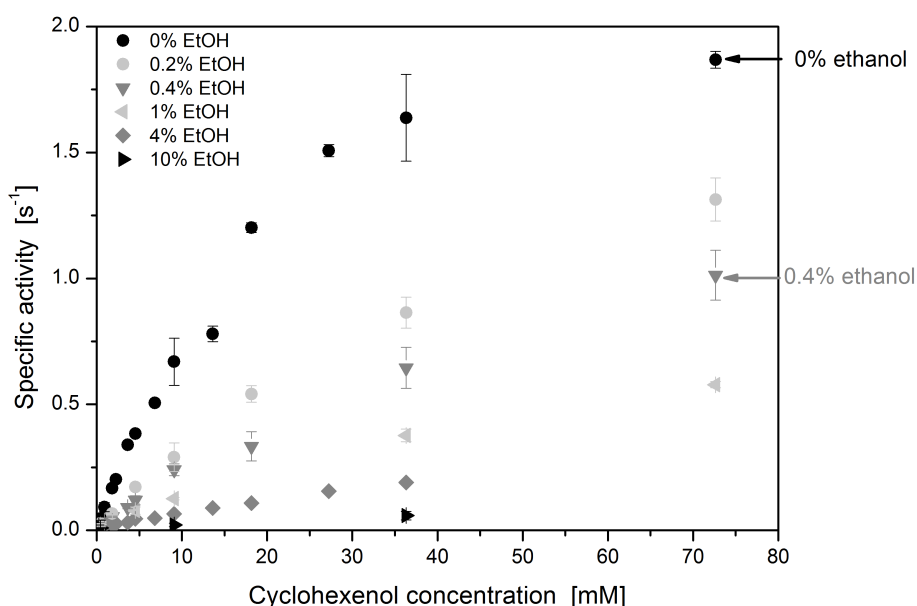


Figure 2.37: Plot of ADH activity with cyclohexenol (6a) and different ethanol concentrations.

The measurements were performed in triplicates; the results are plotted with mean ± 1 SD.

The experiment was performed at different ethanol concentrations (Figure 2.37). The substrate cyclohexenol (**6a**) was added in acetonitrile; additionally ethanol in concentrations up to 10 % (v/v) was added. The activity of the ADH was recorded with different substrate concentrations. The activity of the LK-ADH decreased with rising ethanol concentrations.

In an additional experiment, the activity of ADH was not affected, even with 4 % (v/v) acetonitrile (double the concentration applied in the kinetic measurements).

For determination of the inhibition parameters of ethanol on the ADH, the data shown in Figure 2.37 were plotted as a Lineweaver-Burk plot to determine the type of inhibition (Figure 2.38).

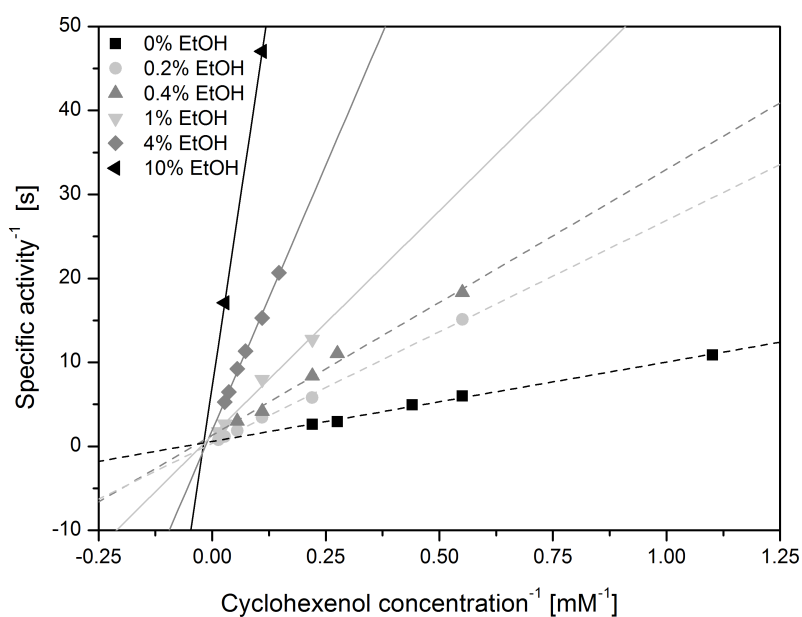


Figure 2.38: Lineweaver-Burk plot of cyclohexenol (6a) activity with different ethanol concentrations.

For parameter determination of the observed mixed type inhibition (Figure 2.39), the data were plotted in two different representations, shown in Figures 2.40 and 2.41.

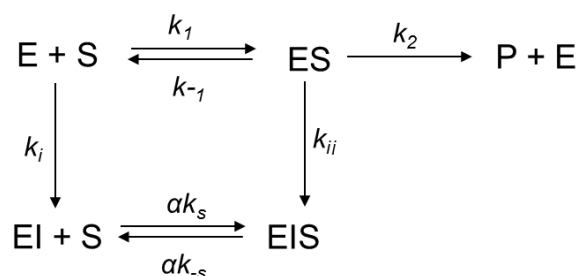


Figure 2.39: Scheme of a mixed type inhibition.

E: enzyme; S: substrate; P: product; I: inhibitor; various k = velocity constants.

The parameter that needed to be determined were the inhibition constant for the enzyme (K_I) and the enzyme substrate complex (K_{II}) (eq. 2.7).

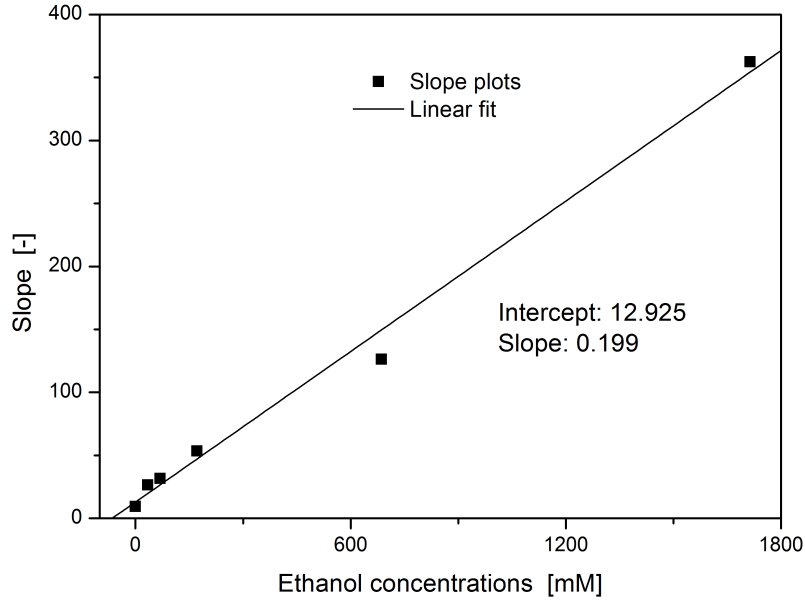


Figure 2.40: Determination of the inhibitory parameter K_I .

The plot of the different slopes extracted from Figure 2.38 was used to calculate the $K_I = 64.9$ mM at $y = 0$ from the linear regression (equation 2.14) over the applied ethanol concentrations. The slope of the different Lineweaver-Burk plots plotted over ethanol concentration.

$$slope = \frac{K_S}{v_{max}K_I} \frac{1}{[I]} + \frac{K_S}{v_{max}} \quad (2.14)$$

The x-intercept in this plot represents the negative K_I value.

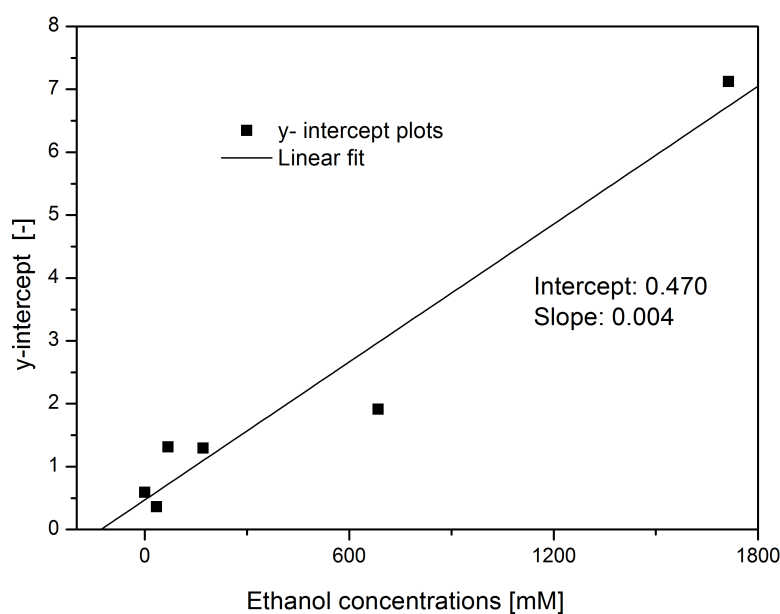


Figure 2.41: Determination of the inhibitory parameter K_{II} .

The plot of the different y-intercepts extracted from Figure 2.38 was used to calculate the $K_{II} = 126.9$ at $y = 0$ from the linear regression (equation 2.15) over the applied ethanol concentrations.

The y-intercept of the different Lineweaver-Burk plots with different concentrations of ethanol plotted over the ethanol concentration (Figure 2.41).

$$y - intercept = \frac{K_S}{v_{max} K_{II}} \frac{1}{[I]} + \frac{1}{v_{max}} \quad (2.15)$$

The x-intercept in this plot represents the negative K_{II} value.

These constants (K_I , K_{II}) were then used for all the rate laws that described ADH-catalyzed reactions.

2.2.5 Determination of Michaelis-Menten parameters

The initial rates of all reactions in the cascade were measured using a standard protocol (see Material and Methods chapter) with one major adaptation: the nicotinamide cofactors were not supplied in such excess, that all enzymes were saturated, but rather added at the intracellular concentration of *E. coli* (0.12 mM for NADPH, 0.10 mM for NADP⁺).^{[153][154]} The resulting estimate for velocity (k_{cat}) was thus not directly comparable to values obtained at saturation. That notwithstanding, the adaptation would increase the meaningfulness of *in vitro* data for the use in modeling of *in vivo* processes.

The highest impact of incomplete saturation by the cofactors was determined for the ADH: the results indicated that it would operate *in vivo* at $0.8 \times k_{cat}$ in oxidative direction ($[NADP^+]_{E. coli} = 3.3 \times K_M$), and at $0.5 \times k_{cat}$ in reductive direction ($[NADPH]_{E. coli} = 1.2 \times K_M$) (Table 2.4). The difference in K_M values was beneficial to the productive flux of the cascade, including the recovery of the side product **6d** by re-oxidation. The other two enzymes would largely remain unaffected by the low concentration ($[NADPH]_{E. coli} \geq 0.95 \times k_{cat}$ for the ERED (Table 2.5), $\geq 0.85 \times k_{cat}$ for the BVMO (Table 2.6)).

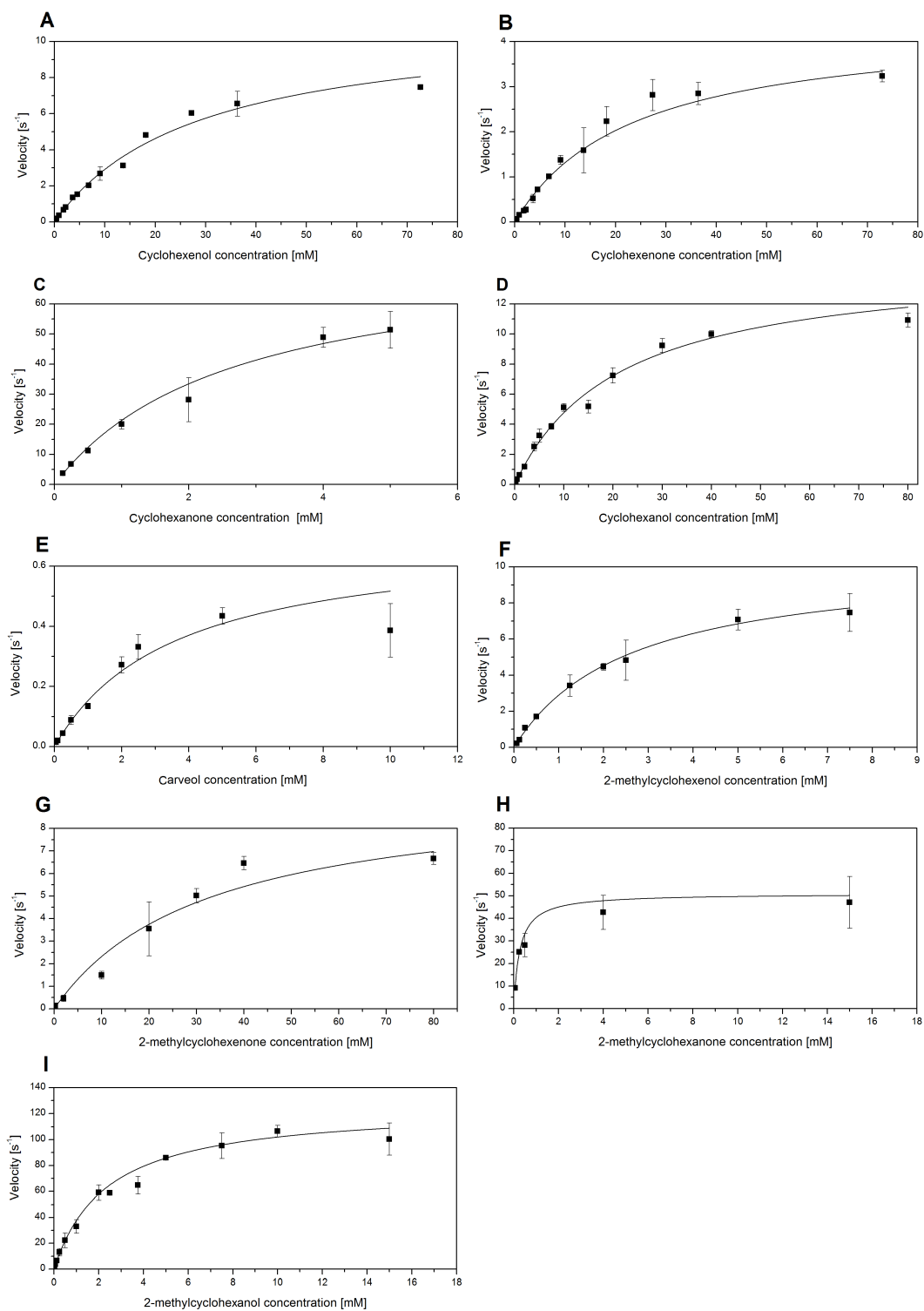


Figure 2.42: LK-ADH kinetic parameters.

A: 6a; 6b; C: 6c; D: 6d; E: 7a; F: 8a; G: 8b; H: 8c; I: 8d.

The data for the Michaelis-Menten plots were fitted with the ordinary Michaelis-Menten equation using instrumental weights with Origin Pro 2015. All kinetic data were measured in triplicates and are reported with mean \pm 1 SD.

Table 2.4: Michaelis-Menten parameters for LK-ADH reactions.

Substrate	K_M	$k_{cat,app}$	$k_{cat,app}$	$k_{cat} K_M^{-1}$
	[mM]	oxidation [s ⁻¹]	reduction [s ⁻¹]	[mM ⁻¹ s ⁻¹]
6a	28.5 ± 2.7		11.2 ± 0.8	0.39 ± 0.06
6b		23.6 ± 1.6	4.4 ± 0.2	0.19 ± 0.02
6c ^[a]		2.7 ± 0.3	78.0 ± 6.9	28.90 ± 5.77
6d ^[a]	21.3 ± 1.0		14.9 ± 0.6	0.70 ± 0.05
7a	3.6 ± 0.7		0.7 ± 0.1	0.30 ± 0.09
7b	-	No activity detected		
7c	-	No activity detected		
7d	-	Activity towards a mixture of isomers detected		
8a	2.6 ± 0.2	10.4 ± 0.6		4.00 ± 0.59
8b	32.2 ± 16.4		9.8 ± 2.6	0.30 ± 0.23
8c ^[a]	0.22 ± 0.03		46.0 ± 3.8	209.09 ± 41.82
8d ^[a]	2.4 ± 0.1	126.1 ± 2.5		52.54 ± 3.25
NADP ⁺	0.03 ^[b]	Not applicable		
NADPH	0.14 ^[b]	Not applicable		
[a]: side reaction; [b]: taken from ^[30]				

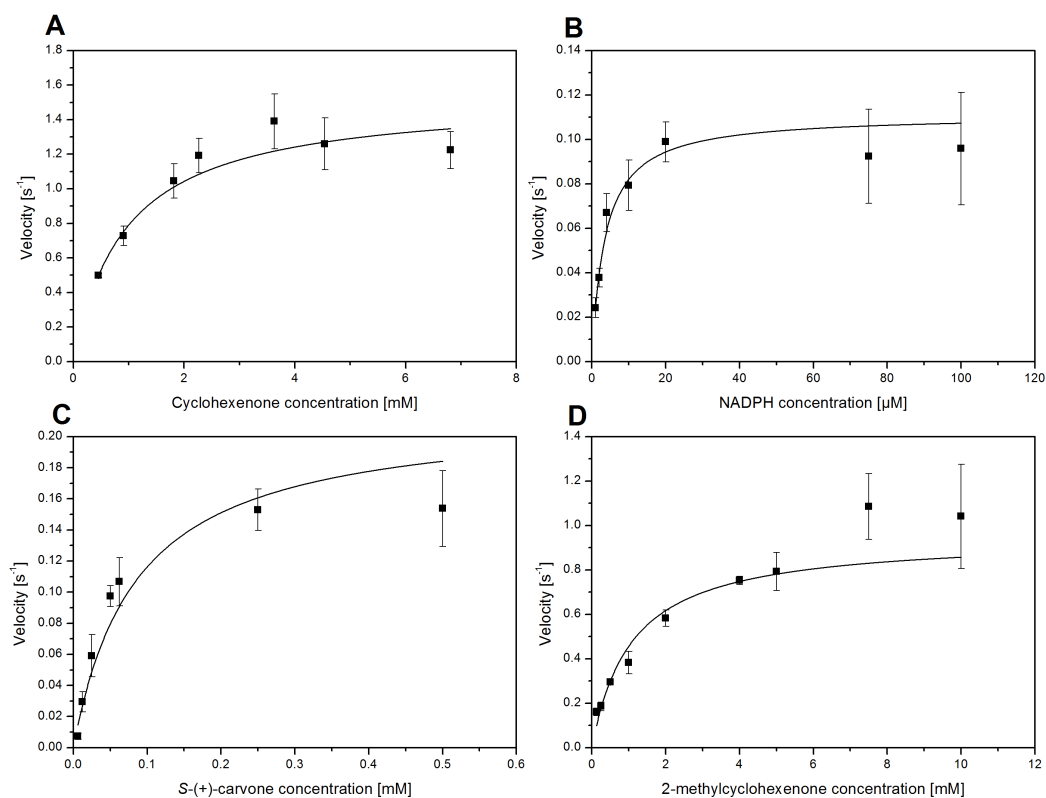


Figure 2.43:

Kinetic parameters of XenB.

A: **9b**; B: NADPH; C: **10b**; D: **11b**.

The data for the Michaelis-Menten plots were fitted with the ordinary Michaelis-Menten equation using instrumental weights with Origin Pro 2015. All kinetic data were measured in triplicates and are reported with mean \pm 1 SD.

Table 2.5: Michaelis-Menten parameters reactions with XenB.

Substrate	K_M [mM]	$k_{cat,app}$ [s ⁻¹]	$k_{cat} K_M^{-1}$ [mM ⁻¹ s ⁻¹]
6b	0.94 ± 0.08	1.53 ± 0.08	1.62 ± 0.22
7b	0.09 ± 0.03	0.22 ± 0.04	2.54 ± 1.30
8b	1.08 ± 0.14	0.95 ± 0.06	0.88 ± 0.17
NADPH	0.0036 ± 0.0005	Not applicable	

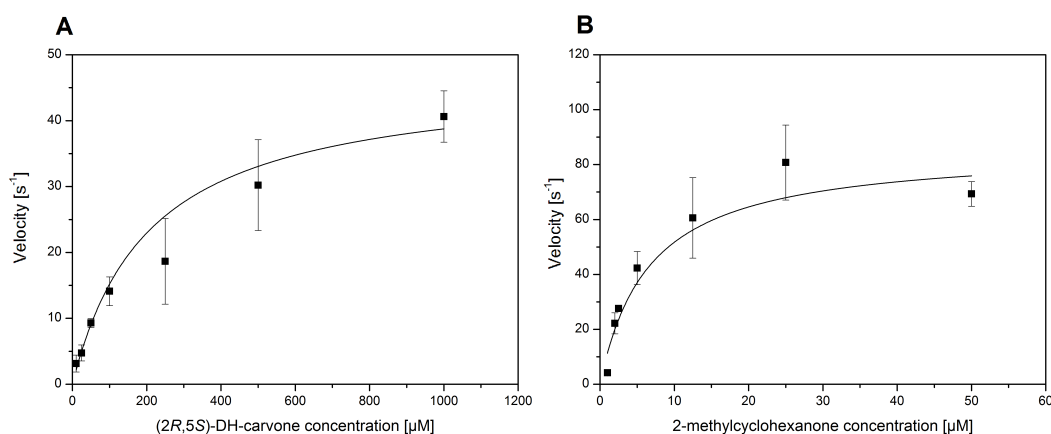


Figure 2.44: Kinetic parameters of CHMO.

A: 10b; B: 11b.

The data for the Michaelis-Menten plots were fitted with the ordinary Michaelis-Menten equation using instrumental weights with Origin Pro 2015. All kinetic data were measured in triplicates and are reported with mean \pm 1 SD.

Table 2.6: Michaelis-Menten parameters for reactions with CHMO.

Substrate	K_M [mM]	$k_{cat,app}$ [s ⁻¹]	$k_{cat} K_M^{-1}$ [mM ⁻¹ s ⁻¹]
6c	0.0069 ^[a]	22.6 ^[a]	3275.4 ^[a]
7c	0.21 \pm 0.03	46.82 \pm 3.94	225.0 \pm 51.0
8c	0.0066 \pm 0.0027	85.93 \pm 21.53	13019.7 \pm 8470.0
NADPH	0.018 ^[a]	Not applicable	
taken from ^[149]			

In the first cascade (**6a-e**), all ADH-promoted steps had similar rates and affinity parameters, with the exception of the unproductive reduction of **6c** to **6d**, which proceeded with approx. 100-fold higher catalytic efficiency (k_{cat}/K_M). The high affinity of ADH for **6c** created the possibility of a kinetic dead end, where material was diverted to **6d** quickly, and even at low concentration of **6c**. The side product **6d** would then accumulate because of its low affinity, before being re-oxidized at a slow rate. This unproductive substrate promiscuity could best be mitigated by an efficient final step, catalyzed by the BVMO, thus preventing

the build-up of **6c**. In the second cascade (**7a-e**), the ADH only converted the starting material, carveol **7a**, with no detectable activity for back or side reactions. The other two enzymes had a higher affinity for their respective substrates than the ADH (up to 104-fold). In the third cascade (**8a-e**), both oxidations were preferred due to higher catalytic efficiency. As already observed for the first cascade (**6a-e**), the third cascade (**8a-e**) showed the highest catalytic efficiency towards the intermediate **c**, which led to side product formation. The rates of the ERED-catalyzed reactions were the slowest of all steps, whereas the BVMO were the highest in the productive flux. In summary, the results from *in vitro* kinetics suggested that, at approx. equal concentration of all enzymes, bottlenecks would be caused by the promiscuous activity of the ADH, or by accumulation of intermediates **b** due to the inefficient Michael-addition (ERED).

2.2.6 Modeling of the cascade reactions

The experimental Michaelis-Menten values were inserted as constant parameters into equations 2.8-2.13, and non-linear fitting of this set of differential equations by iterative least-squares regression was performed, leaving the concentrations of enzymes as variable parameters to the fit. That implied the assumption that the biocatalysts would not degrade over the course of the reaction. Any terms for evaporation of the volatile compounds were omitted, since the cascade reactions were run in closed vessels^[55]. The headspace of the vial was 10×fold higher than the volume of the biotransformation to avoid oxygen limitation. The fitting algorithm estimated the following concentrations: $123 \pm 10 \mu\text{M}$ ADH, $51 \pm 5 \mu\text{M}$ ERED and approx. $0.03 \mu\text{M}$ BVMO (Figures 2.45,2.46 and 2.47).

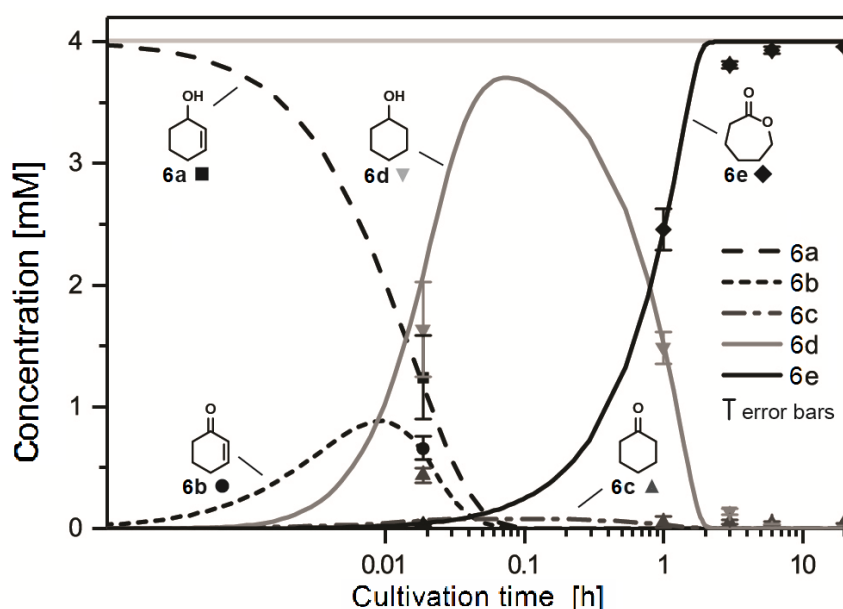


Figure 2.45: Comparison of experimental (data points) with the simulated (lines) concentrations for cascade **6a-e**. Experimental data were plotted as mean \pm 2 SD (Standard Deviation). Conditions for calculations: 4 mM **6a**, constant concentration of 0.10 mM NADP^+ and 0.12 mM NADPH , $[\text{ADH}] = 123 \mu\text{M}$, $[\text{ERED}] = 51 \mu\text{M}$, $[\text{BVMO}] = 0.033 \mu\text{M}$.

The model of cascade **6a-e** showed a qualitative representation of the *in vivo* biotransformation. The only intermediate, which was significantly different, was the intermediate **6c**.

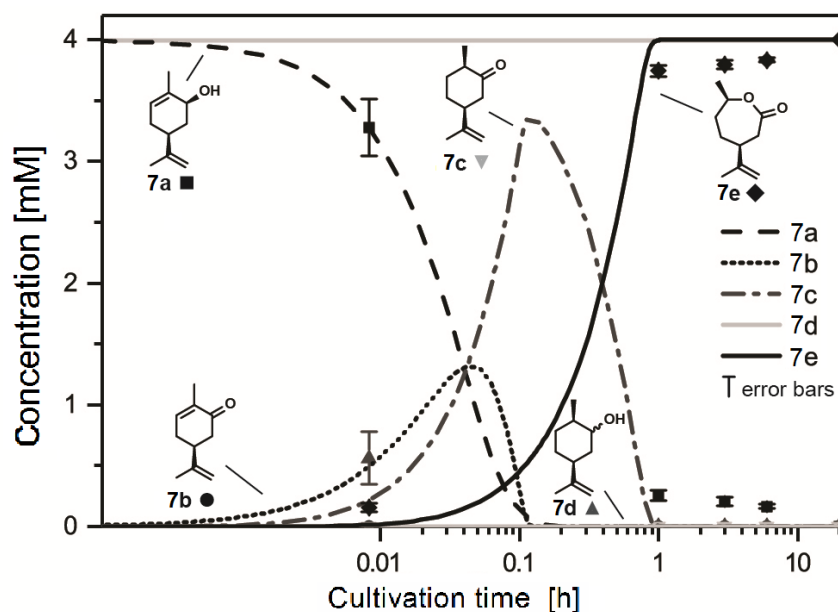


Figure 2.46: Comparison of experimental (data points) with the simulated (lines) concentrations for cascade **7a-e**. Experimental data were plotted as mean \pm 2 SD. Conditions for calculations: 4 mM **7a**, constant concentration of 0.10 mM NADP⁺ and 0.12 mM NADPH, [ADH] = 123 μ M, [ERED] = 51 μ M, [BVMO] = 0.033 μ M.

The model of cascade **7a-e** showed a qualitative representation of the *in vivo* biotransformation. As already observed with cascade **6a-e**, cascade **7a-e** showed a deviation of model vs. experimental data with the intermediate **7c**.

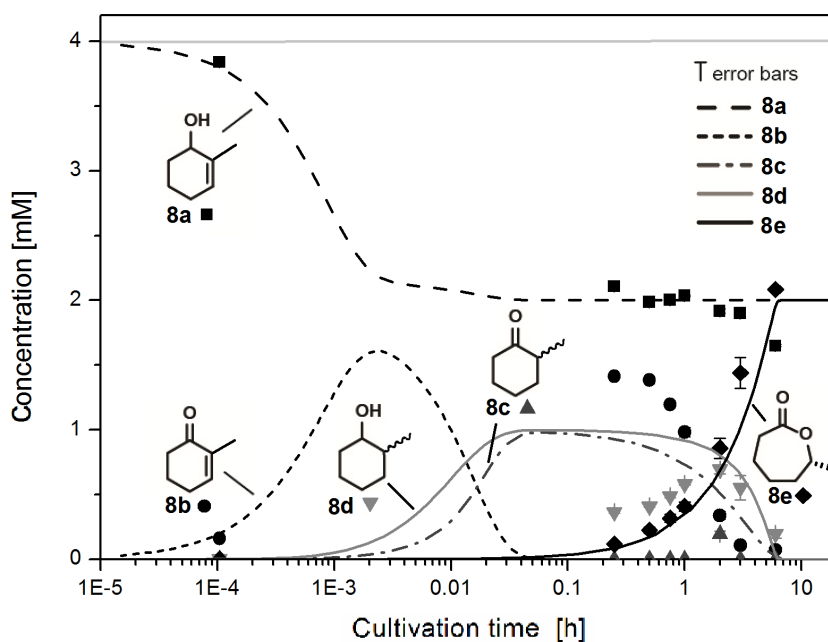


Figure 2.47: Comparison of experimental (data points) with the simulated (lines) concentrations for cascade 8a-e. Experimental data were plotted as mean \pm 2 SD. Conditions for calculations: 4 mM **8a**, constant concentration of 0.10 mM NADP⁺ and 0.12 mM NADPH, [ADH] = 123 μ M, [ERED] = 51 μ M, [BVMO] = 0.033 μ M.

In contrast to cascades **6a-e** and **7a-e**, cascade **8a-e** did not show a high correlation to the model. The main reason was that only 50 % of the substrate (one enantiomere of the racemic mixture) was consumed by the ADH in the model. However, in reality, the second enantiomere is as well accepted, but the conversion is slower than the one of the first enantiomere.

Using the enzymatic concentrations shown above, we obtained a highly accurate model for the first two cascades (quantified using adjusted R^2 (equation 2.16, Table 2.7), thus validating our mechanistic assumptions and the adapted Michaelis-Menten parameters, with some exceptions.

$$\overline{R^2} = 1 - (1 - R^2) \frac{n - 1}{n - p - 1} \quad (2.16)$$

With p = number of explanatory variables, n = sample size and R^2 as defined in equation

2.17.

$$R^2 = 1 - \frac{\sum_{i=1}^n (\hat{y}_i - \bar{y})}{\sum_{i=1}^n (y_i - \bar{y})} \quad (2.17)$$

With n = the sample size, \hat{y}_i = fitted values from the regression model for the specific i , \bar{y} = mean of the observed data, y_i = the observed data for the specific i .

Table 2.7: Adjusted coefficient of determination (R^2) values comparison of modeled vs experimental data.

Cascade	a	b	c	d	e
6	0.99	0.98	-5.00	0.60	0.98
7	0.91	n.a.	-1.23	n.a.	0.93
8	0.85	-5.75	-204.19	-6.26	0.86
n.a = not applicable: intermediates not detected					

Experimentally, the intermediates **6c** and **7c** only appeared at the first data point, and could not be modeled correctly (negative adj. R^2). Compound **6d** was determined less accurately by the model than the other components, and intermediate **7b** was not detected in the experiment, but was predicted by the model to be present for the first 6 minutes; these errors likely resulted from insufficient precision and sampling frequency in the experimental data. For cascade **8a-e**, only **8a** and **8e** showed a correlation between the experimentally determined and modeled data, which meant that some assumptions for this example were not correct. Although the misrepresentation of **6c** and **7c** in the cases of the first two cascades detracted only little from the overall accuracy of the model, it indicated that some of the assumptions in these cases were also not entirely correct.

Similarly, the model predicted cascades **6a-e** and **7a-e** to complete within 1-2 h, when only approx. 90 % conversion were reached in the experiments within that time; it took another 18 h to reach 100 %. The further assessment of the model was performed with cascade **6a-e**. The following hypotheses were established: (i) the equilibration of nicotinamides in *E. coli* was too slow to compensate for the artificial pathway ($d[NADP(H)]/dt \neq 0$), and (ii) the enzymes' specific activity decreased significantly over the course of the experiment. Whereas

the prior case would influence all steps, resulting in a complex effect, the latter scenario would become more apparent at longer reaction times and later in the cascade (by count of steps). The decelerating rate in the last reaction corroborated that the BVMO was decaying significantly.^[155]

Furthermore, it needed to be investigated, why the fitting algorithm had estimated the concentration of active BVMO at four to five orders of magnitude lower, than of the other two enzymes. Based on the semi-quantitative protein analysis *via* SDS-PAGE, the BVMO was estimated to be present at approx. 10 % of the ERED's mass concentration in the soluble protein fraction of the cell. (Figure 2.1.4 of Supplementary Information from^[55]). That result indicated that the average specific activity of the BVMO over the course of the reaction was much lower than that of the other enzymes, since the model estimated a ratio of approx. 10^4 vs. 10^1 from *in vivo* analysis. This observations led to the speculation, that most of the total amount of BVMO was inactive in the cell. Thus, the cascade was simulated with increasing titers of BVMO, up to the same order of magnitude as the other two enzymes ($\geq 5 \mu\text{M}$).

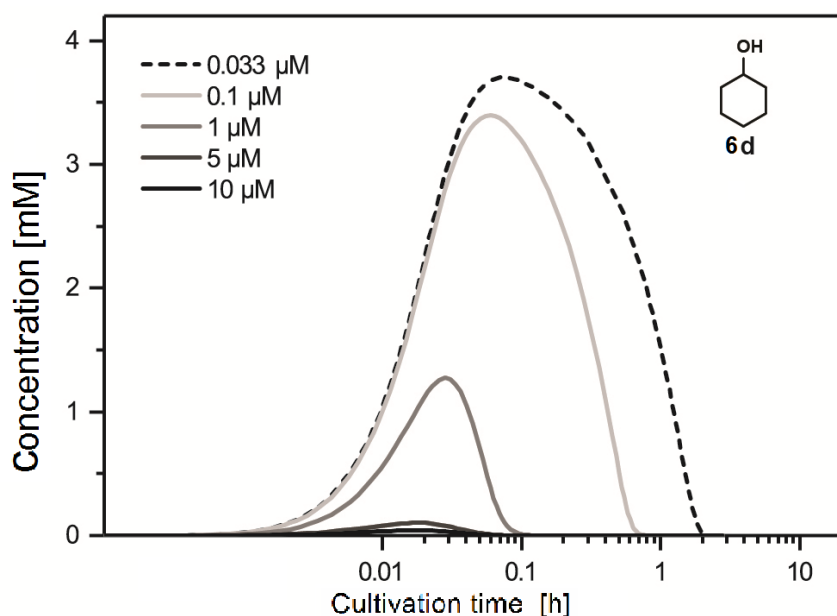


Figure 2.48: Simulated influence of the BVMO concentration on 6d formation.

4 mM **6a**, constant concentration of 0.10 mM NADP^+ and 0.12 mM NADPH ,
[ADH] = 123 μM , [ERED]= 51 μM , [BVMO] varied from 0.033-10 μM .

The model predicted a complete suppression of the accumulation of **6d** (Figure 2.48) and a

much shorter reaction time (0.1 h vs. 2.2 h; Figure 2.49), thereby supporting the hypothesis.

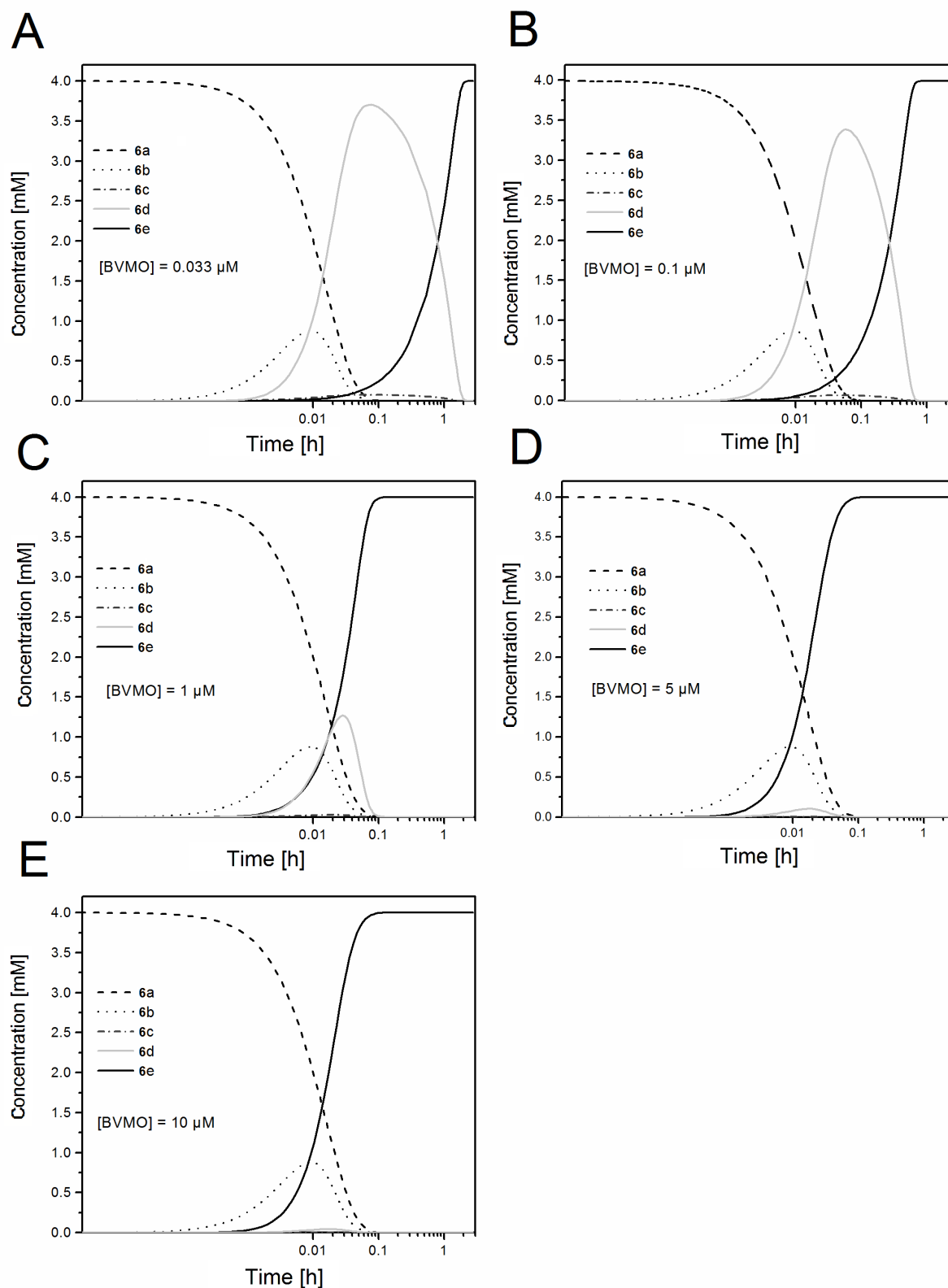


Figure 2.49: Simulated influence of the BVMO concentration on 6d formation.

4 mM **6a**, constant concentration of 0.10 mM NADP^+ and 0.12 mM NADPH , $[\text{ADH}] = 123 \mu\text{M}$, $[\text{ERED}] = 51 \mu\text{M}$, $[\text{BVMO}]$ varied from 0.033-10 μM A: 0.033 μM ; B: 0.1 μM ; C: 1 μM ; D: 5 μM ; E: 10 μM .

Next, possible reasons for the low specific activity of the BVMO were investigated. The previous hypothesis - that cofactors would not be recycled sufficiently fast - was amended with the assumption that FAD and its precursors would not be in adequate supply to maintain all BVMO in its active, FAD-bound form. To test this hypothesis, the effect of excess NADP⁺/NADPH and flavin nucleotides (FMN/FAD) on the performance of the cascade *in vitro* was investigated. Therefore, cell-free extracts of the cascade enzymes were obtained, simultaneously produced in the same host, and under the same conditions as for the *in vivo* biotransformations. Nicotinamide cofactors were added in stoichiometric excess to the substrates; flavins were added sub-stoichiometric to the ERED, but in excess to the BVMO. Two sets of experiments were performed, starting from **6a**: (i) with NADP⁺/NADPH only (Figure 2.50A), and (ii), with NADP⁺/NADPH and FMN/FAD (Figure 2.50B). The concentrations of the enzymes were at the same ratio as the estimates in the model (calculated: 1845 μ M ADH, 750 μ M ERED, 0.5 μ M BVMO). In both experiments, the substrate was added in acetonitrile instead of ethanol to exclude the effects of inhibition.

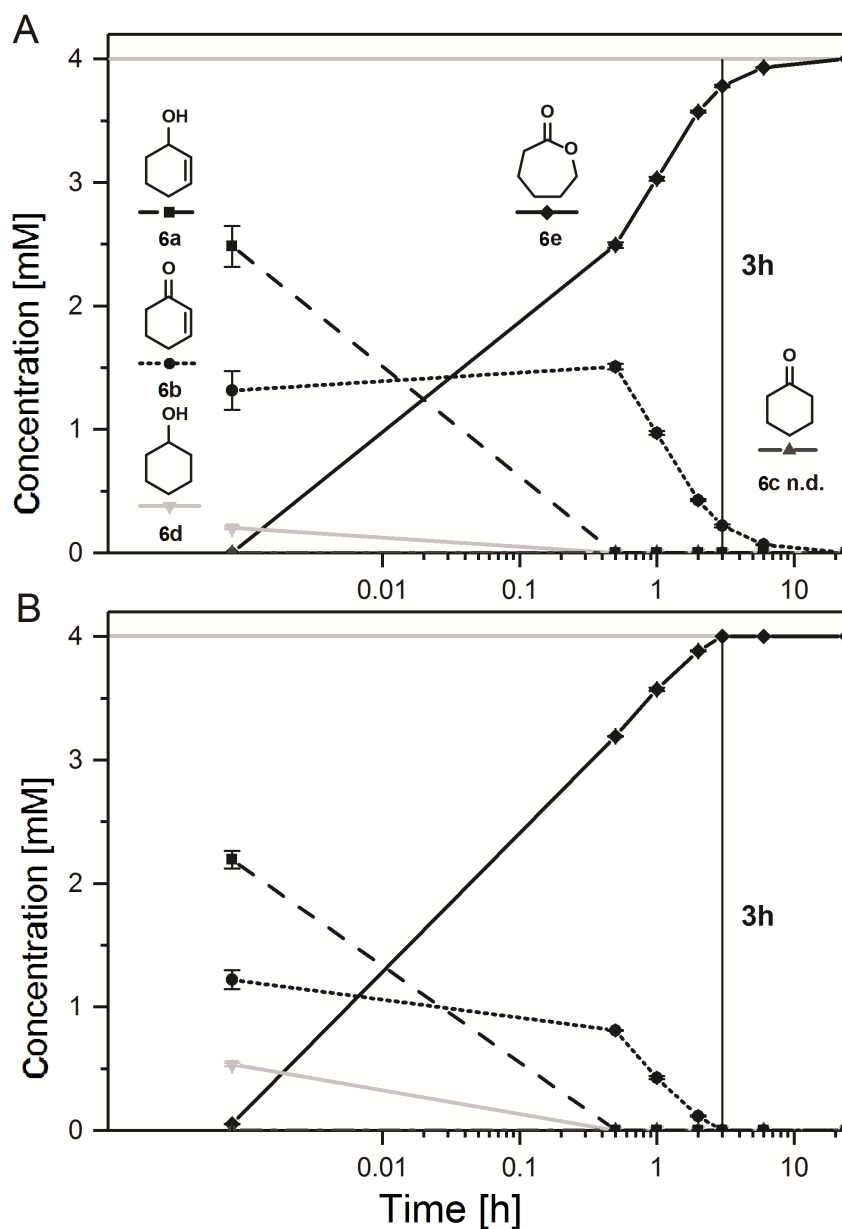


Figure 2.50: Influence of the cofactors on the *in vitro* cascade biotransformation.

A: Stoichiometric amounts of NADP⁺ and NADPH for the reaction (5 mM each), 4 mM **6a**; B: Stoichiometric amounts of NADP⁺ and NADPH for the reaction (5 mM each) and addition of FMN and FAD (0.1 mM each) to the cell free extracts, 4 mM **6a**; n.d. not determined. Results reported as mean \pm 1 SD.

In the first experiment (Figure 2.50A) the byproduct **6d** was detected at a lower concentration, and for a shorter period of time, than in the *in vivo* experiments. That strongly suggested that its accumulation was not only promoted by the suspected low BVMO concentration *in vivo*, but was also caused by an unfavorable balance of the nicotinamides. In the second experiment (Figure 2.50B), which included FMN/FAD, we additionally observed

a much shorter reaction time (3 h vs. 24 h *in vivo*); both flavin-dependent enzymes had a higher activity than *in vivo*, with a larger increase for the BVMO than for the ERED.

This led to the speculation that unequal improvement resulted from the sequence in the biosynthesis of flavin nucleotides: FAD is only produced *via* FMN as a direct precursor. Bound FMN (e.g. to the ERED) would not be available for further conjugation with adenine to form FAD^[156]. The amount of available FAD in the cell would thus be lowered by, and proportional to, the ERED, consequently reducing the specific activity of the BVMO. Hence, an excess of FAD should have a stronger influence on the activity of the last enzyme, as seen experimentally. Since our kinetic model did not account for inactive enzyme or stability, the initially fitted value did not reflect the estimated total concentration of BVMO, but only the active fraction.

An immediate solution for a flux improvement would be the addition of cofactors to the cellular system. This is not feasible due to the lack of their cell permeability. Another strategy would be the addition of cofactor precursors like riboflavin which are cell permeable. The group of Stewart^[129] investigated the influence of riboflavin addition to a whole-cell BVMO oxidation but no influence on the overall cascade flux was observed. Furthermore the introduction of a more stable BVMO, as recently discovered by Romero *et al.*^[157] would be beneficial for the overall flux through the cascade.

As a last step, the influence of ethanol on the modeled system was investigated, since the ADH was inhibited by ethanol (Figure 2.51).

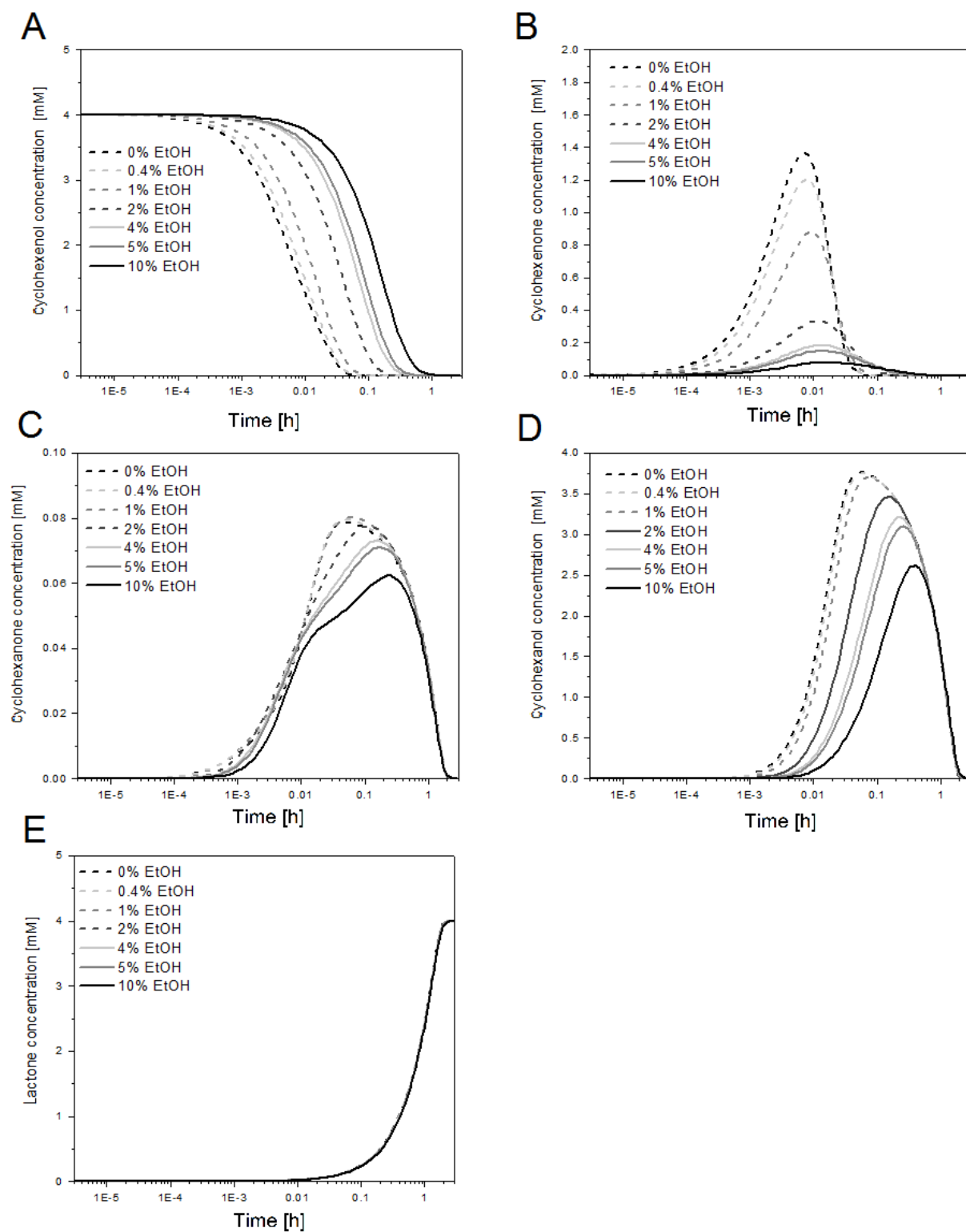


Figure 2.51: Simulation of the influence of ethanol on cascade performance.

A: **6a**; B: **6b**; C: **6c**; D: **6d**; E: **6e**. 4 mM **6a** at $t = 0$ h, constant concentration of 0.10 mM NADP^+ and 0.12 mM NADPH , $[\text{ADH}] = 123 \mu\text{M}$, $[\text{XenB}] = 51 \mu\text{M}$, $[\text{CHMO}] = 0.033 \mu\text{M}$.

Without ethanol, the ADH reaction would proceed the fastest. With rinsing ethanol concentrations, the ADH reaction would slow down, which would lead to lower concentrations of all intermediates, including the side product. Ethanol concentrations up to 10 % would not speed up product formation, since the BVMO is the rate determining step.

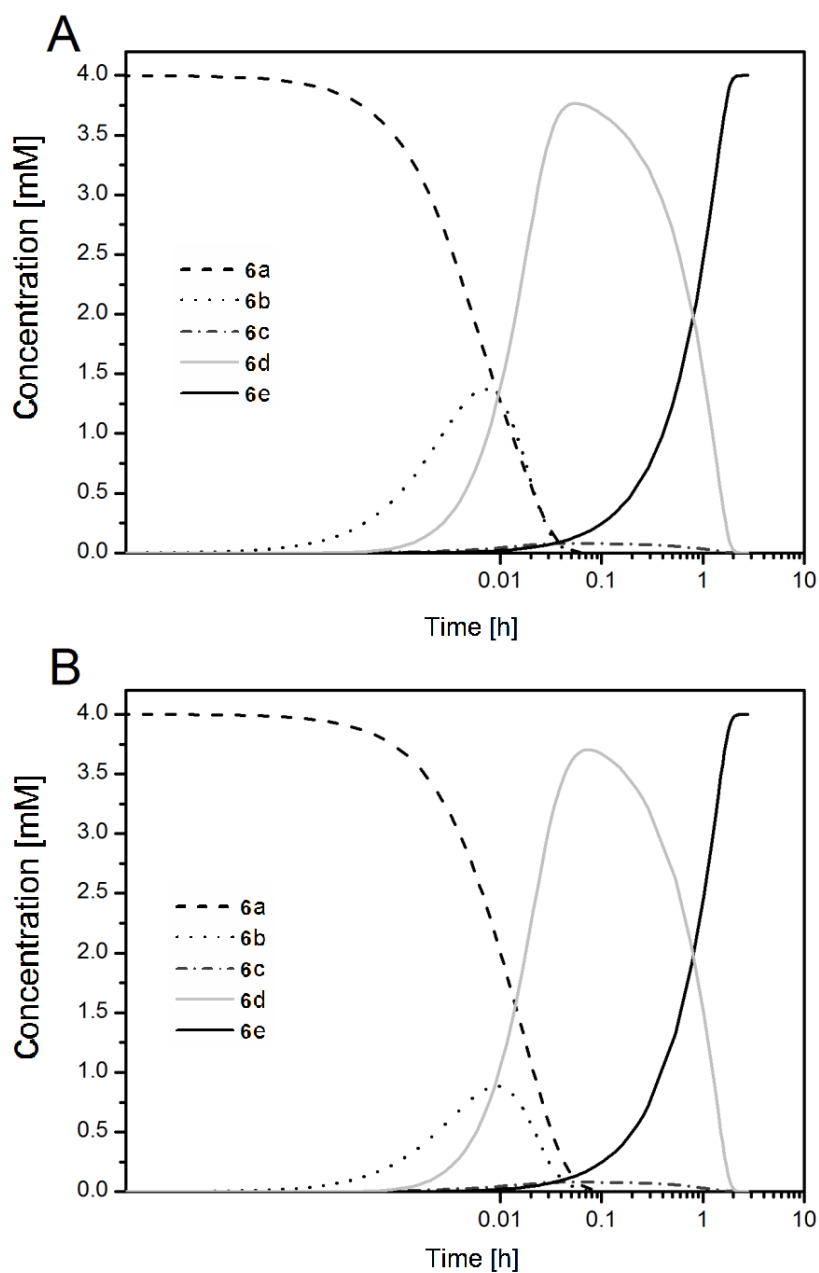


Figure 2.52: Simulation of time courses of the cascade starting from 6a.

A: without ethanol addition; B: with 0.4 % (v/v) ethanol. 4 mM **6a** at $t = 0$ h, constant concentration of 0.10 mM NADP^+ and 0.12 mM NADPH , $[\text{ADH}] = 123 \mu\text{M}$, $[\text{XenB}] = 51 \mu\text{M}$, $[\text{CHMO}] = 0.033 \mu\text{M}$.

In the used set up with 0.4 % ethanol ((Figure 2.52)), the simulation revealed that the influence of ethanol on the cascade performance even with regard to changes in the intermediate concentrations were rather low.

In summary, the assumption was that further flux improvements of our cascade can be achieved by changing the host organism, which provides increased cofactor availability (NADP⁺/NADPH and FMN/FAD) and applying a more stable CHMO enzyme. For the improvement of the biotransformation on the catalyst level, several strategies were proposed; however the low activity of CHMO *in vivo* needed to be further investigated.

2.2.7 Conclusion and outlook

An accurate kinetic model for an artificial *in vivo* redox cascade was successfully developed, using adapted Michaelis-Menten parameters from *in vitro* experiments. The concentrations of active enzyme *in vivo* were estimated by non-linear fitting of the rate laws to the experimental data. This way, the change in the formation of by-products, and the change in productivity upon varying the levels of the rate-determining catalyst (large influence), or of the co-solvent (no influence) could be simulated.

More importantly, the model identified a bottleneck resulting from an unexpectedly low specific activity of the last catalyst (BVMO), which was not evident from *in vitro* kinetics and SDS-PAGE analysis of *in vivo* protein titers. It became obvious, that the estimation of intracellular enzyme concentrations is an important parameter for the optimization of cascades. Furthermore, the assumption of stable and continuous supply of cofactors (FAD and NADPH) by *E. coli* was tested, suspecting that a lack thereof would have caused the low activity of the BVMO. An *in vitro* experiment with an excess of cofactors was compatible with this hypothesis, reducing the overall reaction time from 24 to 3 h. Additionally, the data suggest that the same effect of flavins which has been observed in this chapter on the BVMO, may also be true for the ERED, since addition of FMN led to a faster reaction. This hypothesis should be tested in the future.

In summary, the findings suggested that the optimization of cascades in a cellular environment should also strongly consider the availability of redox cofactors, their fluxes upon operation of the artificial pathway as well as the amount and stability of all enzymes involved. The identification of the limits of the whole-cell biocatalyst (catalyst level development) with means of kinetic modeling was successful; additionally optimization strategies were proposed. However, the next step was the identification of the reasons for the low CHMO activity *in vivo*.

2.3 Stability and activity of the prominent BVMO cyclohexanone monooxygenase CHMO_{*Acinetobacter*} *in vivo*

2.3.1 General aspects

Flavin-dependent monooxygenases (FMOs), and especially Baeyer-Villiger monooxygenases (BVMOs), are useful for synthetic purposes because of their promiscuous acceptance of substrates^{[158][1][159][160]}, and their mostly excellent stereoselectivity. Their dependence on oxygen as a terminal oxidant, and high activity at ambient temperature, can also offer technical advantages over their chemical counterparts.^[158] As the last chapter dealt with identifying bottlenecks of an enzymatic cascade on a catalyst level, in this chapter, the focus was set on the last step of this cascade, which was identified as the rate-determining step. The optimization on the catalyst level required a deeper investigation of the underlying reasons for the poor performance of CHMO *in vivo*.

E. coli is a widely applied host for heterologous production of BVMOs, and subsequently also a whole-cell biocatalyst.^{[161][138]} Among the benefits of *E. coli* as host organism are its ease of use (non-pathogenic, high growth rates^[162]) and well-characterized genetics (simple molecular cloning strategies and a variety of expression vectors^[163]). In the biocatalytic community it is generally assumed that the conditions required for the maintenance of the host's proteome, and its homeostasis, would also provide a stabilizing environment for the product of over-expression, and would recycle the required redox cofactors for the reaction. These assumptions, however, have not been tested for BVMOs. Recently, a prominent member of this class of enzymes, the cyclohexanone monooxygenase (CHMO) from *Acinetobacter* NCIB 9871^[149] was found to be highly unstable in a cell-free setting.^[155] Such instability is probably common to many BVMOs, with few exceptions (PAMO^[164] and TmCHMO^[157]). Despite the synthetic advantages of BVMOs, their poor operational stability complicates the applications on industrial scale for bulk chemicals^[165]. Only one industrial process using BVMOs has been described, catalyzing the final step in the synthesis of esomeprazole (the API in the proton-pump inhibitor Nexium) on a multi-ten gram scale by applying a heavily mutated CHMO variant (41 mutations).^[166]

Mostly, genetic engineering strategies have been used to enhance BVMO stability and activity *in vitro*. A promising strategy introduced stabilizing disulfide bonds, which lead to an

augmented thermodynamic stability by increasing the melting temperature of CHMO from *Acinetobacter* by 6 °C^[155], or 5 °C^[167]. Still, even the improved variants had a poor kinetic stability (e.g. 33% residual activity after 24 h). The wild-type enzyme had a half-life of less than two minutes.^[168]

A recent mechanistic study identified the following factors as influential in the deactivation of BVMOs *in vitro*: concentrations of i) the BVMO itself, ii) of the reduced cofactor NADPH, and, iii) of the coenzyme FAD.^[168] High intracellular concentrations of NADPH were previously reported to be beneficial for BVMO activity^[129], but the mechanistic link between activity and operational stability of the BVMOs had not been hypothesized clearly, nor established experimentally.

Similarly, the stability of BVMOs *in vivo* has not been investigated in a mechanistic study. Previous reports focused on the effects of substrate and product inhibition, oxygen limitation, temperature and pH on the operational stability of BVMOs in a whole-cell system.^{[161] [35] [135] [169]}

The approach questioned the assumption that *E. coli* provides a generically beneficial environment for CHMO. Thus, the crucial factors for CHMO's activity and stability, which had been identified in an earlier study *in vitro* (NADPH, FAD and protein concentration^[168]) were monitored in a whole-cell over-expression system. The activity and stability of the CHMO, and the overall performance of the cellular biocatalyst were analyzed by measurement of *E. coli* metabolomics, and the intracellular concentration of CHMO.

2.3.2 Development of hypothesis and their experimental validation

The study was based on the following hypotheses:

- A. CHMO, produced by over-expression, is stable *in vivo* over the duration of a preparative experiment.
- B. CHMO is produced by *E. coli* to a sufficient concentration to maintain high specific activity of the whole-cell catalyst.
- C. the cofactors FAD and NADP(H) are produced by *E. coli* to sufficiently high concentrations to efficiently maintain a high specific activity of the CHMO.
- D. *E. coli* is a suitable organism to act as an efficient whole-cell biocatalyst with FAD- and NADP(H)-dependent enzymes.

An experiment for the production of CHMO (pET22b_CHMO) under controlled conditions in a bioreactor (pH, temperature, oxygen saturation) was designed, the intracellular concentration of CHMO was measured, and the activity of CHMO to characterize the performance of the whole-cell biocatalyst was determined. Specifically, the concentrations of the cofactors FAD and NADPH, and their respective precursors (GXP, ATP), plus several indicative metabolites were determined: amino acids (building blocks for the synthesis of CHMO), and compounds of the central carbon metabolism and tricarboxylic acid cycle (TCA) to monitor the physiology of *E. coli*. The sampling pattern is depicted in Table 2.8.

Table 2.8: Experimental protocol of the CHMO fermentation

Time [h]	Event	OD sample [-]	Protein sample [$\mu\text{g mL}^{-1}_{\text{cultureOD1}}$]	Metabolomic sample	Activity sample
0.00	Inoculation				
0.02		0.11			
1.00		0.12			
2.00		0.13			
3.00		0.18			
4.00		0.27			
5.00		0.41			
6.00		0.65			
7.00	Cooling to 20 °C	1.05			
7.77		1.4	0.61	M1 (3x)	
8.12	Induction 0.1 mM IPTG				
9.17		1.8	0.54	M2 (2x)	
10.12		2.3	0.64	M3 (3x)	
11.08		2.5	0.82	M4 (1x)	A1
12.07		3.1		M5 (3x)	
13.08		3.9	2.39	M6 (1x)	
14.07		4.2	5.89	M7 (3x)	A2
15.00		5.0	5.89	M8 (1x)	
16.05		5.8	8.43	M9 (3x)	
17.05		6.8	7.46	M10 (1x)	A3
18.03		7.6	9.89	M11 (3x)	
19.03		8.0	9.96	M12 (1x)	
20.00		9.0	7.89	M13 (3x)	A4
21.03		8.9	8.46	M14 (1x)	
21.13	Glucose addition (20 mL 50%)				
22.02		8.9	10.83	M15 (3x)	
23.03		8.8	7.54	M16 (1x)	A5
24.02		8.7	7.57	M17 (3x)	
25.03		8.7	8.40	M18 (1x)	
26.03		8.6		M19 (3x)	A6
27.00		8.6	6.58		
27.12				M20 (1x)	
28.08		8.5		M21 (3x)	
29.05		8.2		M22 (1x)	A7
29.98		8.3		M23 (3x)	
31.05		8.6	6.68	M24 (1x)	
32.00		8.3	7.39	M25 (3x)	A8
33.00		8.2	7.39	M26 (1x)	
34.13		8.3	5.96	M27 (2x)	
35.08		8.4	7.14	M28 (1x)	A9

From the experiment in the bioreactor, the following analyses were conducted:

Samples of biomass were taken, the cells, were lysed and the soluble fraction of the total cellular protein was analyzed by SDS-PAGE, and the concentration of CHMO was quantified from the gel *via* densitometry, using pure CHMO as a calibration standard. During the nitrogen-limited phase of the cultivation, the CHMO was not synthesized anymore; its concentration should not change. A significant decrease of the concentration of soluble CHMO would disprove hypothesis A.

The activity of the cells was measured in a Baeyer-Villiger oxidation. The measurement was performed every three hours after induction of the protein production, by transferring a small sample from the bioreactor to a satellite culture; this culture was incubated at the same temperature and comparable aeration/mixing conditions as in the bioreactor^[170], then a model substrate rac-bicyclo[3.2.0]hept-2-en-6-one **9** (fast reaction) was added and the conversion process to the corresponding lactone was monitored by GC measurement of organic extracts. The specific activity of the CHMO was calculated by normalizing it to the dry cell weight and the protein concentration. A significant decrease in the specific activity, resulting from the decrease in CHMO concentration (see above), would disprove hypothesis B.

The intracellular concentration of NADPH and FAD were determined. The sampled biomass was harvested by fast filtration and spiked with fully ¹³C-labeled standards of FAD and NADPH for accurate quantification. The intracellular concentrations of FAD and NADPH were compared to that of intracellular soluble CHMO. These concentrations were estimated based on a published value of the cytosolic volume.^[171] Additionally, the biosynthetic precursors to FAD (AXP and GXP) were measured to identify any bottlenecks in the production of the cofactors. A concentration of NADPH or FAD insufficient to fully saturate the CHMO, or a significant decrease of the concentration of the metabolites, would disprove hypothesis C.

In addition to the above, the concentrations of other intracellular metabolites were determined to check the activity of the cells' central carbon metabolism (intermediates from glycolysis / tricarboxylic acid cycle), and to monitor possible bottlenecks in synthesis of proteins (canonical amino acids). A decrease in the concentration of central carbon metabolites, or amino acids, before the onset of the nitrogen limitation would reject hypothesis D.

2.3.3 Establishment of conditions for CHMO expression

As a first step it was important to identify the best expression conditions in terms of inducer (IPTG) concentration in M9 minimal medium, since our usual protocol has been established in complex medium (Figure 2.53).

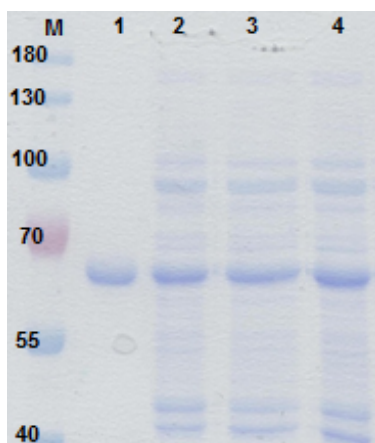


Figure 2.53: Optimization of CHMO Expression (pET22b_CHMO)

M: Marker, 1: pure CHMO, 2-4: soluble fraction of cultures grown in M9 medium with $0.8 \text{ g L}^{-1} (\text{NH}_4)_2\text{SO}_4 + 2:25 / 3:50 / 4:100 \text{ } \mu\text{M IPTG}$

Since the expression was slightly increased, if $100 \text{ } \mu\text{M IPTG}$ was applied, this concentration was chosen for all further experiments. However, all tested concentrations of inducer showed a good CHMO expression.

2.3.4 Preparation of ^{13}C internal standard for metabolomics

The ^{13}C internal standard was prepared by cultivating yeast, namely *Saccharomyces cerevisiae* (*S. cerevisiae*) FY4 on minimal medium with fully ^{13}C -labeled glucose (Figure 2.54). The strain produces ethanol as an overflow metabolite during the growth on glucose, which usually shows high concentrations of glycolytic compounds. Once glucose is fully consumed, the strain grows further on the produced ethanol, showing higher concentrations of glyconeogenic compounds. Therefore, the culture is usually spiked with glucose, to obtain a flux in both pathways and then subsequently harvested and extracted. The extracts contain all the required metabolites for LC-MS/MS measurements.

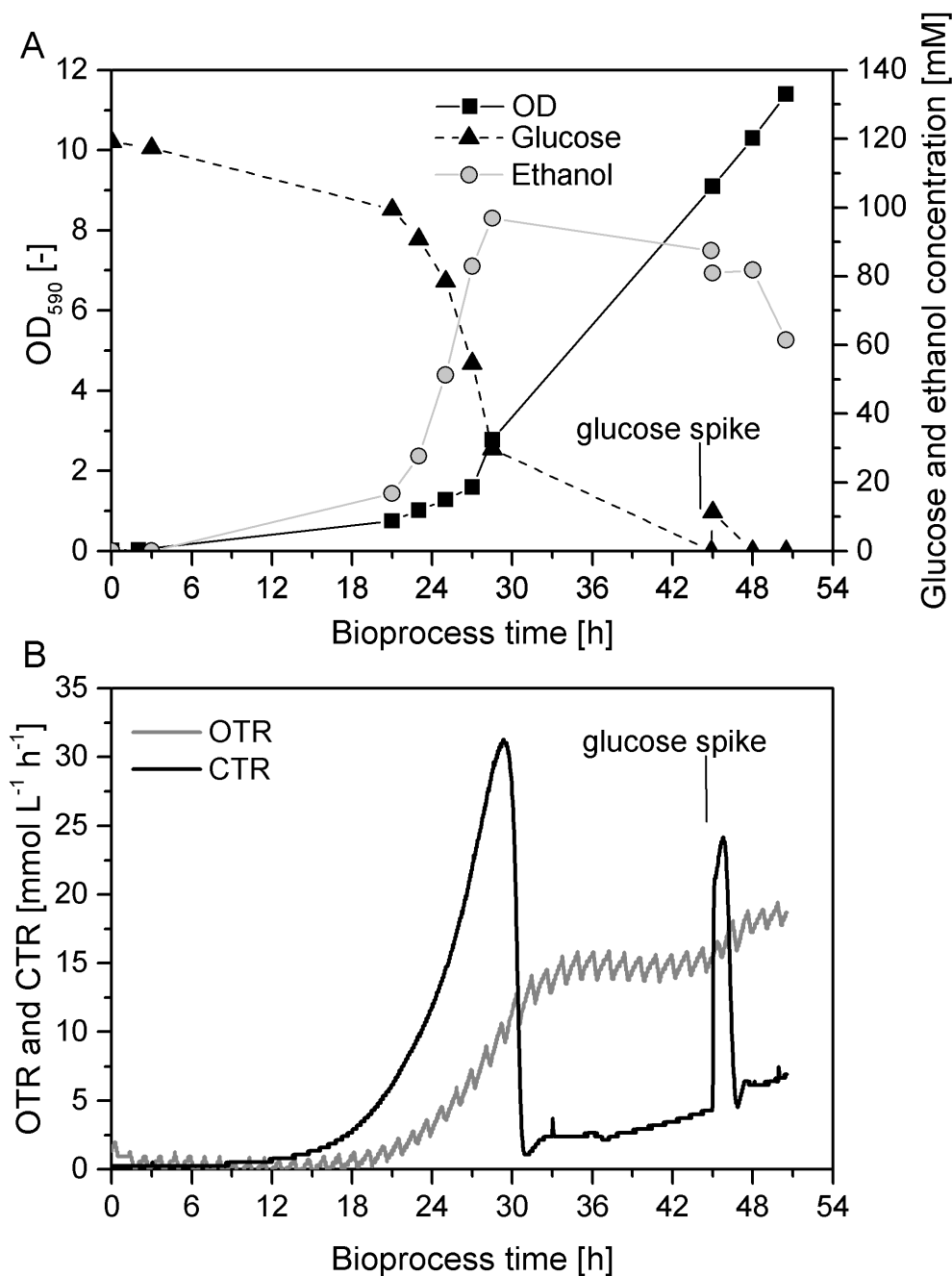


Figure 2.54: Verification of the yeast strain characteristics for preparation of ¹³C internal standard.

A: OD, concentrations of glucose and overflow metabolite ethanol; B: OTR and CTR of the cultivation

The strain was first characterized in terms of its physiology, to make sure, the ethanol production was taking place and that the off-gas signals corresponded with the measured glucose and ethanol concentrations. Indeed, the strain showed growth on glucose and ethanol (Figure 2.54A). After glucose depletion, the culture was spiked with glucose. The carbon

dioxide transfer rate showed an increase of up to $30 \text{ mmol L}^{-1} \text{ h}^{-1}$ after approx 32 h (Figure 2.54B), followed by a sudden decrease due to glucose depletion and the onsetting growth on ethanol. After approx. 46 h, glucose was added to the culture, resulting in a sudden increase of the CTR value. The harvest should then be performed after 30 minutes. The actual preparation of ^{13}C internal standard was performed with a different off-gas system (infrared sensors), which was not able to detect the labeled CO_2 , reducing the signal to 1/1000 of its strength (data not shown). However, it was still possible to recognize the different growth phases but the use of analyzers which rely on other properties than IR is highly important.

2.3.5 CHMO bioprocess in whole cells - elucidating stability, activity and metabolomics

The overexpression system was cultivated under controlled conditions in a bioreactor, using a defined medium. The production of CHMO was induced in the exponential phase with IPTG, and the culture was held in stationary phase for 15 h after reaching limitation by nitrogen with at all times minimum of 60 mM of glucose (Figure 2.55).

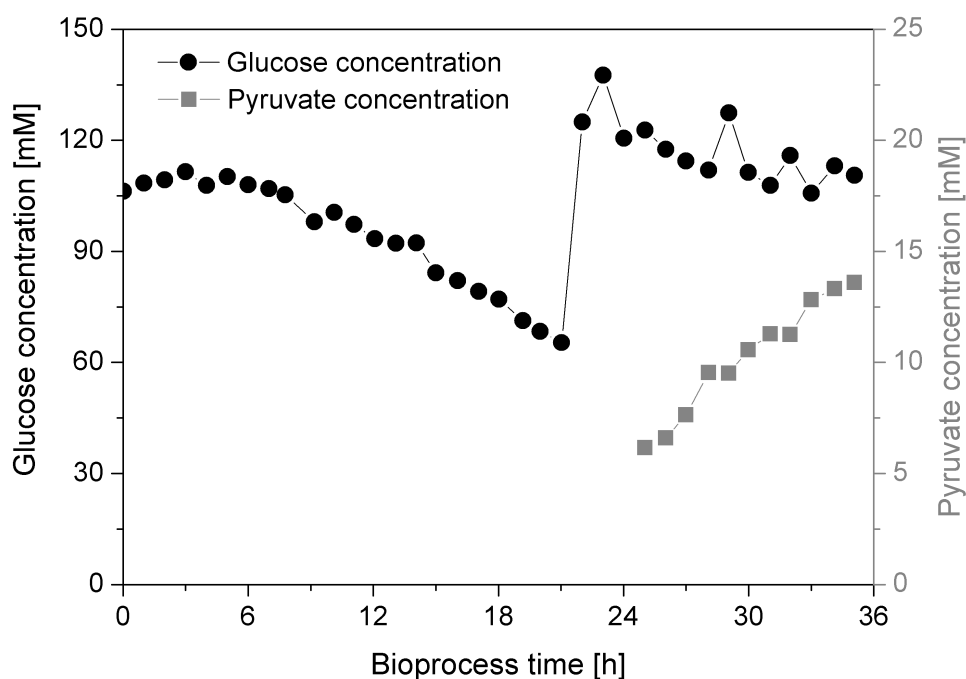


Figure 2.55: Supernatant analysis of CHMO fermentation.

Glucose and pyruvate concentration in the supernatant of the fermentation broth over fermentation time. After 20 hours, glucose was pulsed to the fermentation

The lag phase of the microorganism was observed during the first three hours of cultivation and documented in the growth curve (Figure 2.57), the constant glucose concentration (Figure 2.55) as well as in the off-gas analysis (Figure 2.56). In the growing phase of the culture, no overflow metabolite formation was observed. In the non-growing phase of the experiment a glucose pulse triggered pyruvate production (Figure 2.55). The temperature change as well as the incution with IPTG could also be observed in the OTR signal of the cultivation, since the respiratory activity immediately dropped as a response and recovered ≈ 30 minutes later. Overall, the supernatant analysis *via* HPLC as well as the off-gas analysis showed a

second substrate limitation if the culture, since glucose was in excess but did not enhance growth and oxygen consumption.

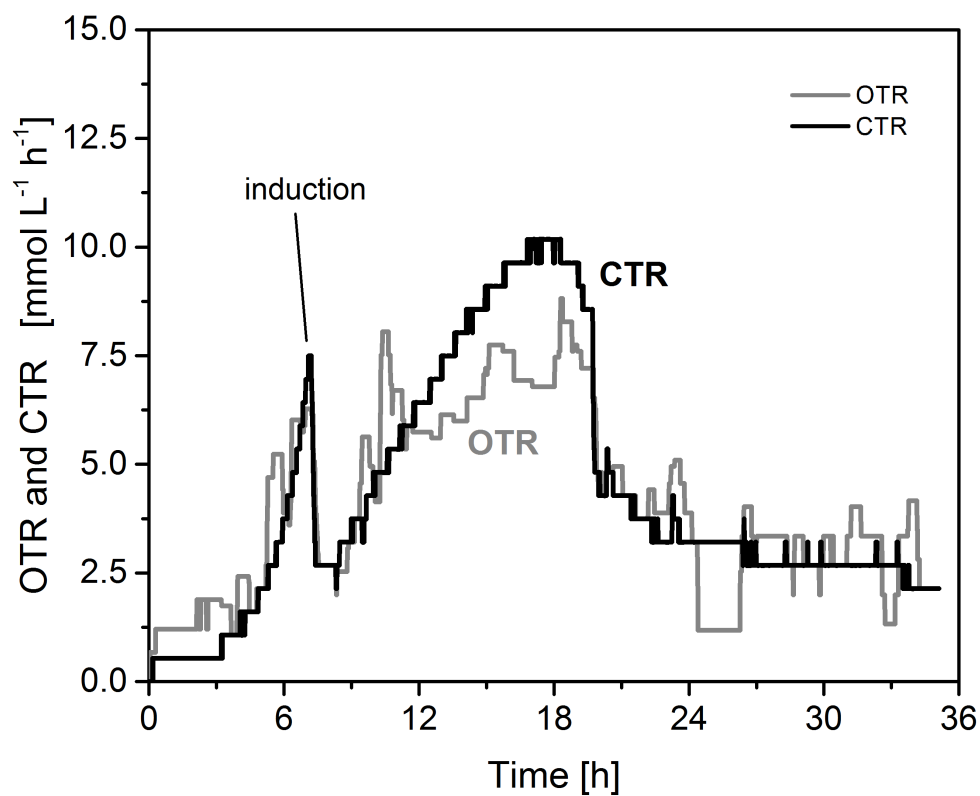


Figure 2.56: Off-gas analysis of CHMO fermentation.

(A) OTR, (B) CTR of the CHMO cultivation over time.

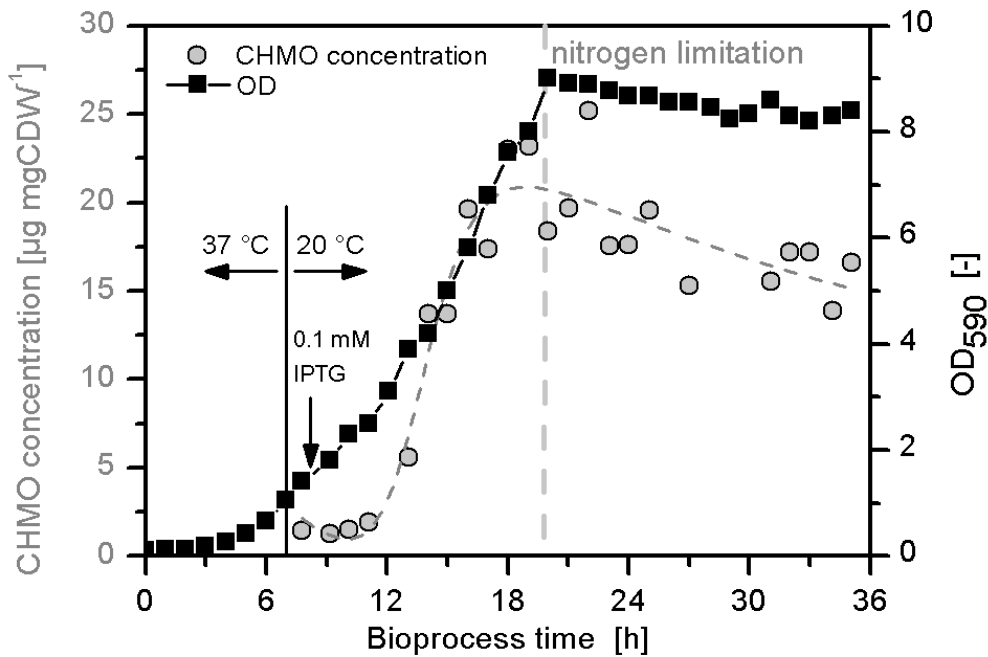


Figure 2.57: The concentration of soluble CHMO *in vivo* decreased during the nitrogen-limited stationary phase.

E. coli BL21(DE3) pET22b_CHMO was grown in minimal medium with sufficient aeration (Figure 2.56). The initial temperature of 37 °C (exponential growth, growth rate at 37 °C: 0.44 h^{-1}) was lowered to 20 °C after 8 h, shortly prior to induction with IPTG at a biomass concentration of $0.6 \text{ g dry cell weight per liter (gDCW L}^{-1}$; $\text{OD}_{590}=1.40$). The culture reached nitrogen limitation after 20 h (maximum biomass concentration: 3.87 gDCW L^{-1}). After that, the culture was maintained in the stationary phase for 15 h with a slight decrease of biomass to the final value of 3.61 gDCW L^{-1} . The concentration of CHMO was determined by SDS-PAGE (Figure 2.58).

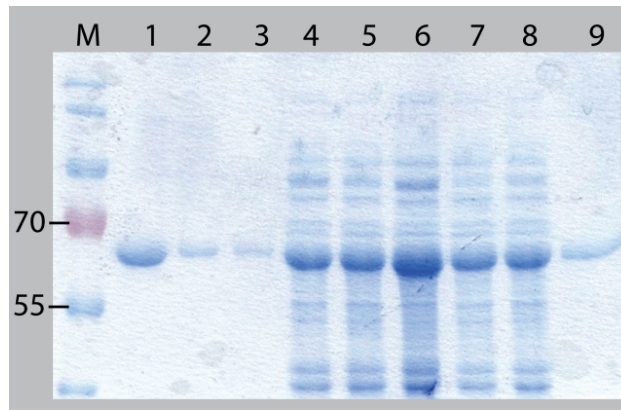


Figure 2.58: SDS-PAGE gel for quantification of soluble CHMO.

(M) marker: PageRuler Prestained Protein Ladder; (1) 2.5 μg purified CHMO; (2) 0.60 μg purified CHMO; (3) 0.40 μg purified CHMO; (4) - (8) exemplary culture samples; (9) 1.2 μg purified CHMO.

The maximum value of soluble CHMO was 20.9 $\mu\text{g mgDCW}$ after 19 h, and was empirically interpolated using a composite function (exponential growth-exponential decay) by non-linear fitting (OriginPro 2015, Equation 2.18).

$$y = A_2 + \frac{A_1 - A_2}{1 + \frac{x^p}{x_0}} + y_0 + A_3 \times e^{-xk} \quad (2.18)$$

with $A_1 = 5.30$, $A_2 = 6.60$, $A_3 = 13.98$, $p = 10.84$, $k = 0.04$ and $y_0 = 3.43$

The maximum value of 20.9 $\mu\text{g mgDCW}$ decreased towards the end of the experiment to 15.2 $\mu\text{g mgDCW}^{-1}$ (Figure 1) with a small exponential decay constant of approx. 0.04. A total loss of 27 % of the soluble CHMO was observed. This observation disproved hypothesis A.

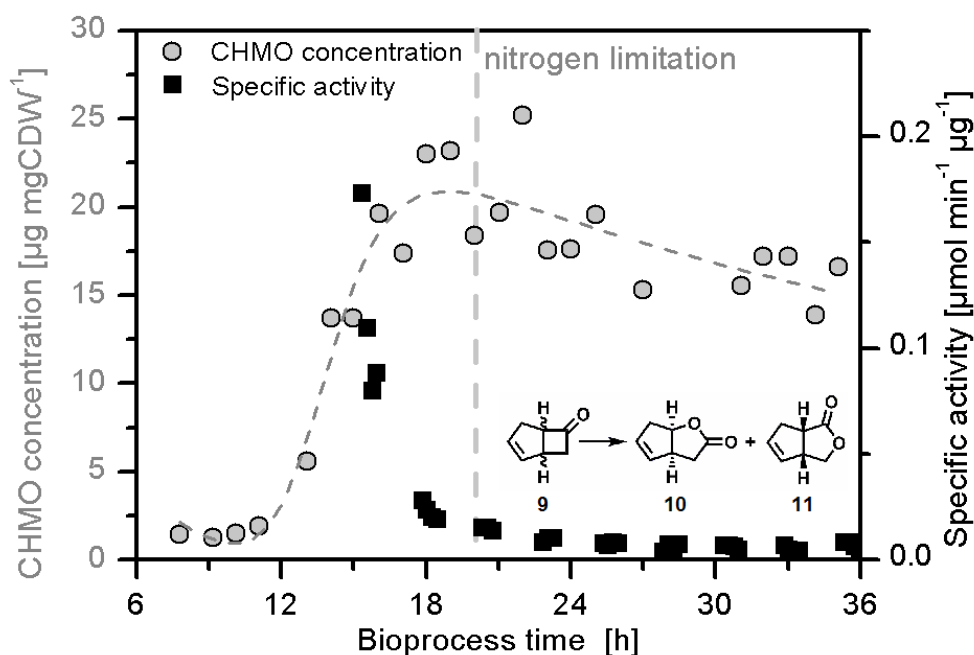


Figure 2.59: The specific activity of CHMO decayed rapidly to a basal level, based on the conversion of the commercially available 8 mM ketone 9 to lactones 10 and 11.

The obtained values for activity were normalized to the concentration of CHMO_{sol} determined by SDS-PAGE and fitted with equation 2.18.

A fast decrease in the specific activity with rising soluble CHMO concentrations was observed; the highest activity was observed at the first measurement. The specific activity dropped by approx. 90% within the first 5 h, and then remained constant for the next 21 h (Figure 2.59). The specific activity had an inverse relationship to the CHMO concentration. Theoretically, *E. coli* produced enough CHMO to reach high specific activity. This observation thus supported hypothesis B.

The changes of intracellular concentrations of the key metabolites FAD, NAD(P)H, guanosine and adenosine mono-, di- and triphosphate (GMP, GDP, GTP and AMP, ADP, ATP) were interpreted, to gain insights into potential bottlenecks in metabolic upkeep of active CHMO, specifically FAD, NADPH, or compounds that are required for the synthesis of FAD (Figure 2.60).

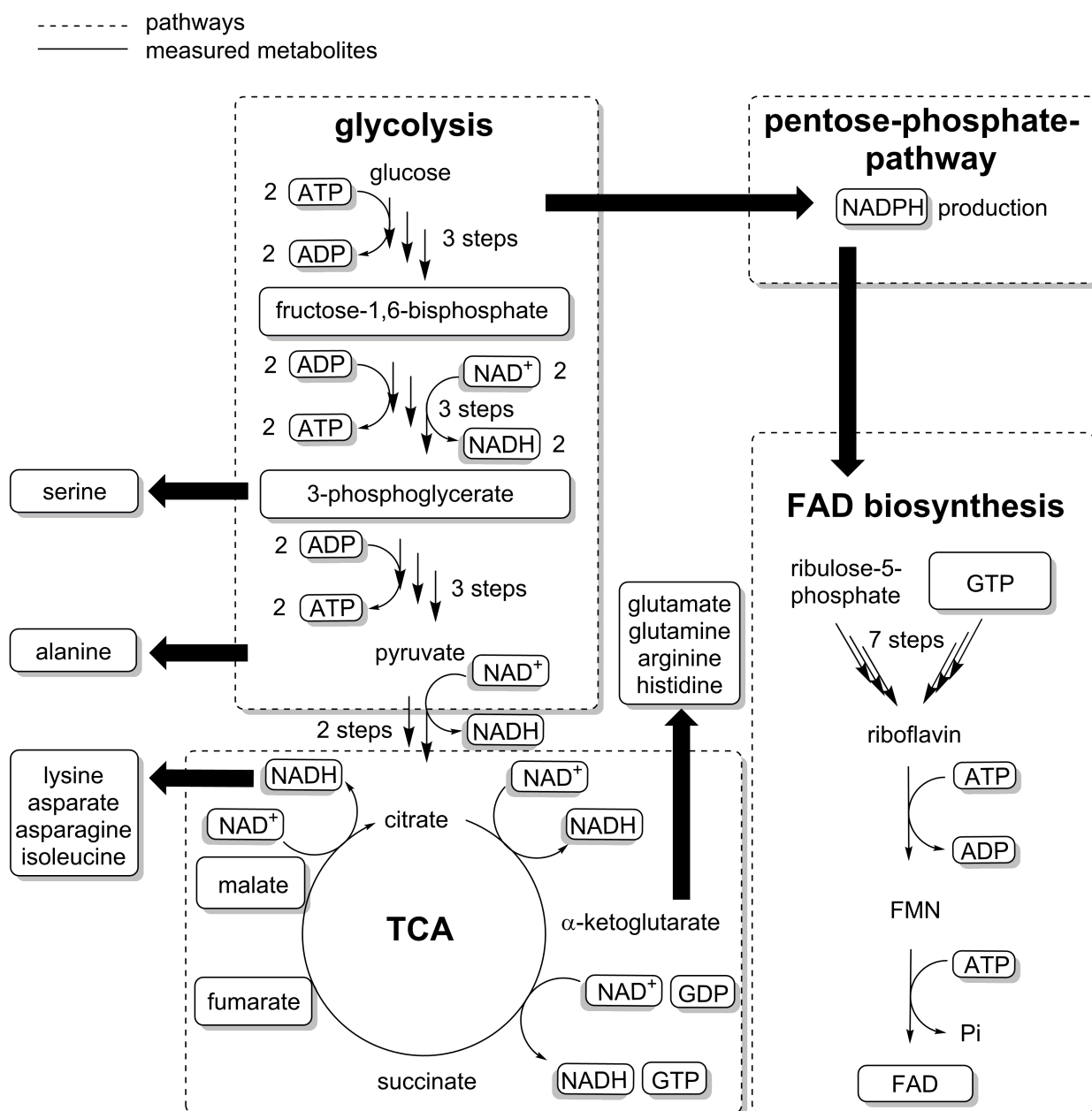


Figure 2.60: Overview over the metabolomics measurements.

Measured metabolites are shown in boxes.

The biosynthesis of FAD requires GTP, ATP and ribulose-5-phosphate. GTP and ribulose-5-phosphate are precursors for riboflavin, which after phosphorylation and reaction with ATP results at first in FMN (flavin mononucleotide) and then in FAD. Metabolites were extracted from *E. coli* samples and measured with LC-MS/MS. Not detectable metabolites were not measured due to either high insolubility in water or missing resolution of the method.

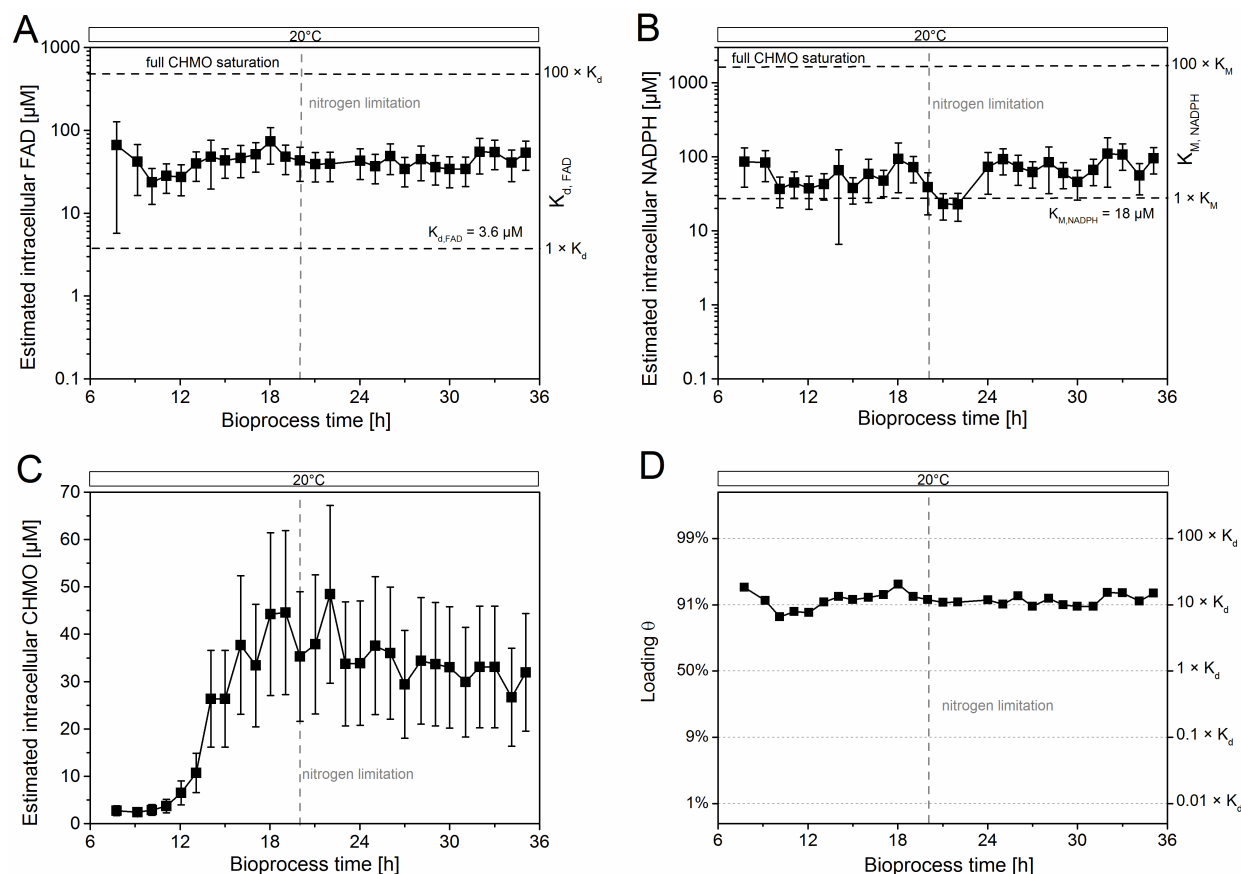


Figure 2.61: The intracellular concentrations of FAD and NADPH were insufficient to stabilize CHMO.

Estimated intracellular concentrations of (A) FAD (B) NADPH and (C) CHMO. (D) Hypothetical loading of CHMO of with intracellular FAD concentrations. We assumed an average intracellular volume of $3.6 \mu\text{L mL}^{-1}$ of cells per unit of OD of the culture.^[171] Data are reported as mean \pm propagated errors.

The estimated intracellular FAD and NADPH concentrations were stable over time (Figure 2.61 A, B). The estimated intracellular CHMO was stable under nitrogen limiting conditions within the margin of errors (Figure 2.61C) as well as the hypothetical loading of CHMO with FAD (Figure 2.61D). An average intracellular volume of $3.6 \mu\text{L mL}^{-1}$ of cells per unit of OD of the culture was assumed.^[171] The compounded errors were propagated from the uncertainty of the single components.

Stable intracellular concentrations of FAD ($40 \pm 16 \mu\text{M}$, Figure 2.61A) and NADPH ($63 \pm 29 \mu\text{M}$, Figure 2.61B) were observed after adaption to 20°C (increase in oxygen uptake, Figure 2.56). The same was true for the intracellular concentrations of CHMO with approx.

30 μM . Unfortunately, the propagated error from the estimated volume did not allow the identification of a significant trend (see Figure 2.61C) compared to the CHMO concentration normalized to the dry cell weight (Figure 2.57). The present high intracellular CHMO concentrations, however, were stabilizing for the enzyme to a certain extent, since the activity of CHMO remained constant for 15 h after the culture reached nitrogen limitation (Figure 2.59).

Since the cells were extracted vigorously in sampling procedure, the measurement could not differentiate between the free and bound form of FAD (or of any other metabolite that would form non-covalent complexes), preventing the exact calculation of equilibrium concentrations. That notwithstanding, and given the large uncertainty in the estimated values, the following, extremely simplifying assumptions to obtain at least one boundary condition were made: (i) the total concentration of FAD in the cell was equal to the concentration of unbound FAD, and (ii) CHMO was the only FAD-dependent enzyme in the cell. This way, a completely hypothetical, but optimum scenario was created for the population of the CHMO•FAD complex, calculated using a plain logistic function:

$$\frac{[CHMO \bullet FAD]}{[CHMO_{apo}]} = 1 - \frac{1}{1 + \frac{[FAD]}{K_d}} \quad (2.19)$$

with $[CHMO \bullet FAD]$ as the concentration of the loaded CHMO • FAD complex, $[CHMO_{apo}]$ as the concentration of the CHMO apoenzyme, K_d as the dissociation constant of FAD ($3.5 \pm 0.6 \mu\text{M}^{[168]}$), and $[FAD]$ as the total intracellular concentration of FAD. Even under these theoretical conditions, the intracellular concentration of FAD was only sufficient to load on average 90-95% of CHMO with the coenzyme, far from thermodynamic saturation ($\gg 99\%$ at $[FAD] > 100 \times K_d$; Figure 2.61D).

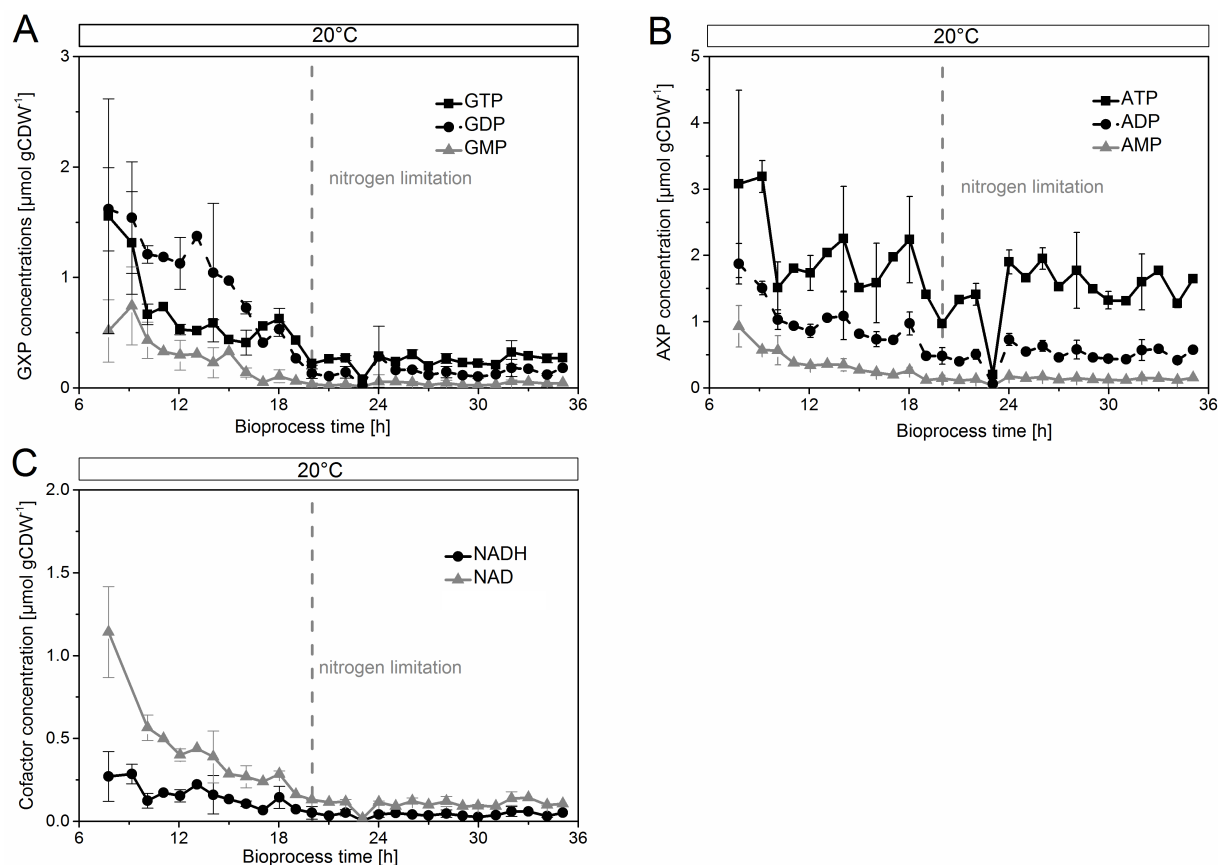


Figure 2.62: Concentrations of GXP (A), AXP (B) and redox cofactors NADH and NAD (C) decrease in the growing phase and are stable under nitrogen limited conditions.

The concentrations were normed by cell dry weight. Data is reported as mean \pm SD.

To determine if a shortage of the precursors of FAD influenced its availability to CHMO, the concentration of several precursors (Figure 2.60) was measured. GTP decreased already during the exponential growth phase of the cells (Figure 2.62A). After the culture had reached nitrogen-limited conditions, the concentration of the GXP pool was stable at approx. $0.3 \pm 0.01 \mu\text{mol gCDW}^{-1}$; these three compounds can be interconverted by the host metabolism. The concentration of ATP was stable over the entire observed period (approx. $2 \pm 0.2 \mu\text{mol gCDW}^{-1}$) (Figure 2.62B); the concentrations of AMP and ADP decreased until the onset of the nitrogen limitation, and were then stable. Neither an apparent, meaningful correlation between the concentrations of ATP and GTP with FAD, nor a bottleneck in their supply could be discerned. The lack in FAD was thus not directly, or not obviously, caused by a poor supply of its precursors.

The concentrations of NAD and NADPH were monitored (Figure 2.62C) to see if the trend of NAD/NADH concentration was similar to the NADPH concentrations, since the entities can be interconverted. In contrast to the decrease in NAD/NADH concentrations until the steady concentrations under nitrogen-limited conditions, the concentration of NADPH did not change much over time. The estimated intracellular concentration of NADPH was sufficiently high to largely saturate the enzyme ($73\% = 0.73 \times v_{\max}$, $K_{M,NADPH} = 18 \mu\text{M}$ ^[149]). Nevertheless, the concentration of NADPH was much lower than the level required for a strong stabilization, as earlier determined *in vitro*: there, a titer of $>1 \text{ mM}$ was found to have a surprisingly large, beneficial effect on the thermodynamic and kinetic stability of CHMO.^[168] The same was the case for the FAD concentrations. According to the calculations, FAD would largely saturate the CHMO, but still far from thermodynamic saturation ($\gg 99 \%$), as shown above. Given the large compounded uncertainty, and the extreme assumptions, the speculation was that most of CHMO was present in its apo form. The decay of specific activity to a residual non-zero value corroborated the insufficient loading, indicating a rising lack of FAD with rising CHMO concentrations in the cell. These results could not clearly disprove hypothesis C on the basis of FAD; still, our data clearly showed that the cells could not provide enough of the coenzyme to saturate most CHMO molecules.

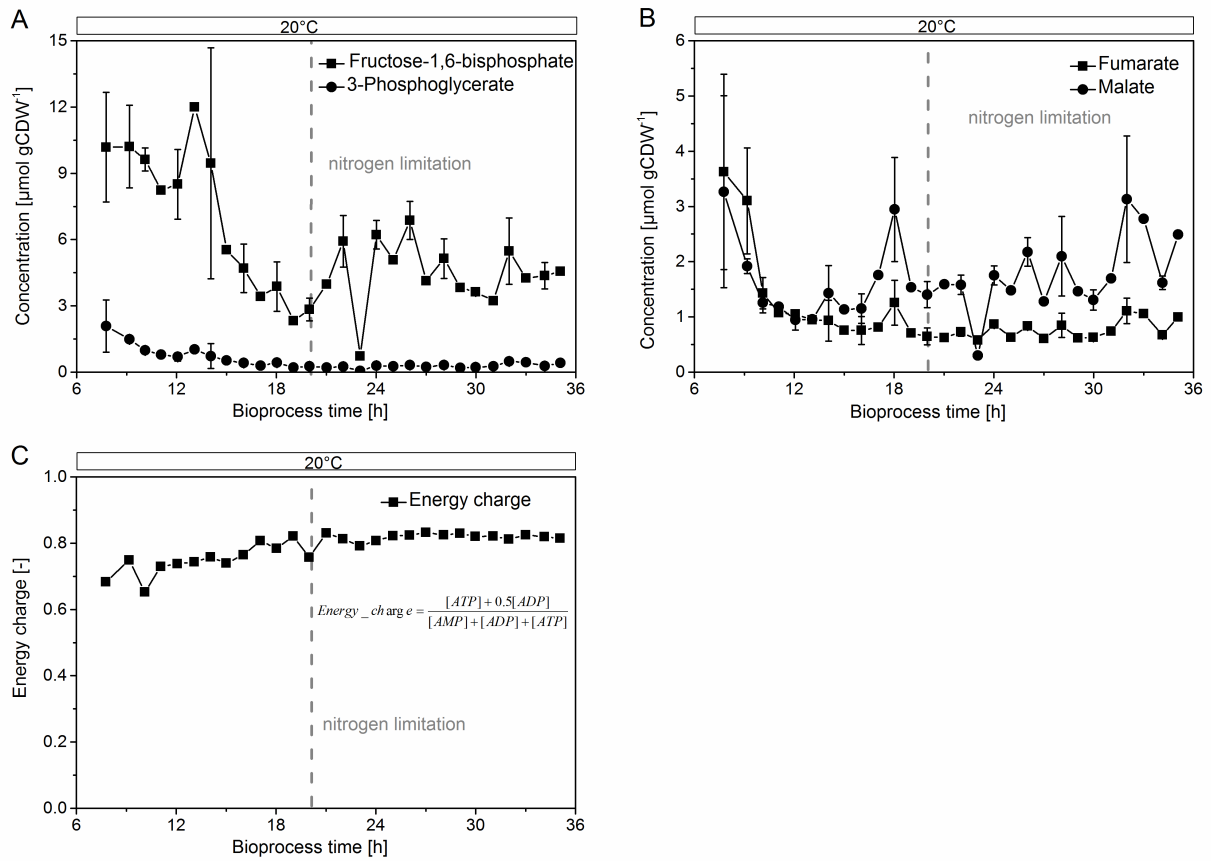


Figure 2.63: Glycolytic intermediates (A): fructose-1,6-bisphosphate, 3-phosphoglycerate; TCA intermediates (B): fumarate, malate and the energy charge calculated from ATP, ADP and AMP concentrations (C) were stable under nitrogen-limited conditions.

The concentrations were normed by cell dry weight. Data is reported as mean \pm SD.

The energy charge was calculated according to equation 2.23:

$$\text{Energy_charge} = \frac{[ATP] + 0.5 \times [ADP]}{[ATP] + [ADP] + [AMP]} \quad (2.20)$$

To test hypothesis D, the overall growth, physiological and biocatalytic performance of *E. coli* were measured, resulting in an overall decrease of the glycolytic intermediates fructose-1,6-bisphosphate and 3-phosphoglycerate (Figure 2.63A), and the TCA components fumarate and malate (Figure 2.63B), after the onset of the nitrogen limitation. All these metabolites remained constant within experimental error after physiological adaptation of the culture to 20 °C.

The heavy metabolic burden of heterologous overexpression became apparent in an unfavor-

able value for the adenylate energy charge (Figure 2.63C) of 0.65 at the beginning of protein overproduction. It later stabilized to 0.83 under nitrogen limitation. This value reflected a balanced pool of adenosine phosphates^[172], and cell viability until the end of the cultivation.

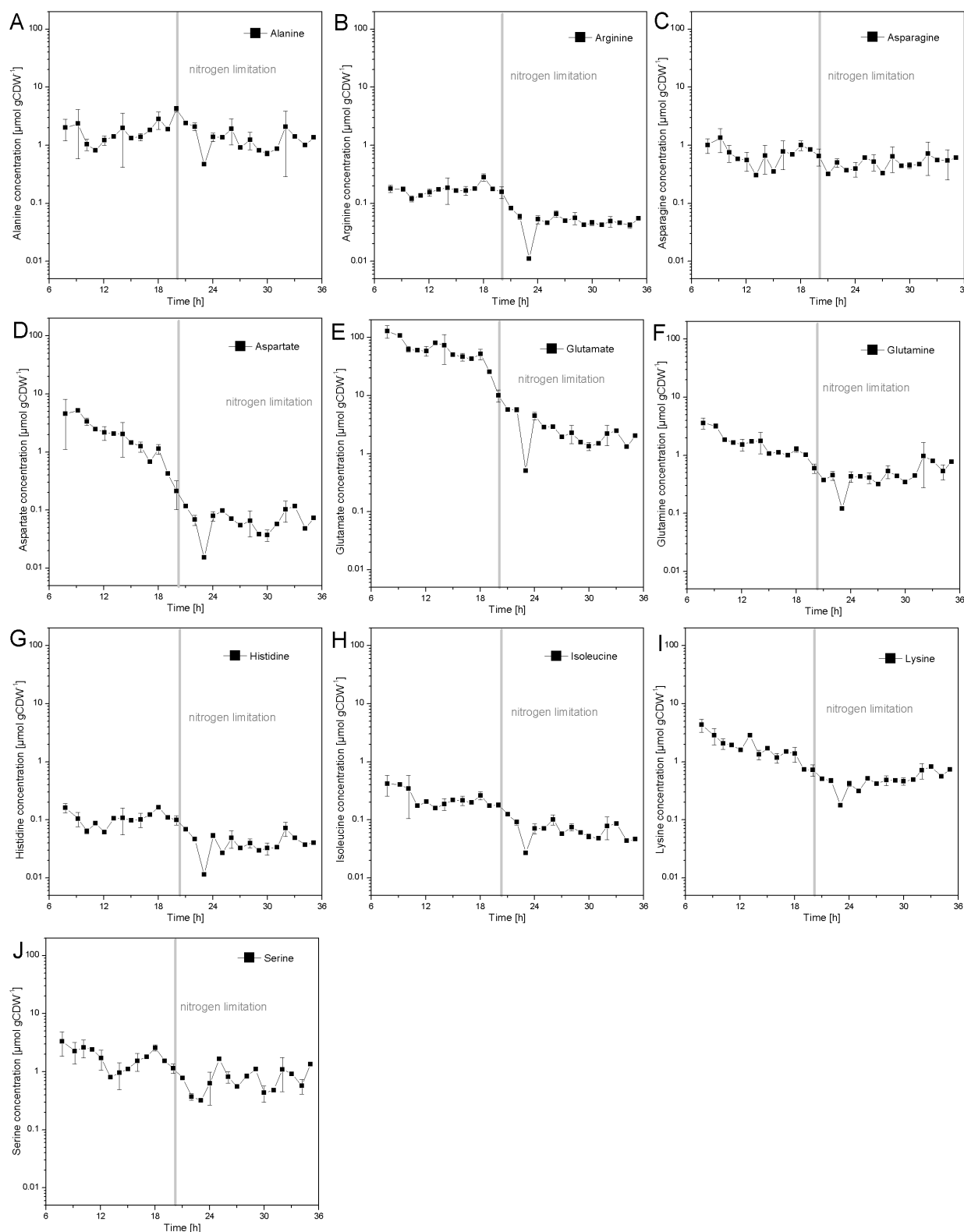


Figure 2.64: Intracellular concentration of several amino acids.

The concentration of the metabolites (A) alanine, (B) arginine, (C) asparagine, (D) aspartate, (E) glutamate, (F) glutamine, (G) histidine, (H) isoleucine, (I) lysine, (J) serine is normed by gram cell dry weight (gCDW) for each time point. Data is reported as mean \pm SD.

The protein production stopped when the culture reached the nitrogen limitation, which was reflected in the concentration curves of most amino acids. Specifically, the low concentrations of glutamine, glutamate and aspartate after the nitrogen limitation prevented the organism from further synthesizing CHMO (or other proteins, Figure 2.64, D-F). However, for most amino acids, a decline in concentration can be seen throughout the whole exponential phase (Figure 2.64, D-J), because it is the period, where protein production is at its peak.

In summary, the host organism *E. coli* was found capable of maintaining the NADPH requirements of CHMO, providing a stable environment with sufficiently high levels of precursors for the protein itself, as well as for cofactors. However, due to the low concentration of FAD, it failed to fully saturate CHMO in overexpression, and thus most likely other such biocatalysts with similar affinity to the coenzyme. Hence, hypothesis D was rejected.

The paradigm of placing a poorly stable biocatalyst into a living cell to provide for a stabilizing environment needed experimental support. As a consequence of the demanding requirements to stabilize CHMO (high concentrations of the enzyme itself, and its cofactors NADPH and FAD), *in vitro*^[168] and *in vivo* reaction modes were compared. This comparison provided substantial evidence that generic *in vivo* stabilization utterly failed with CHMO. Additionally, it is very likely that that this host organism would also fail with similar enzymes.

Under the applied controlled reaction conditions, the peak concentration of soluble CHMO decreased slightly, but without any meaningful correlation to the significant loss in activity (Figure 2.59). This finding was in contrast to a previous study, which identified the loss of CHMO itself as main reason for loss of activity.^[129] The supply of NADPH in this standard *E. coli* strain was found to be sufficient to saturate the enzyme to 73 % of its maximum efficiency, but it was still orders of magnitude below a stabilizing concentration (approx. 1 mM).

Similarly, the intracellular concentration of FAD was insufficient to completely saturate the enzyme. To explain the specific activity drop in the growing phase, the hypothesis was that the processes of deactivation and synthesis of the target enzyme were competing. With ceasing synthesis in the final phase of the experiment, a constant residual activity

of CHMO was observed, likely resulting from a small fraction of FAD-loaded CHMO. The aim was to identify the lack of FAD in the *E. coli* cell. The biosynthetic pathway for FAD was followed, starting from GTP and ribulose-5-phosphate, an intermediate of the pentose phosphate pathway (PPP)^[156] (Figure 2.60). Nitrogen limitation caused a decrease in PPP metabolites^[173], and thus interfered with the supply of building blocks for FAD. Even under the extreme assumption that CHMO was the only FAD-dependent enzyme in *E. coli*, the host failed. Moreover, the genome of *E. coli* encodes for approx. 80 flavin-dependent enzymes.^[174] They presumably all are essential for growth, or homeostasis, to unknown relative proportions, and are thus constantly competing for the pool of available, free FAD. Given the low stability of the CHMO • FAD complex, even an FAD-overproducing organism might not provide sufficient amounts for complete functional stabilization.

For the improvement of biostranformation process on the catalyst level, in this case, several changes need to be performed: (i) a change of the host organism to a FAD overproducing strain; (ii) further metabolic engineering of the strain to boost FAD production, and (iii) an FAD dependent enzyme with a higher affinity to FAD or even a covalent linkage.

2.3.6 Conclusion and outlook

Overall, by rejecting two indicative hypotheses (A and D) and strongly supporting a third (C), these results clearly demonstrated that the investigated organism *E. coli* BL21 (DE3) is incapable of efficiently maintaining the activity of CHMO, an important FMO, under commonly used conditions for over-expression. Overall, its performance as a stabilizing host would only be sufficient for NADPH-dependent enzymes, but not if they also rely on FAD with similar affinity. Analysis of the central carbon metabolism and the biosynthetic pathway indicated that this was a deep-rooted and widely distributed problem. Other well-explored species for heterologous expression, but with reportedly better flavin production (e.g. *Pichia pastoris*, *Bacillus subtilis*, *Candida famata*)^[156] might thus offer a more suitable artificial habitat for CHMO.

In this chapter, the identification of limitations on the biocatalyst stage was successful and optimization strategies were proposed. In the next chapter, with stoichiometric modeling, a different approach for development and optimization of a biotransformation on a biocatalyst and cultivation level is applied.

2.4 Characterization and stoichiometric modeling of a system connected to the central carbon metabolism of *E. coli* for boosting DHAP - dependent aldolase activity *in vivo*

2.4.1 General aspects

The optimization of a linear cascade in a whole-cell environment, as proposed in the second chapter, can be indentified with kinetic models. When it comes to more complicated systems, e.g. cascades that are coupled to the central carbon metabolism *via* an aldol reaction, the optimization of the biotransformation is more complicated, since more variables are unknown. In the following chapter, the optimization strategies on the catalyst level as well as on the process level were identified by means of stoichiometric modeling and metabolomics.

Carbohydrates and their derivatives are play an important role in many cellular processes (e.g. cell signalling, cellular recognition, inflammation etc.)^{[175][176][177]} These various functions in natural systems promoted the development of synthetic strategies for these carbohydrates derivatives.^[178] The majority of synthetic strategies for carbohydrate synthesis were derived from modifications of chiral compounds and therefore required many protection and deprotection steps.^[179] Asymmetric aldol reactions are a versatile alternative for synthesis of polyhydroxylated compounds by introduction of chiral hydroxyl groups through the formation *via* carbonylation of small molecules.^{[180][181][182][183]} Enzymes can be also applied for the formation carbonylation, either as aldolases or transketolases.^[184] Aldolases catalyse the stereoselective addition of a donor molecule (carbon nucleophile) to an acceptor carbon electrophile (e.g. aldehyde). In contrast to chemical aldol reactions, biological aldol reactions are mostly limited in terms of substrate acceptance of the particular enzyme, especially of the ketone donor. The enzymes have to be engineered in order to accept a variety of different donor ketones.^[185] Subsequently, native aldolases are very specific for their donor molecule and usually form up to two chiral centres with defined stereochemistry in one reaction step. Aldolases are divided by their reaction mechanisms into type I and II aldolases (Figure 2.65).

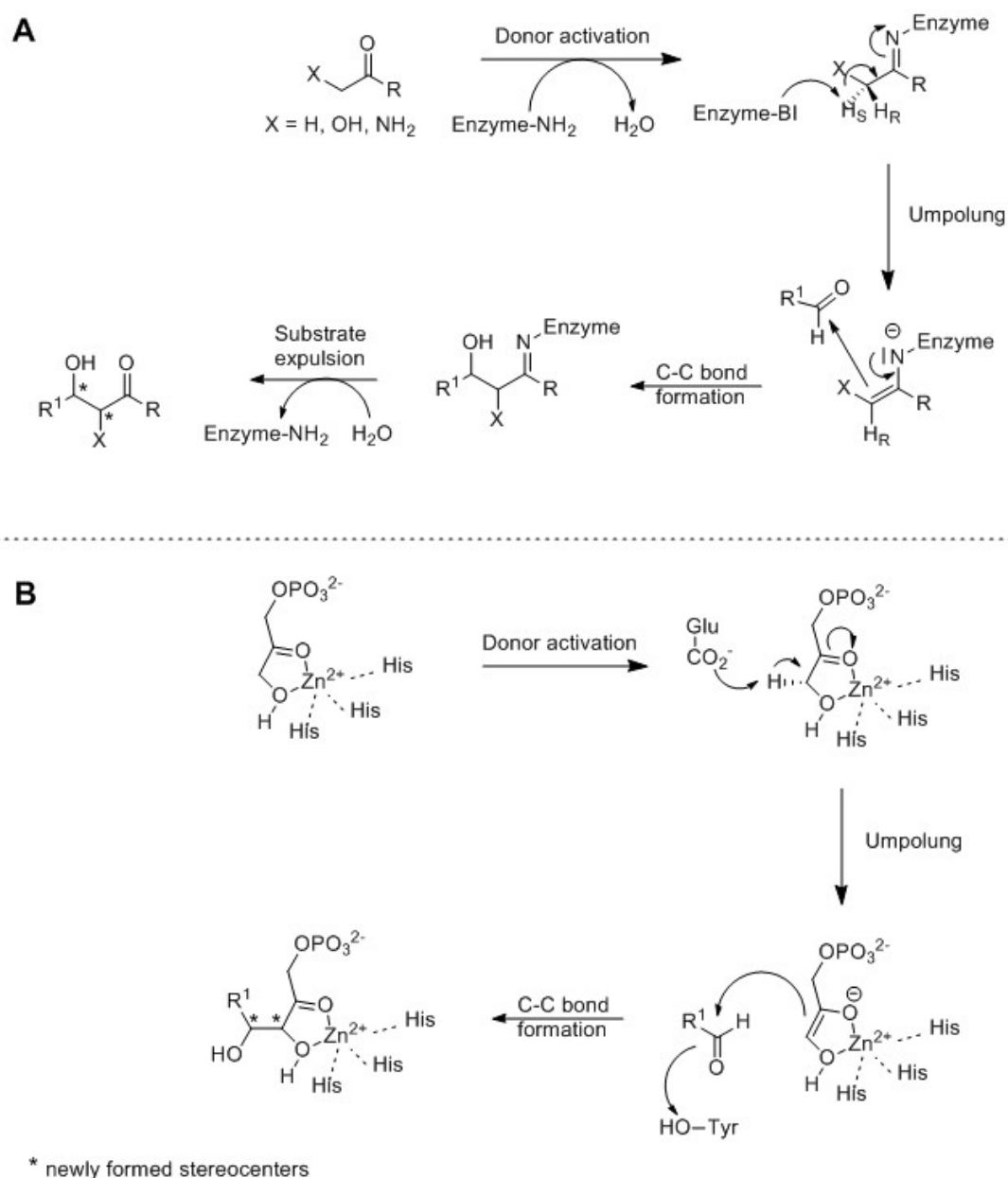


Figure 2.65: Mechanism of Type I and II aldolases.

A: type I aldolases; B: type II aldolases. Adapted from^[7].

Type I aldolases form a protonated Schiff base intermediate, which undergoes a tautomerization to form an enamine species. This species performs a nucleophilic attack on the carbonyl group of the aldehyde acceptor forming two new chiral centers. In the last step, the Schiff base is hydrolyzed, the diol is liberated and the enzyme is regenerated. Type II aldolases polarize the carbonyl group with a divalent cation such as Zn^{2+} , coordinated by three nitrogen groups of the histidine residues of the active site. This facilitates proton abstraction from the donor, resulting in an enolate, which performs a nucleophilic attack

onto the aldehyde acceptor.

In the cascade, discussed in this chapter, the donor molecule is dihydroxyacetone phosphate (DHAP) as we are dealing with DHAP-dependent aldolases. In one recent example, a DHAP-dependent cascade for production of polyhydroxylated compounds with an aldolase and a phosphatase was established *in vivo*.^[186] Despite their gram-scale synthesis, the yields were 50 % or less for all tested intracellular conditions. One reason for the low yields is the possible side reactions the aldehyde acceptor can undergo in a whole-cell system (e.g. reduction to the alcohol), since aldehydes are toxic for living cells and several detoxification pathways exist. To circumvent effect of toxicity and side product formation, one strategy is to generate the aldehyde *in-situ* from the corresponding, non-toxic alcohol.

A second reason for the low yields may be the low intracellular DHAP concentrations. In order to facilitate aldol reaction itself *in vivo*, it is favorable to operate at DHAP concentrations which are above the aldolase K_M value for DHAP. If the concentration of DHAP is below the K_M value, the enzymatic reaction is either slow or not proceeding at all. The intracellular DHAP value can be enhanced with additional enzymes introduced into the host cell. Dihydroxyacetone kinase (DhaK) from *Citrobacter freundii* (EC 2.7.1.29) is a dimeric enzyme, which phosphorylates dihydroxyacetone (DHA) to DHAP by consuming ATP. So far, no detailed mechanism was published. However, if one takes the crystal structure and the regular kinase mechanism into account, a mechanism can be proposed (Figure 2.66).^[187]

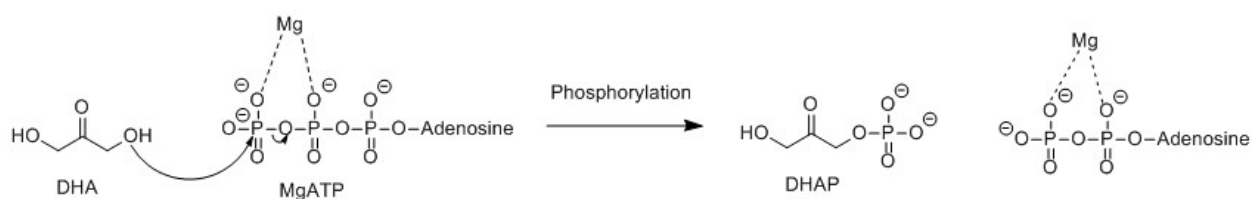


Figure 2.66: Proposed mechanism of DhaK.

In the following chapter, this highly specific enzyme (K_M (ATP) = 70 μM , K_M (DHA) = 30 μM)^[188] was used to increase intracellular dihydroxyacetone phosphate pools in order to be able to perform aldol reactions *in vivo* with higher yields than previously reported^[186]. Prior to this, a characterization of DhaK overexpressed in *E. coli* with regard to intracellular DHAP concentrations as well as modeling of intracellular fluxes is presented and compared

to a *E. coli* wt strain. Compared to the kinetic modeling presented in the second chapter, modeling of intracellular fluxes (stoichiometric modeling) in our case is time-independent (steady-state conditions) and is based on the stoichiometric network of *E. coli*. With the applied modeling approach, optimization strategies for an *in vivo* cascade for the production of polyhydroxylated compounds would be identifiable, which can not be determined with classical experimental approaches as single knock-out studies.

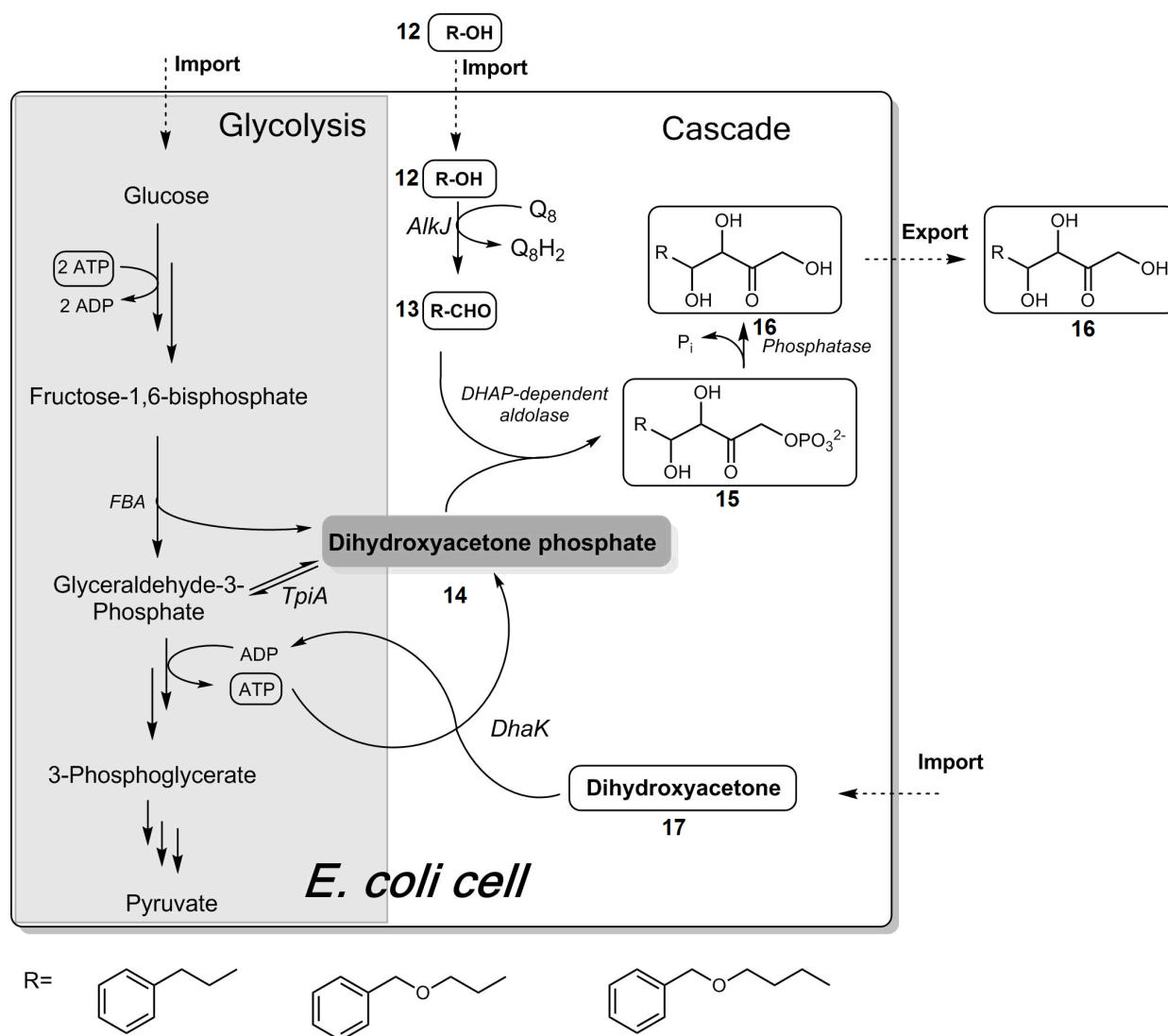


Figure 2.67: Scheme of the DHAP-dependent *in vivo* cascade in *E. coli*.

AlkJ = alcohol dehydrogenase. For other abbreviations see Table 2.9.

The cascade was designed to convert primary alcohols **12** with aromatic residues into polyhydroxylated aldol products **16** by tapping into the central carbon metabolism of the *E. coli* cell (Figure 2.67). In the first step of the cascade, the alcohols as stable substrate feed would

be converted to the corresponding aldehydes **13** by the coenzyme Q₈-dependent alcohol dehydrogenase AlkJ from *Pseudomonas putida*^{[189][190][191]}. The aldehydes would undergo an aldol reaction with intracellular DHAP **14** catalysed by an aldolase. The choice of the aldolase would determine the stereochemistry of the aldol reaction. Four different DHAP-dependent aldolases are known to produce complementary isomers: fructose-1,6-diphosphate aldolase^[192], fuculose-1-phosphate aldolase^[193], tagatose-1,6-diphosphate aldolase^[194] and rhamnulose-1-phosphate aldolase.^[195] The phosphorylated aldol product would undergo a dephosphorylation step for two main reasons: i) the aldol reaction is reversible and a dephosphorylation would shift the equilibrium of the reaction towards aldol formation and ii) phosphorylated compounds cannot pass the cell membrane; a dephosphorylation would enable export of the aldol product **16** out of the *E. coli* cell by passive diffusion.

As a first step, all models, representing the different constructs required for this study, were designed.

2.4.2 Model development

The freely available Ec_iJR904 model for the COBRA Toolbox was used as the *E. coli* wild-type (wt)^[196]. This model contains 931 unique biochemical reactions and does not account for any regulation mechanisms.

The following models were constructed:

- Ec_iJR904 wt
- Ec_iJR904 + DhaK
- Ec_iJR904 + Cascade
- Ec_iJR904 + DhaK + Cascade

2.4.3 Pareto-analysis for cascade optimization

As a foundation for all further modeling approaches, the Ec_iJR904 wt model was compared to the model with DhaK production by feeding the model with standard settings (10 mmol gCDW⁻¹ h⁻¹ glucose uptake, aerobic conditions, minimal media). Theoretically, DHA **17** could enter into the central carbon metabolism of *E. coli* at two different stages (Figure 2.68). The enzyme abbreviations are listed in table 2.9.

Table 2.9: Abbreviations of enzymes in glycolysis and PPP.

Abbreviation	Enzyme name
<i>PtsG</i>	D-glucose transporter (phosphotransferase system)
<i>Pgi</i>	phosphoglucose isomerase
<i>PfkA/B</i>	phosphofructokinase
<i>Fba</i>	fructose-bisphosphate aldolase
<i>Tpi</i>	triose-phosphate isomerase
<i>GapA</i>	glyceraldehyde-3-phosphate dehydrogenase
<i>PgkA</i>	phosphoglycerate kinase
<i>PgmA</i>	phosphoglycerate mutase
<i>Eno</i>	enolase
<i>PykF</i>	pyruvate kinase
<i>Gnd</i>	6-phosphogluconate dehydrogenase
<i>Rpe</i>	ribulose-5-phosphate-3-epimerase
<i>Rpi</i>	ribulose-5-phosphate isomerase
<i>TkA</i>	transketolase A
<i>TkB</i>	transketolase B
<i>TalA</i>	transaldolase
<i>DhaK</i>	dihydroxyacetone kinase
<i>FSA</i>	fructose-6-phosphate aldolase

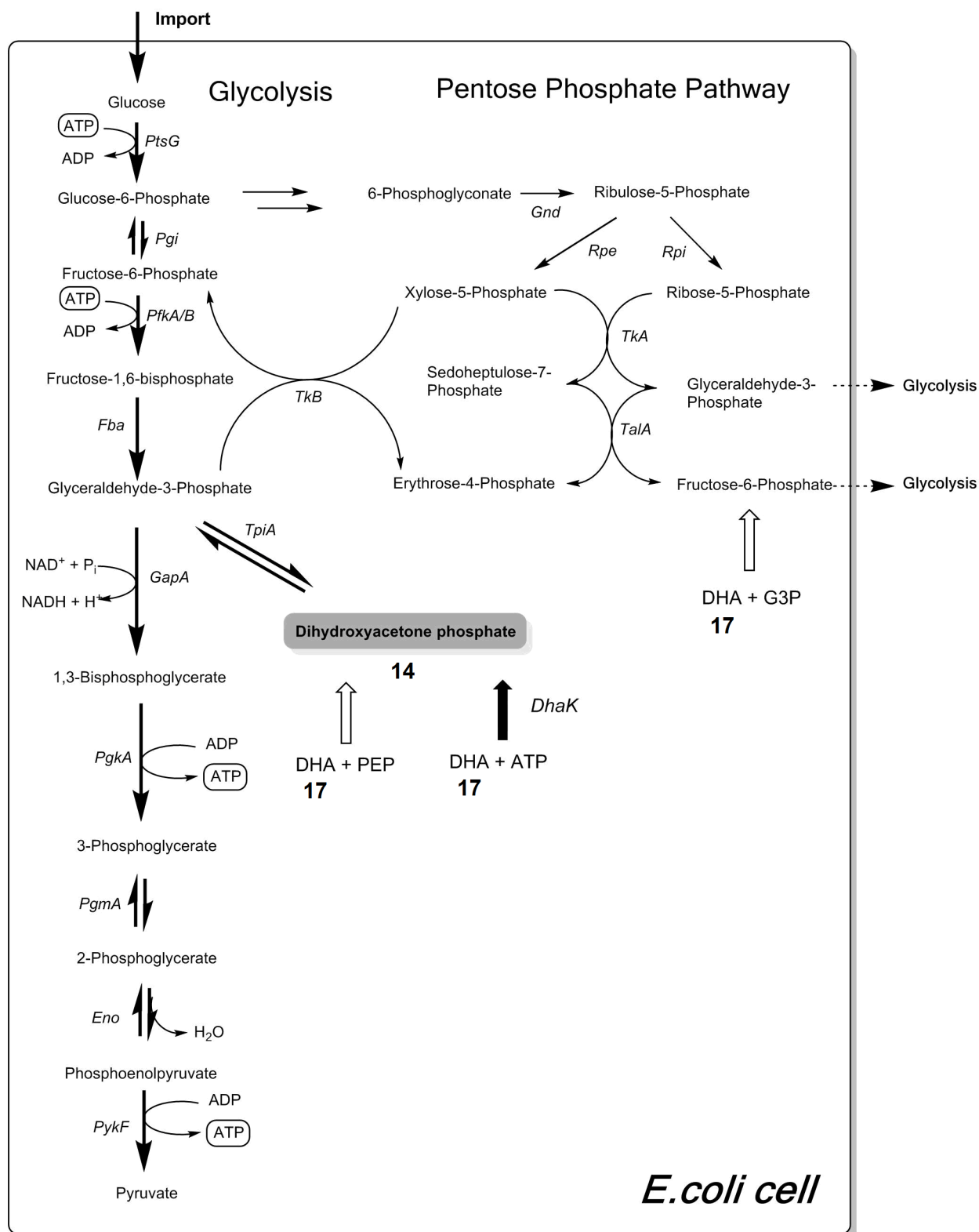


Figure 2.68: Glycolysis and Pentose Phosphate Pathway in *E. coli*.

The DHA 17 entry steps are shown as white arrows in the *E. coli* wt, and additional black arrow in the DhaK producing strain. For full enzyme names see Table 2.9.

The influence of DHA uptake onto the biomass formation at a certain DHA uptake rate was

investigated (Figure 2.69).

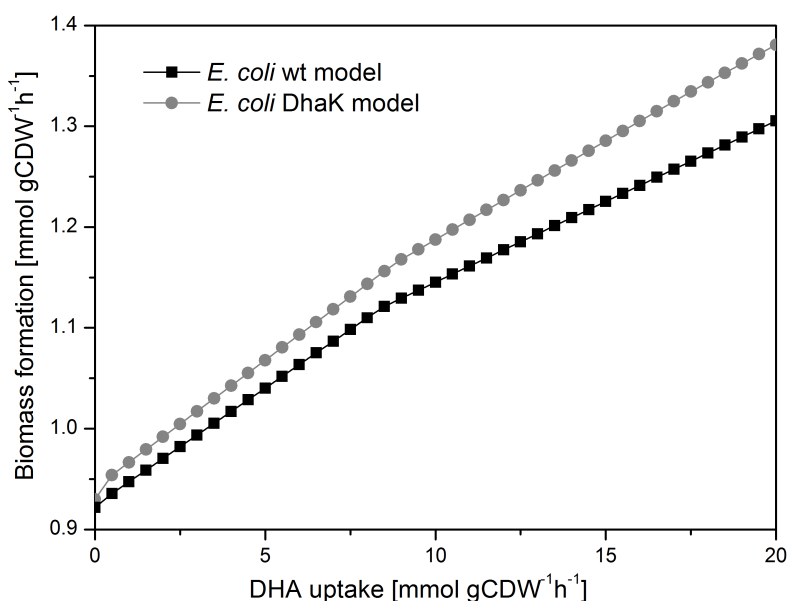
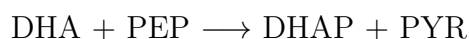


Figure 2.69: 2D Pareto analysis: DHA uptake vs. biomass formation.

E. coli BL21 (DE3) wt in comparison to the DhaK expressing strain. Specific glucose uptake rate: 10 mmol gCDW⁻¹ h⁻¹, aerobic conditions.

With the assumption, that both strains are capable of the same DHA uptake in minimal medium, and, with a standard glucose uptake rate of 10 mmol gCDW⁻¹ h⁻¹ (standard model setting), the simulation with the objective function of biomass formation showed that the *E. coli* wt strain is inferior to the DhaK producing strain in terms of biomass formation with rising DHA concentrations. The DhaK strain is predicted to utilize DHA in a more efficient manner, since it directly feeds the DHA in form of DHAP in the lower glycolysis whereas the wt strain is limited to two native reactions to utilize DHA:



This reaction is catalyzed by the dihydroxyacetone phosphotransferase, which catalyzes the transfer of the phosphate group from phosphoenolpyruvate (PEP) to DHA **17**, creating DHAP **14** and pyruvate (PYR). This reaction is irreversible.



This reaction is catalyzed by fructose-6-phosphate aldolase, which breaks the fructose-6-phosphate (F6P) to DHA **17** and glyceraldehyde-3-phosphate (G3P). Since this reaction is reversible, the enzyme can also catalyse the formation of F6P from DHA **17** and G3P, feeding it directly into the upper glycolysis (Figure 2.68).

The pareto analysis is usually a helpful method to decide, which setting point is the best one for a certain operation. However, in this case, the initial parameters of the model are purely theoretical and are not measured with an actual, DhaK producing strain and therefore only illustrate, that the DhaK producing strain would benefit more from DHA uptake than the wt strain.

The same theoretical prediction as shown above was performed for the models with the cascade, either with or without DhaK. The performance of the cascade is in those cases dependent on biomass formation and DHA uptake, if we maximize for biomass formation. Therefore, the flux through the cascade and the DHA uptake had to be adjusted manually and for each condition, the biomass formation was maximized. Since this operation would take a long time, a MATLAB script was written and applied to automatize the procedure (see experimental section).

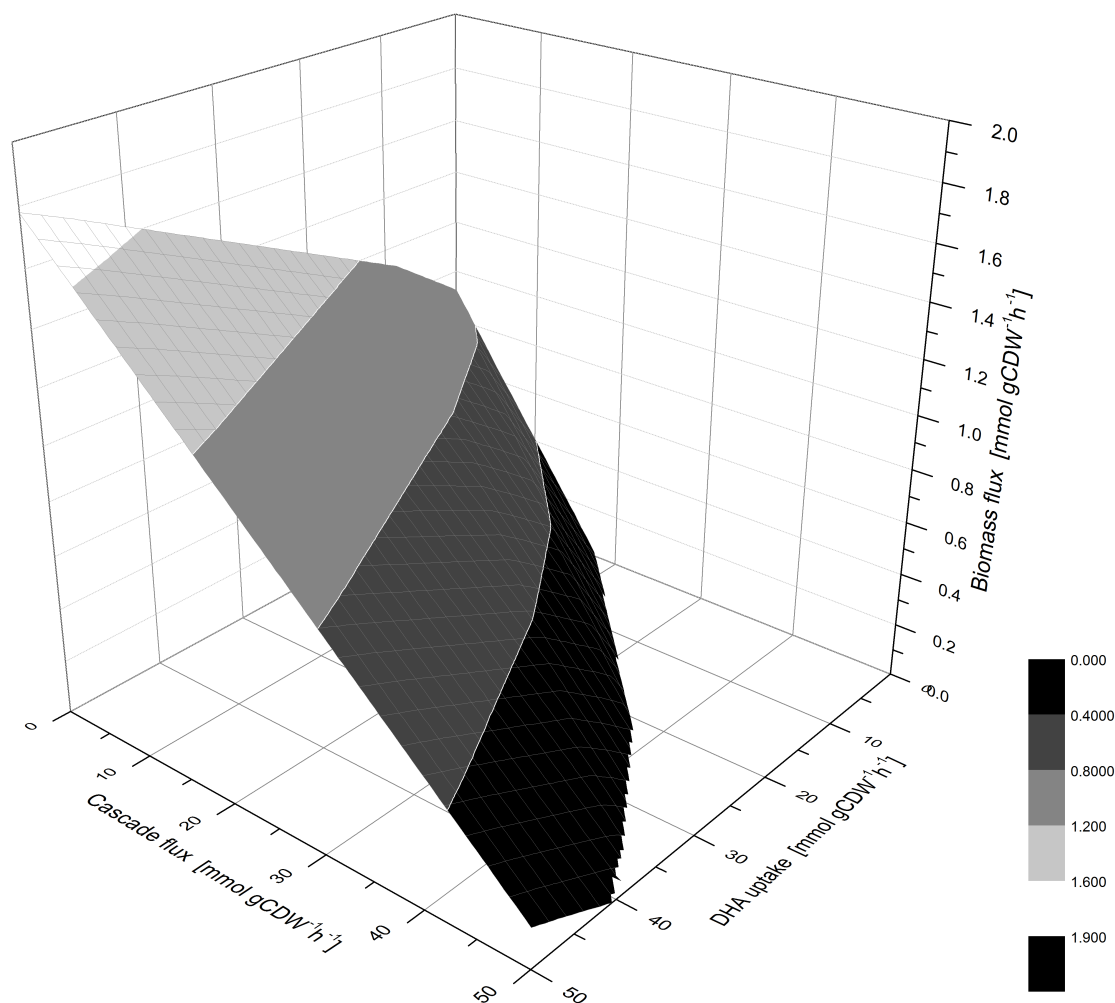


Figure 2.70: 3D Pareto analysis: theoretical DHA uptake vs. biomass formation in *E. coli* with DHAP-dependent cascade.

Specific glucose uptake rate: $10 \text{ mmol gCDW}^{-1} \text{ h}^{-1}$, aerobic conditions, Objective function: biomass formation, DHA sampling performed with DHA sampling script.

In the model without Dhak activity, the DHA uptake was beneficial for the biomass formation as well as the flux through the cascade. The maximal theoretical biomass formation with $1.78 \text{ mmol gCDW}^{-1} \text{ h}^{-1}$ was present with the simulated highest DHA uptake of $50 \text{ mmol gCDW}^{-1} \text{ h}^{-1}$ and a cascade flux of $0 \text{ mmol gCDW}^{-1} \text{ h}^{-1}$, since the newly formed DHAP was not used for formation of the aldol product. The 3D pareto surface (Figure 2.70) showed that the DHA uptake benefitted the flux through the cascade.

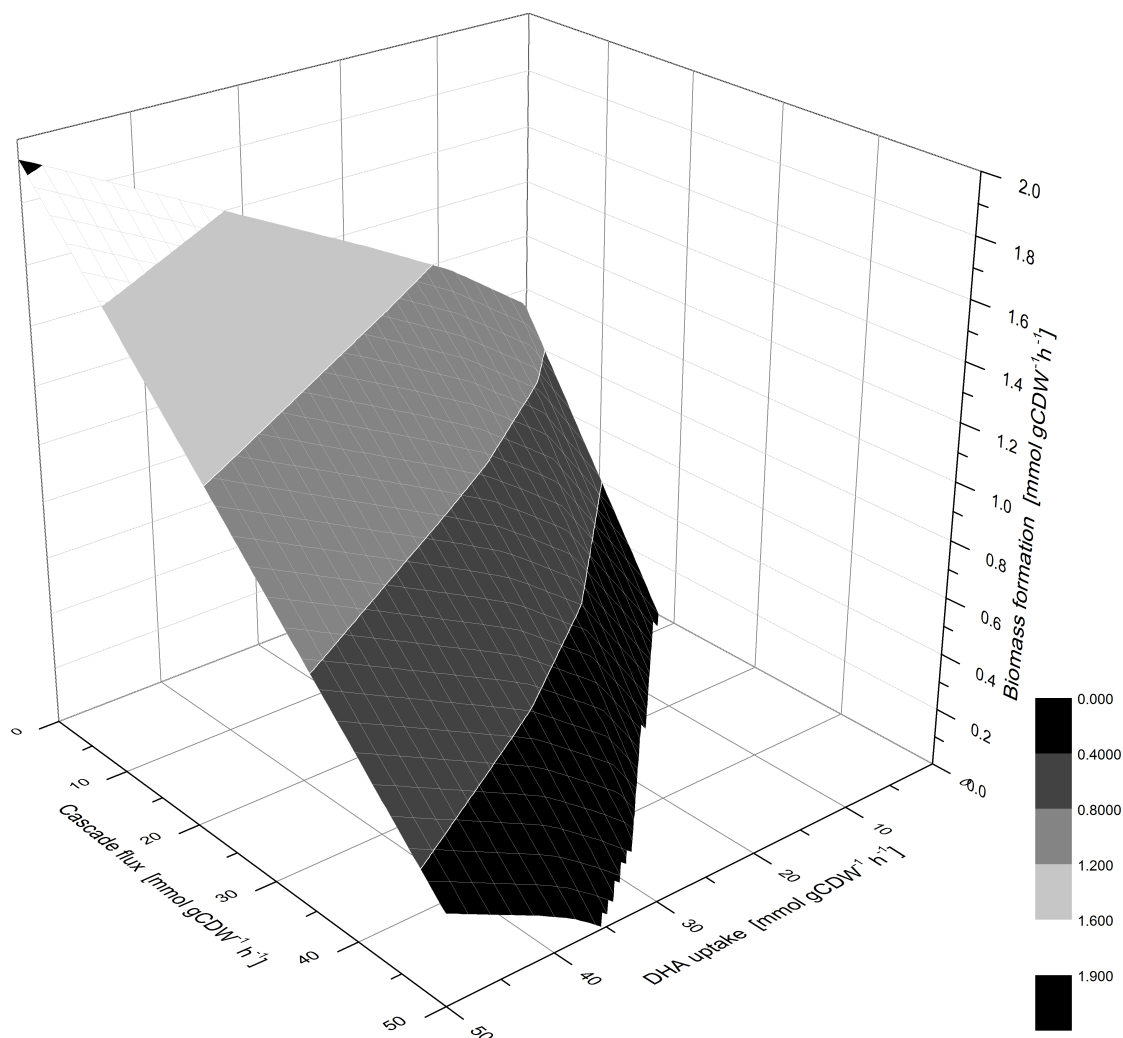


Figure 2.71: 3D Pareto analysis: theoretical DHA uptake vs. biomass formation in *E. coli* with DHAP-dependent cascade and DhaK production.

Specific glucose uptake rate: $10 \text{ mmol gCDW}^{-1} \text{ h}^{-1}$, aerobic conditions, Objective function: biomass formation, DHA sampling performed with DHA sampling script.

The model with DhaK activity showed a higher benefit from the DHA uptake for flux through the cascade and the biomass formation. Higher maximal biomass formation with approx. $1.9 \text{ mmol gCDW}^{-1} \text{ h}^{-1}$ was reached than in the model without DhaK. Additionally, the flux through the cascade was higher at lower DHA uptake rates compared to the model without DhaK. This resulted from a direct phosphorylation of DHA **17** by DhaK to DHAP **14** and its subsequent utilization by the aldolase in the artificial cascade. Overall, the DhaK expressing model is superior to the cascade-only model and predicted a more efficient system for production of polyhydroxylated aldol products, which would be a great improvement on

a catalyst level compared to literature-known *in vivo* aldol reactions.^[186]

2.4.4 Dihydroxyacetone kinase as a tool for increasing intracellular DHAP concentrations

To investigate the effect of DhaK expression e.g. the prediction of DhaK strain being superior to the wild-type *E. coli*, a laboratory experiment was set up. The two strains were grown in M9-N* minimal media. Both strains were compared regarding their physiology (growth, glucose and DHA consumption) as well as their intracellular metabolite concentrations (metabolomics: aminoacids, several glycolytic compounds as well as compounds from the TCA, cofactors). All parameters were characterized in the exponential, as well as the stationary phase, to determine which mode of operation would be more beneficial.

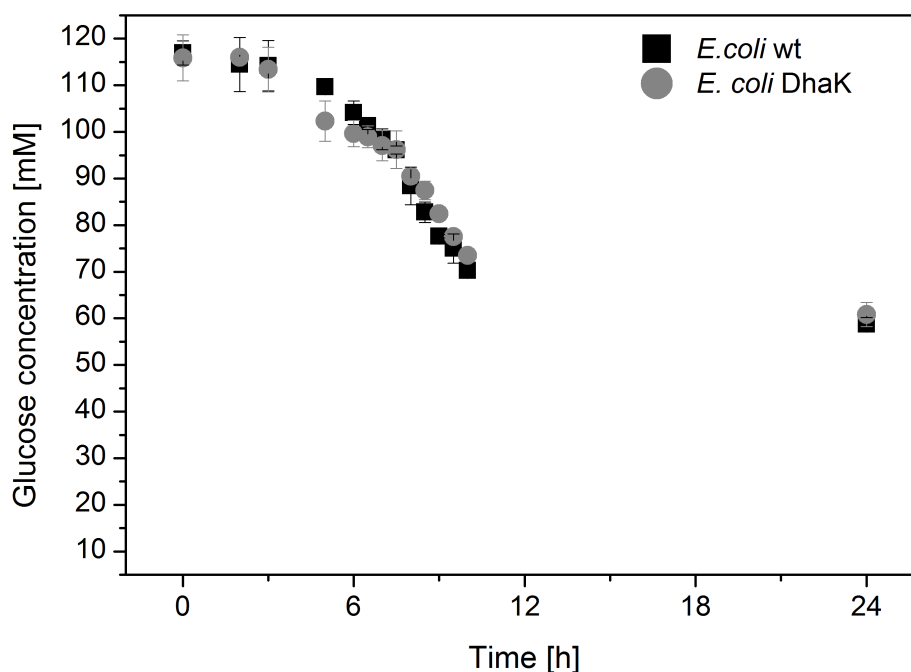


Figure 2.72: Glucose consumption of *E. coli* wt and *E. coli* DhaK strain in the exponential growth phase.

The measurement was performed in triplicates. The temperature shift from 37°C to 20 °C was performed after 3 h. Addition of 20 mM DHA **17** was performed after 5.8 h.

The wt as well as the DhaK producing strain had similar glucose consumption during the exponential phase (Figure 2.72). Shortly after the temperature shift after 3 h cultivation time, the DhaK producing strain showed a higher glucose uptake than the wt strain. After approx. 12 h cultivation time, the cultures entered the nitrogen-limited state, which was

accompanied by a decrease in glucose consumption.

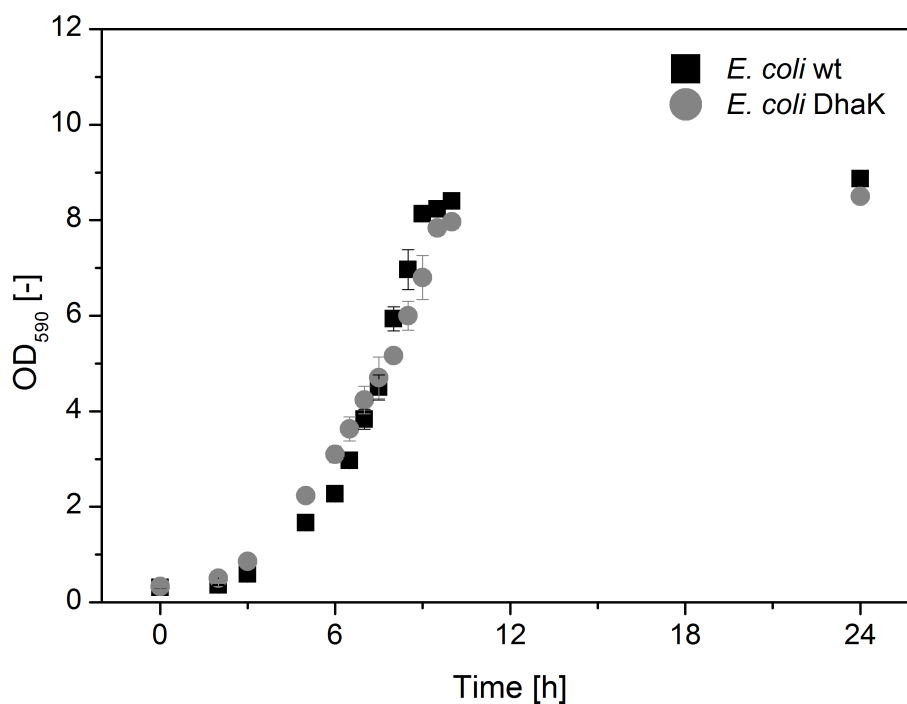


Figure 2.73: Growth of *E. coli* wt and *E. coli* DhaK strain in the exponential growth phase.

The measurement was performed in triplicates. The temperature shift from 37°C to 20 °C was performed after 3 h. Addition of 20 mM DHA **17** was performed after 5.8 h.

Both strains showed similar biomass formation in the exponential phase (Figure 2.73). The DhaK producing strain showed a slight faster growth after DHA addition compared to the wt strain. After approximately 10 h the growth rate decelerated due to the onset of nitrogen-limiting conditions. The final OD for both strains (due to the nitrogen limited conditions) was 8.7.

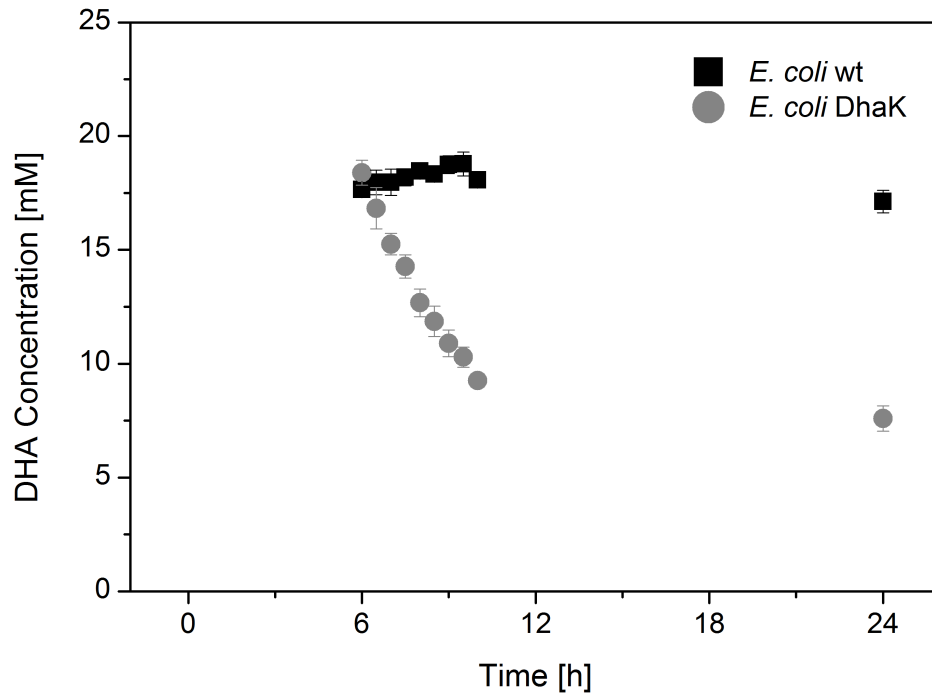


Figure 2.74: DHA uptake of *E. coli* wt and *E. coli* DhaK strain in the exponential growth phase.

The measurement was performed in triplicates. The temperature shift from 37°C to 20 °C was performed after 3 h. Addition of 20 mM DHA **17** was performed after 5.8 h.

In contrast to the very similar behaviour in terms of glucose consumption and growth (Figures 2.72, 2.73), only the DhaK expressing strain showed consumption of DHA during the exponential phase while the wt strain did not measurably consume any DHA from the medium. With onset of the nitrogen-limitation, the DHA uptake of the DhaK producing strain decreased.

The data acquired during this experiment were used to calculate specific uptake rates during the steady-state exponential phase for glucose and DHA **17** for both strains according to equations 2.21 and 2.22 (Table 2.10).

$$Y_{X/S} = \frac{dX/dt}{dS/dt} \quad (2.21)$$

$$q_S = \frac{\mu}{Y_{X/S}} \quad (2.22)$$

Table 2.10: Specific uptake rates for glucose and DHA in the exponential growth phase.

Strain	Specific glucose uptake rate q_{Glc} [mmol gCDW ⁻¹ h ⁻¹]	Specific DHA uptake rate q_{DHA} [mmol gCDW ⁻¹ h ⁻¹]
<i>E. coli</i> wt	3.62 ± 0.09	no uptake
<i>E. coli</i> DhaK	3.00 ± 0.44	1.04 ± 0.11

In the stationary phase of the same experiment, DHA was added again at 24.5 h to determine, if a higher DHA concentration can boost the DHA uptake under non-growing conditions (Figure 2.75). Non-growing conditions are generally preferable to growing conditions, since the cells can be longer maintained in the non-growing state without complicated instrumental set-up.

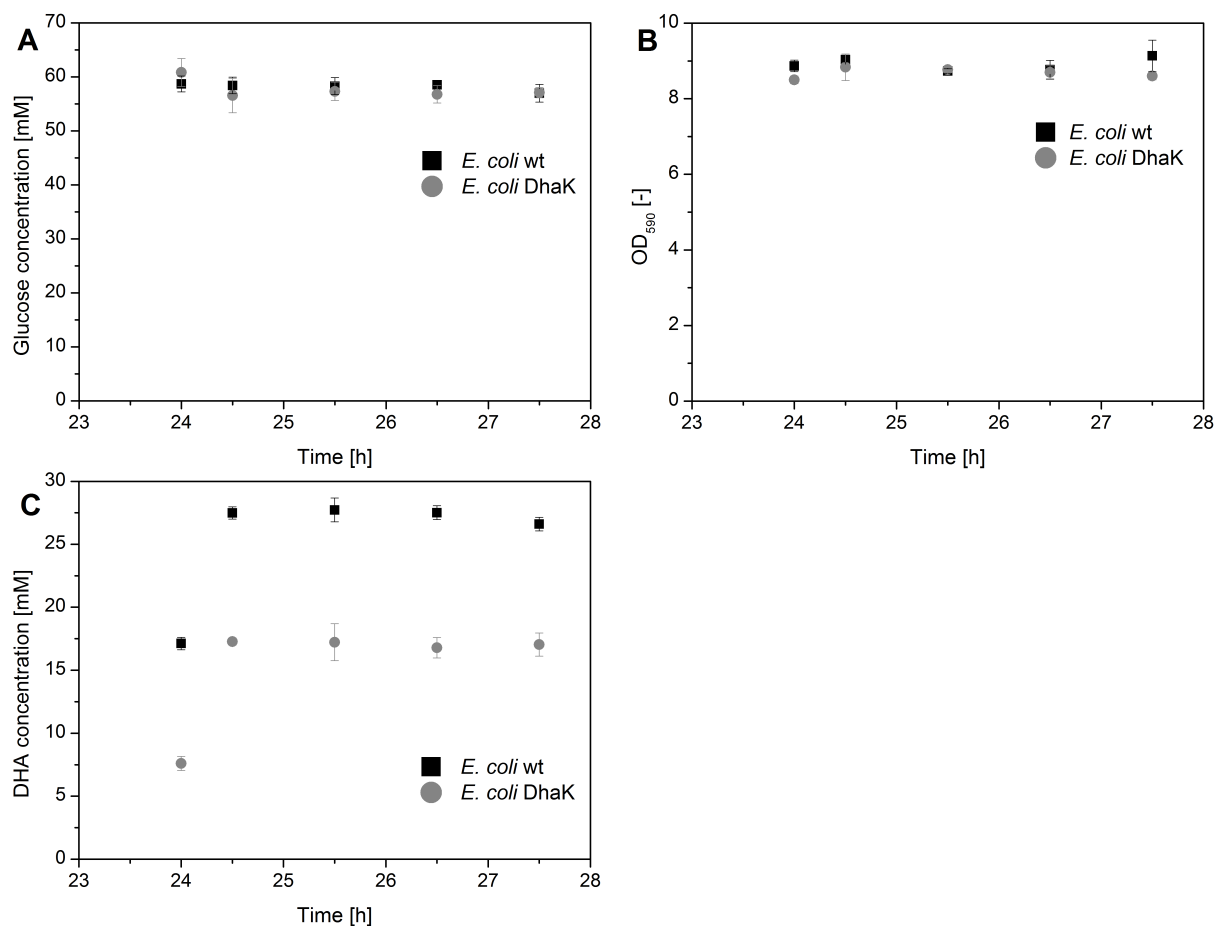


Figure 2.75: Glucose concentration, Growth and DHA concentrations of *E. coli* wt and *E. coli* DhaK strain in the stationary phase.

(A) Glucose concentration (B) Growth (c) DHA concentration plotted over cultivation time. The measurement was performed in triplicates. Addition of ≈ 10 mM DHA **17** was performed after 24.5 h.

Over the observed period of time under non-growing conditions, glucose consumption was minimal and the growth did not change over time as expected. In contrast to the DHA uptake under growing conditions, the non-growing conditions did not lead to a measurable DHA uptake after spiking DHA to the medium. It is likely, that DHA uptake only occurs if DHAP is removed from the equilibrium by additional reactions as it is the case during biomass formation.

Additionally, DHA uptake is considered to follow a facilitated diffusion mechanism^[197], as also reported for the glycerol diffusion^{[198][199][200]}, which is expected to also facilitate the diffusion of similar molecules like DHA. Although the exact mechanism is not reported, it is possible (and also seems highly reasonable), that certain intracellular DHA concentrations

inhibit further diffusion of DHA, coupling the uptake to an actual consumption in the cell. The next step was to evaluate the intracellular metabolomics during the experiment in the two strains. The most important factor was the intracellular DHAP concentration (Figure 2.76), since this is expected to be the limiting step in a future implementation of an aldol reaction *in vivo*. The K_M values of known DHAP-dependent aldolases are high compared to other enzymes (approx. 0.5-1 mM; e.g. 0.6 mM for L-rhamnulose-1-phosphate aldolase^[201]), making it indispensable to raise the intracellular DHAP concentration. The concentration of the acceptor molecule in the aldol addition can be easily increased by adding more substrate to the cells, since it passes through the cell membrane, but aldol formation would always be limited by the intracellular DHAP concentration, which is produced in the cell and does not pass the cell membrane.

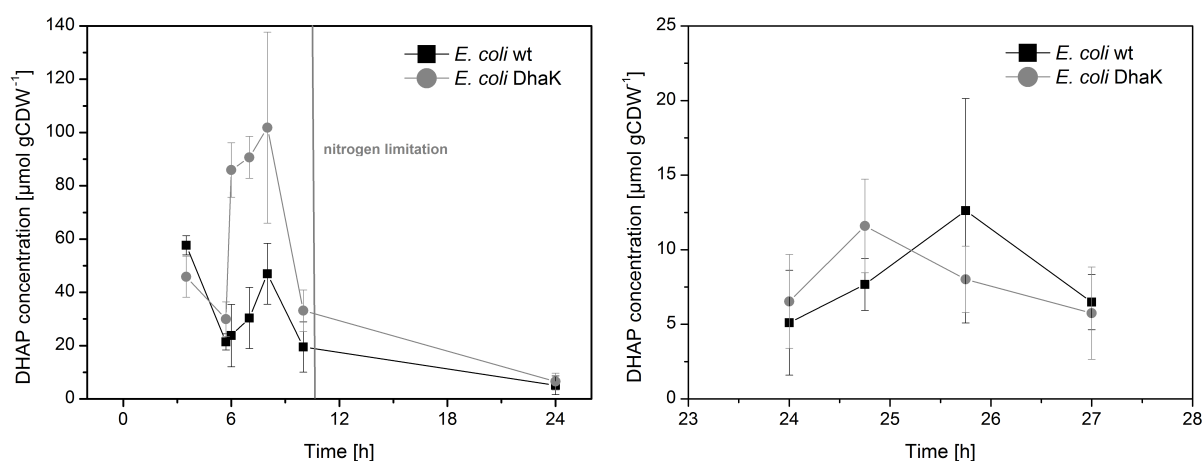


Figure 2.76: Intracellular DHAP concentration in *E. coli* wt and *E. coli* DhaK strain in (A) exponential and (B) stationary phase.

The measurement was performed in triplicates. Addition of (A) 20 mM DHA after 5.8 h and (B) ≈ 10 mM DHA after 24.5 h.

After the DHA addition in the exponential phase, the DhaK producing strain showed an ≈ 4 -fold increase in the intracellular DHAP concentration compared to the wt strain. This elevated DHAP concentrations were stable for two hours and then decreased again. The wt strain also showed increased DHAP concentrations after DHA addition, which can be explained with a metabolization of DHA through natural pathways for a short period of time. Since the DHA concentration in the cultivation medium remained constant over time, this increase can be neglected for intracellular production of aldol products.

During the stationary phase, no increase in DHAP concentration in neither strain was ob-

served. In general, the DHAP concentration during the stationary phase was 4 to 5-fold smaller than during the exponential phase, which is disadvantageous for aldol reactions *in vivo*.

Since the transformation of DHA to DHAP by DhaK is an ATP consuming reaction, it was important to establish how *E. coli* deals with this interference with its energy metabolism. Therefore it is important to quantify ATP, ADP and AMP and calculate the energy charge^[202] (Figure 2.77). The energy charge is defined in Equation 2.23 and in healthy growing cells, the energy charge is around 0.8^[172].

$$\text{Energy Charge} = \frac{[ATP] + 0.5 [ADP]}{[AMP] + [ADP] + [ATP]} \quad (2.23)$$

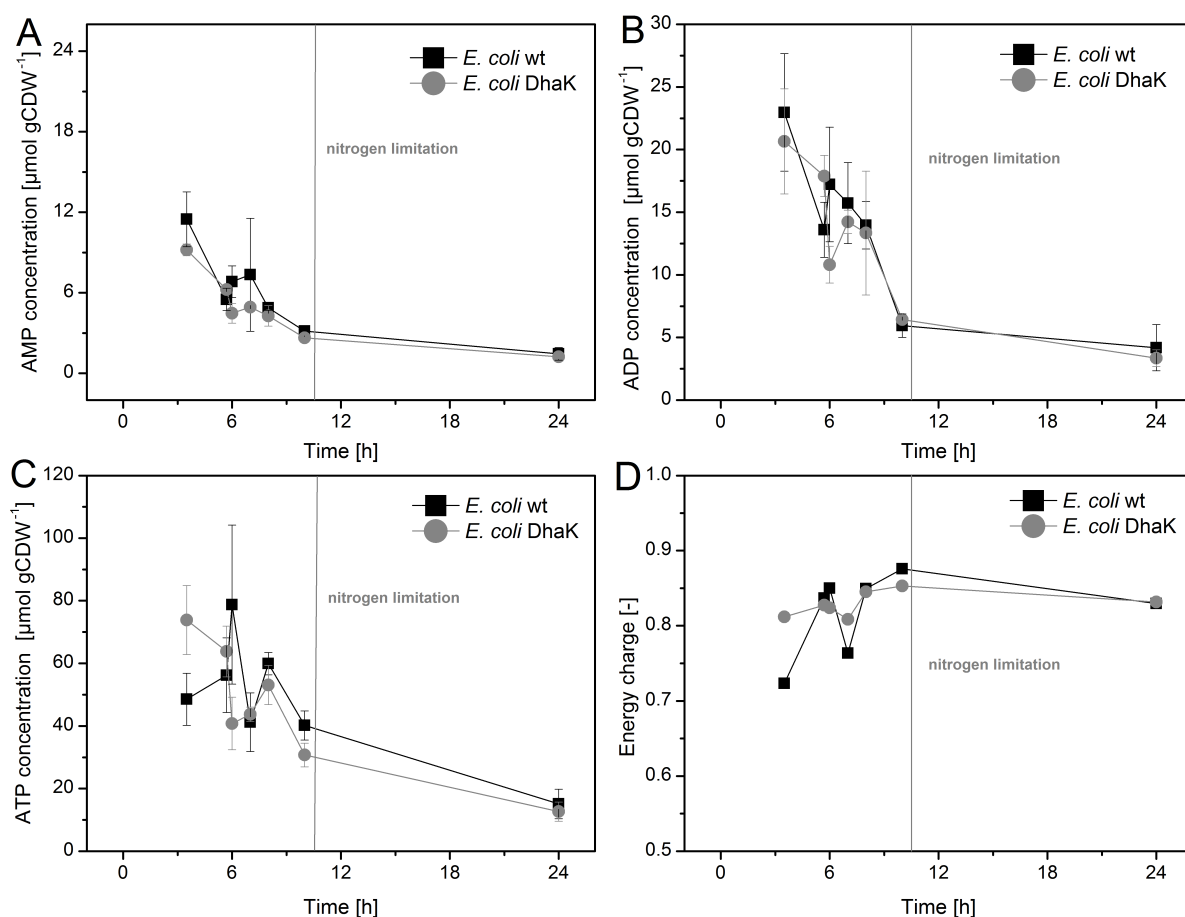


Figure 2.77: Intracellular (A) AMP (B) ADP (C) ATP concentrations (reported as mean \pm SD) and the (D) energy charge in *E. coli* wt and *E. coli* DhaK strain in the exponential growth phase.

The measurement was performed in triplicates. 20 mM DHA were added after 5.8 h, Standard deviation in (D) omitted for clarity.

After the DHA addition, a difference in concentration was observed for all three energy metabolites in both strains for a short period of time. The energy charge stabilized itself at 0.85 after a short adaptation period in both strains, which represents a functioning metabolism with working cofactor recycling.

The question remained, why DHA was only taken up during the growing phase of the culture. The hypothesis, which was developed after the comparison of the presented physiological and metabolomics results, was, that the intracellular ATP concentration may be the key element to the lack of DHA metabolization by DhaK under non-growing conditions. Therefore, the actual intracellular ATP concentration was calculated by using the intracellular volume of $3.6 \mu\text{L}/\text{cell}^{[171]}$ and was plotted with the DHA uptake (Figure 2.78).

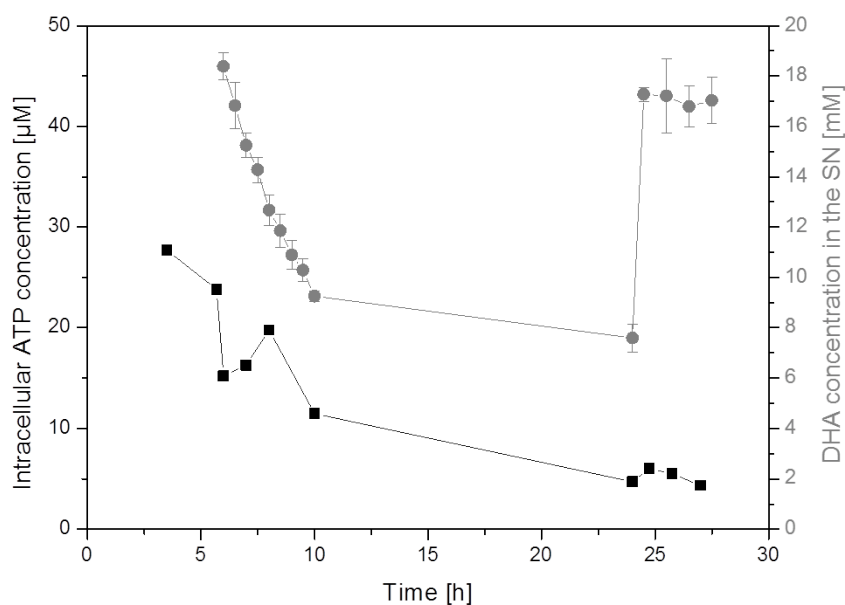


Figure 2.78: Correlation of intracellular ATP concentration and DHA uptake.

Both measurements were performed in triplicates and are reported as mean \pm 1SD. 20 mM DHA were added after 5.8 h and 24.5 h.

During the growing phase, the DHA and ATP concentrations were both decreasing until the onset of nitrogen-limited conditions. The intracellular ATP at the end of the growing phase dropped to approx. $10 \mu\text{M}$. Considering that the K_M value of DhaK for ATP is $70 \mu\text{M}^{[188]}$, the low ATP concentration may not be enough to perform the phosphorylation under non-growing conditions, especially because the ATP concentration dropped further to $5 \mu\text{M}$ after

24 h. This result lead to the conclusion that the cells need to be maintained in a growing state to effectively use the biocatalyst for boosting aldol reactions. This improvement on the cultivation level was successful and the next step was to perform modeling with the obtained physiological values.

2.4.5 Stoichiometric modeling of the influence of a DHAP - producing reaction *in vivo* on intracellular fluxes of *E. coli*

After measuring the physiology of both strains and obtaining the uptake rates for glucose and DHA, the previously described models were used to simulate the intracellular fluxes during the exponential growth of both strains. The glucose and the DHA uptake rates were set to the values obtained in the previous section (Table 2.10).

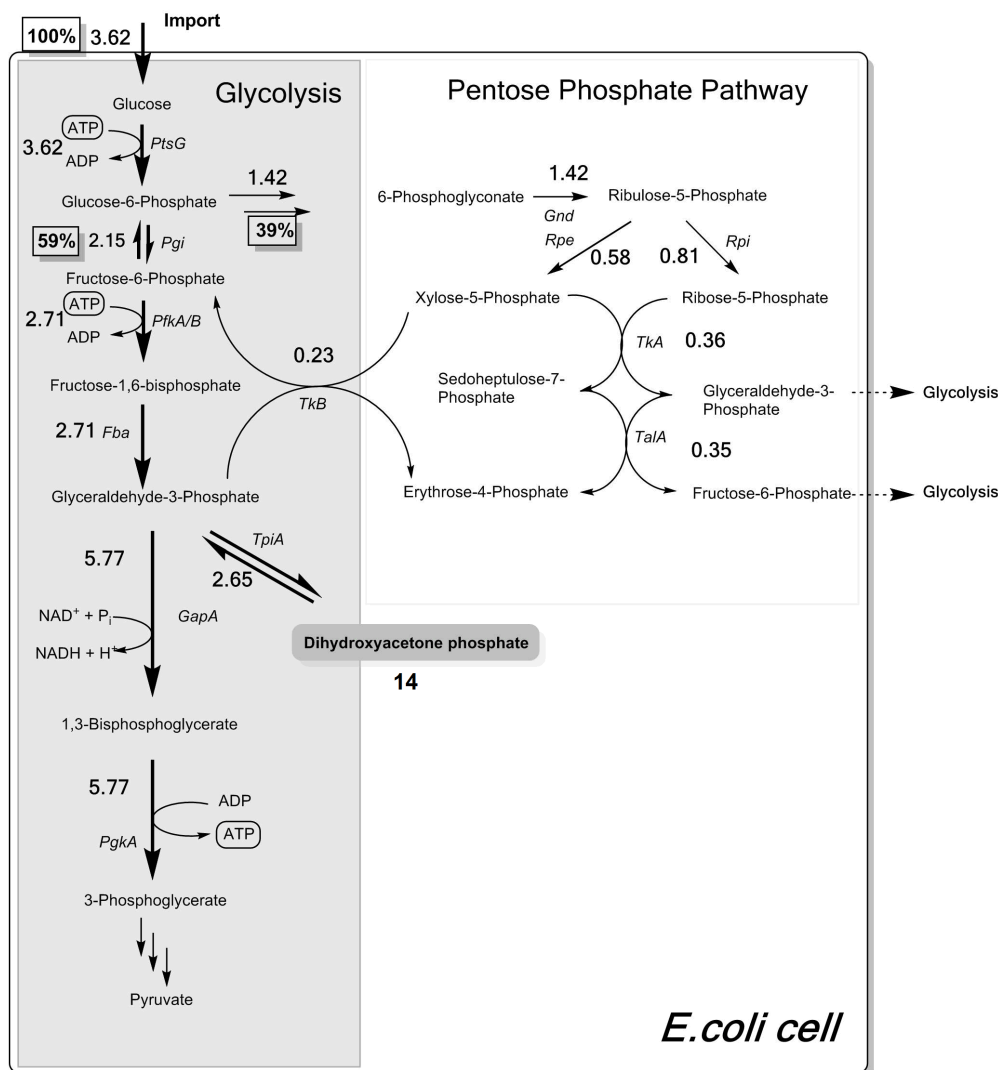


Figure 2.79: Stoichiometric modeling of the *E. coli* BL21 (DE3) wt strain.

The fluxes are given in mmol gCDW⁻¹ h⁻¹. For full enzyme names see Table 2.9.

The visualization of modeled intracellular fluxes (Figure 2.79) for *E. coli* wt strain showed a distribution of 59 % to 39 % between glycolysis and the pentose phosphate pathway (PPP). The remaining 2 % were consumed in reactions not depicted in the visualization e.g. anabolic pathways. After the fructose-1,6-bisphosphate aldolase mediated cleavage of FBP to DHAP and G3P in the glycolysis, the flux value approx. doubled from 2.71 to 5.77 after the triose-phosphate isomerase reaction, since both molecules molecular weight is half of the molecular weight of the precursor molecule. The flux entering the PPP was distributed between the different reactions, because this metabolic pathway is mainly used for synthesis of different sugars, to provide precursors for nucleotide and amino acid biosynthesis and NADPH synthesis.^[203]

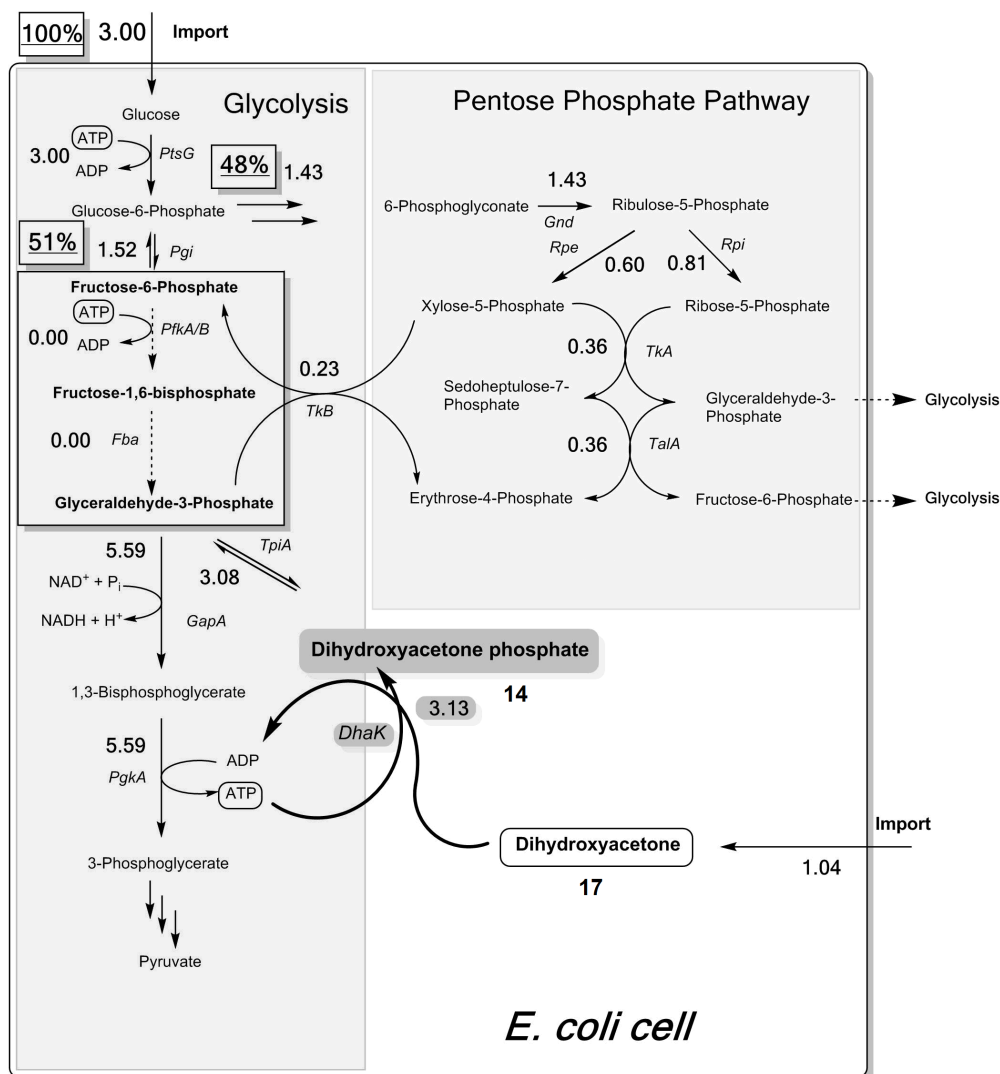


Figure 2.80: Stoichiometric modeling of the *E. coli* BL21 (DE3) DhaK strain

The fluxes are given in $\text{mmol gCDW}^{-1} \text{h}^{-1}$ intracellular fluxes as shown for wt in Figure 2.79. For full enzyme names see Table 2.9.

For the DhaK producing strain, the flux distribution is slightly different than for the wt strain. Apart from the lower absolute glucose influx, the distribution between glycolysis and PPP is 51 % to 48 %. This means, that from the influx of glucose, 9 % more go to the PPP in the DhaK producing than in the wt strain. In absolute values, the flux to the PPP was constant in both strains. In contrast to the constant flux through the glycolysis of the wt strain, the simulation for the DhaK strain revealed that there was no flux between fructose-6-phosphate and glyceraldehyde-3-phosphate. This gap in the glycolysis seems to originate in supply of DHAP by the influx from DHA phosphorylation by DhaK. Additionally, another

DHA utilizing reaction was predicted to be activated in this strain, which was not activated in the wt simulation (Figure 2.81).

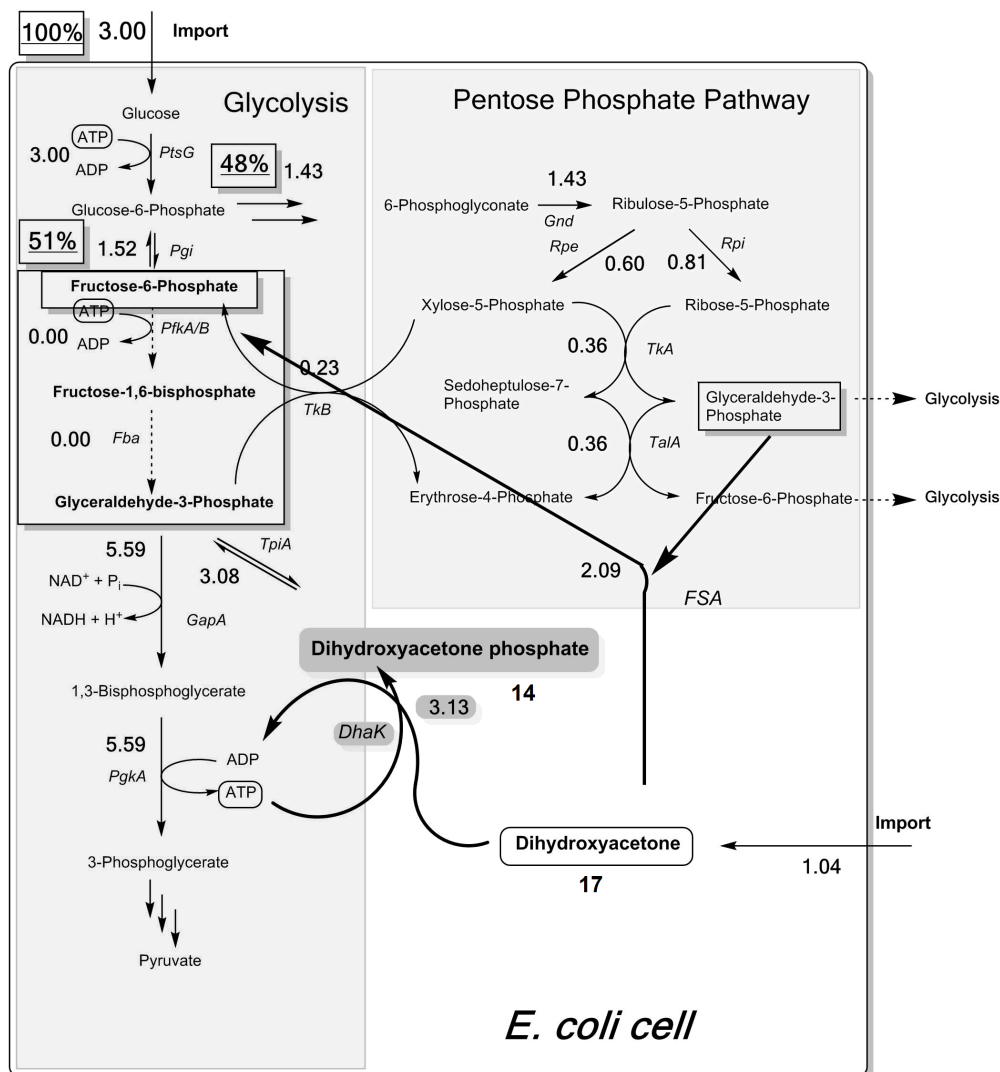


Figure 2.81: Stoichiometric modeling of the *E. coli* BL21 (DE3) DhaK strain.

The fluxes are given in $\text{mmol gCDW}^{-1} \text{h}^{-1}$ additional active aldolase reaction depicted for DhaK producing strain. For full enzyme names see Table 2.9.

The stoichiometric modeling predicted the native fructose-6-phosphate aldolase (Fsa) to be active. This enzyme catalyzed the aldol addition of G3P and DHA 17 to fructose-6-phosphate, which could subsequently enter the central carbon metabolism of *E. coli* at both glycolysis and PPP. These two reactions with DHA would explain the gap in the glycolysis, because they would make the two glycolytic reactions obsolete. However, it was rather unusual for a microorganism to have such a shutdown of the most important central carbon metabolism pathway. The hypothesis was that due to the reduced number of constraints

(glucose and DHA uptake rates) and the missing regulation of the whole network, the flux distribution might be incorrect. Therefore, the intracellular concentration of fructose-1,6-bisphosphate was measured in both strains after DHA addition, to either prove or disprove the hypothesis.

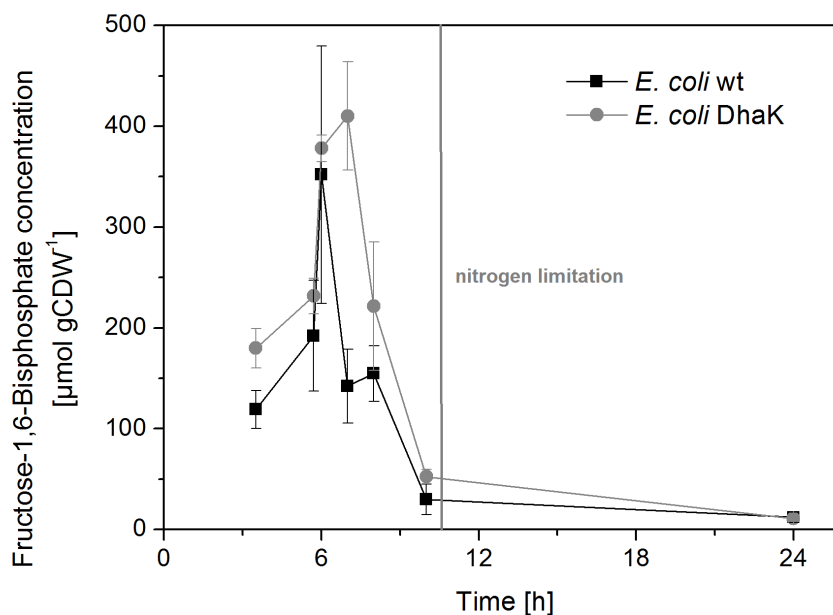


Figure 2.82: Intracellular fructose-1,6-bisphosphate concentration of the *E. coli* BL21 (DE3) DhaK strain.

Results are reported as mean \pm 1 SD. DHA addition after 5.8 h.

After DHA addition at 5.8 h, the DhaK producing strain showed approx. 3 times higher concentrations of fructose-1,6-bisphosphate as the wt strain. This observation proves our hypothesis of the partially incorrect modeling of intracellular fluxes, most likely due to a limited number of constraints. To improve the model, it would be important to gain more knowledge about the actual flux distribution in the modeled system. Therefore, a HPLC-MS/MS method for measurement of different isotopomers needed to be developed to be able to perform ^{13}C metabolic flux analysis (MFA), as described in the general introduction. This method facilitates the experimental investigation of actual fluxes within a living microorganism, classically under steady-state conditions.

2.4.6 Development of a HPLC-MS/MS method for measurement of isotopomers to perform ^{13}C -metabolic flux analysis (^{13}C -MFA)

For measurement of isotopic distributions, an LC-MS/MS method needed to be developed. So far, such methods for HPLC systems have been developed. However, all of them were based on measurement with an ion trap MS detector.^[204] In our case, a triple quadrupole MS detector, was used. As a first step towards method development, for several metabolites, which gave good signals in our established metabolomics method, all possible labeled fragment patterns of isotopomers were calculated (Figure 2.83).

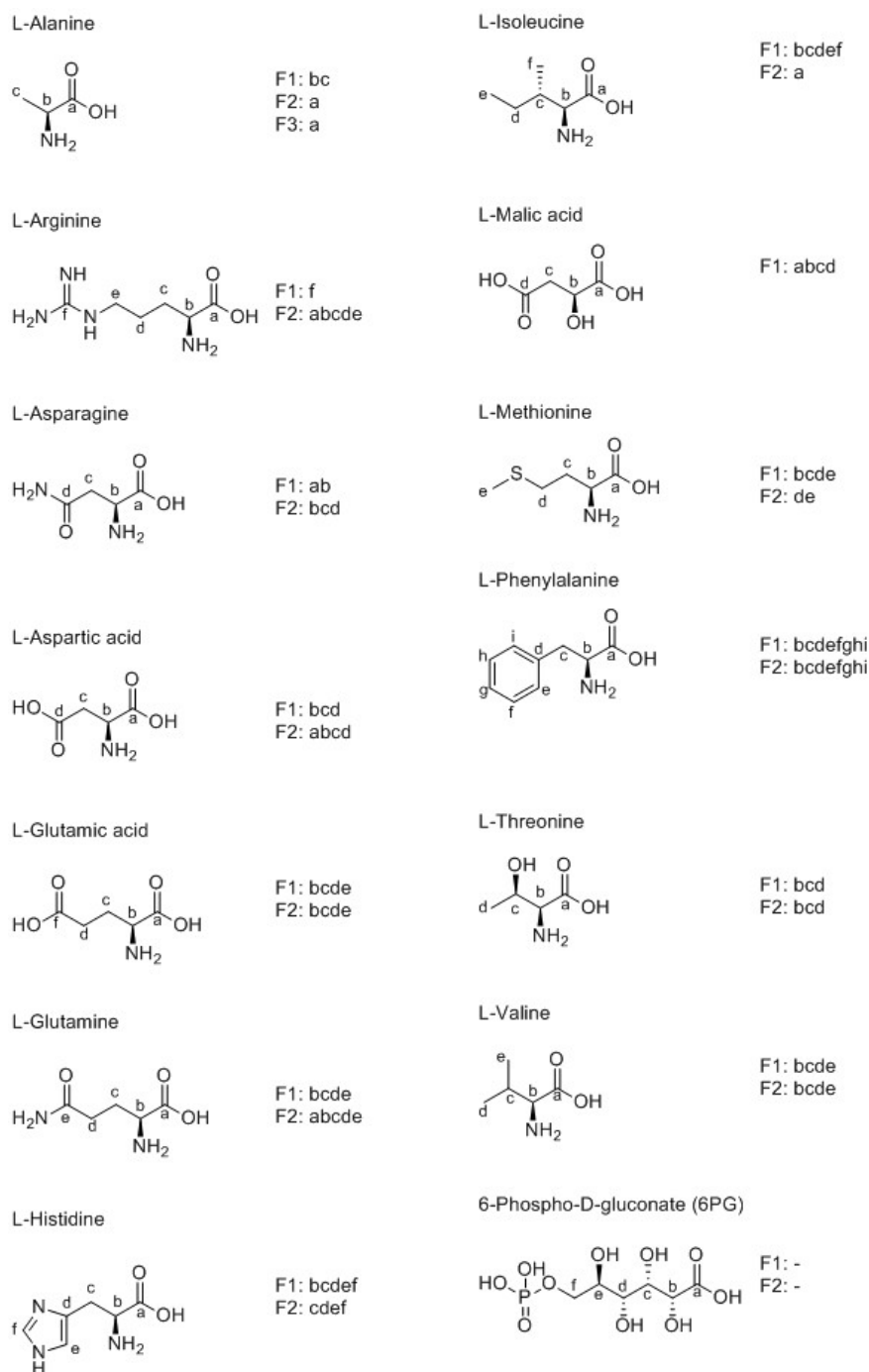


Figure 2.83: Metabolite fragment patterns in the LC-MS/MS measurements.

F1-F3 are fragments of the molecules in the LC-MS/MS measurement

The measurement of the different isotopomers was then performed by adjusting the multi-reaction-monitoring method of the triple quadrupole MS detector. For example, aspartic acid has four carbon atoms. During the fragmentation in the mass detector, two main fragments (F1: bcd / F2: abcd) are formed. In the first case, the α -carbon atom cleaved. In the second case, only the hydroxygroup is released, but the carbon chain remains intact.

From these fragments, all the possible combinations for the molecule have to be considered. For the unlabeled aspartic acid with a mass of 132 g mol^{-1} (isotope m_0), only the unlabeled fragments are considered. For the aspartic acid with one labeled carbon (m_1), two different fragment combinations can exist: one where F1 with three of four carbons contains the labeled carbon, and one where the labeled carbon is at position a. In both cases, the carbon is included in the F2 fragment with all the four carbon atoms. This is performed in the same manner for aspartic acid with two (m_2), three (m_3) and four (m_4) labeled carbon atoms. In the end, the distribution of the isotopomers $m_0 - m_4$ is calculated and compared with the predicted natural distribution. Additionally, aspartic acid, which was extracted from *E. coli* grown on glucose, was compared to the predicted and the measured distribution of analytical standards (Figure 2.84).

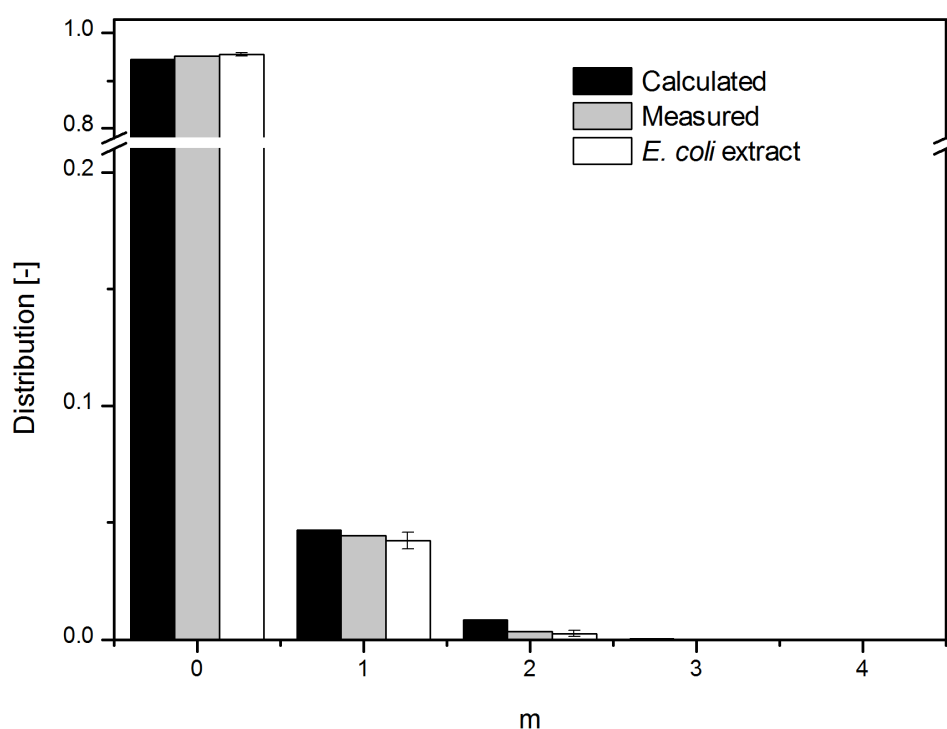


Figure 2.84: Calculated and measured isotopic distribution of aspartic acid standards.

Results are reported as mean \pm 1 SD.

As can be seen for aspartic acid, the calculated isotopic distribution as well as the distribution measured for the analytical standard of aspartic acid and the extracted aspartic acid are in accordance with each other. The measured distributions show a slight decrease in the m_2 fragment, which can originate from the low concentration of the analyte. If the concentration

of the analyte is already below the limit of quantification, the error of the measurement rises.

As shown for aspartic acid, the MS-method was used to measure unlabeled chemical standards to confirm a natural isotopic distribution and therefore support the developed method. Furthermore, *E.coli* cells grown in M9-N* minimal medium with glucose as carbon source were extracted according to the fast filtration metabolomics protocol^[102] and compared to the theoretical predicted isotopic distribution and the standard measurement (Figure 2.85).

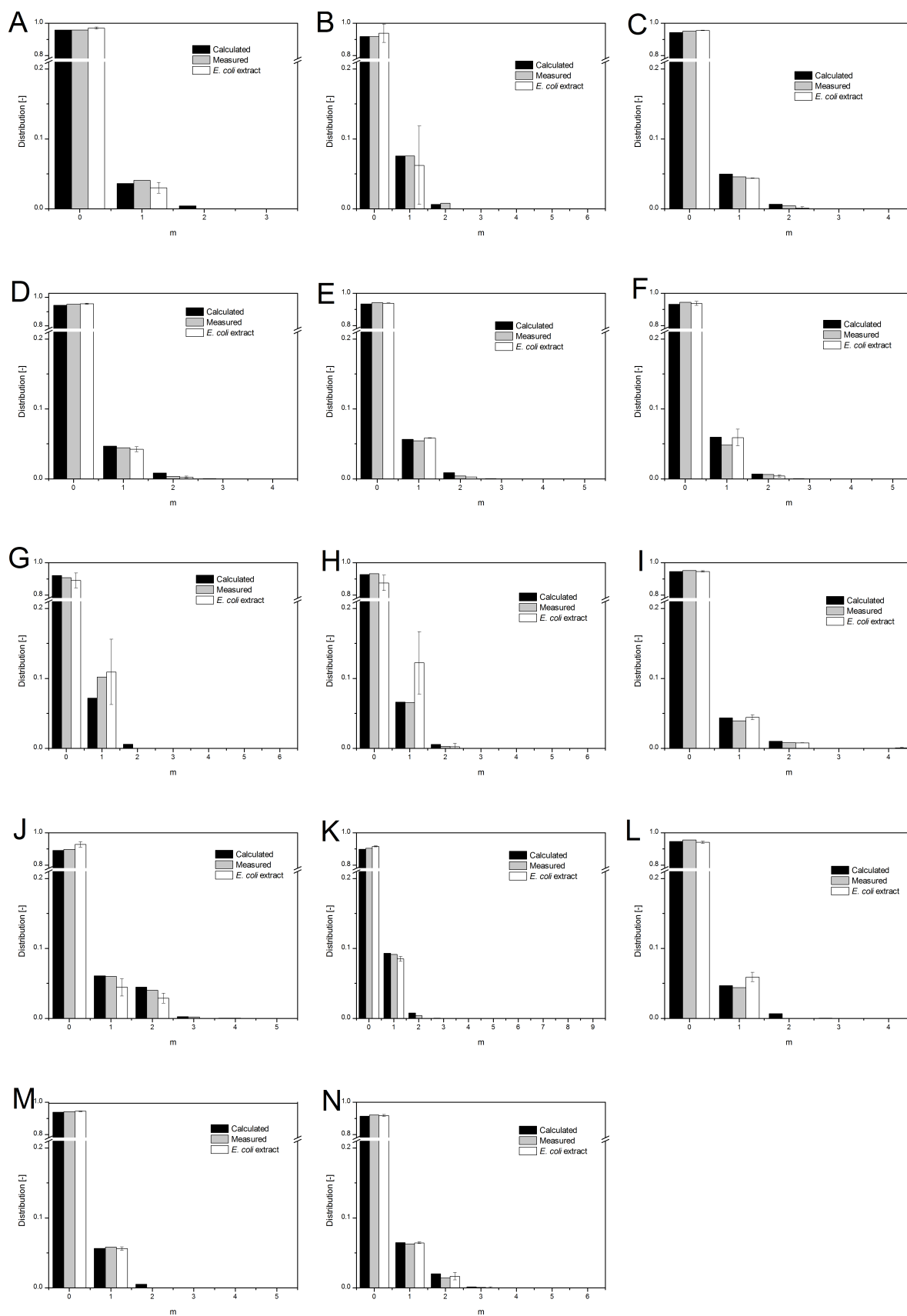


Figure 2.85: Calculated and measured isotopic distribution of chemical standards.

A: alanine; B: arginine; C: asparagine; D: aspartic acid; E: glutamic acid; F: glutamine; G: histidine; H: isoleucine; I: malic acid; J: methionine; K: phenylalanine; L: threonine; M: valine; N: 6-PG. Results are reported as mean \pm 1 SD.

The calculated isotopic distribution matched very well with the measured isotopic distribution of standards using the established MS/MS method described in the experimental section (Tables 3.28-3.30). Even though the *E.coli* extracts contained a matrix with many different metabolites, the isotopic distribution for many of the selected compounds was still precise in comparison to both, the theoretical predicted and the measured distribution of standard compounds. For isoleucine (H) and threonine (L), the isotopic distribution of the *E. coli* extracts slightly differed from the calculated and analytical standard distributions. This result can be explained with interfering matrix effects of the extract, which is rich in many different metabolites. These analytes might not be suitable for measurement of isotopic distributions with a triple quadrupole mass detector.

2.4.7 Conclusion and outlook

In this chapter, a system for enhancing DHAP production in *E. coli* by phosphorylating DHA was investigated. Three different models were developed from the Ec_iJR904 model by adding Dhak and/or the cascade reactions. Pareto analyses were performed for the comparison of the different functionalities. The modeling revealed that DhaK could have a positive influence on both, the growth of *E. coli* and the performance of the artificial cascade, which would lead to the optimization on the biocatalyst level. The production of DhaK showed uptake of DHA and increased DHAP levels over three hours after DHA addition. The introduction of DhaK into *E. coli* was an improvement on the catalyst level. However, the rise in intracellular DHAP concentrations occurred only in the growing state, which revealed the optimal conditions on the cultivation level and also for further process development. The modeling of intracellular fluxes with gained parameters from laboratory experiments with the DhaK and *E. coli* wt strains showed a rerouting of the glycolysis. However, this result needs to be confirmed with ^{13}C -MFA. For this reason, an HPLC method for measuring isotopomer distributions was set up and successfully validated. In the future, ^{13}C -MFA can provide information about constraints for the modeled system and improve the quality of *in silico* experiments. Nevertheless, DhaK was found to be an important tool for future aldol reactions *in vivo*.

2.5 Conclusion and outlook of the thesis

The strategies to optimize biotransformations on different levels - biocatalyst level, fermentation/cultivation level, the process and DSP level - were successfully applied in this thesis. In the first chapter, all levels of optimization were addressed. On the biocatalyst level, a suitable enzyme was chosen to have a non-stereoselective biotransformation of ketone **1**. The enzyme expression system was changed to facilitate the cultivation in minimal medium, which would have been challenging with the previously used L-leucine auxotrophic *E. coli* TOP10 strain. On the fermentation/cultivation level, the minimal medium was optimized to support higher cell densities, eventually leading to nitrogen-limited conditions to obtain non-growing cells. Non-growing conditions assured a high oxygen saturation of the medium for the oxygen-consuming Baeyer-Villiger oxidation. On the process level, a multi-gram scale CPDMO biotransformation with the application of SFPR concept was established. One drawback of the SFPR concept was the deposition of the applied resin on the reactor walls, which can be easily solved in future bioprocesses by application of a diffusable container. The downstream processing was optimized by a continuous extraction of the applied resin material with adsorbed product on the surface. The following recrystallization of the extract yielded high purity lacton for further chemical steps towards the nylon-9 monomers.

In the second chapter, the optimization strategies on the biocatalyst level were investigated. In contrast to the first chapter, the biocatalyst level was more complex, as the *E. coli* cell expressed three non-related enzymes, which formed a linear cascade. The cascade produced enantiomerically pure lactones from racemic non-saturated alcohols in three steps with an alcohol dehydrogenase (ADH), an enoate reductase (ERED) and a Baeyer-Villiger monooxygenase (BVMO), the cyclohexanone monooxygenase (CHMO). This cascade was coupled only *via* the redox metabolism to the *E. coli* host. The approach of kinetic modeling was used to identify the bottleneck of the lactone production by the whole-cell biocatalyst. Modeling and further laboratory experiments revealed the CHMO to be the bottleneck of the lactone producing system. Follow-up experiments showed that FAD-dependent CHMO and also the FMN-dependent ERED exhibited lower activities due to a lack of FAD and FMN, a precursor for FAD. In this case, two steps of the cascade would benefit from a FAD overproducing microorganism.

In the third chapter, possible limitations and optimization strategies on the biocatalyst level were investigated. As a model enzyme, the last step of the cascade discussed in chapter 2, the CHMO, was applied. The limitations for the enzymatic activity in *E. coli* were identified by measuring the CHMO concentration, the CHMO activity and concentrations of intracellular key metabolites leading to either FAD or NADPH. The concentrations of both cofactors were the main contributing factors for a high CHMO activity. The proposed optimization was a change of the host to a FAD overproducing microorganism, possibly with further modifications to drastically increase the intracellular FAD concentrations, which are crucial for CHMO activity *in vitro* and *in vivo*.

In the fourth and last chapter, a non-linear cascade optimization was performed. In contrast to the linear cascade from chapter three, the cascade was coupled to the central carbon metabolism of *E. coli* by an aldol reaction with dihydroxyacetone phosphate (DHAP), an intermediate produced in the glycolysis of the cell. The cascade consisted of an ADH, an aldolase and a phosphatase. Since the product yield is dependent on the fluxes through the central carbon metabolism, a different modeling approach was chosen: stoichiometric modeling. This modeling was applied at steady-state conditions and required little information about the kinetic constraints of the system. This strategy mostly depended on the stoichiometric network of *E. coli*. At first, the prerequisites for an aldol reaction *in vivo* were identified by comparing a system with and without dihydroxyacetone kinase (DhaK), an enzyme which produced DHAP from dihydroxyacetone. Stoichiometric modeling and metabolomics measurements revealed an increase in intracellular DHAP concentrations when DhaK is produced. However, the comparison of process modes revealed, that was only the case, if growing-conditions were applied. Furthermore, pareto analysis with a cascade with and without DhaK predicted benefits for the cascade reaction, if DhaK is simultaneously produced in *E. coli*. As a future control mechanism for the modeling results, an HPLC method for ^{13}C -MFA isotopomer measurements was established and validated.

The combination of the different methods applied in this thesis - modeling, metabolomics and optimizational tools for process design- should furthermore be used to facilitate bio-transformations in living systems and optimize processes on the different levels discussed in this thesis. Further studies should focus more on establishment of metabolic flux analysis

protocols to promote a more realistic stoichiometric modeling with measured constraints. Additionally, use of dynamic stoichiometric models could even combine the modeling of processes with the modeling of intracellular fluxes, ultimately aligning cause and effect, and simplifying the optimization of processes in terms of productivity.

3 Experimental Part

3.1 Chemicals and materials

Unless otherwise noted, chemicals were purchased from commercial suppliers and used without further purification.

3.2 Bacterial strains, culture conditions and plasmids

All materials and media compounds were sterilized by autoclaving at 121 °C for 20 minutes unless otherwise stated for heat-sensitive aqueous solutions. These were sterilized by filtration either through 0.20 μm sterile syringe filters (VWR) for small volumes or 0.20 μm Bottle Top Filters for big volumes up to 1 L (Nalgene, Thermo Fisher Scientific) under sterile conditions.

3.2.1 Lysogeny Broth (LB) medium

The LB medium contained the following substances: 10 g L⁻¹ bacto-peptone, 5 g L⁻¹ yeast extract and 10 g L⁻¹ sodium chloride.^[205] For LB plate preparation, 15 g L⁻¹ agar were added to the solution prior to autoclaving. For LB plate preparation, the required antibiotic was added in the corresponding concentration prior to pouring the plates at approximate 60 °C. For one standard petri dish, 25 mL LB-agar solution were required.

3.2.2 Teriffic Broth (TB) medium

The TB medium contained the following substances: 12 g L⁻¹ tryptone, 24 g L⁻¹ yeast extract, 16.4 g L⁻¹ K₂HPO₄ and 2.3 g L⁻¹ KH₂PO₄.^[206]

3.2.3 LB-0.8G medium

The LB-0.8G medium contained the LB components and was autoclaved with 929 mL for preparing 1 L medium. After autoclaving, the missing volume was filled up with 20 mL L⁻¹ 40 % glucose solution (final concentration 0.8 % glucose) , 1 mL L⁻¹ 1 M MgSO₄ and 50 mL L⁻¹ 20x NPS salts (Table 3.1).^[37]

Table 3.1: 20x NPS salts

Compound	Concentration
(NH ₄) ₂ SO ₄	66.0 g L ⁻¹
KH ₂ PO ₄	136.0 g L ⁻¹
Na ₂ HPO ₄	142.0 g L ⁻¹

3.2.4 Autoinduction medium (AIM)

The autoinduction medium contained the LB components and was autoclaved with 929 mL for preparing 1 L medium. After autoclaving, the missing volume was filled up with 20 mL 50x 5052-solution (Table 3.2), 1 mL L⁻¹ 1 M MgSO₄ and 50 mL L⁻¹ 20x NPS salts (Table 3.1).^[207]

Table 3.2: 50x 5052

Compound	Concentration
glycerol	250.0 g L ⁻¹
glucose	25.0 g L ⁻¹
a-lactose	100.0 g L ⁻¹

3.2.5 M9 medium

The M9 medium main solution contained the substances presented in Table 3.3. The resting cell - M9 medium was prepared accordingly without addition of (NH₄)₂SO₄ to the main solution. The modified M9 medium (M9-N*) was prepared accordingly with triplication of (NH₄)₂SO₄ (2.4 g L⁻¹) and MgSO₄ (3 mL L⁻¹ of 1 M solution).^[206]

Table 3.3: M9 medium main solution

Compound	Concentration
$(\text{NH}_4)_2\text{SO}_4$	0.8 g L^{-1}
NaCl	0.5 g L^{-1}
KH_2PO_4	3.0 g L^{-1}
$\text{Na}_2\text{HPO}_4 \times 2\text{H}_2\text{O}$	7.5 g L^{-1}
1 M MgSO_4	1 mL L^{-1}
0.1 M CaCl_2	1 mL L^{-1}
0.1 M $\text{FeCl}_3 \times 6 \text{ H}_2\text{O}$	0.6 mL L^{-1}
1 mM thiamine $\times \text{HCl}$	2 mL L^{-1}
trace element solution	10 mL L^{-1}

The components in the lower part of Table 3.3 were sterilized separately by filtration and then added to the main solution. Filter-sterilized glucose was added to a final concentration of 20 g L^{-1} . The composition of the trace element solution is depicted in Table 3.4.

Table 3.4: $100 \times$ M9 trace element solution

Compound	Concentration
$\text{ZnSO}_4 \times 7 \text{ H}_2\text{O}$	0.18 g L^{-1}
$\text{CuCl}_2 \times 2 \text{ H}_2\text{O}$	0.12 g L^{-1}
$\text{MnSO}_4 \times \text{H}_2\text{O}$	0.12 g L^{-1}
$\text{CoCl}_2 \times 6 \text{ H}_2\text{O}$	0.18 g L^{-1}
H_3BO_3	0.03 g L^{-1}
$\text{NaMoO}_4 \times 2 \text{ H}_2\text{O}$	0.025 g L^{-1}
$\text{Na}_2 - \text{EDTA} \times 2 \text{ H}_2\text{O}$	0.084 g L^{-1}

3.2.6 Verduyn medium

The composition of the Verduyn medium for yeast cultivation was as follows: 771 mL L^{-1} 0.133 M filter-sterilized KH-phthalate-water pH 5, 200 mL L^{-1} $5 \times$ salt solution (Table

3.5), 10 mL L⁻¹ 100 × trace elements solution, 1 mL L⁻¹ vitamin solution and 20 mL L⁻¹ filter sterilized 50% glucose solution (final concentration in the medium 10 g L⁻¹).^[208]

Table 3.5: 5 × salt solution

Compound	Concentration
(NH ₄)SO ₄	25 g L ⁻¹
KH ₂ PO ₄	15 g L ⁻¹
2.5 MgSO ₄ × 7 H ₂ O	2.5 L ⁻¹

The 5 × salt solution (Table 3.5) was autoclaved.

Table 3.6: 100 × trace element solution

Compound	Concentration
EDTA	0.15 g L ⁻¹
ZnSO ₄ × 7 H ₂ O	0.45 g L ⁻¹
CoCl ₂ × 6 H ₂ O	0.03 g L ⁻¹
MnCl ₂ × 4 H ₂ O	0.10 g L ⁻¹
CuSO ₄ × 5 H ₂ O	0.03 g L ⁻¹
CaCl ₂ × 2 H ₂ O	0.45 g L ⁻¹
FeSO ₄ × 7 H ₂ O	0.30 g L ⁻¹
NaMoO ₄ × 2 H ₂ O	0.04 g L ⁻¹
H ₃ BO ₃	0.10 g L ⁻¹
KI	0.01 g L ⁻¹

The 100 × trace element solution (Table 3.6) was filter-sterilized and stored at 4 °C.

Table 3.7: 1000 × vitamin solution

Compound	Concentration
Biotin	0.05 g L ⁻¹
Ca-pantothenate	1.00 g L ⁻¹
Nicotinic acid	1.00 g L ⁻¹
Inositol	25.0 g L ⁻¹
Pyridoxine	1.00 g L ⁻¹
<i>p</i> -Aminobenzoic acid	0.20 g L ⁻¹
Thiamine	1.00 g L ⁻¹

The 1000 × vitamin solution (Table 3.7) was filter-sterilized and stored at 4 °C.

3.2.7 Antibiotics and inducers

Antibiotics and inducers were usually kept as concentrated stocks at -20 °C and added prior to inoculation to the medium (Table 3.8).

Table 3.8: Antibiotics and inducers

Type	Compound	Stock concentration	Working concentration
Antibiotic	Ampicillin	50 mg mL ⁻¹	100 μm mL ⁻¹
	Kanamycin	50 mg mL ⁻¹	50 μm mL ⁻¹
Inducer	IPTG	0.1 M	varying concentrations
	Rhamnose	20 g L ⁻¹	2 g L ⁻¹

3.2.8 Permanent cultures and working cryo stocks

The desired bacterial strain was inoculated from a single colony and this preculture in this desired medium was grown overnight. The main culture was inoculated in a dilution of 1:100 with the preculture and grown until the late exponential growth phase. The culture was then diluted 1:2 with sterile 500 g L⁻¹ glycerol in water in a total volume of 1 mL and stored in cryo vials at -80 °C. When used as working cryo stocks, the cultures were used

for inoculation of precultures in a ratio of 1:100. The stocks could be used up to 5 times without loss in viability.

For yeast permanent cultures the culture was cultivated according to the described protocol except for mixing the culture in a dilution of 1:3 with sterile 500 g L⁻¹ glycerol in water in a total volume of 1 mL.

3.3 General methods

3.3.1 Agarose gel electrophoresis

Table 3.9: 50 × TAE buffer

Compound	Concentration
TRIS	242 g L ⁻¹
Glacial acetic acid	57.1 mL L ⁻¹
0.5 M EDTA pH 8.0	100 mL L ⁻¹

Agarose gels were prepared with 1 % agarose dissolved in 1 × TAE buffer, heated up in the microwave until the agarose was completely dissolved. After a short cooling period, 1 × SYBR Safe stain was added from a 10000 × SYBR Safe stock and the gel was poured. The DNA samples were diluted with 6 × DNA loading dye so that the samples contained 1 × loading dye and loaded on the gel. The 6 × DNA loading dye had the following composition:

Table 3.10: 6 × DNA loading dye for agarose gel electrophoresis

Compound	Concentration
30 % glycerol solution	300 mL L ⁻¹
0.25 % bromphenol blue solution	500 mL L ⁻¹

3.3.2 Chemical transformation of plasmids into *E. coli* cells

Unless otherwise noted, all steps are performed on ice under the sterile hood. All solutions must be sterile. Consumables and other materials must be autoclaved prior to use if not

sterile upon purchase.

The day before the transformation, a 4 mL culture in LB medium (containing the appropriate antibiotic if necessary) was prepared and cultivated over night at 37 °C and 200 rpm in a preculture tube (total volume 14 mL). The next day, a fresh 1 % (v/v) culture from the over night culture in LB medium (containing the appropriate antibiotic if necessary) was inoculated and cultivated at 37 °C and 200 rpm in a baffled shake flask until the OD₅₉₀ reached a value between 0.2 and 0.4. At that point, the culture was dispensed in 1.5 mL aliquots, centrifuged at 5000 rpm and 4 °C for 10 minutes. The supernatant was discarded and the cells were resuspended in 0.5 mL ice cold 0.1 M CaCl₂. The cells were incubated on ice for 15 minutes and then centrifuged again at 5000 rpm and 4 °C for 10 minutes. The supernatant was discarded and the cells were resuspended in 100 μL ice cold 0.1 M CaCl₂. At this stage, 1 μL of plasmid DNA (50-100 ng) was added and the cells were incubated on ice for 1 hour. Subsequently, the heat shock was performed at 42 °C for 1 minute and the cells were afterwards again incubated on ice for 2 minutes. After that, 500 μL of fresh and pre-warmed LB medium were added to the transformation mixture and incubated at 37 °C and 550 rpm for one hour in the Eppendorf thermomixer comfort. Thereafter, 100 μL of the transformation mixture were plated on an LB agar plate with an appropriate selection marker and incubated over night at 37 °C. The resulting colonies were picked from the plate, and used for inoculation of precultures. A cryo stock of every preculture was prepared and the rest of the preculture was used for plasmid isolation with a plasmid isolation Kit from Thermo Scientific.

3.3.3 SDS-PAGE

The SDS page was performed for qualitative control of expression of proteins in cell-free extracts and quality control for purified proteins.^[209]

Table 3.11: SDS gel composition for one gel

Compound	Resolving gel	Stacking gel
Buffer	1.000 mL 1.5 M Tris-HCl, pH 8.8	0.750 mL 0.5 M Tris-HCl, pH 6.8
30 % acrylamide solution	1.600 mL	0.390 mL
dH ₂ O	1.360 mL	1.830 mL
10 % SDS solution	0.040 mL	0.030 mL
10 % APS solution	0.020 mL	0.015 mL
TEMED	0.002 mL	0.003 mL

TEMED and the 10 % APS solution were added freshly prior to pouring the gel, since they induce the polymerization process. The resolving gel was poured first and covered with a layer of 2-propanol. After the polymerization was complete, the 2-propanol was removed and the stacking gel was poured.

The composition of the required solutions is described below.

Table 3.12: 30 % acrylamide solution

Compound	Concentration
acrylamide	292 g L ⁻¹
N'N'-bis-methylene-acrylamide	8.0 g L ⁻¹

The 30 % acrylamide solution (Table 3.12) was filtered and stored in a dark bottle at 4 °C in the dark for a maximum of 30 days.

The 10 % (w/v) SDS solution was prepared by dissolving the SDS with gentle stirring in 90 % of the total volume since it is foam-forming. After the SDS was dissolved, the solution was filled up to 100 % of the total volume.

The 10 % (w/v) APS solution by dissolving the ammonium persulfate in water and prepare aliquots which were stored at -20 °C and thawed prior to usage.

Table 3.13: SDS reducing buffer: 9.5 mL stock

Compound	Amount
dH ₂ O	3.55 mL
0.5 M Tris-HCl, pH 6.8	1.25 mL
Glycerol	2.50 mL
10 % SDS solution	2.00 mL
0.5 % (w/v) bromphenol blue	0.20 mL

The SDS reducing buffer was stored at room temperature. For sample preparation, 950 μL SDS reducing buffer were mixed with 50 μL β -Mercaptoethanol. The sample was diluted at least 1:2 with sample buffer, heated at 95 °C for 4 minutes and then cooled on ice prior to load the SDS gel.

Table 3.14: 10 \times Electrode (Running) Buffer, pH 8.3

Compound	Concentration
Tris base	30.3 g L ⁻¹
Glycine	144.0 g L ⁻¹
SDS	10.0 g g L ⁻¹

The different components were dissolved in water. There was no need for pH adjustment, since the buffer already had the desired pH of 8.3. The buffer was stored at 4 °C. In case of precipitation the buffer was warmed to room temperature before use. For SDS Page the buffer was diluted 1:10 with dH₂O for each run and mixed thoroughly before application. For the SDS-PAGE, 10 μL to 20 μL of the sample was loaded into one SDS gel pocket. PageRuler Prestained Protein Ladder from Thermo Scientific (10-180 kDa) was used for protein size estimation (5 μL per lane). The protein separation was performed with 12.5 mA per gel for the stacking phase and 25 mA per gel for the separation phase. SimplyBlue™ SafeStain was used for visualisation of protein bands and applied according to the microwave method. The gels were stored in 20 % NaCl until scanning.

3.3.4 OD measurements

Optical density was measured at 590 nm in 10 mm cuvettes with a Colourwave CO7500 colorimeter (Biochrom, Cambridge, UK): values over OD = 1.5 were determined from 1:10 dilutions with sterile, medium at rt.

3.3.5 OTR/CTR calculations *via* the gas-balancing method

Oxygen transfer rate (OTR) and carbon dioxide transfer rate (CTR) were calculated according to the following equations 3.1 and 3.2^{[210] [211] [212]}

$$OTR = \frac{Q}{V}(c_{O_2}^{in} - c_{O_2}^{out}) \quad (3.1)$$

$$CTR = \frac{Q}{V}(c_{CO_2}^{in} - c_{CO_2}^{out}) \quad (3.2)$$

With Q being the oxygen gas flow, V being the volume of the bioreactor and c_{in} and c_{out} being the carbon and oxygen concentrations measured at bioreactor inlet and outlet.

Calculation of OTR and CTR by gas balancing method from the gas composition of inlet and outlet gas of the reactor:

These equations are derived from simple balancing of the main components in air: nitrogen, oxygen and carbon dioxide. For molecular nitrogen the transfer rate (NTR) equals zero 3.3, since it is neither consumed nor produced during the cultivation of *E. coli*:

$$NTR = \frac{1}{V_{mo}}(q_{in}y_{N_2}^{in} - q_{out}y_{N_2}^{out}) = 0 \quad (3.3)$$

This can be transformed to 3.7:

$$q_{out} = q_{in} \frac{y_{N_2}^{in}}{y_{N_2}^{out}} \quad (3.4)$$

Since the sum of all fractions in the gas should equal 1, the following equations can be derived (3.5, 3.6):

$$y_{N_2}^{in} = 1 - y_{O_2}^{in} - y_{CO_2}^{in} \quad (3.5)$$

$$y_{N_2}^{out} = 1 - y_{O_2}^{out} - y_{CO_2}^{out} \quad (3.6)$$

Both equations (3.5, 3.6) can be introduced into the equation for q_{out} (3.7):

$$q_{out} = q_{in} \frac{1 - y_{O_2}^{in} - y_{CO_2}^{in}}{1 - y_{O_2}^{out} - y_{CO_2}^{out}} \quad (3.7)$$

Which itself can be introduced into the general equation for the oxygen balance 3.8:

$$OTR = \frac{1}{V_{mo}} (q_{in} y_{O_2}^{in} - q_{out} y_{O_2}^{out}) \quad (3.8)$$

Leading to 3.9:

$$OTR = \frac{q_{in}}{V_{mo}} \left(y_{O_2}^{in} - \frac{1 - y_{O_2}^{in} - y_{CO_2}^{in}}{1 - y_{O_2}^{out} - y_{CO_2}^{out}} y_{O_2}^{out} \right) \quad (3.9)$$

The CTR equation is derived by following the same pattern, leading to 3.10:

$$OTR = \frac{q_{in}}{V_{mo}} \left(y_{CO_2}^{out} \frac{1 - y_{O_2}^{in} - y_{CO_2}^{in}}{1 - y_{O_2}^{out} - y_{CO_2}^{out}} - y_{CO_2}^{in} \right) \quad (3.10)$$

Table 3.15: Parameters in off-gas analysis calculation

Parameter	Description	Unit
V_{mo}	molar gas volume at standard conditions	L mol ⁻¹
q_{in}	specific aeration rate at inlet	vvm
q_{out}	specific aeration rate at outlet	vvm
y_x^{in}	X mole fraction in inlet gas	mol mol ⁻¹
y_x^{out}	X mole fraction in outlet gas	mol mol ⁻¹

3.4 Preparation of labeled ¹³C-internal standard for metabolomics

3.4.1 Yeast fermentation with labeled ¹³C - glucose

The ¹³C-internal standard was prepared by quenching and extraction of whole-cell broth of a *Saccharomyces cerevisiae* FY4 fermentation. Throughout the whole cultivation process for production of the ¹³C-internal standard fully labeled ¹³C-glucose was applied instead of the unlabeled glucose. The test fermentations for process parameter estimation were performed

with unlabeled glucose. The preculture was cultivated in Verduyn medium over night in a volume of 30 mL in a 500 mL non-buffed flask at 30 °C and 350 rpm. The preculture was inoculated 1:100 from a permanent culture of FY4 in Verduyn medium. 25 mL of preculture were used for inoculation of the bioreactor with a total volume of 3 L and a filling volume of 475 mL (Infors, Switzerland). The total filling volume after preculture addition was 500 mL. The reactor was gassed with 3 VVM for analytical reasons, since the infrared offgas-analysis (Typ THW 2008.05, Dr. Marino M \ddot{A} $\frac{1}{4}$ ller Systems AG, Esslingen, Switzerland) requires a certain gas-flow. The off-gas analysis was used to observe the different growth stages e.g. the growth on glucose and the production of ethanol and the growth on ethanol. After several hours of growth on ethanol, the culture was spiked with a final concentration of 2.5 g L⁻¹ glucose and harvested 30 minutes after the glucose addition.

3.4.2 Quenching procedure of the fermentation broth

The 500 mL fermentation broth were sampled in 100 mL portions each into 400 mL -40 °C quenching solution. The quenching solution consisted out of 60:40 methanol/water with 10 mM ammonium acetate. The pH was adjusted to 7.5 with 25 % ammonium hydroxide solution. The quenched broth was transferred into six centrifugation flasks (500 mL volume) and centrifuged (Centrifuge Sigma 6K15, 4000 × g, 15 minutes, -20 °C). The supernatant was discarded and the six resulting pellets were each resuspended in 16 mL quenching solution, pooled, vortexed and were aliquoted in volumes of 20 mL into 50 mL Falcon tubes. After another centrifugation step (4000 × g, 15 minutes, -20 °C), the supernatant was again discarded and the pellets were stored at -80 °C until extraction. All components during the quenching procedure were strictly kept below -20 °C.

3.4.3 Extraction of labeled biomass

For the extraction step, extraction solution with 75:25 ethanol/water with 10 mM ammonium acetate pH 7.0 was prepared. The pH was adjusted with 25 % ammonium hydroxide solution. 5 × 20 mL extraction solution in 50 mL Falcon tubes were preheated in a water bath at 78 °C. The quenched pellets were preheated in a cryostat to -20 °C for the extraction procedure. For the extraction, 20 mL of preheated extraction solution were poured onto the

pellet of the quenched sample and immediately resuspended with a 25 mL pipette. The sample was incubated in the water bath at 78 °C for three minutes while being vortexed every 60 seconds. The resulting extracts were incubated in the cryostat at -20 °C until centrifugation (4000 × g, 15 minutes, -20 °C). After centrifugation, all the extracts were pooled, aliquoted in 500 μL and stored at -80 °C.

3.5 Preparation of the metabolomics MonsterMix for calibration of the LC-MS/MS

For the LC-MS/MS calibration for metabolomics measurements, a mixture of intracellular metabolites in a concentration of 100 μM was prepared (MonsterMix) (Tables 3.16, 3.17, 3.18). The 50 mL MonsterMix was aliquoted in 50 μL or 500 μL aliquotes and stored at -80 °C. For LC-MS/MS calibration, a mixture of cofactors (NAD⁺, NADP⁺, NADH and NADPH) in the same concentration as the calibration points was added freshly to the MonsterMix-dilutions from separated 10 mM stocks in water. These stocks were controlled in the photometer if the concentration remained constant. If not, the addition volume was adjusted so that the final concentration of the cofactors was correct. ¹³C-internal standard was added in a ratio of 1:1 to the desired final volume of the calibration standard. The samples were dried in a vacuum concentrator at 30 °C and stored at -80 °C until measurement. The samples were resuspended in water, centrifuged for 3 minutes at 14 000 × g and measured. The MRMs of the LC-MS/MS method are depicted in Table 3.19.

Table 3.16: Metabolomics MonsterMix for LC-MS/MS calibration (1/3)

Order No	Short name	Chemical name	Purity	Amount in 50 mL	Stock
P7877-100MG	6PG	6-Phosphogluconic acid trisodium salt ($\geq 97\%$ (enzymatic))	97	10.37 μL	17 mg/100 μL
A2056-5MG	AcCoA	Acetyl coenzyme A sodium salt ($\geq 93\%$ (HPLC), powder)	93	19.56 μL	5 mg/100 μL
01905-250MG-F	ADP	Adenosine 5'-diphosphate ($\geq 95\%$ (HPLC))	95	18.14 μL	12.4 mg/100 μL
79248-5X2ML	AA	Amino Acids Mix Solution	100	2 mL	2.5 mM
A1752-5G	AMP	Adenosine 5'-monophosphate sodium salt, (from yeast, ($\geq 99\%$))	99	10.26 μL	17.1 mg/100 μL
A2383-1G	ATP	Adenosine 5'-triphosphate disodium salt hydrate. Grade I, $\geq 99\%$, from microbial	99	20.54 μL	27.1 mg/200 μL
A9501-1G	cAMP	Adenosine 3',5'-cyclic monophosphate ($\geq 98.5\%$ (HPLC), powder)	98.5	1.67 mg	-
W302600-SAMPLE	citrate	Sodium citrate dihydrate ($\geq 99\%$, FG)	99	8.64 μL	17.2 mg/100 μL
D7137-5MG	DHAP	Dihydroxyacetone phosphate dilithium salt ($\geq 93\%$ (enzymatic))	93	19.56 μL	5mg/100 μL

Table 3.17: Metabolomics MonsterMix for LC-MS/MS calibration (2/3)

Order No	Short name	Chemical name	Purity	Amount in 50 mL	Stock
G7879-500MG	G6P	D-Glucose 6-phosphate sodium salt (Sigma Grade, crystalline)	98	9.59 μ L	15 mg/100 μ L
F6803-10MG	FBP	D-Fructose 1,6-bisphosphate trisodium salt hydrate ($\geq 98\%$ (TLC))	98	62.13 μ L	10 mg/300 μ L
F1506-25MG	fumarate	Sodium fumarate dibasic	99	9.18 μ L	8.8 mg/100 μ L
G6918-100ML	glucose	Glucose Standard Solution (1 mg/mL)	100	900.78 μ L	1 mg/mL
46940-U	malate	D-Malic acid (analytical standard)	100	11.17 μ L	6 mg/100 μ L
860077-250MG	PEP	Phospho(enol)pyruvic acid monopotassium salt, ($\geq 99\%$)	99	11.57 μ L	9 mg/100 μ L
W327700-SAMPLE-K	succinate	Disodium succinate ($\geq 98\%$)	98	8.91 μ L	9.2 mg/100 μ L
P8877-10MG	3PG	D-(-)-3-Phosphoglyceric acid disodium salt ($\geq 93\%$, powder)	93	37.08 μ L	10 mg/300 μ L
79470-50MG	2 PG	D(+)-2-Phosphoglyceric acid sodium salt hydrate	75	16.31 μ L	10.3 mg/100 μ L
A0542-25G	Asn	L-Asparagine Monohydrate, $\geq 99\%$ (TLC)	99	0.67 mg	-
83875-250MG	R5P	D-Ribose 5-phosphate disodium salt dihydrate, $\geq 99\%$ (TLC)	99	9.73 μ L	16.1 mg/100 μ L
G3126-100G	Gln	L-Glutamine, $\geq 99\%$ (TLC)	99	0.74 mg	-

Table 3.18: Metabolomics MonsterMix for LC-MS/MS calibration (2/3)

Order No	Short name	Chemical name	Purity	Amount in 50 mL	Stock
G7127-10MG	GDP	Guanosine 5'-diphosphate sodium salt, (Type I, $\geq 96\%$ (HPLC))	96	46.16 μL	10 mg/200 μL
G9002-10MG	GTP	Guanosine 5'-triphosphate tris salt, 95% (HPLC), powder	95	139.98 μL	10 mg/300 μL
T0254-1G	Trp	L-Tryptophan	98	1.04 mg	-
G8377-500MG	GMP	Guanosine 5'-monophosphate disodium salt hydrate, from yeast, $\geq 99\%$	99	14.48 μL	14.2 mg/100 μL
94124-10MG	GAP	sn-Glycerol 3-phosphate lithium salt	95	27.18 μL	10 mg/300 μL
F6625-100MG	FAD	Flavin adenine dinucleotide disodium salt hydrate, 95%	95	73.62 μL	17.8 mg/300 μL
555682	Riboflavin	Riboflavin fÄ¼r biochemische Zwecke	99	1.9 mg	-

Table 3.19: MRM precursor ions and fragments for metabolomics measurement

Compound	Precursor (m/z)	Fragments (m/z)			Mode
		1	2	3	
¹³ C NADH	687.2	670.1	530.5	-	positive
¹² C NADH	666.2	649.1	514.05	-	positive
¹³ C Iso-Leucine	137.9	91.1	45.1	-	positive
¹² C Iso-Leucine	131.9	86.1	44.1	-	positive
¹³ C Alanine	92.9	45.2	46	29	positive
¹² C Alanine	89.9	44.2	45	28	positive
¹³ C Glutamine	151.7	88.05	135.05	-	positive
¹² C Glutamine	146.7	84.05	130.05	-	positive
¹³ C Arginine	180.7	61.1	121.1	-	positive
¹² C Arginine	174.7	60.1	116.1	-	positive
¹³ C Serine	109.2	91.1	73.15	-	positive
¹² C Serine	106.2	88.1	70.15	-	positive
¹³ C Histidine	161.6	115.05	87.05	-	positive
¹² C Histidine	155.6	110.05	83.05	-	positive
¹³ C Asparagine	136.8	76.05	90	-	positive
¹² C Asparagine	132.8	74.05	87	-	positive
¹³ C Lysine	152.9	89.1	136.1	-	positive
¹² C Lysine	146.9	84.1	130.1	-	positive
¹³ C NAD	684.7	141	438.05	-	positive
¹² C NAD	663.7	136	428.05	-	positive
¹³ C Aspartate	136	91.05	119.05	-	negative
¹² C Aspartate	132	88.05	115.05	-	negative
¹³ C Glutamate	153.2	88.05	60.05	-	positive
¹² C Glutamate	148.2	84.05	56.05	-	positive
¹³ C Malate	137	119	92.1	-	negative
¹² C Malate	133	115	89.1	-	negative
¹³ C Fumarate	119	74.1	28.15	-	negative
¹² C Fumarate	115	71.1	27.15	-	negative
¹³ C AMP	357.9	141.05	97.05	-	positive
¹² C AMP	347.9	136.05	97.05	-	positive
¹³ C GMP	373.9	157	97.05	-	positive
¹² C GMP	363.9	152	97.05	-	positive
¹³ C NADPH	767	750	141	313.05	positive
¹² C NADPH	746	729	136	302.05	positive
¹³ C 3-PG	188	97	79.1	-	negative
¹² C 3-PG	185	97.1	79.1	-	negative
¹³ C ADP	437.7	141.05	358.05	-	positive
¹² C ADP	427.7	136.05	348.05	-	positive
¹³ C F-1.6-BP	344.9	96.85	79.1	-	negative
¹² C F-1.6-BP	338.9	96.85	79.1	-	negative
¹³ C GDP	453.9	157	97	-	positive
¹² C GDP	443.9	152	97	-	positive
¹³ C ATP	518	145.95	438	97.05	positive
¹² C ATP	508	135.95	428	97.05	positive
¹³ C GTP	534	157.05	97.05	-	positive
¹² C GTP	524	152.05	97.05	-	positive
¹³ C FAD	813.05	358	141.15	456.05	positive
¹² C FAD	786.05	348	439.05	136.15	positive

3.6 Biocatalytic oxidation of nylon-9 monomer by CPDMO

3.6.1 Cultivation media

The M9 medium was used in different variations (Table 3.20):

Table 3.20: Variations in M9 medium for CPDMO experiments

Compound	Concentration
$(\text{NH}_4)_2\text{SO}_4$	0.8 or 2.4 g L ⁻¹
1 M MgSO ₄	1 or 3 mL L ⁻¹
Glucose/Glycerol	20 g L ⁻¹

For cultivation of the auxotrophic strain *E. coli* TOP10 with pBAD_cpdmo, the medium was supplemented with 4 g L⁻¹ L-leucine ($\geq 99\%$ purity, Merck, Darmstadt, Germany).

3.6.2 Preculture cultivation

Precultures were inoculated (1:100) from permanent cultures (harvested in the late exponential phase, stored at -80 °C with 25 % (v/v) glycerol) in M9 medium with either glucose or glycerol as carbon source and the appropriate antibiotic. They were grown for 16 h in a volume of 10 mL in non-baffled 250 mL Erlenmeyer flasks for shake flasks experiments, and in a volume of 40 mL in non-baffled 500 mL Erlenmeyer flasks for reactor experiments, at 37 °C and 350 rpm in an orbital shaker (InforsHT Multitron 2 Standard, Bottmingen, Switzerland), and were used for the inoculation of the main culture (1:100).

3.6.3 Cloning of the CPDMO into the pET26b(+) vector

As a first step, the pBAD_cpdmo construct as well as the empty pET26b(+) were digested with *Sal*I and *Nde*I and the constructs were separated on agarose gel (90 V). The CPDMO insert as well as the pET26b(+) backbone (Figure 2.5) were cut out of the gel and purified with the Promega kit. The insert and backbone were ligated according to the fast ligation protocol from Promega and transformed with chemical transformation (CaCl₂) into *E. coli* BL21 (DE3). The plasmid map of the construct is shown in Figure 3.1

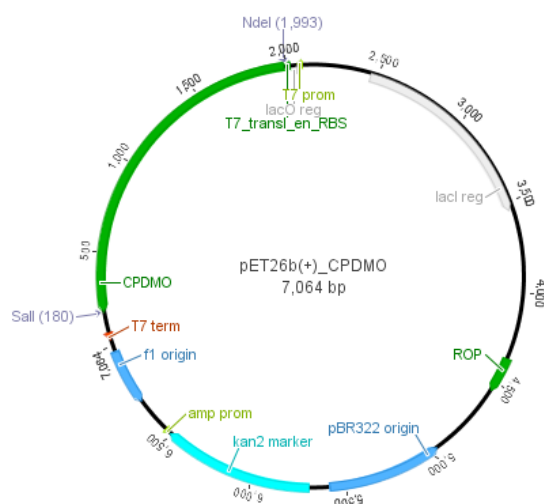


Figure 3.1: Plasmid map of the pET26b(+)_cpdmo construct.

3.6.4 Cultivation experiments for the characterization of CPDMO constructs on the shake flask scale

The *E. coli* Top10 pBAD_cpdmO system and the *E. coli* BL21 (DE3) pET26b(+)_cpdmO expression systems were cultivated in M9 minimal medium with glucose or glycerol as carbon source, supplemented with either kanamycin ($100 \mu\text{g mL}^{-1}$) for the *E. coli* BL21(DE3) pET26b(+)_cpdmO construct or ampicillin ($100 \mu\text{g mL}^{-1}$) and L-leucine (4 g L^{-1}) for the *E. coli* TOP10 pBAD_cpdmO construct. The main culture on the shake-flask scale was cultivated in 10 mL in a non-baffled 250 mL Erlenmeyer flasks at $37 \text{ }^\circ\text{C}$ and 350 rpm until an $\text{OD}_{590} = 1$. Subsequently, the culture was cooled to $24 \text{ }^\circ\text{C}$ and induced with IPTG for the pET26b(+)_cpdmO or rhamnose for the pBAD_cpdmO system. One hour after induction, the ketone **1** was added as a 2.5 M solution in dioxane to a final concentration of 5 mM.

3.6.5 Conditions for scale-up reactor experiments

For the reactor experiments, biotransformation was performed in a 7 L RALF bioreactor (Bioengineering, Wald, Switzerland) in M9 minimal medium (upscaling experiments) or modified M9 minimal medium (modification: 3 x nitrogen and magnesium sources; SFPR experiment) with an operational volume of 4 L. The aeration was set to 1 vvm, controlled by a MX4/4 gas module (DASGIP, Jülich, Germany). The stirring frequency was 1000 rpm with Rushton turbines and the pH was manually adjusted to 6.5 with 3 M NaOH and 3 M H_3PO_4 .

Off-gas analysis was performed with a GA4 off-gas analyzer (DASGIP, Jülich, Germany). Antifoam (O-30, Sigma-Aldrich, St. Louis, USA) was added in 0.1 mL batches whenever necessary. The culture was initially incubated at 37 °C. At $OD_{590} = 1.0$ (see optimization experiments) or $OD_{590} = 2.6$ (biotransformation with resin), the bioreactor was cooled to 24 °C and CPDMO expression was induced with 0.2 mM IPTG. The resin material Lewatit VP OC 1163 (177.1 g, $X_{eq} = 0.40$) was suspended in sterile deionized water (approx. 250 mL) in a baffled shake flask. Then the ketone **1** (42.5 g, 281 mmol) was added and the mixture was shaken overnight (200 rpm, 24 °C). The resin slurry, containing the adsorbed ketone, was added to the bioreactor at 2.5 h after induction of CPDMO expression.

3.6.6 CPDMO activity measurement after the SFPR biotransformation

For the activity assay after the reactor experiment, 10 mL of culture broth without resin were withdrawn from the reactor before the downstream processing. The satellite culture was incubated at 24 °C and 350 rpm in a 250 mL unbaffled shake flask. The ketone was added as a 2.5 M solution in dioxane to a final concentration of 5 mM.

3.6.7 Downstream processing

The bacterial culture-resin suspension was pumped to a flask and the bioreactor (including probes, lid, agitation and sparging gear) was rinsed with approx. 2.5 L water to collect as much of the polymer as possible. The resulting yellow suspension was filtered through a coarse sinter funnel; the filtrate was centrifuged (Centrifuge Sigma 6K15, 17000 RCF, 4 °C, 15 min), the collection flask was exchanged by a new one, and the resin was washed and triturated with 2 x 250 mL MTBE. This organic extract was transferred to a separation funnel (the previous collection flask was washed with 100 mL MTBE), and the combined volume was washed with 100 mL brine. The resin itself was transferred to a 500 mL Soxhlet continuous extraction apparatus (Brand, Wertheim, Germany) using 1 L MTBE; additional 500 mL MTBE were added to the reservoir and the solvent was heated *via* heating jacket to ensure a cycle time of 710 min. After 20 cycles, the extract was combined with the resin wash solution and concentrated under reduced pressure, yielding 39.0 g of crude mixture of ketone and lactone as yellow liquid. Further extraction of the resin (refill with 1.5 L MTBE, approx. 40 cycles) provided additional 3.0 g crude reaction product.

Approx. 7 L of centrifuged culture medium was decanted from the cell pellet. This so-

lution was equally distributed to a separation funnel and a continuous extractor. Manual extraction by vigorous shaking in a separation funnel was performed with 3 x 1 L MTBE, and the approx. 3000 mL of pooled extracts were washed with brine (approx. 500 mL), yielding the 0.9 g crude product as yellow liquid after removal of the solvent. In parallel, a magnetically stirred 5 L continuous extractor was charged with the second half portion of the supernatant, and approx. 2.3 L MTBE were added to the main vessel as well as approx. 1 L to the reservoir. The reservoir was heated to strong reflux using a heating jacket and agitation of the extractor was set to 750 rpm. After 3 h emulsification had reached the top of the apparatus and the process was stopped until the next day. Then, stable extraction was possible for the whole period of 12 h. The organic phases were combined, washed with 250 mL brine and concentrated under reduced pressure, yielding another 2.2 g crude product batch as yellow oil. All fractions were combined after composition quantification *via* calibrated GC. Remaining starting material was recovered as colorless liquid by vacuum Kugelrohr distillation (100-125 °C oven temperature, $\leq 1 \times 10^{-5}$ bar). Various lactone fractions were obtained as colorless oils at higher temperature and lower pressure (125-150 °C, $\leq 1 \times 10^{-6}$ bar), which partly solidified at room temperature. The distillation bottoms also solidified after ketone traces were removed to ≤ 5 mol%. The separate batches were then recrystallized from EtOAc / MTBE 1:1. Depending on lactone content, seed crystals (obtained from earlier reactions, purified *via* column chromatography, or crystallization at 4 °C or 30 °C) were added. The colorless crystals were separated from the yellow supernatants by decantation, then filtered and washed with cold heptane, which does not dissolve the product. Mother liquors were concentrated under reduced pressure and subjected to 2-3 additional recrystallization iterations. All obtained fractions were analyzed by GC and combined for drying (rotary evaporator, slow rotation, rt, $\leq 1 \times 10^{-3}$ bar, approx. 12 h). 33.1 g (198 mmol, 70 %) lactone was obtained as colorless flakes in $\geq 99\%$ purity according to calibrated GC. 7.0 L out of 8.3 L used MTBE from all extraction steps were recovered from rotary evaporation in sufficient spectroscopic purity (indistinguishable by NMR from the purchased material) and good efficiency with 84%.

3.6.8 Analytical techniques

The OD - g Cell Dry Weight (gCDW) relationship was determined from biological triplicates, with three technical replicates each, as $1 \text{ OD} = 0.447 \text{ gCDW L}^{-1}$.

The biotransformation process (ketone and lactone concentrations) was monitored *via* GC-FID (Thermo Finnigan Focus GC/DSQ II, Thermo Fisher, Waltham, USA) equipped with a standard capillary column (BGB5, 30 m x 0.32 mm ID, BGB Analytik, Schlossboeckelheim, Germany). 100 μL sample were extracted with 200 μL ethyl acetate, containing 1 mM methyl benzoate as internal standard.

GC temperature protocol: 200 $^{\circ}\text{C}$ for 1 min, ramp 40 $^{\circ}\text{C}/\text{min}$, 280 $^{\circ}\text{C}$ for 1 min. The concentrations of ketone/lactone were calculated from calibration curves relative to the internal standard. The linear range was 0.2 - 12.8 mM for the ketone and 0.2 - 7.7 mM for the lactone. In the SFPR experiments, the samples were taken from the liquid phase and from the resin, and extracted separately.

The supernatant analysis was performed *via* HPLC using refractive index detection and a photodiode array detector for detection of glucose, acetate, pyruvate and ethanol. Separation was achieved on an ROA-Organic Acid H^+ column (300 x 7.8 mm, Phenomenex, Torrance, USA) with isocratic elution (5 mM H_2SO_4 in water) with an isocratic flow of 0.5 mL min^{-1} . 500 μL culture broth were centrifuged (5000 rpm, 10 min, 4 $^{\circ}\text{C}$). The supernatant was filtered with a 0.2 μm syringe filter and stored at 20 $^{\circ}\text{C}$ until HPLC (Nexera, Shimadzu, Kyoto, Japan) analysis. The supernatant was analyzed with the refractive index detector (RID-10A, Shimadzu, Kyoto, Japan) for glucose detection and photodiode array detector (SPD-M20A, Shimadzu, Kyoto, Japan) for quantification of possible overflow metabolites. The injection volume was 10 μL . During the stationary phase of the bacterial culture, approximate glucose concentrations were determined with glucose strips (Akku-Chek, Roche, Basel) by centrifuging the sample, diluting the supernatant 1:10 and use the supernatant according to the instructions of the manufacturer.

3.6.9 Fitting of the biomass concentration curve

The fitting of the biomass concentration was performed according to a logistic function for description of substrate-independent growth (3.11).^{[213] [28] [214]}

$$X = \frac{X_0 e^{\mu_{max} t - t_0}}{1 - \frac{X_0}{X_m} (1 - X_0 e^{\mu_{max} t - t_0})} \quad (3.11)$$

Where X is biomass concentration [gCDW L^{-1}], X_0 is the biomass concentration at $t=0$ [gCDW L^{-1}], X_m is the maximum biomass concentration [gCDW L^{-1}], μ_{max} is the maximum

specific growth rate [h^{-1}] and t is the time [h]. Additionally, t_0 is the time of the sigmoid's midpoint of the fitted curve.

3.6.10 Carbon balancing

Carbon balancing was performed according to the equation 3.12.

$$c(C_{glucose}) - c(C_{biomass}) - c(C_{CTR}) = c(C_{unbalanced}) \quad (3.12)$$

3.7 Cloning, expression and purification of the stand-alone cascade (SAC) enzymes

3.7.1 Tagging of the alcohol dehydrogenase from *Lactobacillus kefir* (LK-ADH) with a His-Tag

The alcohol dehydrogenase from *Lactobacillus kefir* (LK-ADH) was initially cloned into the vector pET21a with an ampicillin resistance. Since the enzyme did not contain a polyhistidine-tag for purification, the gene was cloned into the pET28a vector which contains a N-terminal polyhistidine tag and a kanamycin resistance. The cloning was performed by isolating the pET21a_LK-ADH plasmid from an *Escherichia coli* BL21 (DE3) culture by a commercial plasmid isolation kit from Thermo Scientific and digesting it with the restriction enzymes *NdeI* and *XhoI* according to the Promega protocol in Promega Restriction Enzyme Reaction Buffer D for four hours at 37 °C. The same isolation and digestion was performed with the pET28a plasmid. Both digested plasmids were analysed by agarose gel electrophoresis ($1 \times \text{TAE}$). The LK-ADH gene and the pET28a backbone were isolated from the agarose gel *via* the Florida method. Therefore, the corresponding band was cut out from the gel using a GelDoc preparative UV mode (GelDoc 2000, BioRad), the gel slice was transferred into an 1.5 mL eppendorf reaction tube and incubated at -80 °C for 30 minutes. Subsequently, the gel slice was thawed at 37 °C and 550 rpm for 15 minutes and the mixture was centrifuged at 4 °C and $17000 \times g$ for 10 minutes (Sigma 3K15 centrifuge). The supernatant was transferred into a sterile 1.5 mL eppendorf reaction tube. 100 μL DNase-/RNase-free water were added to the gel pellet and the pellet was disturbed with the pipette tip, following by another freeze and thaw cycle with the conditions described above. The mixture

was again centrifuged at 4 °C and $17000 \times g$ for 10 minutes. The resulting supernatant was combined with the first supernatant fraction.

As the next step, ethanol precipitation of the DNA from the supernatant was performed. Therefore, the volume of the supernatant mix was determined and 3 M sodium acetate solution (pH 5.2) was added to the supernatant. To the resulting volume ice-cold absolute ethanol was added (2.5 volume - equivalents). The mixture was incubated at -20 °C for at least 1 h (preferably over night) to precipitate the DNA. The mixture was again centrifuged at 4 °C and

$17000 \times g$ for 10-15 minutes. The supernatant was carefully discarded in order to not disturb the DNA pellet and the pellet was washed with 1 mL ice-cold 70 % ethanol, without being disturbed. After another centrifugation step at 4 °C and $17000 \times g$ for 10-15 minutes, the ethanol was carefully removed and the DNA pellet was dried in a vacuum concentrator under reduced pressure until dryness. The pellet was dissolved in 50 μ L DNase-/RNase-free water and the DNA content was measured *via NanoDrop*[®]. Additionally, the size of the isolated DNA was controlled *via* agarose gel electrophoresis with 1 % agarose (1 \times TAE).

The ligation was performed according to the fast ligation T4 DNA ligase protocol from Thermo with 1 μ L gel purified vector and 3-4 μ L gel purified LK-ADH gene with an approximate molar ratio vector/insert of 1:4.

The ligated construct was introduced into *E.coli* BL21 DE3 *via* chemical transformation with CaCl₂.

3.7.2 Tagging of the alcohol dehydrogenase from *Lactobacillus kefir* (LK-ADH) with an intein-CBD-Tag

The tagging of the LK-ADH with the intein-CBD-Tag was performed by T. Bayer.^[215]

The untagged lk-adh gene was amplified from the pET21b(+) template with the following primers:

LKSapI fwd: 5'-GGTGGTTGCTCTTCCAACATGACTGACCGTTTG-3'

LKNcoI rev: 5'-GGTCCATGGCTATTGAGCAGTGTAG-3'

The preparation of the PCR mixture and the thermal cycle conditions are summarized in Table 3.21 and Table 3.22, respectively.

Table 3.21: PCR mix for *lk-adh* amplification.

Pfu+ PCR mix	Final concentration
5.0 μL 10X Pfu+ buffer	1X
2.0 μL dNTP mix (5 mM each)	0.2 mM each dNTP
2.5 μL LKSapI fwd (5 μM)	0.25 μM
2.5 μL LKNcoI rev (5 μM)	0.25 μM
1.0 μL pET21b(+)_ <i>lk-adh</i> (50 ng μL^{-1})	1 ng μL^{-1}
1.0 μL DMSO	2.0% (v/v)
0.5 μL Pfu+ polymerase (5 U μL^{-1})	2.5 U
35.5 μL nuclease-free water	-

Table 3.22: Thermal cycle conditions for *lk-adh* amplification.

PCR Step	Temperature [$^{\circ}\text{C}$]	Time	No. of cycles
Initial denaturation	95.0	2 min	1
Denaturation	95.0	30 s	30
Annealing	63.4	20 s	
Extension	72.0	47 s	
Terminal extension	72.0	2 min	1
Hold	12.0	∞	1

PCR yielded a single amplification product of expected size (calculated: 0.76 kb; experimental: 0.8 kb) analyzed on 1% (w/v) agarose. The PCR product was purified with the Wizard SV Gel and PCR Clean-Up Kit (Promega). Subsequently, the *lk-adh* coding fragment was double digested in CutSmart buffer with *SapI* (R0569, NEB) and *NcoI* (R0193, NEB) at 37 $^{\circ}\text{C}$ for 1 h. The target vector pTYB21 (IMPACT Kit, E6901S, NEB) was double digested accordingly (Table 3.23). The restriction enzymes were inactivated at 65 $^{\circ}\text{C}$ for 20 min. Both

the trimmed *lk-adh* insert and the linearized vector were purified with the Wizard SV Gel and PCR Clean-Up Kit as before. Insert and vector were ligated by T4 ligase (Fermentas) at 22°C for 1 h (Table 3.24). The construct was transformed using competent *E. coli* BL21 (DE3) cells. The plasmid DNA from five putative positive clones was isolated using the GeneJET Plasmid Miniprep Kit (Thermo Scientific) and submitted to *PvuII* (ER0631, Thermo Scientific) control digestion at 37°C for 2.5 h. Finally, the sequence of plasmid DNA isolated was sequenced by Sanger sequencing. Sanger sequencing was performed with PT7 and TT7 standard primers, T7prom fwd and T7term rev (LGC Genomics), respectively, and confirmed the in-frame fusion of the intein-CBD tag coding region to the N-terminus of the *lk-adh* gene.

Table 3.23: *SapI/NcoI* double digestion.

Double digestion mix	Final concentration
2.0 μL CutSmart buffer	1X
2.0 / 11.0 μL pTYB21 (0.5 $\mu\text{g}\mu\text{L}^{-1}$) / insert	50 $\text{ng}\mu\text{L}^{-1}$ / -
1.0 μL SapI (10 $\text{U}\mu\text{L}^{-1}$)	0.5 U
1.0 μL NcoI (10 $\text{U}\mu\text{L}^{-1}$)	0.5 U
14.0 / 5.0 μL nuclease-free water	-

Table 3.24: Ligation of pTYB26_lik-adh.

T4 DNA ligation mixtures	Final concentration
1.0 μL 10X T4 DNA ligase buffer	1X
1.0 μL linearized vector DNA (30 $\text{ng}\mu\text{L}^{-1}$)	3 $\text{ng}\mu\text{L}^{-1}$
1.0 / 4.0 μL trimmed insert DNA	-
0.5 μL T4 DNA ligase (5 Weiss $\text{U}\mu\text{L}^{-1}$)	2.5 Weiss U
6.5 / 3.5 μL nuclease-free water	-

3.7.3 Control digest with *PvuII* restriction enzyme

The isolated plasmids were digested with *PvuII* (Promega) in order to test if they contained an insert. The restriction was performed with *PvuII* according to the Promega restriction

protocol in Promega Restriction Enzyme Reaction Buffer B. The restriction was performed for four hours at 37 °C. Additionally, an empty pET28a/pTYB21 vector was digested as negative control. All digested plasmids were analyzed *via* agarose gel electrophoresis.

3.7.4 Expression of the different cascade enzymes

Unless otherwise noted, all steps other than centrifugation steps are performed under sterile conditions. All solutions except the reagents for the Bradford assay must be sterile. Consumables and other materials must be autoclaved prior to usage if not sterile upon purchase. As the first step, an over night preculture of the desired strain was prepared. Therefore the desired volume of LB or M9 medium supplemented with the appropriate selection marker was inoculated 1:100 (v/v) from permanent cultures. The next day, the main culture was prepared in the desired medium with the appropriate selection marker by inoculation 1:100 (v/v) from the precultures and cultivated at 37 °C prior to induction. If the expression was performed in baffled flasks, the filling volume to flask volume ratio was 0.2 and the shaking frequency was usually 200 rpm if not stated otherwise. If the expression was performed in non-baffled flasks to ensure reproducibility, the filling volume to flask volume ratio was 0.05 and the shaking frequency was 350 rpm. When the OD₆₀₀ value was around 0.4-0.6 in complex and 0.8-1.0 in minimal media, the appropriate amount of inducer was added and the temperature was set to the optimal expression temperature. The culture was subsequently incubated for 16-24 hours while shaking at appropriate temperature as given in the expression protocol (Table 3.25).

Table 3.25: Conditions for enzyme expression

Enzymes	Plasmid	Marker	T [°C]	Inducer	Duration
LK-ADH	pET28a	Kanamycin	30 °C	1 mM IPTG	20-22 hours
LK-ADH	pET21a	Ampicillin	30 °C	1 mM IPTG	20-22 hours
XenB	pGaston	Ampicillin	25 °C	0.2 % L-rhamnose	20-22 hours
CHMO	pET22b	Ampicillin	20 °C	0.1 mM IPTG	20-22 hours
Combined construct	pET28a_CHMO_XenB + pET21a	Ampicillin + Kanamycin	25 °C	0.1 mM IPTG	20-22 hours

After the expression, the culture was harvested by centrifugation at 4 °C, 5000 × g for 15 minutes (Sigma 6K15 centrifuge). The supernatant was discarded and the pellet resuspended in an appropriate volume with 50 mM TRIS HCl pH 7.5 and centrifuged again at 4 °C, 5000 × g for 15 minutes. The supernatant was discarded after this washing step and the pellet was again resuspended in a volume of 2 – 10 mL dependent on the culture volume.

3.7.5 Enzyme purification *via* affinity chromatography

In case of His-tagged LK-ADH all buffers were supplemented with 1 mM CaCl₂ and 1 mM MgCl₂. In case of the enoate reductase XenB, no additions to the medium were necessary. For the cyclohexanone monooxygenase from *Acinetobacter* (CHMO_{acineto}) the buffers contained 10 mM FAD. In general, cell pellets were resuspended in 50 mM Tris-HCl buffer, pH 7.5, containing phenylmethylsulfonyl fluorid (0.1 mM PMSF). Cells were placed on ice and sonicated using a Bandelin MS72 sonotrode connected to a Bandelin Sonoplus HD 3200 in 9 cycles (5 s pulse, 55 s break, amplitude 25%). Precipitates were removed by centrifugation (Sigma 3K30 centrifuge, 15000 × g, 15 minutes, 4°C) and the clear supernatants containing the polyhistidine-tagged enzymes were loaded on a Ni²⁺-sepharose HP affinity column (1 mL, GE Healthcare bioscience) equilibrated with Tris-HCl buffer (50 mM), pH 7.5. Unspecifically bound enzymes were eluted with a binding buffer containing 40 mM imidazole in 7 column volumes. The enzyme of interest was eluted with elution buffer containing 250 mM imidazole in 3 column volumes. Fractions containing the enzymes were identified by SDS-PAGE analysis, pooled and concentrated by ultrafiltration by using ultracentrifugal tubes with a cut-off of 10 kDa. Protein concentrations were determined by the dye-binding method of Bradford at 595 nm using a pre-fabricated assay (BioRad) and bovine serum albumin as the calibration standard.

For the CBD-intein-tagged LK-ADH, in general, cell pellets were resuspended in 20 mM Tris-HCl buffer with 0.5 M NaCl, pH 8.5 (column buffer), containing phenylmethylsulfonyl fluorid (0.1 mM PMSF). Cells were placed on ice and sonicated using a Bandelin MS72 sonotrode connected to a Bandelin Sonoplus HD 3200 in 9 cycles (5 s pulse, 55 s break, amplitude 25%). Precipitates were removed by centrifugation (15000 × g, 15 minutes, 4°C) and the clear supernatants were slowly loaded on a chitin column, which was prior equilibrated with 10 column bed volumes of column buffer. Subsequently, the column was quickly washed with

20 column bed volumes of column buffer to remove the unbound proteins. A sample of the chitin resin composition was taken prior to washing the column with 3 column bed volumes cleavage buffer (column buffer with 50 mM Dithiothreitol (DTT)). The column was incubated in cleavage buffer for 40 hours at 20 °C. The cleavage process was checked by taking a sample of the chitin resin. The elution of the untagged LK-ADH was performed with column buffer. The protein-containing fractions (Bradford protein assay) were pooled, washed with TRIS-HCl pH 7.5 with 50 mM MgCl₂ and concentrated with centrifugal concentrators with a cut-off of 10 kDa. The Chitin Resin was then regenerated according to the procedure in the IMPACT KIT Instruction Manual^[42].

3.7.6 Partial enzyme purification *via* centrifugal devices with a 50 kDa cut-off

For the untagged LK-ADH in the pET21b vector, the supernatant was centrifuged with an ultracentrifugal tube with the cut-off of 50 kDa. The concentrate was washed twice with 50 mM Tris-HCl buffer, pH 7.5 with 50 mM MgCl₂ and the protein concentration was determined with dye-binding method of Bradford at 595 nm.

3.7.7 Thrombin restriction of the LK-ADH-His₆ construct

The thrombin stock was prepared freshly with a concentration of 2 mg mL⁻¹ (Sigma, 40-300 NIH units/mg protein) in thrombin cleavage buffer (Table 3.26), pH 8.4.

Table 3.26: 10x thrombin cleavage buffer

Compound	Concentration
TRIS-HCl	200 mM
NaCl	1.5 M
MgCl ₂	1 mM
CaCl ₂	25 mM
pH was adjusted with HCl to 8.4	

The restrictions were performed according to the following scheme (Table 3.27) in a total volume of 10 mL:

Table 3.27: Thrombin restriction of LK-ADH-His₆

Compound	Amount
10x cleavage buffer	1 mL
Thrombin stock (2 mg/mL)	0.1 mL
LK-ADH-His ₆	2 mg
deionized water	filled up to 10 mL

The controls contained either no thrombin or no LK-ADH-His₆. Both settings were incubated at 20 °C for 14 hours while shaking. After the incubation, Bradford was measured and an SDS gel was prepared to evaluate the digestion progress.

3.8 Activity assays of the stand-alone cascade (SAC)

3.8.1 Activity assay for LK-ADH

The first activity confirmation of the pET28a_LK-ADH construct was performed *in vitro* as cell-free extracts with the conversion of cyclohexanone to cyclohexanol and a GDH recycling system. The total volume of the test biotransformation was 1 mL. The substrate was applied with 2.5 mg mL⁻¹ cell-free extracts of LK-ADH in 5 mM concentration in 50 mM Tris-HCl buffer pH 7.5. 200 μM NADP⁺, 10 mM glucose-6-phosphate, 1 U glucose-6-phosphate dehydrogenase were added to the biotransformation. The reaction was performed at 25 °C. The reaction progress was monitored *via* GC-FID by extracting 100 μL sample with 400 μL ethyl acetate with 1 mM methyl benzoate as internal standard.

The activity assay of the cell-free extracts/ His-tag-purified LK-ADH was performed *in vitro* on a 500 μL reaction scale in the UV-Vis photometer (Shimadzu UV-1800). 10 mM of acetophenone in an 1 M ethanol stock were applied in 50 mM Tris-HCl pH 7.5 with 50 mM MgCl₂, 1 μM LK-ADH monomer and 100 μM NADPH. The reaction was started by NADPH addition. The activity was measured *via* absorbance at 340 nm for the reduction of acetophenone with NADPH by 1 μM LK-ADH at 25 °C if not stated otherwise. The activity was calculated by fitting the linear range of the measurement. The slope was used to calculate the NADPH conversion in one second according to Lambert-Beer law with $\epsilon_{\lambda} = 6.22 \text{ mM}^{-1} \text{ cm}^{-1}$ for NADPH .

The activity assay of partially purified LK-ADH (purification with the 50 kDa cut-off) was performed in the photometer. 50 mM Tris-HCl pH 7.5 supplemented with 50 mM MgCl₂ was used as buffer. The activity was measured *via* absorbance at 340 nm (NADPH depletion) for the reduction of 10 mM acetophenone from an 2 M stock in acetonitrile with 100 μM NADPH by 1 μM LK-ADH at 25 °C if not stated otherwise. The activity was calculated by fitting the linear range of the measurement. The slope was used to calculate the NADPH conversion in one second according to Lambert-Beer law with $\epsilon_{\lambda} = 6.22 \text{ mM}^{-1} \text{ cm}^{-1}$ for NADPH.

3.8.2 Activity assay for XenB

The activity assay with purified XenB was performed *in vitro* on a 500 μL reaction scale in the UV-Vis photometer (Shimadzu UV-1800). 10 mM cyclohexenone (**6b**) in an 2 M acetonitrile stock were added to 50 mM Tris-HCl buffer, pH 7.5 and 5 μM XenB at 25 °C. The reaction was started by addition of 100 μM NADPH. The activity was measured *via* absorbance at 340 nm by fitting the linear range of the NADPH depletion. The slope was used to calculate the NADPH conversion in one second according to Lambert-Beer law with $\epsilon_{\lambda} = 6.22 \text{ mM}^{-1} \text{ cm}^{-1}$ for NADPH.

3.8.3 Activity assay for CHMO_{acineto}

The activity assay with purified CHMO was performed *in vitro* on a 500 μL reaction scale in the UV-Vis photometer (Shimadzu UV-1800). 0.5 mM cyclohexanone (**6c**) with an intermediate dilution to 40 mM was added from an 2 M acetonitrile stock to 50 mM Tris-HCl buffer, pH 7.5 and 0.05 μM CHMO. The reaction was started with 100 μM NADPH. The activity was measured *via* absorbance at 340 nm by fitting the linear range of the NADPH depletion. The slope was used to calculate the NADPH conversion in one second according to Lambert-Beer law with $\epsilon_{\lambda} = 6.22 \text{ mM}^{-1} \text{ cm}^{-1}$ for NADPH.

3.9 Kinetic parameter estimation for the stand-alone cascade (SAC)

For kinetic modeling of the stand-alone cascade, parameters of the Michaelis-Menten-kinetics were measured for every enzyme/substrate combination for the parameters not reported in the literature. Activity measurements were performed spectrophotometrically with the Shimadzu UV-1800 photometer at 340 nm by monitoring the initial rates of NADPH formation or depletion in 700 μL cuvettes ($\epsilon_{\text{NADPH}} = 6.22 \text{ mM}^{-1} \text{ cm}^{-1}$). The Michaelis-Menten parameters of the ADH were measured in Tris-HCl buffer (50 mM, pH 7.5, 50 mM MgCl_2) at 25 °C with different substrate concentrations in triplicates and 0.1 mM for NADP^+ (for oxidations) and 0.12 mM for NADPH (for reductions). The enzyme concentration was between 0.8 and 10 μM depending on the velocity of the reaction. The total volume was 500 μL and the measurement was started by addition of cofactor.

For the ERED, the Michaelis-Menten parameters were measured in Tris-HCl buffer (50 mM, pH 7.5) at 25 °C in triplicates. The measurement was started with 0.12 mM NADPH. The enzyme was applied in a concentration of 4 μM and total reaction volume was 500 μL .

For the BVMO, the Michaelis-Menten parameters were determined in Tris-HCl buffer (50 mM, pH 7.5, 0.1 mM FAD) at 25 °C in triplicates. The measurement was started with 0.12 mM NADPH. The enzyme was applied in a concentration of 0.05 μM and the total reaction volume was 500 μL .

All substrate stocks were prepared in acetonitrile. For determination of the ethanol effect on the ADH the ethanol was added to the measurements prior to starting the reaction.

The specific activity was calculated according to

$$k_{cat} = \text{volumetricactivity} \times [ENZ]^{-1} \quad (3.13)$$

The fitting of the Michaelis-Menten curves to determine kinetic parameters was performed with Origin 2015G with the Michaelis-Menten equation.

3.10 Synthesis of non-commercial substrates for kinetic measurement

3.10.1 Synthesis of (2*R*,5*S*)-dihydrocarvone **7c**

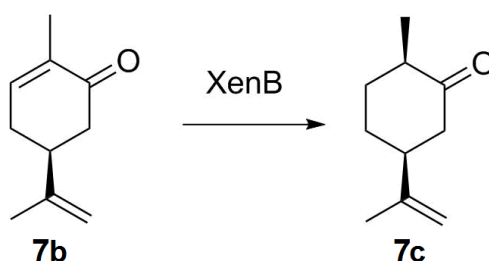


Figure 3.2:

Reduction of **7b** to **7c** by XenB on preparative scale

XenB was expressed in 2 times 400 mL cultures according to the expression protocols and resuspended in N-free M9 medium. To six different batches of non-baffled Erlenmeyer flasks (500 mL) containing 100 mL resting cells expressing XenB, 75 μL of a S-(+)-carvone **7b** stock (50 mg mL⁻¹ in acetonitrile) were added. The Erlenmeyer flasks were shaken at 25 °C and 300 rpm. The progress of the reaction was monitored using GC. After 30 min GC showed full conversion and 75 μL of the carvone stock were added. After 1.5 h GC showed full conversion and another 75 μL of the substrate stock were added resulting in a total addition of 700 mg S-(+)-carvone **7b**. After 2.5 h total reaction time all batches were extracted three times with diethyl ether and the combined organic layers were dried over Na₂SO₄, filtered off and concentrated in vacuo. The crude product was purified using 90 g silica and pentane/diethyl ether (gradient, 0-10 % ether). A colorless oil of **7c** (88 % yield) was obtained as cis:trans 8:1 mixture.

GC samples were taken after 30 min of each batch separately: 100 μL of the reaction mixture were added to a 1.5 mL Eppendorf tube containing 200 μL of ethyl acetate (containing 1 mM methyl benzoate as internal standard) and vortexed for 30-35 s and centrifuged for 1 min. The organic layer was desiccated with Na₂SO₄ and analyzed by achiral GC.

NMR code: major cis isomer:

¹H NMR (400 MHz, CDCl₃) δH = 1.09 (d, J = 6.9 Hz, 3H, CH₃), 1.56 - 1.63 (m, 1H), 1.73 (s, 3H, C=CCH₃), 1.79 - 1.90 (m, 3H), 2.35 - 2.46 (m, 2H), 2.51 - 2.66 (m, 2H), 4.69 (m,

1H, C=CH₂), 4.83 (m, 1H, C=CH₂).

¹³C NMR (100 MHz, CDCl₃) δC = 15.8, 21.7, 26.5, 30.8, 44.1, 44.3, 44.7, 111.6, 147.0, 214.2.

Analytical data was in accordance with literature values^[216].

3.10.2 Synthesis of 2-methylcyclohex-2-en-1-ol **8a**

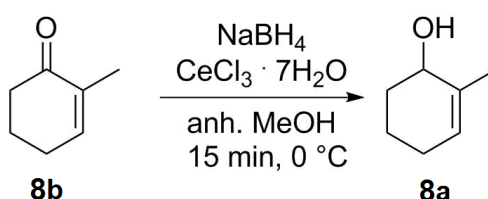


Figure 3.3:

Luche reduction of **8b** to **8a**

Cerium chloride heptahydrate (3.60 g, 9.72 mmol, 1.1 eq.) were suspended in 15 mL anhydrous methanol and mixed with a solution of 2-methyl-2-cyclohexenone **8b** (0.97 g, 8.84 mmol) in 5 mL methanol. The mixture was cooled to 0 °C and set under argon atmosphere. Sodium borohydride was added portionwise and the temperature was maintained between 0-5 °C.

After 15 min TLC showed full conversion and the solution was quenched using saturated NH₄Cl solution at 0 °C. The aqueous phase was extracted three times with diethyl ether. The combined organic layers were washed with saturated NaCl solution, dried over Na₂SO₄, filtered off and concentrated *in vacuo*.

The crude product **8a** was obtained as slightly reddish colorless oil in 88 % yield and used without any further purification.

¹H NMR (400 MHz, CDCl₃) δH = 1.48 (s, 1H), 1.52 - 1.68 (m, 2H), 1.71 - 1.83 (m, 5H), 1.87 - 2.07 (m, 2H), 3.99 (t, J = 4.9 Hz, 1H), 5.47 - 5.59 (m, 1H) ppm.

¹³C NMR (100 MHz, CDCl₃) δC = 18.3 (CH₃), 20.8 (C5), 25.6 (C4), 32.3 (C6), 68.6 (C-OH), 125.7 (C3), 135.4 (C2) ppm.

Analytical data in accordance with literature values^[216].

3.11 Biocatalytic screenings of the stand-alone cascade (SAC)

For the *in vivo* reactions of cyclohexenol (**6a**) or carveol (**7a**) as substrate, the *E. coli* BL21 (DE3) with all three enzymes (ADH, ERED and BVMO) in one cell was expressed in TB, supplemented with ampicillin and kanamycin, according to the expression protocol as shown in Table 3.25. To the expressed culture 1 % glucose was added and the culture was transferred into vials with 10 × higher volume as the volume of the biotransformation. The glass vials were sealed during the reaction, evaporation would be reduced to a minimum. The reaction was started by substrate addition (1 M stock in ethanol) to a final concentration of 4 mM^[55]. For the *in vitro* screening of cyclohexenol (**6a**), the expressed *E. coli* BL21 (DE3) with ADH, ERED and BVMO was centrifuged, resuspended in 15 × less Tris-HCl (50 mM, pH 7.5) and divided into two different fractions. One fraction was only supplemented with 0.1 mM PMSF and the other fraction was supplemented with 0.1 mM PMSF and additionally with 0.1 mM FMN and FAD. Both fractions were sonicated on ice using a Bandelin KE76 sonotrode connected to a Bandelin Sonoplus HD 3200 in 9 cycles (5 s pulse, 55 s break, amplitude 50 %). Precipitates were removed by centrifugation (Sigma 3K30 centrifuge, 15000 × g, 15 min, 4°C). The supernatant was applied in a biotransformation with 90 % of the total biotransformation volume (19 mg mL⁻¹ enzyme, which is approx. 15 × more concentrated than in the whole-cell reaction mixture). The other 10 % of the biotransformation volume were cofactors, added to the final concentration of 5 mM NADP⁺ and 5 mM NADPH. The reaction was started by addition of the substrate cyclohexenol (**6a**). In both cases, the reactions were performed at 20°C with shaking and samples were taken and analysed *via* GC-FID. 100 μL sample were extracted with 500 μL ethyl acetate supplemented with 1 mM methyl benzoate as internal standard. Conversion was determined by GC using a ThermoQuest Trace GC 2000 with a FID detector equipped with a BGB175 (30 m × 0.25 mm ID, 0.25 μm film).

3.12 Stability and activity of CHMO *in vivo*

3.12.1 Bacterial strain and culture conditions in the fermentation

E. coli BL21 (DE3) was used as expression host for CHMO (cyclohexanone monooxygenase from *Acinetobacter calcoaceticus* NCIMB 9871) expression (pET22b_CHMO). *E. coli* was cultivated in modified M9 minimal medium.

3.12.2 Physiology

Samples for physiology analysis were taken every hour. 1 mL of fermentation broth was transferred into a 1.5 mL Eppendorf reaction tube on ice and centrifuged ($5000 \times g$, 10 minutes). The supernatant was filtered with a $0.2 \mu\text{m}$ syringe filter and stored at $-20 \text{ }^\circ\text{C}$ until UHPLC (Nexera Shimadzu) analysis. The supernatant was analyzed with the refractive index detector (RI) for glucose detection, photodiode array detector (PDA) for quantification of acetic and pyruvic acid and an Electrospray ionization (ESI) ion source with a quadrupole mass analyzer for additional confirmation of the substances (LC-MS 2020 Shimadzu). Separation was performed with an ROA-Organic Acid H^+ (8 %) column ($300 \times 7.8 \text{ mm}$, Phenomenex) with an isocratic flow of 0.4 mL min^{-1} 5 mM formic acid in water.

3.12.3 Quantification of soluble CHMO

The sampled volume normalized to $\text{OD} = 7$ was centrifuged ($5000 \times g$, 10 minutes). The resulting pellet was washed with 1 mL Tris-HCl buffer pH 7.5, centrifuged again ($5000 \times g$, 10 minutes) and stored at $-20 \text{ }^\circ\text{C}$ until further workup. Prior to cell sonification, the pellets were re-suspended in 0.5 mL Tris-HCl pH 7.5 containing 0.1 mM phenylmethylsulfonyl fluorid (PMSF). Cells were placed on ice and sonicated in 9 cycles (5 s pulse, 55 s break, amplitude 50 %). Precipitates were removed by centrifugation (15 minutes, $15,000 \times g$) and the clear supernatants containing the soluble proteome including CHMO were analyzed by SDS-PAGE. Every SDS-PAGE gel was loaded with an at least three point calibration of prior purified CHMO in order to quantify the soluble CHMO concentration in every sample. The gels were stained overnight with Coomassie Brilliant Blue G-250, scanned with the Molecular Imager Gel Doc XR System (BioRad) and quantified with the Image Lab Software (BioRad).

The fitting of the protein concentration was performed with origin with the fitting function $y = 6.6 + (-5.3 - 6.6)/(1 + (x/13.98)^{10.82514}) + (-3.42668 + 13 * \exp(-x * 0.03876))$

3.12.4 *E. coli* Metabolomics

Immediately after wetting the nitrocellulose filter (0.45 μ m nitrocellulose MF Membrane Filters, Millipore) with M9 medium (with or without nitrogen), 2 mL sample were dispersed onto the filter and washed with 4 mL of the corresponding M9 medium (with or without nitrogen). It was important that the filter did not run dry. The filter was removed with tweezers, placed into a 15 mL centrifuge tube and frozen in liquid nitrogen. The samples were stored at -80 °C until extraction. 2 mL of the extraction solution (60:40 % ethanol (p.a)/water) were preheated to 78 °C in a water bath. U-¹³C internal standard was added to the centrifuge tube with the filtered sample and the 2 mL extraction solution were added. The centrifuge tube was transferred to the water bath and extracted for three minutes at 78 °C while vortexing every minute. The samples were stored at -40 °C in precooled ethanol until centrifugation (12000 \times g, 10 minutes, -9 °C). The samples were dried at 30 °C and 0.12 mbar to complete dryness in a vacuum concentrator (Christ RVC 2-25 CD plus) and subsequently stored at -80 °C until LC-MS/MS measurement.

3.12.5 LC-MS/MS measurements

Dry extracts were resuspended in water (100 μ L), centrifuged (12000 \times g, 3 minutes) and the supernatant was used for analysis. Separation was achieved with a Luna 3u NH2 100A column (150 \times 2.00 mm, Phenomenex) with a binary gradient method (Solvent A: acetonitrile / Solvent B: 10 mM ammonium acetate, pH 9.9). Gradient parameters: 0 - 24 min: 20 % - 100 % B; 25 - 34 min: 100 % B; 35 min: 20 % B. Detection was performed with a tandem mass spectrometry detector with an ESI ion source (Shimadzu LCMS-8040) in Multi Reaction Monitoring (MRM) mode. Peak areas were normalized to fully ¹³C-labeled internal standards and absolute quantification of metabolites was achieved with linear calibration curves of standards. Finally, concentrations were normalized to the amount of biomass.

3.12.6 CHMO activity measurements *in vivo*

The activity measurements of the CHMO were performed every three hours. The first measurement was done three hours post induction with IPTG. For the activity measurement 5 mL of fermentation broth were transferred to a 250 mL non-baffled Erlenmeyer flask and 8 mM bicyclo[3.2.0]hept-2-en-6-one (**9**; 1 M solution in dioxane) were added as substrate. The first sample was taken immediately after substrate addition. Therefore 100 μL of the culture broth were extracted with 500 μL ethyl acetate with 1 mM methyl benzoate as internal standard and transferred into GC-vials for further GC analysis (Focus GC with FID detector, Thermo Fisher Scientific). The culture was placed into an orbital shaker (InforsHT Multitron 2 Standard) at 20 °C and 350 rpm to mimic the fermentation conditions. The activity test was performed for an hour and samples were taken every 15 minutes. In the GC analysis the consumption of substrate as well as formation of the corresponding lactone was monitored. The activity was normalized by OD on the one hand and by the soluble CHMO content on the other hand to obtain the specific activity.

3.12.7 Propagation of uncertainty

For calculation of the errors of intracellular concentrations, the propagation of uncertainty was performed for every compound X (Equation 3.14).

$$\sigma_X = \sqrt{\left(\frac{\sigma_X}{[X]}\right)^2 + \left(\frac{\sigma_{V_{cell}}}{V_{cell}}\right)^2 + \left(\frac{\sigma_{cells_{mL}}}{[cells_{mL}]}\right)^2} \quad (3.14)$$

with σ_X being the standard deviation of compound X, $[X]$ being the concentration of the compound, $\sigma_{V_{cell}}$ being the standard deviation of the cell volume and V_{cell} being the cell volume; $\sigma_{cells_{mL}}$ being the standard deviation of the amount of cells in one mL and $[cells_{mL}]$ being the amount of cells in one mL culture.

Due to the analytical failure of common, simple methods for the propagation of uncertainty for the logistic function, the standard deviation for intracellular FAD loading of CHMO was estimated by calculating the extreme combinations of errors.

3.13 Characterization of dihydroxyacetone kinase (DhaK) in *E. coli*

The DhaK_pRSETA construct was transformed in *E. coli* BL21 (DE3) *via* chemical transformation. The experiments were carried out in modified M9 medium. An *E. coli* BL21 (DE3) wt strain was run in parallel as a control and treated the same way as the DhaK expressing strain. The preculture was cultivated o/n and the main culture was inoculated to an OD to around 0.3. The culture was cultivated in a volume of 30 mL in 500 mL non-baffled Erlenmeyer flasks at 350 rpm and 37 °C until an OD of around 0.5. The DhaK production was induced with 1 mM IPTG and the temperature was reduced to 30 °C for proper protein folding. 20 mM DHA were added after 5.8 hours. The sampling for physiological parameters as OD and supernatant analysis was performed every 30 minutes during the exponential phase from three parallel cultures for each strain. The sampling for metabolomics was also performed in triplicates from different parallel cultures. All cultivations were carried out in the same medium batch and inoculated with the same preculture of the corresponding strain.

3.13.1 Physiology

Samples for physiology analysis were taken every hour. 0.5 mL culture was transferred to a 1.5 mL Eppendorf reaction tube on ice and centrifuged ($5000 \times g$, 10 minutes). The supernatant was filtered with a 0.2 μm syringe filter and stored at -20 °C until UHPLC (Nexera Shimadzu) analysis. The supernatant was analyzed with the refractive index detector (RI) for glucose detection and photodiode array detector (PDA) for quantification of DHA and the internal standard at 270 nm and an Electrospray ionization (ESI) ion source with a quadrupole mass analyzer for additional confirmation of the substances (LC-MS 2020 Shimadzu). Separation was performed with an ROA-Organic Acid H⁺ (8 %) column (300 \times 7.8 mm, Phenomenex) with an isocratic flow of 0.5 mL min⁻¹ 0.1% formic acid in water and 0.25 mM 2-phenylacetic acid as internal standard.

3.13.2 Metabolomics measurements

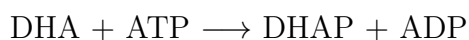
The sampling procedure was performed as described in Chapter 3.15.4 with the difference that the samples were not dried in a vacuum concentrator, but lyophilized until complete

dryness. The LC-MS/MS-measurements were performed as in chapter 3.15.5.

3.14 Stoichiometric modeling of the different *E. coli* constructs

3.14.1 Model construction

The model Ec_iJR904 was used as the model for *E. coli* BL21 (DE3).^[196] This model contains 931 unique biochemical reactions with 625 metabolites. Among the included reactions are exchange reactions, the central carbon metabolism, amino acid synthesis, cofactor biosynthesis, nucleotide metabolism, alternate carbon sources and an artificial biomass formation reaction^[196]. This model was modified for the *E. coli* BL21 (DE3) DhaK construct by adding the DhaK reaction, the cascade reactions and the corresponding transport reactions either alone or in combinations to construct models with different genetic configurations.



The source code for the reaction was implemented into the Ec_iJR904 model as shown below:

```

<notes>
  <html:p>GENE_ASSOCIATION: b000</html:p>
  <html:p>PROTEIN_ASSOCIATION: DhaK</html:p>
  <html:p>SUBSYSTEM: S_Alternate_Carbon_Metabolism</html:p>
  <html:p>PROTEIN_CLASS: </html:p>
</notes>
<listOfReactants>
  <speciesReference species="M_dha_c"
    stoichiometry="1.000000" />
    <speciesReference species="M_atp_c"
      stoichiometry="1.000000" />
</listOfReactants>
<listOfProducts>
  <speciesReference species="M_dhap_c"
    stoichiometry="1.000000" />
  <speciesReference species="M_adp_c"
    stoichiometry="1.000000" />
</listOfProducts>
<kineticLaw>
  <math xmlns="http://www.w3.org/1998/Math/MathML">
    <apply>
      <ci> LOWER_BOUND </ci>
      <ci> UPPER_BOUND </ci>
      <ci> OBJECTIVE_COEFFICIENT </ci>
      <ci> FLUX_VALUE </ci>
      <ci> REDUCED_COST </ci>
    </apply>
  </math>
  <listOfParameters>
    <parameter id="LOWER_BOUND" value="0.000000"
      units="mmol_per_gDW_per_hr" />
    <parameter id="UPPER_BOUND" value="999999.000000"
      units="mmol_per_gDW_per_hr" />
    <parameter id="OBJECTIVE_COEFFICIENT"
      value="0.000000" />
    <parameter id="FLUX_VALUE" value="0.000000"
      units="mmol_per_gDW_per_hr" />
    <parameter id="REDUCED_COST" value="0.000000" />
  </listOfParameters>
</kineticLaw>
</reaction>

```

The wt as well as the DhaK producing model did already contain DHA as a possible metabolite for uptake, but the initial value of this reaction was set to zero.

The cascade, that was implemented in the model and was undergoing construction *in vivo* (Figure 2.67). For the implementation of the cascade reactions into the Ec_iJR904 model, the substrate, intermediates and product of the cascade had to be defined first. Additionally, for the substrate and product, the corresponding extracellular and boundary metabolites needed to be defined for later construction of transport reaction into and out of the boundary phase of the *E. coli* cell.

```

<notes>
  <html xmlns="http://www.w3.org/1999/xhtml">
    <p>FORMULA: C8H10O</p></html>
  </notes>
</species>
<species id="M_alc1_c" name="Alcohol1_Cascade" compartment="C_c">
  <notes>
    <html xmlns="http://www.w3.org/1999/xhtml">
      <p>FORMULA: C8H10O</p></html>
    </notes>
  </species>
<species id="M_ald1_c" name="Aldehyde1_Cascade" compartment="C_c">
  <notes>
    <html xmlns="http://www.w3.org/1999/xhtml">
      <p>FORMULA: C8H9O</p></html>
    </notes>
  </species>
<species id="M_aldol1_c" name="Aldol1_Cascade" compartment="C_c">
  <notes>
    <html xmlns="http://www.w3.org/1999/xhtml">
      <p>FORMULA: C11H15O6P</p></html>
    </notes>
  </species>
<species id="M_final1_c" name="Product1_Cascade" compartment="C_c">
  <notes>
    <html xmlns="http://www.w3.org/1999/xhtml">
      <p>FORMULA: C11H14O3</p></html>
    </notes>
  </species>
<species id="M_final1_e" name="Product1_Cascade" compartment="C_e">
  <notes>
    <html xmlns="http://www.w3.org/1999/xhtml">
      <p>FORMULA: C11H14O3</p></html>
    </notes>
  </species>
<species id="M_alc1_b" name="alc1_b" compartment="C_e" />
<species id="M_final1_b" name="final1_b" compartment="C_e" />

```

The compartments used in the cascade extension were C_c for cytoplasmatic compartment and C_e for extracellular compartment. Additionally, metabolites with the _b tag, were classified as boundary metabolites in the extracellular compartment. These boundary metabolites were part of the exchange system, which were the reactions which were set to a certain value, if an uptake (negative value) or secretion (positive value) was simulated. The values of all reactions had the dimension of mmol per gramm dry weight per hour. The

exchange reaction from the boundary phase and and transport reaction across the membrane for the alcohol (first step of the cascade) were defined as:

```

<notes>
  <html xmlns="http://www.w3.org/1999/xhtml">
    <p>GENE_ASSOCIATION: 0000</p>
    <p>GENE_LIST: 0000</p>
    <p>SUBSYSTEM: Exchange</p></html>
  </notes>
  <listOfReactants>
    <speciesReference species="M_alc1_e"/>
  </listOfReactants>
  <listOfProducts>
    <speciesReference species="M_alc1_b"/>
  </listOfProducts>
  <kineticLaw>
    <math xmlns="http://www.w3.org/1998/Math/MathML">
      <ci> FLUX_VALUE </ci>
    </math>
    <listOfParameters>
      <parameter id="LOWER_BOUND" value="0 "
        units="mmol_per_gDW_per_hr"/>
      <parameter id="UPPER_BOUND" value="1000 "
        units="mmol_per_gDW_per_hr"/>
      <parameter id="OBJECTIVE_COEFFICIENT" value="0"/>
      <parameter id="FLUX_VALUE" value="500 "
        units="mmol_per_gDW_per_hr"/>
    </listOfParameters>
  </kineticLaw>
</reaction>
<reaction id="R_ALC1t" name="alcohol_transport">
  <notes>
    <html xmlns="http://www.w3.org/1999/xhtml">
      <p>GENE_ASSOCIATION: b0000</p>
      <p>GENE_LIST: b0000</p>
      <p>SUBSYSTEM: Transport, Extracellular</p></html>
    </notes>
    <listOfReactants>
      <speciesReference species="M_alc1_e"/>
    </listOfReactants>
    <listOfProducts>
      <speciesReference species="M_alc1_c"/>
    </listOfProducts>
    <kineticLaw>
      <math xmlns="http://www.w3.org/1998/Math/MathML">
        <ci> FLUX_VALUE </ci>
      </math>
      <listOfParameters>
        <parameter id="LOWER_BOUND" value="0 "
          units="mmol_per_gDW_per_hr"/>
        <parameter id="UPPER_BOUND" value="1000 "
          units="mmol_per_gDW_per_hr"/>
        <parameter id="OBJECTIVE_COEFFICIENT" value="0"/>
        <parameter id="FLUX_VALUE" value="0 "
          units="mmol_per_gDW_per_hr"/>
      </listOfParameters>
    </kineticLaw>
  </reaction>

```

The same exchange and transport reactions were defined for the dephosphorylated product of the cascade:

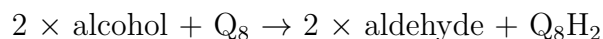
```

<notes>
  <html xmlns="http://www.w3.org/1999/xhtml">
    <p>GENE_ASSOCIATION: b0000</p>
    <p>GENE_LIST: b0000</p>
    <p>SUBSYSTEM: Transport, Extracellular</p></html>
  </notes>
  <listOfReactants>
    <speciesReference species="M_finall_e"/>
  </listOfReactants>
  <listOfProducts>
    <speciesReference species="M_finall_c"/>
  </listOfProducts>
  <kineticLaw>
    <math xmlns="http://www.w3.org/1998/Math/MathML">
      <ci> FLUX_VALUE </ci>
    </math>
    <listOfParameters>
      <parameter id="LOWER_BOUND" value="-1000 "
        units="mmol_per_gDW_per_hr"/>
      <parameter id="UPPER_BOUND" value="1000 "
        units="mmol_per_gDW_per_hr"/>
      <parameter id="OBJECTIVE_COEFFICIENT" value="0"/>
      <parameter id="FLUX_VALUE" value="0 "
        units="mmol_per_gDW_per_hr"/>
    </listOfParameters>
  </kineticLaw>
</reaction>
<reaction id="R_EX_FIN1_e" name="product_exchange">
  <notes>
    <html xmlns="http://www.w3.org/1999/xhtml">
      <p>GENE_ASSOCIATION: 0000</p>
      <p>GENE_LIST: 0000</p>
      <p>SUBSYSTEM: Exchange</p></html>
    </notes>
    <listOfReactants>
      <speciesReference species="M_finall_e"/>
    </listOfReactants>
    <listOfProducts>
      <speciesReference species="M_finall_b"/>
    </listOfProducts>
    <kineticLaw>
      <math xmlns="http://www.w3.org/1998/Math/MathML">
        <ci> FLUX_VALUE </ci>
      </math>
      <listOfParameters>
        <parameter id="LOWER_BOUND" value="0 "
          units="mmol_per_gDW_per_hr"/>
        <parameter id="UPPER_BOUND" value="1000 "
          units="mmol_per_gDW_per_hr"/>
        <parameter id="OBJECTIVE_COEFFICIENT" value="0"/>
        <parameter id="FLUX_VALUE" value="500 "
          units="mmol_per_gDW_per_hr"/>
      </listOfParameters>
    </kineticLaw>
  </reaction>

```

All three cascade reactions were implemented into the model:

the AlkJ reaction:

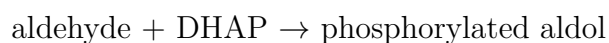


```

<notes>
  <html xmlns="http://www.w3.org/1999/xhtml">
    <p>GENE_ASSOCIATION: b0000</p>
    <p>GENE_LIST: b0000</p>
    <p>SUBSYSTEM: Glycolysis/Gluconeogenesis</p></html>
  </notes>
  <listOfReactants>
    <speciesReference species="M_alc1_c" stoichiometry="2.000000"/>
    <speciesReference species="M_q8_c" stoichiometry="1.000000"/>
  </listOfReactants>
  <listOfProducts>
    <speciesReference species="M_ald1_c" stoichiometry="2.000000"/>
    <speciesReference species="M_q8h2_c" stoichiometry="1.000000"/>
  </listOfProducts>
  <kineticLaw>
    <math xmlns="http://www.w3.org/1998/Math/MathML">
      <ci> FLUX_VALUE </ci>
    </math>
    <listOfParameters>
      <parameter id="LOWER_BOUND" value="-1000"
        units="mmol_per_gDW_per_hr"/>
      <parameter id="UPPER_BOUND" value="1000"
        units="mmol_per_gDW_per_hr"/>
      <parameter id="OBJECTIVE_COEFFICIENT" value="0"/>
      <parameter id="FLUX_VALUE" value="0"
        units="mmol_per_gDW_per_hr"/>
    </listOfParameters>
  </kineticLaw>
</reaction>

```

the aldolase reaction:

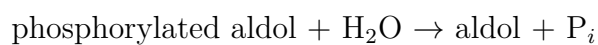


```

<notes>
  <html xmlns="http://www.w3.org/1999/xhtml">
    <p>GENE_ASSOCIATION: b0000</p>
    <p>GENE_LIST: b0000</p>
    <p>SUBSYSTEM: Glycolysis/Gluconeogenesis</p></html>
  </notes>
  <listOfReactants>
    <speciesReference species="M_ald1_c" />
    <speciesReference species="M_dhap_c" />
  </listOfReactants>
  <listOfProducts>
    <speciesReference species="M_aldol1_c" />
  </listOfProducts>
  <kineticLaw>
    <math xmlns="http://www.w3.org/1998/Math/MathML">
      <ci> FLUX_VALUE </ci>
    </math>
    <listOfParameters>
      <parameter id="LOWER_BOUND" value="-1000 "
        units="mmol_per_gDW_per_hr" />
      <parameter id="UPPER_BOUND" value="1000 "
        units="mmol_per_gDW_per_hr" />
      <parameter id="OBJECTIVE_COEFFICIENT" value="0" />
      <parameter id="FLUX_VALUE" value="0 "
        units="mmol_per_gDW_per_hr" />
    </listOfParameters>
  </kineticLaw>
</reaction>

```

and the phosphatase reaction:



```

<notes>
  <html xmlns="http://www.w3.org/1999/xhtml">
    <p>GENE_ASSOCIATION: b0000</p>
    <p>GENE_LIST: b0000</p>
    <p>SUBSYSTEM: Glycolysis/Gluconeogenesis</p></html>
  </notes>
  <listOfReactants>
    <speciesReference species="M_aldol1_c" />
    <speciesReference species="M_h2o_c" />
  </listOfReactants>
  <listOfProducts>
    <speciesReference species="M_final1_c" />
    <speciesReference species="M_pi_c" />
  </listOfProducts>
  <kineticLaw>
    <math xmlns="http://www.w3.org/1998/Math/MathML">
      <ci> FLUX_VALUE </ci>
    </math>
    <listOfParameters>
      <parameter id="LOWER_BOUND" value="0 "
        units="mmol_per_gDW_per_hr" />
      <parameter id="UPPER_BOUND" value="1000 "
        units="mmol_per_gDW_per_hr" />
      <parameter id="OBJECTIVE_COEFFICIENT" value="0" />
      <parameter id="FLUX_VALUE" value="0 "
        units="mmol_per_gDW_per_hr" />
    </listOfParameters>
  </kineticLaw>
</reaction>

```

3.14.2 Pareto analysis

For predictive modeling, the standard conditions were minimal medium, glucose as only carbon source and aerobic conditions. The specific glucose uptake rate was set to $10 \text{ mmol gCDW}^{-1} \text{ h}^{-1}$ and the objective function was the maximization of biomass. The solver was always set to LK (solverOK = changeCobraSolver('glpk','LP')). For 2 dimensional pareto analyses, one parameter was varied and for each step, the biomass formation was maximized manually. This was not possible for 3 dimensional analyses. For the pareto calculations of dihydroxyacetone uptake, cascade flux and biomass formation, a MATLAB script was applied (see below) and plotted with the Origin Software Pro 8.5. The applied computer was a HP Z220 workstation with an intel core i5 processor with 3.2 GHz CPU, 8 GB RAM and 64-bit Windows 7.

```
n = 0;
m = 0;
k = 1;
X = zeros(110,110);
while n<=50
    model = changeRxnBounds(model, 'EX_ALC1(e)', -n, 'b');
    model = changeRxnBounds(model, 'EX_FIN1(e)', n, 'b');
    m = 0;
    l = 1;
    while m<=50
        model = changeRxnBounds(model, 'EX_dha(e)', -m, 'b');
        FBAsolution = optimizeCbModel(model, 'max');
        X(k,l) = [FBAsolution.f];
        l=l+1;
        m=m+0.5;
    end
    k=k+1;
    n=n+0.5;
end
```

3.14.3 Method development for ^{13}C metabolic flux analysis

The HPLC method was the same as described above for the measurement of metabolomics.

The MRMs were adjusted as shown in Tables 3.28 - 3.30.

Table 3.28: Isotopomer label patterns of the measured fragments (1)

Substance	C # total	m	F1	C # F1	F2	C # F2	F3	C # F3				
Alanine	3	m ₀ 89.90	44.20	2	45.00	1	28.00	1				
			44.20		46.00		29.00					
			45.20		45.00		28.00					
		m ₂ 91.90	45.20	46.00	29.00							
			46.20	45.00	28.00							
		m ₃ 92.90	46.20	46.00	29.00							
		Arginine	6	m ₀ 174.70	60.10	1	116.10	5	X	X		
61.10	116.10											
m ₂ 176.70	60.10			117.10								
	61.10			117.10								
m ₃ 177.70	60.10			118.10								
	61.10			118.10								
m ₄ 178.70	60.10			119.10								
	61.10			119.10								
m ₅ 179.70	60.10			120.10								
	61.10			120.10								
m ₆ 180.70	61.10			121.10								
	61.10			121.10								
Asparagine	4			m ₀ 132.80	74.05		2				87.00	3
		74.05	88.00		X	X						
		75.05	88.00		X	X						
		75.05	87.00		X	X						
		m ₂ 134.80	74.05	89.00	X	X						
			76.05	88.00	X	X						
			75.05	88.00	X	X						
		m ₃ 135.80	75.05	90.00	X	X						
			76.05	89.00	X	X						
			75.05	89.00	X	X						
		m ₄ 136.80	76.05	90.00	X	X						
		Aspartic acid	4	m ₀ 132.00	88.05	3		115.05	4	X	X	
					88.05			116.05				
m ₂ 134.00	89.05			116.05								
	89.05			117.05								
m ₃ 135.00	90.05			117.05								
	91.05			118.05								
m ₄ 136.00	91.05			119.05								
Glutamic acid	5			m ₀ 148.20	84.05		4	56.05				4
		84.05	56.05									
		m ₁ 149.20	85.05	57.05								
			85.05	57.05								
		m ₂ 150.20	86.05	58.05								
			86.05	58.05								
		m ₃ 151.20	87.05	59.05								
			87.05	59.05								
		m ₄ 152.20	88.05	60.05								
			89.05	61.05								

Table 3.29: Isotopomer label patterns of the measured fragments (2)

Substance	C # total	m	F1	C # F1	F2	C # F2	F3	C # F3
Glutamine	5	m ₀ 146.70	84.05	4	130.05	5	X	X
			84.05		131.05			
		m ₁ 147.70	85.05		131.05			
			86.05		132.05			
		m ₂ 148.70	84.05		132.05			
			87.05		133.05			
		m ₃ 149.70	86.07		133.05			
			88.05		134.05			
		m ₄ 150.70	87.05		134.05			
			88.05		135.05			
m ₅ 151.70	88.05	135.05						
Histidine	6	m ₀ 155.60	110.05	5	83.05	4	X	X
			110.05		83.05			
		m ₁ 156.60	111.05		83.05			
			111.05		84.05			
			111.05		83.05			
			111.05		84.05			
		m ₂ 157.60	111.05		83.05			
			111.05		84.05			
			112.05		85.05			
			112.05		84.05			
		m ₃ 158.60	112.05		84.05			
			113.05		85.04			
			113.05		86.04			
			113.05		85.05			
		m ₄ 159.60	113.05		85.05			
			114.05		86.05			
			114.05		87.05			
			114.05		86.05			
		m ₅ 160.60	114.05		86.05			
			115.05		87.05			
115.05	87.05							
115.05	87.05							
Isoleucine	6	m ₀ 131.90	86.10	5	44.10	1	X	X
			87.10		44.10			
		m ₁ 132.90	86.10		45.10			
			87.10		45.10			
		m ₂ 133.90	87.10		44.10			
			88.10		45.10			
		m ₃ 134.90	88.10		44.10			
			89.10		45.10			
		m ₄ 135.90	89.10		44.10			
			90.10		45.10			
		m ₅ 136.90	90.10		44.10			
			91.10		45.10			
m ₆ 137.90	91.10	45.10						
Malic acid	4	m ₀ 133.00	115.00	4	X	X	X	X
		m ₁ 134.00	116.00					
		m ₂ 135.00	117.00					
		m ₃ 136.00	118.00					
		m ₄ 137.00	119.00					

Table 3.30: Isotopomer label patterns of the measured fragments (3)

Substance	C # total	m	F1	C # F1	F2	C # F2	F3	C # F3	
Methionine	5	m ₀ 150.20	104.10	4	61.00	2	X	X	
			m ₁ 151.20		104.10				61.00
					105.10				62.00
		m ₂ 152.20	105.10		62.00				
			106.10		61.00				
			106.10		63.00				
		m ₃ 153.20	106.10		61.00				
			107.10		62.00				
			107.10		63.00				
		m ₄ 154.20	107.10		62.00				
			108.10		63.00				
		m ₅ 155.2	108.10		63.00				
Phenylalanine	9	m ₀ 165.80	120.10	8	103.10	8	X	X	
			120.10		103.10				
		m ₁ 166.80	121.10		104.10				
			121.10		104.10				
		m ₂ 167.80	121.10		105.10				
			122.10		105.10				
		m ₃ 168.80	122.10		105.10				
			123.10		106.10				
		m ₄ 169.80	123.10		106.10				
			124.10		107.10				
		m ₅ 170.80	124.10		107.10				
			125.10		108.10				
		m ₆ 171.80	125.10		108.10				
			126.10		109.10				
m ₇ 172.80	126.10	109.10							
	127.10	110.10							
m ₈ 173.80	127.10	110.10							
	128.10	111.10							
m ₉ 174.80	129.10	112.10							
Threonine	4	m ₀ 120.10	74.10	3	56.05	3	X	X	
			74.10		56.05				
		m ₁ 121.10	75.10		57.05				
			75.10		57.05				
		m ₂ 122.10	75.10		57.05				
			76.10		58.05				
		m ₃ 123.10	76.10		58.05				
77.10	59.05								
m ₄ 124.10	78.10	60.05							
Valine	5	m ₀ 117.90	72.20	4	55.04	4	X	X	
			72.20		55.04				
		m ₁ 118.90	73.20		56.04				
			73.20		56.04				
		m ₂ 119.90	73.20		57.04				
			74.20		57.04				
		m ₃ 120.90	74.20		57.04				
			75.20		58.04				
		m ₄ 121.90	75.20		58.04				
76.20	59.04								
m ₅ 122.90	76.20	59.04							
6-Phospho-D-gluconate	6	m ₀ 275.00	97.05	0	79.05	0	X	X	
			97.05		79.05				
		m ₁ 276.00	97.05		79.05				
		m ₂ 277.00	97.05		79.05				
		m ₃ 278.00	97.05		79.05				
		m ₄ 279.00	97.05		79.05				
		m ₅ 280.00	97.05		79.05				
m ₆ 281.00	97.05	79.05							



Sofia Milker

Curriculum vitae Sofia Milker

Personal Information

Date of birth 27.08.1987
Place of birth St. Petersburg, Russia
Marital status Single
Address Singrienergasse 5/7
1120 Vienna
Phone +43 676 504 795 9
Email sofia.milker@rwth-aachen.de

Academic Studies

Doctoral Studies in Technical Sciences

Since 01/2013 at the Vienna University of Technology (TU Wien)
Institute of Applied Synthetic Chemistry

Title Optimization of biotransformations in *Escherichia coli*: from biocatalyst to the process level

Supervisor Univ.Ass. Dipl.-Ing. Dr.techn. Florian Rudroff and Prof. Dipl.-Ing. Dr.techn. Marko D. Mihovilovic

Master Studies "Biotechnology / Molecular Biotechnology"

10/2010-12/2012 at RWTH Aachen University, *overall grade: 1.3*
Major Field of Study: Biochemical Engineering

12/2012 Master Thesis (Institute of Applied Microbiology at RWTH Aachen University)
grade: 1.3

Title Fundamental physiological characterization of *Clostridium ljungdahlii* especially with regards to itaconic acid toxicity, metabolization and transformation activity

Supervisor Dr. rer. nat. Alexander Henrich and Prof. Dr. Miriam Agler-Rosenbaum

Bachelor Studies "Biotechnology / Molecular Biotechnology"

10/2007-9/2010 at RWTH Aachen University, *overall grade: 1.9*

9/2010 Bachelor Thesis (Institute of Biochemical Engineering), *grade: 1.0*

Title Investigation of influence of organic acids on *Ustilago maydis* to unlock new fuel sources
Supervisor M.Sc. Tobias Klement and Prof. Dr.-Ing. Jochen Büchs

Education

8/1998-7/2007 Mathematisches-Naturwissenschaftliches Gymnasium in Mönchengladbach, Germany, A-Levels, *overall grade: 1.3*

Professional Experience

1/2013-7/2017 Project assistant
at the Institute of Applied Synthetic Chemistry at TU Wien
3/2011-3/2012 Research assistant
at the Institute of Biochemical Engineering at RWTH Aachen University
10/2010-3/2011 Lab course assistant
at the Institute of Biochemical Engineering at RWTH Aachen University

Research Internships

10/2011-01/2012 Research Internship at the Institute of Enzyme Process Engineering, RWTH Aachen University
Topic: Influence of benzaldehyde on the activity of benzaldehyde lyase by means of progress curve experiments
11/2010-02/2011 Research Internship in a cooperation project between the Institutes of Chemical and Biochemical Engineering, RWTH Aachen University
Topic: Continuous *Ustilago maydis* - fermentation with cell retention

Languages

Russian native language
German bilingual
English fluent
Spanish basic knowledge
French basic knowledge

IT skills

Microsoft Office, LaTeX, Origin Pro, GraphPad Prism, MATLAB, Shimdazu Labsolutions, INCA

List of Publications

- 2017 **S. Milker**, M. J. Fink, L. C. P. Goncalves, D. Kracher, R. Ludwig, M. D. Mihovilovic and F. Rudroff. ***Escherichia coli* fails to efficiently maintain an important flavin monooxygenase in recombinant over-expression.** In preparation.
- 2017 T. Wiesinger, T. Bayer, **S. Milker**, M. D. Mihovilovic, and F. Rudroff. **Cell Factory Design and Optimization for the Stereoselective Synthesis of Polyhydroxylated Compounds.** Submitted.

- 2017 **S. Milker**, M. J. Fink, N. Oberleitner, A. K. Ressmann, U. T. Bornscheuer, M. D. Mihovilovic, and F. Rudroff. **Kinetic modeling of an enzymatic redox cascade in vivo reveals cofactor-caused bottlenecks.** *ChemCatChem*. Accepted Author Manuscript. doi: 10.1002/cctc.201700573
- 2017 L. C. P. Goncalves, D. Kracher, **S. Milker**, M. J. Fink, F. Rudroff, R. Ludwig, A. S. Bommarius, and M. D. Mihovilovic. **Mutagenesis-Independent Stabilization of Class B Flavin Monooxygenases in Operation.** *Adv. Synth. Catal.* doi: 10.1002/adsc.201700585
- 2017 **S. Milker**, M. J. Fink, F. Rudroff, and M. D. Mihovilovic. **Non-hazardous biocatalytic oxidation in Nylon-9 monomer synthesis on a 40 g scale with efficient downstream processing.** *Biotechnol. Bioeng.* doi: 10.1002/bit.26312
- 2017 T. Bayer, **S. Milker**, T. Wiesinger, M. Winkler, M. D. Mihovilovic, and F. Rudroff. **In vivo synthesis of polyhydroxylated compounds from a 'hidden reservoir' of toxic aldehyde species** *ChemCatChem*. doi: 10.1002/cctc.201700469
- 2015 T. Bayer, **S. Milker**, T. Wiesinger, F. Rudroff, M. D. Mihovilovic. **Designer Microorganisms for Optimized Redox Cascade Reactions** *Adv. Synth. Catal.* 357, 1587– 1618
- 2012 T. Klement, **S. Milker**, G. Jäger, P.M. Grande, P. Domínguez de María, J. Büchs. **Biomass pretreatment affects *Ustilago maydis* in producing itaconic acid.** *Microb. Cell Fact.* 11:43

Poster

- 2016 **S. Milker**, T. Bayer, M. D. Mihovilovic, F. Rudroff **Influence of Dihydroxyacetone Kinase on Intracellular Fluxes of *E. coli***, COST Training School "Systems Biocatalysis", Siena, Italy, April 27-30, 2016
- 2015 **S. Milker**, M. J. Fink, F. Rudroff, M. D. Mihovilovic: **Scalable Chemo-Enzymatic Synthesis of Polyamide-9 Precursors**, Biotrans, Vienna, Austria, July 26-30, 2015
- 2012 T. Rodrigues, T. Kirchner, A. Henrich, S. Schmitz, A. Belhadi, **S. Milker**, M. Rosenbaum : **Microbiology of Defined Mixed Cultures**, 5th international TMFB workshop, Aachen, Germany, June 13-14, 2012

Other relevant experiences

- 2008-2010 Tutor for first semester students at RWTH Aachen University
- 2007-2009 Scholarship holder, German National Academic Foundation
- 2006 Scientific competition "Jugend Forscht"
3rd rank in section "Environment" (North Rhine-Westfalia state competition)

Hobbies

Literature, contemporary art, football

Vienna, August 14, 2017

Sofia Milker

Singrienergasse 5/7 – 1120 Vienna

☎ 0676 / 5047959 • ✉ sofia.milker@rwth-aachen.de

3/3

4 Bibliography

- [1] U. T. Bornscheuer, G. W. Huisman, R. J. Kazlauskas, S. Lutz, J. C. Moore, and K. Robins. Engineering the third wave of biocatalysis. *Nature*, 485(7397):185–194, 2012.
- [2] L. A. Underkofler, R. R. Barton, and S. S. Rennert. Production of microbial enzymes and their applications. *Appl. Microbiol.*, 6(3):212–221, 1958.
- [3] Y. Asano, T. Yasuda, Y. Tani, and H. Yamada. A new enzymatic method of acrylamide production. *Agric. Biol. Chem.*, 46(5):1183–1189, May 1982.
- [4] A. Bruggink, E. C. Roos, and E. de Vroom. Penicillin acylase in the industrial production of β -lactam antibiotics. *Org. Process. Res. Dev.*, 2(2):128–133, 1998.
- [5] J. Zhang, J.-H. Xu, and M. C. Flickinger. *Biocatalysis, Cofactor Regeneration*. John Wiley & Sons, Inc., 2009. ISBN 9780470054581.
- [6] M. Dreifke, F. J. Brieler, and M. Froeba. Immobilization of alcohol dehydrogenase from *E. coli* onto mesoporous silica for application as a cofactor recycling system. *ChemCatChem.*, 9(7):1197–1210, 2017.
- [7] K. Faber. *Biotransformations in Organic Chemistry*. Springer, 6 edition, 2011.
- [8] S. P. France, L. J. Hepworth, N. J. Turner, and S. L. Flitsch. Constructing biocatalytic cascades: *In Vitro* and *in Vivo* approaches to de novo multi-enzyme pathways. *ACS Catal.*, 7(1):710–724, 2017.
- [9] J. H. Schrittwieser, S. Velikogne, M. Hall, and W. Kroutil. Artificial biocatalytic linear cascades for preparation of organic molecules. *Chem. Rev.*, 2017. in print.
- [10] L. J. Hepworth, S. P. France, S. Hussain, P. Both, N. J. Turner, and S. L. Flitsch. Enzyme cascades in whole cells for the synthesis of chiral cyclic amines. *ACS Catal.*, 7(4):2920–2925, 2017.
- [11] J. L. Foo, A. V. Susanto, J. D. Keasling, S. S. J. Leong, and M. W. Chang. Whole-cell biocatalytic and *de novo* production of alkanes from free fatty acids in *Saccharomyces cerevisiae*. *Biotechnol. Bioeng.*, 114(1):232–237, 2017.
- [12] L. M. Blank, B. E. Ebert, K. Buehler, and B. Buehler. Redox biocatalysis and metabolism: Molecular mechanisms and metabolic network analysis. *Antioxid. Redox Signal.*, 13(3):349–394, 2010.
- [13] T. Bayer, S. Milker, T. Wiesinger, F. Rudroff, and M. D. Mihovilovic. Designer microorganisms for optimized redox cascade reactions - challenges and future perspectives. *Adv. Synth. Catal.*, 357(8):1587–1618, 2015.

- [14] P. Tufvesson, J. Lima-Ramos, N. A. Haque, K. V. Gernaey, and J. M. Woodley. Advances in the process development of biocatalytic processes. *Org. Process. Res. Dev.*, 17(10):1233–1238, 2013.
- [15] H. E. Schoemaker, D. Mink, and M. G. Wubbolts. Dispelling the myths-biocatalysis in industrial synthesis. *Science*, 299(5613):1694–1697, 2003.
- [16] Z. Sun, Y. Wikmark, J.-E. Baeckvall, and M. T. Reetz. New concepts for increasing the efficiency in directed evolution of stereoselective enzymes. *Chem. Eur. J.*, 22(15):5046–5054, 2016.
- [17] K. Balke, M. Baeumgen, and U. T. Bornscheuer. Controlling the regioselectivity of Baeyer-Villiger monooxygenases by mutation of active-site residues. *ChemBioChem.*, 2017. accepted.
- [18] L. G. Otten, F. Hollmann, and I. W.C.E. Arends. Enzyme engineering for enantioselectivity: from trial-and-error to rational design? *Trends Biotechnol.*, 28(1):46–54, 2010.
- [19] M. S. Weiss, I. V. Pavlidis, P. Spurr, S. P. Hanlon, B. Wirz, H. Iding, and U. T. Bornscheuer. Amine transaminase engineering for spatially bulky substrate acceptance. *ChemBioChem.*, 18(11):1022–1026, 2017.
- [20] L. F. Godinho, C. R. Reis, R. van Merkerk, G. J. Poelarends, and W. J. Quax. An esterase with superior activity and enantioselectivity towards 1,2-O-isopropylidenglycerol esters obtained by protein design. *Adv. Synth. Catal.*, 354(16):3009–3015, 2012.
- [21] V. G.H. Eijsink, A. Bjork, S. Gaseidnes, R. Sirevag, B. Synstad, B. van den Burg, and G. Vriend. Rational engineering of enzyme stability. *J. Biotechnol.*, 113(1):105–120, 2004.
- [22] M. T. Reetz. Selected examples of directed evolution of enzymes with emphasis on stereo- and regioselectivity, substrate scope, and/or activity. In *Directed Evolution of Selective Enzymes*, pages 167–203. Wiley-VCH Verlag GmbH & Co. KGaA, 2016.
- [23] S. B. J. Kan, R. D. Lewis, K. Chen, and F. H. Arnold. Directed evolution of cytochrome c for carbon-silicon bond formation: Bringing silicon to life. *Science*, 354(6315):1048, 2016.
- [24] E. J. Corey. Robert robinson lecture. retrosynthetic thinking-essentials and examples. *Chem. Soc. Rev.*, 17(0):111–133, 1988.
- [25] N. J. Turner and E. O'Reilly. Biocatalytic retrosynthesis. *Nat. Chem. Biol.*, 9(5):285–288, 2013.
- [26] R. O. M. A. de Souza, L. S. M. Miranda, and U. T. Bornscheuer. A retrosynthesis approach for biocatalysis in organic synthesis. *Chem. Eur. J.*, 2017. in print.
- [27] M. Hoenig, P. Sondermann, N. J. Turner, and E. M. Carreira. Enantioselective chemo- and biocatalysis: Partners in retrosynthesis. *Angew. Chem. Int. Ed.*, 2017. in print.

- [28] L. He, Y.-Q. Xu, and X.-H. Zhang. Medium factor optimization and fermentation kinetics for phenazine-1-carboxylic acid production by *Pseudomonas* sp. M18G. *Biotechnol. Bioeng.*, 100(2):250–259, 2008.
- [29] S. E. Broedel, S. M. Papciak, and W. R. Jones. The selection of optimum media formulations for improved expression of recombinant proteins in *E. coli*. *Athena Enzyme Systems Technical Bulletin*, 2, 2001.
- [30] A. Weckbecker and W. Hummel. Cloning, expression, and characterization of an (*R*)-specific alcohol dehydrogenase from *Lactobacillus kefir*. *Biocatal. Biotransform.*, 24(5):380–389, 2006.
- [31] H. F. Lodish. *Molecular cell biology*. W.H. Freeman, New York, 4th edition, 2000. Section 6.1 Growth of Microorganisms in Culture.
- [32] A. M. Klibanov. Improving enzymes by using them in organic solvents. *Nature*, 409(6817):241–246, 2001.
- [33] L. Hilterhaus, A. Liese, U. Kragl, and M. C. Flickinger. Biotransformation, process optimization, kinetics and engineering aspects. In *Encyclopedia of Industrial Biotechnology*. John Wiley & Sons, Inc., 2010.
- [34] X.-M. Yang. Optimization of a cultivation process for recombinant protein production by *Escherichia coli*. *J. Biotechnol.*, 23(3):271–289, 1992.
- [35] C. V. F. Baldwin and J. M. Woodley. On oxygen limitation in a whole cell biocatalytic Baeyer-Villiger oxidation process. *Biotechnol. Bioeng.*, 95(3):362–369, 2006.
- [36] R. H. Ringborg and J. M. Woodley. The application of reaction engineering to biocatalysis. *React. Chem. Eng.*, 1:10–22, 2016.
- [37] T. Bayer, S. Milker, T. Wiesinger, M. Winkler, M. D. Mihovilovic, and F. Rudroff. *In vivo* synthesis of polyhydroxylated compounds from a hidden reservoir of toxic aldehyde species. *ChemCatChem.*, 2017. in print.
- [38] J. M. Woodley, M. Bisschops, A. J. J. Straathof, and M. Ottens. Future directions for *in-situ* product removal ISPR. *J. Chem. Technol. Biot.*, 83(2):121–123, 2008.
- [39] W. Van Hecke, G. Kaur, and H. De Wever. Advances in in-situ product recovery (ispr) in whole cell biotechnology during the last decade. *Biotechnol. Adv.*, 32(7):1245 – 1255, 2014.
- [40] R. Abu and J. M. Woodley. Application of enzyme coupling reactions to shift thermodynamically limited biocatalytic reactions. *ChemCatChem.*, 7(19):3094–3105, 10 2015.
- [41] M.R. Aires-Barros and A.M. Azevedo. 7 - fundamentals of biological separation processes. In *Current Developments in Biotechnology and Bioengineering*, pages 187–237. Elsevier, 2017.
- [42] *Impact Kit Instruction Manual*. New England Biolabs.

- [43] Christine M. Ring, Emil S. Iqbal, David E. Hacker, Matthew C. T. Hartman, and T. Ashton Cropp. Genetic incorporation of 4-fluorohistidine into peptides enables selective affinity purification. *Org. Biomol. Chem.*, 15(21):4536–4539, 2017.
- [44] J. Volmer, A. Schmid, and B. Buehler. The application of constitutively solvent-tolerant *P. taiwanensis* vlb120 δ cttg_v for stereospecific epoxidation of toxic styrene alleviates carrier solvent use. *Biotechnol. J.*, 12(7), 2017. in print.
- [45] F. Carstensen, T. Klement, J. Buechs, T. Melin, and M. Wessling. Continuous production and recovery of itaconic acid in a membrane bioreactor. *Bioresour. Technol.*, 137:179–187, 2013.
- [46] F. Rudroff, V. Alphand, R. Furstoss, and M. D. Mihovilovic. Optimizing fermentation conditions of recombinant *Escherichia coli* expressing cyclopentanone monooxygenase. *Org. Process. Res. Dev.*, 10(3):599–604, 2006.
- [47] I. Hilker, M. C. Gutierrez, R. Furstoss, J. Ward, R. Wohlgemuth, and V. Alphand. Preparative scale Baeyer-Villiger biooxidation at high concentration using recombinant *Escherichia coli* and *in situ* substrate feeding and product removal process. *Nat. Protocols*, 3(3):546–554, 2008.
- [48] K. M. Dombek and L. O. Ingram. Ethanol production during batch fermentation with *Saccharomyces cerevisiae*: changes in glycolytic enzymes and internal pH. *Appl. Environ. Microbiol.*, 53(6):1286–1291, 1987.
- [49] M. Sauer, D. Porro, D. Mattanovich, and P. Branduardi. Microbial production of organic acids: expanding the markets. *Trends Biotechnol.*, 26(2):100–108, 2008.
- [50] E.B. Goh, E. E. K. Baidoo, H. Burd, T. S. Lee, J. D. Keasling, and H. R. Beller. Substantial improvements in methyl ketone production in *E. coli* and insights on the pathway from *in vitro* studies. *Metab. Eng.*, 26(0):67–76, 2014.
- [51] M. T. Reetz. Biocatalysis in organic chemistry and biotechnology: Past, present, and future. *J. Am. Chem. Soc.*, 135(34):12480–12496, 2013.
- [52] R. D. Woodyer, T. W. Johannes, and H. Zhao. *Enzyme technology*. Springer, New York, 2nd edition, 2008.
- [53] G. W. Huisman and S. J. Collier. On the development of new biocatalytic processes for practical pharmaceutical synthesis. *Curr. Opin. Chem. Biol.*, 17(2):284–292, 2013.
- [54] A. Berkessel, C. Rollmann, F. Chamouleau, S. Labs, O. May, and H. Groeger. Practical Two-Step Synthesis of an Enantiopure Aliphatic Terminal (S)-Epoxide Based on Reduction of Haloalkanones with Designer Cells. *Adv. Synth. Catal.*, 349(17-18): 2697–2704, 2007.
- [55] N. Oberleitner, C. Peters, J. Muschiol, M. Kadow, S. Sass, T. Bayer, P. Schaaf, N. Iqbal, F. Rudroff, M. D. Mihovilovic, and U. T. Bornscheuer. An enzymatic toolbox for cascade reactions: A showcase for an *In Vivo* redox sequence in asymmetric synthesis. *ChemCatChem.*, 5(12):3524–3528, 2013.

- [56] R. Agudo and M. T. Reetz. Designer cells for stereocomplementary de novo enzymatic cascade reactions based on laboratory evolution. *Chem. Commun.*, 49(93):10914–10916, 2013.
- [57] A. M. Kunjapur, Y. Tarasova, and K. L. Prather. Synthesis and accumulation of aromatic aldehydes in an engineered strain of *Escherichia coli*. *J. Am. Chem. Soc.*, 136(33):11644–54, 2014.
- [58] S. Wu, Y. Zhou, T. Wang, H.-P. Too, D. I. C. Wang, and Z. Li. Highly regio- and enantioselective multiple oxy- and amino-functionalizations of alkenes by modular cascade biocatalysis. *Nat. Commun.*, 7(11917), 2016.
- [59] M. A. Campodonico, B. A. Andrews, J. A. Asenjo, B. O. Palsson, and A. M. Feist. Generation of an atlas for commodity chemical production in *Escherichia coli* and a novel pathway prediction algorithm, gem-path. *Metab. Eng.*, 25:140–158, 2014.
- [60] K. Tummler, T. Lubitz, M. Schelker, and E. Klipp. New types of experimental data shape the use of enzyme kinetics for dynamic network modeling. *FEBS J.*, 281(2):549–571, 2014.
- [61] M. Almquist, J. Cvijovic, V. Hatzimanikatis, J. Nielsen, and M. Jirstrand. Kinetic models in industrial biotechnology - improving cell factory performance. *Metab. Eng.*, 24:38 – 60, 2014.
- [62] D. A. Fell and H. M. Sauro. Metabolic control analysis. *Eur. J. Biochem.*, 192(1):183–187, 1990.
- [63] D. Visser and J. J. Heijnen. The mathematics of metabolic control analysis revisited. *Metab. Eng.*, 4(2):114 – 123, 2002.
- [64] E. V. Nikolaev. The elucidation of metabolic pathways and their improvements using stable optimization of large-scale kinetic models of cellular systems. *Metab. Eng.*, 12(1):26 – 38, 2010.
- [65] M. Maurer, M. Kühleitner, B. Gasser, and D. Mattanovich. Versatile modeling and optimization of fed batch processes for the production of secreted heterologous proteins with *Pichia pastoris*. *Microb. Cell Fact.*, 5(1):37, 2006.
- [66] M. C. Hogan and J. M. Woodley. Modelling of two enzyme reactions in a linked cofactor recycle system for chiral lactone synthesis. *Chem. Eng. Sci.*, 55(11):2001–2008, 2000.
- [67] C. Scherkus, S. Schmidt, U. T. Bornscheuer, H. Groeger, S. Kara, and A. Liese. Kinetic insights into ϵ -caprolactone synthesis: Improvement of an enzymatic cascade reaction. *Biotechnol. Bioeng.*, 2017.
- [68] G. Franceschini and S. Macchietto. Model-based design of experiments for parameter precision: State of the art. *Chem. Eng. Sci.*, 63(19):4846 – 4872, 2008.
- [69] D. Telen, F. Logist, E. Van Derlinden, I. Tack, and J. Van Impe. Optimal experiment design for dynamic bioprocesses: A multi-objective approach. *Chem. Eng. Sci.*, 78:82 – 97, 2012.

- [70] J. S. Edwards, R. U. Ibarra, and B. O. Palsson. In silico predictions of *Escherichia coli* metabolic capabilities are consistent with experimental data. *Nat. Biotechnol.*, 19(2):125–130, 2001.
- [71] J. D. Orth, I. Thiele, and B. O. Palsson. What is flux balance analysis? *Nature Biotechnology*, 28(3):245–248, 2010.
- [72] R. Schuetz, L. Kuepfer, and U. Sauer. Systematic evaluation of objective functions for predicting intracellular fluxes in *Escherichia coli*. *Mol. Syst. Biol.*, 3, 2007.
- [73] C. S. Henry, M. DeJongh, A. A. Best, P. M. Frybarger, B. Linsay, and R. L. Stevens. High-throughput generation, optimization and analysis of genome-scale metabolic models. *Nat. Biotechnol.*, 28(9):977–982, 2010.
- [74] J. Schellenberger, J. O. Park, T. M. Conrad, and B. O. Palsson. BiGG: a biochemical genetic and genomic knowledgebase of large scale metabolic reconstructions. *BMC Bioinf.*, 11, 2010.
- [75] J. Schellenberger, R. Que, R. M. T. Fleming, I. Thiele, J. D. Orth, A. M. Feist, D. C. Zielinski, A. Bordbar, N. E. Lewis, S. Rahmanian, J. Kang, D. R. Hyduke, and B. O. Palsson. Quantitative prediction of cellular metabolism with constraint-based models: the COBRA toolbox v2.0. *Nat. Protoc.*, 6(9):1290–1307, 2011.
- [76] M. Lakshmanan, G. Koh, B. K. S. Chung, and D. Y. Lee. Software applications for flux balance analysis. *Briefings Bioinf.*, 15(1):108–122, 2014.
- [77] L. Kuepfer, U. Sauer, and L. M. Blank. Metabolic functions of duplicate genes in *Saccharomyces cerevisiae*. *Genome Res.*, 15(10):1421–1430, 2005.
- [78] K. Hoffner, S. M. Harwood, and P. I. Barton. A reliable simulator for dynamic flux balance analysis. *Biotechnol. Bioeng.*, 110(3):792–802, 2013.
- [79] F. Pizarro, C. Varela, C. Martabit, C. Bruno, J. R. Perez-Correa, and E. Agosin. Coupling kinetic expressions and metabolic networks for predicting wine fermentations. *Biotechnol. Bioeng.*, 98(5):986–998, 2007.
- [80] J. Sainz, F. Pizarro, J. R. Perez-Correa, and E. Agosin. Modeling of yeast metabolism and process dynamics in batch fermentation. *Biotechnol. Bioeng.*, 81(7):818–828, 2003.
- [81] F. A. Vargas, F. Pizarro, J. R. Peccoud, Jerez-Correa, and E. Agosin. Expanding a dynamic flux balance model of yeast fermentation to genome-scale. *BMC Syst. Biol.*, 5(1):75, 2011.
- [82] N. J. Stanford, T. Lubitz, K. Smallbone, E. Klipp, P. Mendes, and W. Liebermeister. Systematic construction of kinetic models from genome-scale metabolic networks. *PLOS ONE*, 8(11):e79195, 2013.
- [83] M. A. Henson. Genome-scale modelling of microbial metabolism with temporal and spatial resolution. *Biochem. Soc. Trans.*, 43(6):1164, 2015.
- [84] J. P. Barreto-Rodriguez, C. M. and Ramirez-Angulo, J. M. G. Ramirez, L. Achenie, H. Molina-Bulla, and A. F. G. Barrios. Dynamic flux balance analysis for predicting gene overexpression effects in batch cultures. *J. Biol. Syst.*, 22(03):327–338, 2014.

- [85] C. W. Song, D. I. Kim, S. Choi, J. W. Jang, and S. Y. Lee. Metabolic engineering of *Escherichia coli* for the production of fumaric acid. *Biotechnol. Bioeng.*, 110(7):2025–2034, 2013.
- [86] M. Weiner, J. Troendle, C. Albermann, G. A. Sprenger, and D. Weuster-Botz. Improvement of constraint-based flux estimation during L-phenylalanine production with *Escherichia coli* using targeted knock-out mutants. *Biotechnol. Bioeng.*, 111(7):1406–1416, 2014.
- [87] K. Tokuyama, S. Ohno, K. Yoshikawa, T. Hirasawa, S. Tanaka, C. Furusawa, and H. Shimizu. Increased 3-hydroxypropionic acid production from glycerol, by modification of central metabolism in *Escherichia coli*. *Microb. Cell Fact.*, 13, 2014.
- [88] N. Zamboni, E. Fischer, and U. Sauer. Fiatflux - a software for metabolic flux analysis from C-13-glucose experiments. *BMC Bioinf.*, 6, 2005.
- [89] W. Wiechert, M. Moellney, S. Petersen, and A. A. de Graaf. A universal framework for 13C metabolic flux analysis. *Metab. Eng.*, 3(3):265–283, 2001.
- [90] L.-E. Quek, C. Wittmann, L. Nielsen, and J. Kromer. OpenFLUX: efficient modelling software for 13C-based metabolic flux analysis. *Microb. Cell Fact.*, 8(1):25, 2009.
- [91] T. Dandekar, A. Fieselmann, S. Majeed, and Z. Ahmed. Software applications toward quantitative metabolic flux analysis and modeling. *Briefings Bioinf.*, 15(1):91–107, 2014.
- [92] M. R. Antoniewicz. Methods and advances in metabolic flux analysis: a mini-review. *J. Ind. Microbiol. Biotechnol.*, pages 1–9, 2015.
- [93] E. Fischer, N. Zamboni, and U. Sauer. High-throughput metabolic flux analysis based on gas chromatography-mass spectrometry derived 13C constraints. *Anal. Biochem.*, 325(2):308–316, 2004.
- [94] E. Fischer and U. Sauer. Metabolic flux profiling of *Escherichia coli* mutants in central carbon metabolism using GC-MS. *Eur. J. Biochem.*, 270(5):880–891, 2003.
- [95] N. Zamboni, S.-M. Fendt, M. Ruhl, and U. Sauer. 13C-based metabolic flux analysis. *Nat. Protoc.*, 4(6):878–892, 2009.
- [96] R. R. Bommarreddy, Z. Chen, S. Rappert, and A.-P. Zeng. A *de novo* nadph generation pathway for improving lysine production of *Corynebacterium glutamicum* by rational design of the coenzyme specificity of glyceraldehyde 3-phosphate dehydrogenase. *Metab. Eng.*, 25(0):30–37, 2014.
- [97] Scott B. Crown, Christopher P. Long, and Maciek R. Antoniewicz. Integrated 13C-metabolic flux analysis of 14 parallel labeling experiments in *Escherichia coli*. *Metab. Eng.*, 28(0):151–158, 2015.
- [98] K. Schroer, B. Zelic, M. Oldiges, and S. Luetz. Metabolomics for biotransformations: Intracellular redox cofactor analysis and enzyme kinetics offer insight into whole-cell processes. *Biotechnol. Bioeng.*, 104(2):251–260, 2009.

- [99] L. Wu, M. R. Mashego, J. C. van Dam, A. M. Proell, J. L. Vinke, C. Ras, W. A. van Winden, W. M. van Gulik, and J. J. Heijnen. Quantitative analysis of the microbial metabolome by isotope dilution mass spectrometry using uniformly C-13-labeled cell extracts as internal standards. *Anal. Biochem.*, 336(2):164–171, 2005.
- [100] W. M. van Gulik. Fast sampling for quantitative microbial metabolomics. *Curr. Opin. Biotechnol.*, 21(1):27–34, 2010.
- [101] A. B. Canelas, C. Ras, A. ten Pierick, J. C. van Dam, J. J. Heijnen, and W. M. Van Gulik. Leakage-free rapid quenching technique for yeast metabolomics. *Metabolomics.*, 4(3):226–239, 2008.
- [102] H. Link, J. M. Buescher, and U. Sauer. *Chapter 5 - Targeted and quantitative metabolomics in bacteria*, volume 39, pages 127–150. Academic Press, 2012.
- [103] J. Rucker, J. Paul, B. A. Pfeifer, and K. Lee. Engineering *E. coli* for triglyceride accumulation through native and heterologous metabolic reactions. *Appl. Microbiol. Biotechnol.*, 97(6):2753–2759, 2013.
- [104] Y. Soma, K. Tsuruno, M. Wada, A. Yokota, and T. Hanai. Metabolic flux redirection from a central metabolic pathway toward a synthetic pathway using a metabolic toggle switch. *Metab. Eng.*, 23:175–184, 2014.
- [105] B. Herzog, M. I. Kohan, S. A. Mestemacher, R. U. Pagilagan, and K. Redmond. *Polyamides*. Wiley-VCH Verlag GmbH & Co. KGaA, 2000.
- [106] T. M. Carole, J. Pellegrino, and M. D. Paster. Opportunities in the industrial biobased products industry. *Appl. Biochem. Biotechnol.*, 113:871–885, 2004.
- [107] M. Suastegui, J. E. Matthiesen, J. M. Carraher, N. Hernandez, N. Rodriguez Quiroz, A. Okerlund, E. W. Cochran, Z. Shao, and J.-P. Tessonier. Combining metabolic engineering and electrocatalysis: Application to the production of polyamides from sugar. *Angew. Chem. Int. Ed.*, 55(7):2368–2373, 2016.
- [108] S. Sengupta, S. Jonnalagadda, L. Goonewardena, and V. Juturu. Metabolic engineering of a novel muconic acid biosynthesis pathway via 4-hydroxybenzoic acid in *Escherichia coli*. *Appl. Environ. Microbiol.*, 81(23):8037–43, 2015.
- [109] C. F. Horn, B. T. Freure, H. Vineyard, and H. J. Decker. Nylon 7, a fiber forming polyamide. *J. Appl. Polym. Sci.*, 7(3):887–896, 1963.
- [110] D. Teomim, A. Nyska, and A. J. Domb. Ricinoleic acid-based biopolymers. *J. Biomed. Mater. Res.*, 45(3):258–267, 1999.
- [111] Y.-X. Cao, W.-H. Xiao, D. Liu, J.-L. Zhang, M.-Z. Ding, and Y.-J. Yuan. Biosynthesis of odd-chain fatty alcohols in *Escherichia coli*. *Metab. Eng.*, 29:113–123, 2015.
- [112] H. Wu and K.-Y. San. Efficient odd straight medium chain free fatty acid production by metabolically engineered *Escherichia coli*. *Biotechnol. Bioeng.*, 111(11):2209–2219, 2014.
- [113] C A Finch. *Industrial polymers handbook: Products, Processes, Applications*, volume 1. Wiley-VCH, Weinheim, 2001.

- [114] S. Schaffer and T. Haas. Biocatalytic and fermentative production of α , ω -bifunctional polymer precursors. *Org. Process. Res. Dev.*, 18(6):752–766, 2014.
- [115] N. Ladkau, M. Assmann, M. Schrewe, M. K. Julsing, A. Schmid, and B. Buehler. Efficient production of the nylon 12 monomer ω -aminododecanoic acid methyl ester from renewable dodecanoic acid methyl ester with engineered *Escherichia coli*. *Metab. Eng.*, 36:1–9, 2016.
- [116] L. Cotarca, P. Delogu, A. Nardelli, P. Maggioni, R. Bianchini, S. Sguassero, S. Alini, R. Dario, G. Clauti, G. Pitta, G. Duse, and F. Goffredi. Efficient and scaleable methods for omega-functionalized nonanoic acids: Development of a novel process for azelaic and 9-aminononanoic acids (nylon-6,9 and nylon-precursors). *Org. Process. Res. Dev.*, 5(1):69–76, 2001.
- [117] Hermann Rath. *Lehrbuch der Textilchemie einschliesslich der textilchemischen Technologie*. Springer Berlin Heidelberg, Berlin, Heidelberg, 1972.
- [118] F. Minisci, P. Maggioni, and A. Citterio. Process for producing difunctional aliphatic organic compounds, 1982. Google Patents.
- [119] N. M. Kamerbeek, D. B. Janssen, W. J. H. van Berkel, and M. W. Fraaije. Baeyer-Villiger monooxygenases, an emerging family of flavin-dependent biocatalysts. *Adv. Synth. Catal.*, 345(6-7):667–678, 2003.
- [120] W. D. Fessner and T. Anthonsen, editors. *Modern Biocatalysis - Stereoselective and Environmentally friendly reactions*. Wiley-VCH, 2009.
- [121] P. Chaiyen, M. W. Fraaije, and A. Mattevi. The enigmatic reaction of flavins with oxygen. *Trends Biochem. Sci.*, 37(9):373–380, 2012.
- [122] D. Leys and N. S. Scrutton. Sweating the assets of flavin cofactors: new insight of chemical versatility from knowledge of structure and mechanism. *Curr. Opin. Struct. Biol.*, 41:19–26, 2016.
- [123] M. J. Fink, R. Snajdrova, A. Winninger, and M. D. Mihovilovic. Regio- and stereoselective synthesis of chiral nitrilolactones using Baeyer - Villiger monooxygenases. *Tetrahedron.*, 2015.
- [124] N. Berezina, E. Kozma, R. Furstoss, and V. Alphand. Asymmetric Baeyer-Villiger biooxidation of α -substituted cyanocyclohexanones: Influence of the substituent length on regio- and enantioselectivity. *Adv. Synth. Catal.*, 349(11-12):2049–2053, 2007.
- [125] M. J. Fink. *Application of Baeyer - Villiger Monooxygenases in fine and bulk chemical synthesis*. PhD thesis, TU Wien, 2013.
- [126] H. Iwaki, S. Wang, S. Grosse, H. Bergeron, A. Nagahashi, J. Lertvorachon, J. Yang, Y. Konishi, Y. Hasegawa, and P. C. Lau. *Pseudomonas* cyclopentadecanone monooxygenase displaying an uncommon spectrum of Baeyer-Villiger oxidations of cyclic ketones. *App. Environ. Microbiol.*, 72(4):2707–20, 2006.

- [127] H. Leisch, R. Shi, S. Grosse, K. Morley, H. Bergeron, M. Cygler, H. Iwaki, Y. Hasegawa, and P. C. Lau. Cloning, Baeyer-Villiger biooxidations, and structures of the camphor pathway 2-oxo-delta(3)-4,5,5-trimethylcyclopentenylacetyl-coenzyme a monooxygenase of *Pseudomonas putida* ATCC 17453. *Appl. Environ. Microbiol.*, 78(7):2200–12, 2012.
- [128] M. Kadow, K. Loschinski, S. Sass, M. Schmidt, and U. T. Bornscheuer. Completing the series of bvmos involved in camphor metabolism of *Pseudomonas putida* NCIMB 10007 by identification of the two missing genes, their functional expression in *E. coli*, and biochemical characterization. *Appl. Microbiol. Biotechnol.*, 96(2):419–429, 2012.
- [129] A. Z. Walton and J. D. Stewart. Understanding and improving nadph-dependent reactions by nongrowing *Escherichia coli* cells. *Biotechnol. Progr.*, 20(2):403–411, 2004.
- [130] P. Via, J. Badia, L. Baldoma, N. Obradors, and J. Aguilar. Transcriptional regulation of the *Escherichia coli* rhaT gene. *Microbiology.*, 142(7):1833–1840, 1996.
- [131] S. Bauer and J. Shiloach. Maximal exponential growth rate and yield of *E. coli* obtainable in a bench-scale fermentor. *Biotechnol. Bioeng.*, 16(7):933–941, 1974.
- [132] Q. Hua, C. Yang, T. Oshima, H. Mori, and K. Shimizu. Analysis of gene expression in *Escherichia coli* in response to changes of growth-limiting nutrient in chemostat cultures. *Appl. Environ. Microbiol.*, 70(4):2354–2366, 2004.
- [133] B. T. Koh, U. Nakashimada, M. Pfeiffer, and M. G. S. Yap. Comparison of acetate inhibition on growth of host and recombinant *E. coli* K12 strains. *Biotechnol. Lett.*, 14(12):1115–1118, 1992.
- [134] G. Bratbak and I. Dundas. Bacterial dry matter content and biomass estimations. *Appl. Environ. Microbiol.*, 48(4):755–757, 1984.
- [135] S. D. Doig, P. J. Avenell, P. A. Bird, Pa. Gallati, K. S. Lander, G. J. Lye, R. Wohlgemuth, and J. M. Woodley. Reactor operation and scale-up of whole cell Baeyer-Villiger catalyzed lactone synthesis. *Biotechnol. Progr.*, 18(5):1039–1046, 2002.
- [136] I. Hilker, V. Alphand, R. Wohlgemuth, and R. Furstoss. Microbial transformations, 56. preparative scale asymmetric Baeyer - Villiger oxidation using a highly productive "two-in-one" resin-based *in situ* SFPR concept. *Adv. Synth. Catal.*, 346(2-3):203–214, 2004.
- [137] I. Hilker, C. Baldwin, V. Alphand, R. Furstoss, J. Woodley, and R. Wohlgemuth. On the influence of oxygen and cell concentration in an SFPR whole-cell biocatalytic Baeyer-Villiger oxidation process. *Biotechnol. Bioeng.*, 93(6):1138–1144, 2006.
- [138] K. Geitner, J. Rehdorf, R. Snajdrova, and U. T. Bornscheuer. Scale-up of Baeyer-Villiger monooxygenase-catalyzed synthesis of enantiopure compounds. *Appl. Microbiol. Biotechnol.*, 88(5):1087–1093, 2010.
- [139] ACS GCIPR. American chemical society green chemistry institute pharmaceutical roundtable solvent selection guide, 2011.
- [140] E. Ricca, B. Brucher, and J. H. Schrittwieser. Multi-enzymatic cascade reactions: Overview and perspectives. *Adv. Synth. Catal.*, 353(13):2239–2262, 2011.

- [141] Stuart G. Warren and Paul Wyatt. *Organic synthesis : the disconnection approach*. John Wiley & Sons Ltd., Chichester, UK, 2nd edition, 2008.
- [142] M. Sudar, Z. Findrik, D. Vasic-Racki, P. Clapes, and C. Lozano. Mathematical model for aldol addition catalyzed by two d-fructose-6-phosphate aldolases variants overexpressed in *E. coli*. *J. Biotechnol.*, 167(3):191–200, 2013.
- [143] C. Zhong, P. Wei, and Y.-H. P. Zhang. A kinetic model of one-pot rapid biotransformation of cellobiose from sucrose catalyzed by three thermophilic enzymes. *Chem. Eng. Sci.*, 161:159–166, 2017.
- [144] D. Machado, L. R. Rodrigues, and I. Rocha. A kinetic model for curcumin production in *Escherichia coli*. *Biosystems.*, 125C:16–21, 2014.
- [145] L. Kuepfer, U. Peter, M. and Sauer, and J. Stelling. Ensemble modeling for analysis of cell signaling dynamics. *Nat. Biotech.*, 25(9):1001–1006, 2007.
- [146] J. Hassan, L. L. Bergaust, L. Molstad, S. de Vries, and L. R. Bakken. Homeostatic control of nitric oxide (NO) at nanomolar concentrations in denitrifying bacteria - modelling and experimental determination of NO reductase kinetics in vivo in *Paracoccus denitrificans*. *Environ. Microbiol.*, 18(9):2964–2978, 2016.
- [147] N. Oberleitner, C. Peters, F. Rudroff, U. T. Bornscheuer, and M. D. Mihovilovic. *In vitro* characterization of an enzymatic redox cascade composed of an alcohol dehydrogenase, an enoate reductases and a Baeyer - Villiger monooxygenase. *J. Biotechnol.*, 192:393–399, 2014.
- [148] C. Peters, R. Koelzsch, M. Kadow, L. Skalden, F. Rudroff, M. D. Mihovilovic, and U. T. Bornscheuer. Identification, characterization, and application of three enoate reductases from *Pseudomonas putida* in *In Vitro* enzyme cascade reactions. *Chem-CatChem.*, 6(4):1021–1027, 2014.
- [149] N. A. Donoghue, D. B. Norris, and P. W. Trudgill. The purification and properties of cyclohexanone oxygenase from *Nocardia globerula* CL1 and *Acinetobacter* NCIB 9871. *Eur. J. Biochem.*, 63(1):175–192, 1976.
- [150] S. Spaans, R. Weusthuis, J. Van Der Oost, and S. Kengen. NADPH-generating systems in bacteria and archaea. *Front. Microbiol.*, 6:742, 2015.
- [151] F. J. Weber and J. A. M. de Bont. Adaptation mechanisms of microorganisms to the toxic effects of organic solvents on membranes. *Biochim. Biophys. Acta. Biomemb.*, 1286(3):225–245, 1996.
- [152] Y. L. Khmel'nitsky, V. V. Mozhaev, A. B. Belova, M. V. Sergeeva, and K. Martinek. Denaturation capacity: a new quantitative criterion for selection of organic solvents as reaction media in biocatalysis. *Eur. J. Biochem.*, 198(1):31–41, 1991.
- [153] K. B. Andersen and K. von Meyenburg. Charges of nicotinamide adenine nucleotides and adenylate energy charge as regulatory parameters of the metabolism in *Escherichia coli*. *J. Biol. Chem.*, 252(12):4151–4156, 1977.

- [154] B. D. Bennett, E. H. Kimball, M. Gao, R. Osterhout, S. J. Van Dien, and J. D. Rabinowitz. Absolute metabolite concentrations and implied enzyme active site occupancy in *Escherichia coli*. *Nat. Chem. Biol.*, 5(8):593–599, 2009.
- [155] H. L. van Beek, H. J. Wijma, L. Fromont, D. B. Janssen, and M. W. Fraaije. Stabilization of cyclohexanone monooxygenase by a computationally designed disulfide bond spanning only one residue. *FEBS Open Bio.*, 4(1):168–174, 2014.
- [156] C. A. Abbas and A. A. Sibirny. Genetic control of biosynthesis and transport of riboflavin and flavin nucleotides and construction of robust biotechnological producers. *Microbiol. Mol. Biol. Rev.*, 75(2):321–360, 2011.
- [157] E. Romero, J. R. G. Castellanos, A. Mattevi, and M. W. Fraaije. Characterization and crystal structure of a robust cyclohexanone monooxygenase. *Angew. Chem. Int. Ed.*, 55(51):15852–5, 2016.
- [158] M. Bucko, P. Gemeiner, T. Schenk Mayerova, A. Krajcovic, F. Rudroff, and M. D. Mihovilovic. Baeyer-Villiger oxidations: biotechnological approach. *Appl. Microbiol. Biotechnol.*, 100(15):6585–6599, 2016.
- [159] M. J. Fink, D. V. Rial, P. Kapitanova, A. Lengar, J. Rehdorf, Q. Cheng, F. Rudroff, and M. D. Mihovilovic. Quantitative comparison of chiral catalysts selectivity and performance: A generic concept illustrated with cyclododecanone monooxygenase as Baeyer-Villiger biocatalyst. *Adv. Synth. Catal.*, 354(18):3491–3500, 2012.
- [160] D. E. Torres Pazmino, H. M. Dudek, and M. W. Fraaije. Baeyer-Villiger monooxygenases: recent advances and future challenges. *Curr. Opin. Chem. Biol.*, 14(2):138–144, 2010.
- [161] C. V. F. Baldwin, R. Wohlgemuth, and J. M. Woodley. The first 200-L scale asymmetric Baeyer-Villiger oxidation using a whole-cell biocatalyst. *Org. Process Res. Dev.*, 12(4):660–665, 2008.
- [162] S. Selvarasu, D. S.-W. Ow, S. Y. Lee, M. M. Lee, S. K.-W. Oh, I. A. Karimi, and D.-Y. Lee. Characterizing *Escherichia coli* DH5 α growth and metabolism in a complex medium using genome-scale flux analysis. *Biotechnol. Bioeng.*, 102(3):923–934, 2009.
- [163] G. L. Rosano and E. A. Ceccarelli. Recombinant protein expression in *Escherichia coli*: advances and challenges. *Front. Microbiol.*, 5:172, 2014.
- [164] M. W. Fraaije, J. Wu, D. P. H. M. Heuts, E. W. van Hellemond, J. H. L. Spelberg, and D. B. Janssen. Discovery of a thermostable Baeyer-Villiger monooxygenase by genome mining. *Appl. Microbiol. Biotechnol.*, 66(4):393–400, 2005.
- [165] K. Balke, M. Kadow, H. Mallin, S. Sass, and Uwe T. Bornscheuer. Discovery, application and protein engineering of Baeyer-Villiger monooxygenases for organic synthesis. *Org. Biomol. Chem.*, 10(31):6249–6265, 2012.
- [166] Y.K. Bong, M.D. Clay, S.J. Collier, B. Mijts, M. Vogel, X. Zhang, J. Zhu, J. Nazor, D. Smith, and S. Song. Synthesis of prazole compounds, 2013. European Patent Application No. EP2010836590.

- [167] S. Schmidt, M. Genz, K. Balke, and U. T. Bornscheuer. The effect of disulfide bond introduction and related cys/ser mutations on the stability of cyclohexanone monooxygenase. *J. Biotechnol.*, 214:199–211, 2015.
- [168] L.C.P. Goncalves, D. Kracher, S. Milker, F. Rudroff, M. J. Fink, R. Ludwig, A. Bommarius, and M. D. Mihovilovic. Mutagenesis-independent, stabilization of class B flavin monooxygenases in operation. *Adv. Synth. Catal.* in print.
- [169] S. D Doig, H. Simpson, V. Alphand, R. Furstoss, and J. M Woodley. Characterization of a recombinant *Escherichia coli* TOP10 [pQR239] whole-cell biocatalyst for stereoselective Baeyer-Villiger oxidations. *Enzyme Microb. Technol.*, 32(3-4):347–355, March 2003.
- [170] W. Kloeckner and J. Buechs. Advances in shaking technologies. *Trends Biotechnol.*, 30(6):307–314, 2012.
- [171] B. Volkmer and M. Heinemann. Condition-dependent cell volume and concentration of *Escherichia coli* to facilitate data conversion for systems biology modeling. *PLoS ONE*, 6(7), 2011.
- [172] A. G. Chapman, L. Fall, and D. E. Atkinson. Adenylate energy charge in *Escherichia coli* during growth and starvation. *J. Bacteriol.*, 108(3):1072–1086, 1971.
- [173] M. J. Brauer, J. Yuan, B. D. Bennett, W. Lu, E. Kimball, D. Botstein, and J. D. Rabinowitz. Conservation of the metabolomic response to starvation across two divergent microbes. *Proc. Natl. Acad. Sci. U. S. A.*, 103(51):19302–19307, 2006.
- [174] P. Macheroux, B. Kappes, and S. E. Ealick. Flavogenomics - a genomic and structural view of flavin-dependent proteins. *FEBS J.*, 278(15):2625–2634, 2011.
- [175] P. H. Seeberger and D. B. Werz. Automated synthesis of oligosaccharides as a basis for drug discovery. *Nat. Rev. Drug Discov.*, 4(9):751–763, 2005.
- [176] A. Fernandez-Tejada, F. J Canada, and J. Jimenez-Barbero. Recent developments in synthetic carbohydrate-based diagnostics, vaccines, and therapeutics. *Chem. Eur. J.*, 21(30):10616–10628, 2015.
- [177] B. Lepenies, J. Yin, and P. H. Seeberger. Applications of synthetic carbohydrates to chemical biology. *Curr. Opin. Chem. Biol.*, 14(3):404–411, 2010.
- [178] M. C. Galan, D. Benito-Alifonso, and G. M. Watt. Carbohydrate chemistry in drug discovery. *Org. Biomol. Chem.*, 9(10):3598–3610, 2011.
- [179] T. Hudlicky, D. A. Entwistle, K. K. Pitzer, and A. J. Thorpe. Modern methods of monosaccharide synthesis from non-carbohydrate sources. *Chem. Rev.*, 96(3):1195–1220, 1996.
- [180] C. Palomo, M. Oiarbide, and J. M. Garcia. Current progress in the asymmetric aldol addition reaction. *Chem. Soc. Rev.*, 33(2):65–75, 2004.
- [181] T. Mukaiyama. *The Directed Aldol Reaction*. John Wiley & Sons, Inc., 2004. ISBN 9780471264187.

- [182] M. Markert and R. Mahrwald. Total syntheses of carbohydrates: Organocatalyzed aldol additions of dihydroxyacetone. *Chem. Eur. J.*, 14(1):40–48, 2008.
- [183] J. Mlynarski and B. Gut. Organocatalytic synthesis of carbohydrates. *Chem. Soc. Rev.*, 41(2):587–596, 2012.
- [184] W.-D. Fessner. Enzyme mediated C-C bond formation. *Curr. Opin. Chem. Biol.*, 2(1):85 – 97, 1998.
- [185] D Gueclue, A. Szekrenyi, X. Garrabou, M. Kickstein, S. Junker, P. Clapes, and W.-D. Fessner. Minimalist protein engineering of an aldolase provokes unprecedented substrate promiscuity. *ACS Catal.*, 6(3):1848–1852, 2016.
- [186] M. Wei, Z. Li, T. Li, B. Wu, Y. Liu, J. Qu, X. Li, L. Li, L. Cai, and P. G. Wang. Transforming flask reaction into cell-based synthesis: Production of polyhydroxylated molecules via engineered *Escherichia coli*. *ACS Catal.*, 5(7):4060–4065, 2015.
- [187] C. Siebold, I. Arnold, L. F. Garcia-Alles, U. Baumann, and B. Erni. Crystal structure of the *Citrobacter freundii* dihydroxyacetone kinase reveals an eight-stranded α -helical barrel ATP-binding domain. *J. Biol. Chem.*, 278(48):48236–48244, 2003.
- [188] R. Daniel, K. Stuert, and G. Gottschalk. Biochemical and molecular characterization of the oxidative branch of glycerol utilization by *Citrobacter freundii*. *J. Bacteriol.*, 177:4392–401, 1995.
- [189] J. B. van Beilen, J. Kingma, and B. Witholt. Substrate specificity of the alkane hydroxylase system of *Pseudomonas oleovorans* GPo1. *Enzyme Microb. Technol.*, 16(10):904–911, 1994.
- [190] J. B. van Beilen, S. Panke, S. Lucchini, A. G. Franchini, M. Roethlisberger, and B. Witholt. Analysis of *Pseudomonas putida* alkane-degradation gene clusters and flanking insertion sequences: evolution and regulation of the alk genes. *Microbiology.*, 147(6):1621–1630, 2001.
- [191] L. Kirmair and A. Skerra. Biochemical analysis of recombinant alkj from *Pseudomonas putida* reveals a membrane-associated, flavin adenine dinucleotide-dependent dehydrogenase suitable for the biosynthetic production of aliphatic aldehydes. *Appl. Environ. Microbiol.*, 80(8):2468–2477, 2014.
- [192] L. Iturrate, I. Sanchez-Moreno, I. Oroz-Guinea, J. Perez-Gil, and E. Garcia-Junceda. Preparation and characterization of a bifunctional aldolase/kinase enzyme: A more efficient biocatalyst for C-C bond formation. *Chem. Eur. J.*, 16(13):4018–4030, 2010.
- [193] M. K. Dreyer and G. E. Schulz. The spatial structure of the class II L-fuculose-1-phosphate aldolase from *Escherichia coli*. *J. Mol. Biol.*, 231(3):549–553, 1993.
- [194] W.-D. Fessner and O. Eyrisch. One-pot synthesis of tagatose 1,6-bisphosphate by diastereoselective enzymatic aldol addition. *Angew. Chem. Int. Ed. Engl.*, 31(1):56–58, 1992.
- [195] A. Jimenez, P. Clapes, and R. Crehuet. Protein flexibility and metal coordination changes in DHAP-dependent aldolases. *Chem. Eur. J.*, 15(6):1422–1428, 2009.

- [196] J. L. Reed, T. D. Vo, C. H. Schilling, and B. O. Palsson. An expanded genome-scale model of *Escherichia coli* K-12 iJR904 GSM/GPR. *Genome Biol.*, 4(9):1–12, 2003.
- [197] R. Gutknecht, R. Beutler, L. F. Garcia-Alles, U. Baumann, and B. Erni. The dihydroxyacetone kinase of *Escherichia coli* utilizes a phosphoprotein instead of ATP as phosphoryl donor. *The EMBO Journal*, 20(10):2480–2486, 2001.
- [198] M. O. Jensen, E. Tajkhorshid, and K. Schulten. The mechanism of glycerol conduction in aquaglyceroporins. *Structure.*, 9(11):1083–1093, 2001.
- [199] P. Nollert, W. E.C. Harries, D. Fu, L. J.W. Miercke, and R. M. Stroud. Atomic structure of a glycerol channel and implications for substrate permeation in aqua(glycero)porins. *FEBS Lett.*, 504(3):112–117, 2001.
- [200] J. Henin, E. Tajkhorshid, K. Schulten, and C. Chipot. Diffusion of glycerol through *Escherichia coli* aquaglyceroporin GlpF. *Biophys. J.*, 94(3):832–839, 2008.
- [201] X. Garrabou, J. Joglar, T. Parella, R. Crehuet, J. Bujons, and P. Clapes. Redesign of the phosphate binding site of L-rhamnulose- 1-phosphate aldolase towards a dihydroxyacetone dependent aldolase. *Adv. Synth. Catal.*, 353(1):89–99, 2011.
- [202] D. E. Atkinson. Energy charge of the adenylate pool as a regulatory parameter. interaction with feedback modifiers. *Biochemistry.*, 7(11):4030–4034, 1968.
- [203] A. Stincone, A. Prigione, T. Cramer, M. M. C. Wamelink, K. Campbell, E. Cheung, V. Olin-Sandoval, N.-M. Gruening, A. Krueger, M. Tauqeer Alam, M. A. Keller, M. Breitenbach, K. M. Brindle, J. D. Rabinowitz, and M. Ralser. The return of metabolism: biochemistry and physiology of the pentose phosphate pathway. *Biol. Rev.*, 90(3):927–963, 2015.
- [204] D. McCloskey, J. D. Young, S. Xu, B. O. Palsson, and A. M. Feist. MID Max: LC-MS/MS method for measuring the precursor and product mass isotopomer distributions of metabolic intermediates and cofactors for metabolic flux analysis applications. *Anal. Chem.*, 88(2):1362–1370, 2016.
- [205] G Bertani. Studies on lysogenesis i. : The mode of phage liberation by lysogenic *Escherichia coli*. *J. Bacteriol.*, 62(3):293–300, 1951.
- [206] M. R. Green and J. Sambrook. *Molecular cloning : a laboratory manual*. Cold Spring Harbor Laboratory Press, Cold Spring Harbor, N.Y, 2012.
- [207] F. W. Studier. Protein production by auto-induction in high density shaking cultures. *Protein Expr. Purif.*, 41(1):207–234, 2005.
- [208] C. Verduyn, E. Postma, W. A. Scheffers, and J. P. Van Dijken. Effect of benzoic acid on metabolic fluxes in yeasts: a continuous-culture study on the regulation of respiration and alcoholic fermentation. *Yeast*, 8(7):501–17, 1992.
- [209] *Mini-PROTEAN 3 Cell - Instruction manual*. Biorad.
- [210] P. N. Royce. Effect of changes in the pH and carbon dioxide evolution rate on the measured respiratory quotient of fermentations. *Biotechnol. Bioeng.*, 40(10):1129–1138, 1992.

- [211] S. Suresh, V. C. Srivastava, and I. M. Mishra. Techniques for oxygen transfer measurement in bioreactors: a review. *J. Chem. Technol. Biotechnol.*, 84(8):1091–1103, 2009.
- [212] F. Garcia-Ochoa, E. Gomez, V. E. Santos, and J. C. Merchuk. Oxygen uptake rate in microbial processes: An overview. *Biochem. Eng. J.*, 49(3):289–307, 2010.
- [213] C. Q. Lan, G. Oddone, D. A. Mills, and D. E. Block. Kinetics of *Lactococcus lactis* growth and metabolite formation under aerobic and anaerobic conditions in the presence or absence of hemin. *Biotechnol. Bioeng.*, 95(6):1070–1080, 2006.
- [214] R. Vinayagam, R.M. Vytla, and M. Chandrasekaran. Development of a simple kinetic model and parameter estimation for biomass and nattokinase production by *Bacillus subtilis* 1A752. *Austin J. Biotechnol. Bioeng.*, 2(1), 2015.
- [215] T. Bayer. *Design, application, and optimization of synthetic enzyme cascades in Escherichia coli*. PhD thesis, TU Wien, 2017.
- [216] D. H. Hua and S. Venkataraman. Preparation of (S)-(-)-4-methyl-2-cyclohexen-1-one. a useful chiral building block. *J. Org. Chem.*, 53(5):1095–1097, 1988.

List of Figures

1.1	Biocatalytic examples	1
1.2	From whole cells, to cell-free extracts and isolated enzymes as biocatalysts.	2
1.3	Whole-cell synthesis of chiral cyclic amines	3
1.4	Whole-cell synthesis of alkanes from free fatty acids	4
1.5	Obstacles in whole-cell biocatalysis: decrease in overall productivity.	5
1.6	Schematic representation for development of biocatalytic processes.	6
1.7	Optimization of a biocatalyst: non-natural carbon-silicon bond formation by an engineered cytochrome <i>c</i> variant from <i>Rhodothermus marinus</i>	7
1.8	The RIPP Scheme of downstream processing.	9
1.9	Comparison of <i>in vivo</i> and <i>in silico</i> methods for biocatalysis optimization.	12
1.10	Knock-out of <i>NemA</i> enables stereoselective biocatalysis.	13
1.11	Knock-out of 7 endogeneous genes improves aldehyde stability <i>in vivo</i> for biocatalysis.	14
1.12	Modular <i>in vivo</i> biocatalysis.	15
1.13	Main steps of kinetic model development.	17
1.14	FBA analysis.	20
1.15	Knock-out (KO) strategies for fumaric acid production.	23
1.16	¹³ C-metabolic flux analysis workflow.	25
2.1	Schematic comparison of the chemical Baeyer-Villiger process by Cortaca <i>et al.</i> (dashed arrow) vs the enzymatic BVMO transformation described in this chapter (solid arrow).	32
2.2	Mechanism and catalytic cycle of flavin-containing BVMOs.	33
2.3	Screening of CHMO _{<i>Acineto</i>} , CPMO _{<i>Coma</i>} and their mutants.	35
2.4	Screening of OTEMO and CPDMO towards conversion of racemic ketone 1	36
2.5	Restriction of pBAD _{cpdmo} and pET26b(+) and purification of CPDMO insert and pET26b(+) backbone.	37
2.6	Expression of pET26b(+) _{cpdmo} in M9 minimal medium.	38
2.7	Comparison of two different Leucine batches with purity $\geq 99\%$	39
2.8	Biotransformation on 4 L scale with simultaneous <i>E. coli</i> BL21(DE3) CPDMO expression during the growth phase: biomass formation, glucose consumption.	40
2.9	Biotransformation on 4 L scale with simultaneous <i>E. coli</i> BL21(DE3) CPDMO expression during the growth phase: Off-gas analysis of the process (OTR and CTR).	41
2.10	Biotransformation on 4 L scale with simultaneous <i>E. coli</i> BL21(DE3) CPDMO expression during the growth phase: ketone and lactone concentrations.	42
2.11	Influence of dioxane on <i>E. coli</i> growth.	43
2.12	Growth curves of <i>E. coli</i> TOP10 harbouring pBAD _{CPDMO} plasmid with different concentrations of ketone 1	45
2.13	Influence of ketone 1 addition on the growth of <i>E. coli</i> , with and without CPDMO expression at 24 °C.	46

2.14	Resin loading study, ketone 1 on Lewatit VP OC 1163 resin.	47
2.15	Biotransformation on a 4 L scale with ketone bound to Levatit VP OC 1163 resin material: biomass formation and glucose concentration.	48
2.16	Biotransformation on a 4 L scale with ketone bound to Levatit VP OC 1163 resin material: off-gas analysis (OTR and CTR).	49
2.17	Biotransformation on a 4 L scale with ketone 1 bound to Levatit VP OC 1163 resin material: conversion of ketone 1 to lactone 2	50
2.18	Cascade reaction from cyclohexenol 6a to ϵ -caprolactone 6e	56
2.19	The cascade example from starting from (1S,5S)-carveol 7a	57
2.20	The cascade example from starting from 2-methyl-cyclohex-2-en-1-ol 8a	57
2.21	Plasmid isolation and control digest of the pET28a_LK-ADH construct.	61
2.22	Expression and purification of Poly-His-tagged LK-ADH.	62
2.23	Activity assay of His-tagged LK-ADH after purification with CaCl ₂ addition.	63
2.24	Activity measurement with purified His-tagged LK-ADH with MgCl ₂ addition.	64
2.25	Workflow of the thrombin restriction experiment.	65
2.26	Gel the thrombin restriction experiment.	66
2.27	IMPACT KIT purification strategy.	68
2.28	<i>Pvu</i> II control digestion of pTYB21_intein-CBD:lk-adh plasmids.	69
2.29	Expression of the CBD-intein-LK-ADH constructs at 25 °C.	70
2.30	Purification and start of on-column cleavage of CBD-intein-LK-ADH construct.	71
2.31	Elution fractions of LK-ADH and cleavage progress on column at 4 °C.	72
2.32	On-column cleavage of CBD-intein-LK-ADH construct at 15 °C.	72
2.33	Purification and on-column cleavage of CBD-intein-LK-ADH at 20 °C.	73
2.34	LK-ADH expression and concentration with a 50 kDa centrifugal device.	74
2.35	XenB expression and purification.	75
2.36	Expression and purification of XenB.	76
2.37	Plot of ADH activity with cyclohexenol (6a) and different ethanol concentrations.	77
2.38	Lineweaver-Burk plot of cyclohexenol (6a) activity with different ethanol concentrations.	78
2.39	Scheme of a mixed type inhibition.	78
2.40	Determination of the inhibitory parameter K_I	79
2.41	Determination of the inhibitory parameter K_{II}	80
2.42	LK-ADH kinetic parameters.	82
2.43	Kinetic parameters of XenB.	84
2.44	Kinetic parameters of CHMO.	85
2.45	Comparison of experimental (data points) with the simulated (lines) concentrations for cascade 6a-e	87
2.46	Comparison of experimental (data points) with the simulated (lines) concentrations for cascade 7a-e	88
2.47	Comparison of experimental (data points) with the simulated (lines) concentrations for cascade 8a-e	89
2.48	Simulated influence of the BVMO concentration on 6d formation.	91
2.49	Simulated influence of the BVMO concentration on 6d formation.	93
2.50	Influence of the cofactors on the <i>in vitro</i> cascade biotransformation.	95
2.51	Simulation of the influence of ethanol on cascade performance.	97
2.52	Simulation of time courses of the cascade starting from 6a	99
2.53	Optimization of CHMO Expression	107

2.54	Verification of the yeast strain characteristics for preparation of ^{13}C internal standard.	109
2.55	Supernatant analysis of CHMO fermentation.	111
2.56	Off-gas analysis of CHMO cultivation.	112
2.57	The concentration of soluble CHMO <i>in vivo</i> decreased during the nitrogen-limited stationary phase.	113
2.58	SDS-PAGE gel for quantification of soluble CHMO.	114
2.59	The specific activity of CHMO decayed rapidly to a basal level, based on the conversion of a fast commercial substrate	115
2.60	Overview over the metabolomics measurements.	116
2.61	The intracellular concentrations of FAD and NADPH were insufficient to stabilize CHMO.	117
2.62	Concentrations of GXP (A), AXP (B) and redox cofactors NADH and NAD (C) decrease in the growing phase and are stable under nitrogen limited conditions.	119
2.63	Glycolytic intermediates (A): fructose-1,6-bisphosphate, 3-phosphoglycerate; TCA intermediates (B): fumarate, malate and the energy charge were stable under nitrogen-limited conditions.	121
2.64	Intracellular concentration of several amino acids.	123
2.65	Mechanism of type I and II aldolases.	128
2.66	Proposed mechanism of DhaK.	129
2.67	Scheme of the DHAP-dependent <i>in vivo</i> cascade in <i>E. coli</i>	130
2.68	Glycolysis and Pentose Phosphate Pathway in <i>E. coli</i>	133
2.69	2D Pareto analysis: DHA uptake vs. biomass formation.	134
2.70	3D Pareto analysis: theoretical DHA uptake vs. biomass formation in <i>E. coli</i> with DHAP-dependent cascade.	136
2.71	3D Pareto analysis: theoretical DHA uptake vs. biomass formation in <i>E. coli</i> with DHAP-dependent cascade and DhaK production.	137
2.72	Glucose consumption of <i>E. coli</i> wt and <i>E. coli</i> DhaK strain in the exponential growth phase.	139
2.73	Growth of <i>E. coli</i> wt and <i>E. coli</i> DhaK strain in the exponential growth phase.	140
2.74	DHA uptake of <i>E. coli</i> wt and <i>E. coli</i> DhaK strain in the exponential growth phase.	141
2.75	Glucose concentration, growth and DHA concentrations of <i>E. coli</i> wt and <i>E. coli</i> DhaK strain in the stationary phase.	143
2.76	Intracellular DHAP concentration in <i>E. coli</i> wt and <i>E. coli</i> DhaK strain in (A) exponential and (B) stationary phase.	144
2.77	Intracellular (A) AMP (B) ADP (C) ATP concentrations and the (D) energy charge in <i>E. coli</i> wt and <i>E. coli</i> DhaK strain in the exponential growth phase.	145
2.78	Correlation of intracellular ATP concentration and DHA uptake.	146
2.79	Stoichiometric modeling of the <i>E. coli</i> BL21 (DE3) wt strain.	148
2.80	Stoichiometric modeling of the <i>E. coli</i> BL21 (DE3) DhaK strain	149
2.81	Stoichiometric modeling of the <i>E. coli</i> BL21 (DE3) DhaK strain.	150
2.82	Intracellular fructose-1,6-bisphosphate concentration of the <i>E. coli</i> BL21 (DE3) DhaK strain.	151
2.83	Metabolite fragment patterns in the LC-MS/MS measurements.	153
2.84	Calculated and measured isotopic distribution of aspartic acid standards.	154
2.85	Calculated and measured isotopic distribution of chemical standards.	156

3.1	Plasmid map of the pET26b(+)_cpdmo construct.	179
3.2	Reduction of 7b to 7c by XenB on preparative scale	193
3.3	LuChe reduction of 8b to 8a	194

List of Tables

2.1	List of symbols and abbreviations for MM kinetics.	59
2.2	Activity of fractions in the thrombin restriction experiment of His-LK-ADH.	67
2.3	Expression screening for CBP-intein-LK-ADH.	70
2.4	Michaelis-Menten parameters for LK-ADH reactions.	83
2.5	Michaelis-Menten parameters reactions with XenB.	84
2.6	Michaelis-Menten parameters for reactions with CHMO.	85
2.7	Adjusted coefficient of determination (R^2) values comparison of modeled vs experimental data.	90
2.8	Experimental protocol of the CHMO fermentation	105
2.9	Abbreviations of enzymes in glycolysis and PPP.	132
2.10	Specific uptake rates for glucose and DHA in the exponential growth phase.	142
3.1	20x NPS salts	162
3.2	50x 5052	162
3.3	M9 medium main solution	163
3.4	100 × M9 trace element solution	163
3.5	5 × salt solution	164
3.6	100 × trace element solution	164
3.7	1000 × vitamin solution	165
3.8	Antibiotics and inducers	165
3.9	50 × TAE buffer	166
3.10	6 × DNA loading dye for agarose gel electrophoresis	166
3.11	SDS gel composition	168
3.12	30 % acrylamide solution	168
3.13	SDS reducing buffer	169
3.14	10x Electrode (Running) Buffer	169
3.15	Parameters in off-gas analysis calculation	171
3.16	Metabolomics MonsterMix for LC-MS/MS calibration (1/3)	174
3.17	Metabolomics MonsterMix for LC-MS/MS calibration (2/3)	175
3.18	Metabolomics MonsterMix for LC-MS/MS calibration (2/3)	176
3.19	MRM precursor ions and fragments for metabolomics measurement	177
3.20	Variations in M9 medium for CPDMO experiments	178
3.21	PCR mix for <i>lk-adh</i> amplification.	185
3.22	Thermal cycle conditions for <i>lk-adh</i> amplification.	185
3.23	<i>SapI/NcoI</i> double digestion.	186
3.24	Ligation of pTYB26_ <i>lk-adh</i>	186
3.25	Conditions for enzyme expression	187
3.26	10x thrombin cleavage buffer	189
3.27	Thrombin restriction of LK-ADH-His ₆	190
3.28	Isotopomer label patterns of the measured fragments (1)	209
3.29	Isotopomer label patterns of the measured fragments (2)	210

3.30 Isotopomer label patterns of the measured fragments (3)	211
--	-----